DISS. ETH NO. 15778

KINEMATICS OF THE KARAKORAM-KOHISTAN SUTURE ZONE, CHITRAL, NW PAKISTAN

A dissertation submitted to the
SWISS FEDERAL INSTITUTE OF TECHNOLOGY ZURICH

for the degree of
Doctor of Natural Sciences

presented by

STEFAN HEUBERGER
Dipl. Natw. ETH Zürich

born on August 6, 1976
citizen of Sirnach (TG), Rickenbach (TG) and Wilen (TG)

accepted on the recommendation of

Prof. Dr. J.-P. Burg	ETH Zürich	examiner
Prof. Dr. U. Schaltegger	Université de Genève	co-examiner
Prof. Dr. A. Zanchi	Università di Milano	co-examiner

2004

"Die verstehen sehr wenig,
die nur das verstehen,
was sich erklären lässt"

Marie von Ebner-Eschenbach

Acknowledgements

Thanks:
Daniel Bernoulli, Universität Basel; Jean-Louis Bodinier, ISTEEM Montpellier (F); Martin Bruderer, ETH Zürich; Jean-Pierre Burg, ETH Zürich; Bernard Célérier, ISTEEM Montpellier (F); Nawaz Muhammad Chaudhry, University of the Punjab, Lahore (PK); Nadeem's cousin, Mansehra (PK); Hamid Dawood, PMNH Islamabad (PK); Mohammed Dawood, Madaglasht (PK); Yamina Elmer, St.Gallen; Martin Frank, ETH Zürich; Maurizio Gaetani, Università degli Studi di Milano (I); the family of Gashish (PK); Urs Gerber, ETH Zürich; Vroni Gubler, Alt St.Johann; Robert Hofmann, ETH Zürich; Shahid Syed Hussain, PMNH Islamabad (PK); Irene Ivanov, ETH Zürich; the family of Mir Azar Khan, Madaglasht (PK); Karsten Kunze, ETH Zürich; Sergio Llana-Funez, University of Manchester (UK); Michael Maxelon, ETH Zürich; Othmar Muentener, Universität Bern; Peter Nievergelt, ETH Zürich; Frowin Pirovino, ETH Zürich; Madaglasht porter (PK); Carol Pudsey, British Antarctic Survey, Cambridge (UK); Urs Schaltegger, Université de Genève; Diane Seward, ETH Zürich; Nadeem Shah, Balakot (PK); Mian Shahab Gul, Chitral (PK); Hidat Ullah, Drosh (PK); Nazir Ullah, Ursun (PK); Martine Vernooij, ETH Zürich; Albrecht von Quadt, ETH Zürich; Igor Villa, Universität Bern; Helmut Weissert, ETH Zürich; Wilfried Winkler, ETH Zürich; Andrea Zanchi, Università degli Studi di Milano-Bicocca (I) and Gerold Zeilinger, Universität Bern.

Contents

Abstract

The continental collision between India and Asia is a reference orogenic system on earth. In NW Pakistan, the intervening Kohistan paleo-island arc complicated the suture system between the two continental plates. The Karakoram was the southern, active margin of Asia from at least the Late Jurassic until the accretion of the Kohistan island arc. The Kohistan arc formed within the Neo-Tethys during the Mesozoic and accreted to the Karakoram likely in the mid-Cretaceous. It then became an Andean-type magmatic arc in Paleocene-Early Eocene times. The Karakoram-Kohistan Suture Zone (KKSZ) marks the locus of the collision between the Karakoram, to the north, and the Kohistan paleo-island arc, to the south. Lenses of serpentinites along the suture are considered to be derived from an oceanic back-arc mantle. To date, classification of the other imbricate units along the suture is still tentative.

To constrain the geological setting, a detailed geological map of the KKSZ in Chitral (NW Pakistan) was made. The map covers a 115 km long segment of the KKSZ between the Pakistan-Afghanistan border, west of Drosh, and Sor Laspur. Field data were geo-referenced and complemented by analysis of Landsat Enhanced Thematic Mapper + (ETM+) images. Geochronological (U-Pb on zircon and Ar-Ar on hornblende) and geochemical analyses (Hf isotopes on dated zircons and whole rock compositions) were carried out on plutonites and volcanites. Deformation structures were studied to reconstruct different phases of shearing and folding along the KKSZ. Paleostress analyses were done on brittle faults to document the younger (subrecent) structural history of the KKSZ.

The new map, the structural, age and geochemistry data show that the KKSZ has a complex and long-lasting kinematic and magmatic history. The map displays a NE-SW trending fault zone containing Karakoram-derived lithologies to the NW, some Kohistan-derived lithologies to the SE and suture-related talcschists, serpentinites and ophicarbonates in between.
To the NW of the suture, shallow water Cretaceous limestones and conglomerates are interlayered with calc-alkaline volcanites. They are interpreted as delta deposits on the shelf of the Karakoram active margin of Eurasia. Greenschist facies serpentinites represent meta-harzburgites brecciated near or at the sea floor and are interpreted as mantle exhumed during the development of the passive Karakoram margin, after rifting of Gondwana.
Calc-alkaline intrusions into the Karakoram and suture zone units are dated between 130 and 104 million years (Ma). They tapped enriched (crustal) to near-MORB-type melt sources and represent subduction-related magmatism

associated with a deformation phase at the southern Karakoram margin, before Karakoram-Kohistan suturing. These intrusions were affected by suturing-related and younger deformation events. Suture zone meta-harzburgites, intruded by 130 and 107 Ma mafic rocks, were serpentinised, brecciated and exposed near or at the sea floor before the mid-Albian (107 Ma).
Age constraints in northern Kohistan are given by a 112 Ma calc-alkaline diorite that (1) intruded andesites interlayered with Aptian limestones, (2) is unconformably overlain by red alluvial or deltaic clastites of unknown age and (3) has hafnium isotopic ratios indicative for a MORB-type melt source. Andesites and the diorite represent calc-alkaline, island arc magmatism during Early to mid-Cretaceous times. 50 to 39 Ma gabbros and granites show different melt types (tholeiitic and calc-alkaline) and sources (near-MORB-type and strongly crustally contaminated). They represent magmatism post-dating the Kohistan-India collision and are associated with suture-related, ductile, sinistral transpression that lasted until the Early Eocene.
Paleostress analyses show that most of the brittle faults along the KKSZ are related to (ongoing?) sinistral transpression with a NW-SE compression direction more or less fitting the recent regional stress field.

Kurzfassung

Die Kontinent-Kontinent-Kollision zwischen Indien und Asien gilt als Referenzsystem für Orogene der Erde. Der Kohistan Paläo-Inselbogen liegt zwischen den zwei kontinentalen Platten als Teil des Indien-Asien-Sutursystems in NW Pakistan. Der Karakorum bildete den südlichen, aktiven Kontinentalrand Asiens seit mindestens dem Späten Jura bis zur Akkretion des Kohistan Inselbogens. Der Kohistan Inselbogen entstand in der Tethys im Laufe des Mesozoikums und kollidierte mit dem Karakorum-Kontinentalrand wahrscheinlich in der mittleren Kreide. Später, nach der Kollision mit Indien während des Paläozän-Eozän, wurde er dann zum magmatischen Bogen (Anden-Typ). Die Karakorum-Kohistan Sutur Zone (KKSZ) markiert den Ort der Kollision zwischen dem Karakorum im Norden und dem Kohistan Paläo-Inselbogen im Süden. Man nimmt an, dass Serpentinitlinsen entlang der Sutur vom ozeanischen Mantel auf der Hinterseite (im Norden) des Bogens stammen. Die Klassifikation der anderen eingeschuppten Gesteinseinheiten entlang der Sutur ist jedoch bis heute nur provisorisch.

Eine detailierte geologische Karte der KKSZ in Chitral (NW Pakistan) wurde erstellt um den geologischen Aufbau der Sutur zu dokumentieren und zu verstehen. Die Karte deckt ein 115 km langes Segment der KKSZ zwischen der pakistanisch-afghanischen Grenze, westlich von Drosh, und Sor Laspur ab. Felddaten wurden georeferenziert und mittels Analysen von Satellitenbildern (Landsat Enhanced Thematic Mapper +) ergänzt. Geochronologische (U-Pb an Zirkonen und Ar-Ar an Hornblenden) und geochemische Analysen (Hf Isotope der datierten Zirkone und Gesamtgesteinszusammensetzungen) wurden an Plutoniten und Vulkaniten durchgeführt. Deformationsstrukturen wurden untersucht um verschiedene Scherungs- und Faltungsphasen entlang der KKSZ zu rekonstruieren. Paläospannungsanalysen an spröden Verwerfungen wurden gemacht um die jüngere (subrezente) strukturelle Geschichte der KKSZ zu dokumentieren.

Die neue Karte, die Struktur-, Alters- und Geochemiedaten zeigen, dass die KKSZ eine komplexe und langandauernde, kinematische und magmatische Geschichte hat. Die Karte stellt eine NE-SW verlaufende Störungszone dar, die im NW Lithologien mit Karakorum-Herkunft, im SE Lithologien mit Kohistan-Herkunft und dazwischen Talkschiefer, Serpentinite und Ophikarbonate der Sutur enthält.
Flachwasserkalke und Konglomerate aus der Kreide enthalten einzelne Lagen kalkalkalischer Vulkanite und sind im NW der Sutur aufgeschlossen. Sie werden als Deltaablagerungen auf dem eurasiatischen Schelf des aktiven

Karakorum-Kontinentalrands interpretiert. Grünschieferfazielle Serpentinite in der Sutur repräsentieren Metaharzburgite, die nahe oder am Meeresboden brekkziert wurden. Sie werden als Mantelgesteine interpretiert, die während der Entstehung des passiven Karakorum-Kontinentalrands, nach dem Aufbrechen von Gondwana, exhumiert wurden.
Kalkalkalische Intrusionen in die Einheiten des Karakorums und der Sutur Zone wurden auf 130 bis 104 Millionen Jahre (Ma) datiert. Sie wurden von Schmelzen mit einer angereicherten (krustalen) bis fast-MORB-Typ Signatur gespiesen und stellen einen subduktionsbezogenen Magmatismus dar, der mit der Deformationsphase am südlichen Karakorumrand, vor der Kohistan-Karakorum-Kollision, zusammenhängt. Diese Intrusionen wurden später von suturbezogenen und jüngeren Deformationsereignissen überprägt. Die Metaharzburgite in der Sutur, die zwischen 130 und 107 Ma von mafischen Gesteinen intrudiert wurden, waren vor dem mittleren Apt (107 Ma) schon serpentinisiert, brekkziert und befanden sich nahe oder am Meeresboden.
Gesteinsalter im nördlichen Kohistan sind gegeben durch einen kalkalkalischen, 112 Ma alten Diorit, der (1) Andesite, mit Zwischenlagen von Kalksteinen aus dem Apt, intrudierte, (2) überlagert wird von roten, klastischen Delta- und alluvialen Ablagerungen unbestimmten Alters und (3) Hafnium Isotopenverhältnisse hat, die eine Schmelzesignatur des MORB-Typs zeigt. Andesite und der Diorit repräsentieren kalkalkischen Inselbogen-Magmatismus in der Frühen bis mittleren Kreide. 50 bis 39 Ma alte Gabbros und Granite weisen verschiedene Schmelzetypen (tholeiitisch und kalkalkalin) und -quellen (fast-MORB-Typ und stark krustal kontaminierte) auf. Sie repräsentieren einen Magmatismus, der nach der Kohistan-Indien-Kollision statt fand und mit einer subduktionsbezogenen, duktilen, sinistralen Transpression zusammenhängt, die bis ins frühe Eozän dauerte.
Paläospannungsanalysen zeigen, dass die meisten spröden Verwerfungen entlang der KKSZ mit der (immer noch andauernden?) sinistralen Transpression zusammenhängen, die eine NW-SE Kompressionsrichtung hat, welche ungefähr mit dem heutigen, regionalen Spannungsfeld übereinstimmt.

Chapter 1: Introduction

1. General background

The Karakoram-Kohistan Suture Zone (KKSZ) separates the Karakoram block of the Cretaceous Eurasian margin from the Kohistan paleo-island in north-western Pakistan. This major fault zone is regarded as a suture since the Kohistan was recognised as a paleo-island arc (Tahirkheli *et al.* 1979, Bard *et al.* 1980). It is called Shyok Suture further east, in northern Ladakh where it bounds the Ladakh paleo-island arc (the eastern equivalent of the Kohistan paleo-island arc) from the Karakoram (Honegger *et al.* 1982). The Kohistan intra-oceanic island arc is thought to have accreted to the Karakoram before 85-75 Ma (Treloar *et al.* 1989, Searle *et al.* 1999). It then became an Andean-type magmatic arc in Paleocene-Early Eocene times until collision with India at 65-50 Ma (Gansser 1964, Molnar & Tapponnier 1975, Jaeger *et al.* 1989 and many later authors).
The Indus Suture separates the Kohistan paleo-island arc, to the north, from the Indian plate, to the south. It represents, together with the Karakoram-Kohistan Suture, the western continuation of the Yarlung-Tsangpo Suture separating India from Eurasia to the north of the Himalaya mountain range (Fig. 1.1).
Pudsey *et al.* (1985) and Pudsey (1986) studied the Karakoram-Kohistan Suture between Drosh and Hunza in northern Pakistan and interpreted it as an olistostrome-type mélange zone containing blocks of volcanic greenstones, limestones, red shales, conglomerates, quartzites and serpentinites. This ‘mélange’ was inferred to be derived mainly from the Kohistan arc and formed in a small back-arc basin. Limestone blocks within the mélange were dated as Aptian-Albian and ‘post-tectonic’ intrusions yielded K-Ar ages from 111 to 62 Ma (Albian to early Paleocene, Pudsey 1986). The Karakoram-Kohistan Suture was therefore believed to have formed in the Late Cretaceous during the closure of the back-arc basin between the Kohistan island arc and the Karakoram. Serpentinites were considered to be derived from the back-arc basin. Pudsey (1986) did not find evidence for the consumption of a major ocean along the KKSZ.
Ar-Ar and U-Pb dating of subduction-related intrusions revealed an intense magmatic phase in the Karakoram during the late Early Cretaceous (ca. 120-100 Ma, e.g. Le Fort *et al.* 1983, Parrish & Tirrul 1989, Searle *et al.* 1990, Searle 1991, Debon 1995). In the Kohistan, magmatism was documented between the mid Early Cretaceous until the Oligocene (ca. 112-28 Ma, e.g. Zeitler *et al.* 1981, 1985, Petterson & Windley 1985, Treloar *et al.* 1989) with increased intensity during the Eocene. The cessation of calc-alkaline

magmatism in the Karakoram at around 100 Ma and the intense magmatic phase in the Kohistan during the Eocene led some authors (e.g. Crawford & Searle 1992 and Debon 1995) assume that the southward shift of magmatic activity is related to accretion of the Kohistan island arc to the Karakoram margin some time during the Late Cretaceous-Paleocene.

2. Problem statement

The timing of the Karakoram-Kohistan collision spans a large amount of time. Different ages have been proposed: Petterson & Windley (1985) suggested the time interval between 102 and 75 Ma for the collision, whereas Treloar *et al.* (1996) suggested to reduce the interval to 102 to 85 Ma. Both statements are based on disputable criteria, such as ascribing the deformation fabrics in northern Kohistan - reputedly being penetrative throughout that area - to the Karakoram-Kohistan collision. Geological mapping with detailed descriptions of intrusional relationships and deformation fabrics is sporadic along the KKSZ. In addition, reliable magmatic or metamorphic ages, constraining the kinematics of the Karakoram-Kohistan collision, are rare.
The imprecise timing of the Karakoram-Kohistan collision is a major problem for the understanding of the regional, NW Himalayan collision tectonics. The timing of collision is crucial for the reconstruction the Kohistan arc magmatic history, as it marks the shift from island arc to continental, Andean-type, arc magmatism.
The lacking collision age and detailed structural descriptions are also a problem for the comprehension of the Karakoram-Kohistan suturing process. Are there several deformation and/or magmatic phases related to the collision? Which deformation fabrics in the southern Karakoram and northern Kohistan are related to the collision, which are older or younger?

3. Aims

In view of the problems and questions identified above, this thesis aims to provide fundamental geological data from the KKSZ. Emphasis is given to lithological and structural mapping along several sections across the suture zone and radiometric dating on intrusions. On the basis of these new data, a broad paleogeographic setting of the southern Karakoram margin, the northern Kohistan paleo-island arc and the intervening oceanic basin will be reconstructed. Intrusion ages will provide constraints on tectonomagmatic events to unravel the polyphase kinematic history of the Karakoram-Kohistan

accretion. Furthermore, brittle fault slip data will be used to calculate paleo-stress tensors in order to reconstruct the recent stress field, and thus the recent brittle faulting along the KKSZ.

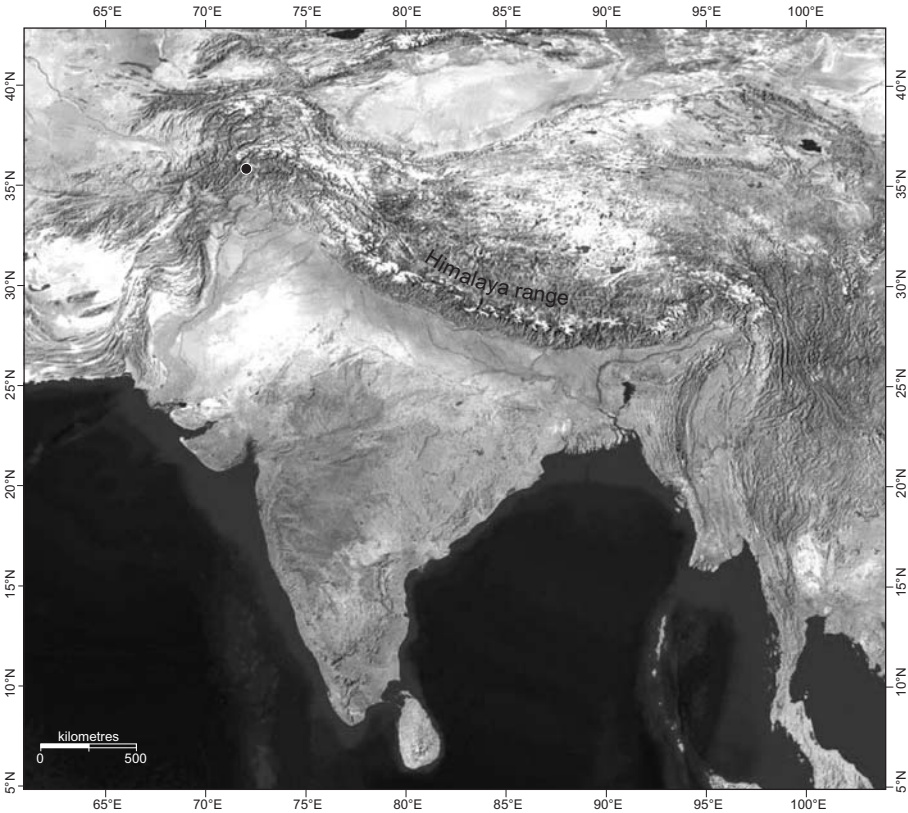

***Fig. 1.1**. Satellite image of SE Asia, from Afghanistan, to the west, to Burma and Thailand, to the east; and from China, to the north, to India, to the south. The Himalaya mountain range trends NW-SE to E-W separating Tibet (China), to the north, from India, to the south. The black circle with a white rim at 72°E/35°N marks the location of the field area in NW Pakistan (image compiled from data at www.geographynetwork.com).*

4. Methodology and organisation of the thesis

This study combines field and analytical work, both performed to achieve the specific aims mentioned above. As introduction and background overview to the new field data, a literature review of the regional geology of the Eastern Hindu Kush, the Karakoram and the Kohistan blocks with their bounding sutures is given in **chapter 2**. It focuses on geological data (petrography,

sedimentology, structures) and stratigraphic and radiometric (U-Pb and Ar-Ar) ages. **Chapter 3** reports the results of 6 months field work and documents the resulting 1:100,000 Geological Map (enclosed) of a 115 km long segment of the KKSZ in NW Pakistan. Field work was focused on lithological and structural descriptions in order to define stratigraphic and tectonic units in, from north to south, (1) the southern Karakoram, (2) the suture zone and (3) the northern Kohistan. The digitalised field map was extended using Landsat Enhanced Thematic Mapper + (ETM+) images. The resulting Geological Map (enclosed) was published together with the chapters 2 and 3 as explanatory notes*. In **chapter 4** paleo-stress analyses from fault slip data from the suture zone are presented. The resulting stress tensors reveal different stress fields that controlled the brittle reactivation of older, suture-related faults and/or growth of new faults. The geochronological results are documented in **chapter 5**. Nine U-Pb intrusion ages, measured on zircon with the standard isotope dilution - thermal ionisation mass spectrometry (ID-TIMS) technique, are presented. Three Ar-Ar ages on hornblende, are used to constrain ambivalent U-Pb zircon data or to obtain an age on one sample that contained no zircon. In addition, Hf isotopes, measured on the dated zircons by multi-collector inductively coupled plasma mass spectrometry (ICP-MS), are utilised to get constraints on the melt sources of the intrusions. Preliminary whole rock geochemistry data are presented in the **Appendix A**. Major, trace and rare earth element content of twenty-two volcanites and twelve intrusions (among which those that were dated) were analysed by X-ray fluorescence (XRF) and ICP-MS techniques. To conclude, the results of the thesis are summarised and discussed in **chapter 6**.

* Heuberger, S., 2004, The Karakoram-Kohistan Suture Zone in NW Pakistan - Hindu Kush Mountain Range, Geological map and explanatory notes, *vdf Hochschulverlag AG an der ETH Zürich*, ISBN 3 7281 2965 8.

Chapter 2: Geological setting and tectonic evolution of the northwestern Himalaya

1. Preface

The Himalayan orogen is a classical example of continent-continent collision (e.g. Argand 1924, Molnar & Tapponnier 1975). The northwestern part of the mountain belt is composed of terranes formed during the India-Asia convergence (Kohistan and Ladakh island arcs, Tahirkheli *et al.* 1979, Honegger *et al.* 1982 and others), as well as blocks of Gondwana affinity (e.g. Karakoram, Eastern Hindu Kush; Tapponnier *et al.* 1981, Boulin 1988, Gaetani *et al.* 1996, Fig. 2.1).

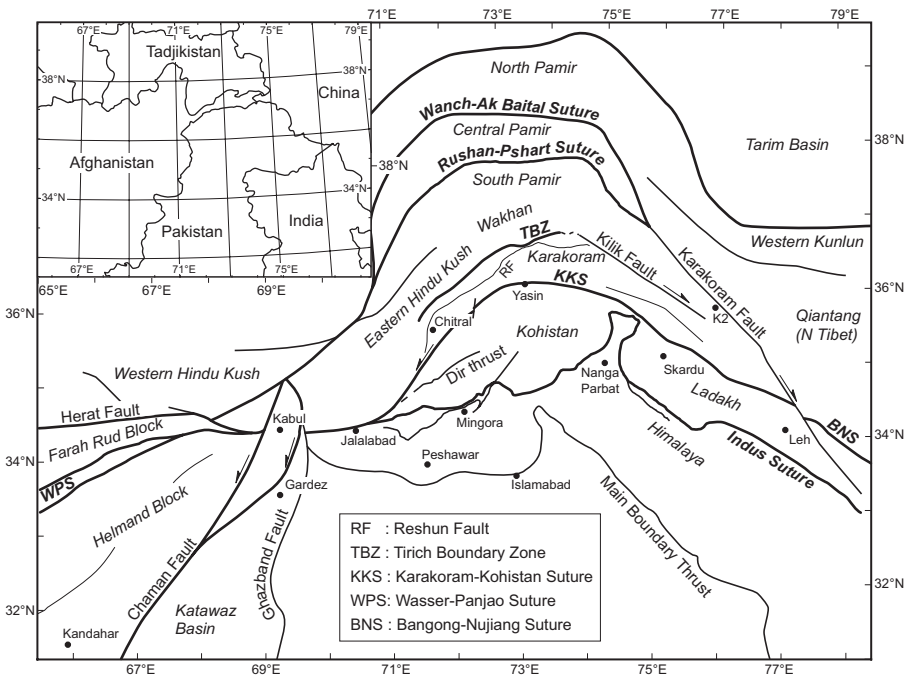

Fig. 2.1. *Tectonic sketch map of Central Asia. Faults and sutures are drawn from Landsat Thematic Mapper images (https://zulu.ssc.nasa.gov/mrsid) and named after Schreiber et al. (1972), Lawrence et al. (1992), Gaetani et al. (1996), Zanchi et al. (2000), Robinson et al. (2000) and Gaetani et al. (2004).*

These continental blocks began separating from the Gondwana super-continent in the latest Paleozoic, drifted northwards and accreted to the Eurasian margin in the Mesozoic and Cenozoic (Boulin 1981). The north-western Himalaya therefore archives a polyphase record of accretion and deformation prior to the India-Asia continent-continent collision at 65-50 Ma (Gansser 1964, Molnar & Tapponnier 1975, Jaeger *et al.* 1989 and many later authors). The distinction between the different terranes is still preliminary and based mainly on stratigraphic correlations (Zanchi *et al.* 2000).

The tectonic evolution and a brief geological setting of the terranes and their sutures in Chitral (NW Pakistan, Fig. 2.2) is described in the light of a literature review. Well constrained geochronological data is summarised in Table 2.1.

Fig. 2.2. *Provinces and districts of Northwestern Pakistan (data from www.geographynetwork.com and www.northernareas.org.pk). Country borders: heavy lines; province borders: bold dashed lines; district borders: thin dashed lines; rivers: thin lines.*

2. Eastern Hindu Kush

2.1 Introduction

Geographically, the Hindu Kush is a NE-SW oriented, more than 600 km long mountain range in northeastern Afghanistan and in the very northwestern edge of Pakistan with the Tirich Mir (7,708 m) marking its highest elevation (Fig. 2.3). The Eastern Hindu Kush terrane, called *Nurestan* by Tapponnier *et al.* (1981), is located in the northeastern part of this range. Little geological documentation is available due to the remoteness of the region.

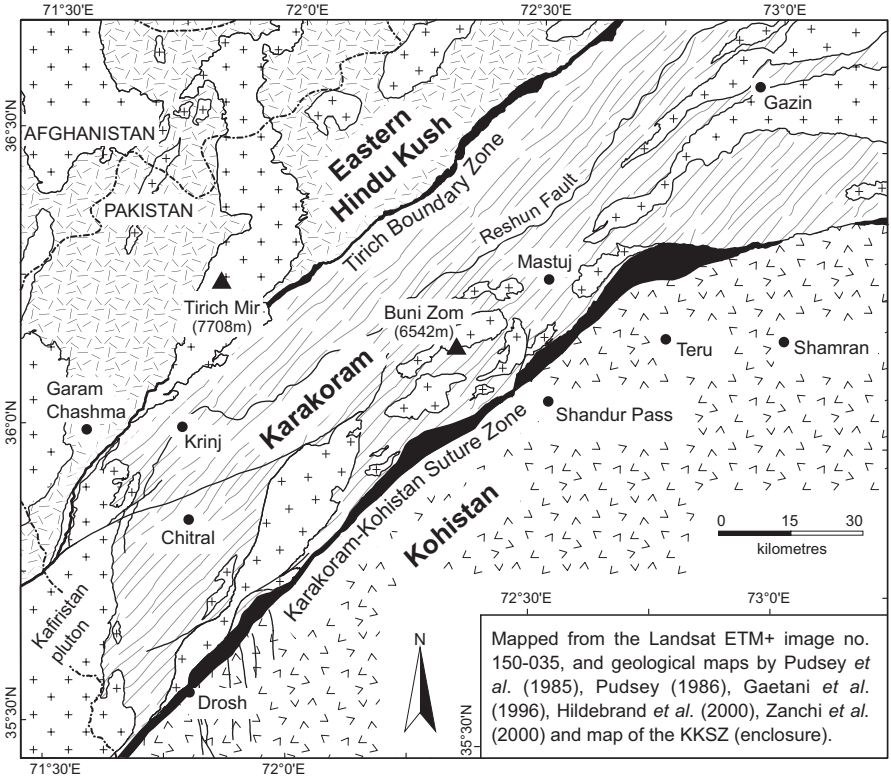

Fig. 2.3. *Geological sketch map of Chitral (NW Pakistan).*

The East Hindu Kush in the Chitral district consists mainly of the Paleozoic Wakhan slates and upper Paleozoic to Oligocene granitoid intrusions, many of which trending N-S to NE-SW (Fig. 2.3). The Tirich Boundary Zone (TBZ,

Zanchi *et al.* 2000) separates the Eastern Hindu Kush to the northwest from the Western Karakoram (Gaetani *et al.*1996) to the southeast (Fig. 2.3).

2.2 Tectonic evolution

In this section the tectonic evolution of the Eastern Hindu Kush is summarised.

2.2.1 Late Paleozoic to Early Jurassic: Northward drift of the Cimmeride continent

The Eastern Hindu Kush seems to be the western continuation of the Wakhan block (Gaetani 1997). The Paleozoic and Triassic successions (the so-called Wakhan slates, Hayden 1915, Desio 1963, Kafarskyi & Abdullah 1976, Buchroithner 1980 and Gaetani & Leven 1993) of the Wakhan block and the Eastern Hindu Kush separate the Karakoram from the South Pamir (Gaetani 1997). They document a terrigenous input from Gondwana and deposition into rapidly subsiding basins denoting a region of thinned continental crust (Gaetani 1997). Several small terranes (e.g. Karakoram, Eastern Hindu Kush, Helmand, Central and South Pamir, Lhasa), forming the so-called *Cimmeride Continent* (Fig. 2.4, Sengör 1984), rifted away from Gondwana and started to drift northwards between the Permian and late Triassic as a consequence of the opening of the Neo-Tethys (Boulin 1981, Sengör 1984, Gaetani 1997). Northward directed subduction of the Paleo-Tethys promoted the accretion of these continental blocks to the southern margin of Eurasia some time in the Jurassic (Dronov *et al.* 1982, Sengör 1984, Gaetani 1997, Fig. 2.4).
The distinction of the Cimmeride terranes is tentative and refers to large-scale stratigraphic correlations and tectonic models.
A Permo-Triassic shallow water carbonate terrigenous sequence, the Atark Unit (Buchroithner 1978, Buchroithner 1980), was deposited on rift-shoulders (Gaetani & Leven 1993). The unit is bounded by the TBZ to the south and an unnamed fault to the north (Gaetani *et al.* 1996). Locally, gallstones and marbles (Atark Unit) are unconformably overlain by a strongly deformed reddish conglomerate (Zanchi *et al.* 1997). To the north, these rocks are intruded by the mid-Cretaceous Tirich Mir pluton (115±4 Ma, Rb-Sr on biotite, Desio *et al.* 1964) and the Rich Gol plutons further northeast (Gaetani & Leven 1993, Zanchi *et al.* 1997). Outcrop-scale, NE-SW trending recumbent folds, some of which associated with southeast-directed thrusts, imply local tectonic repetitions (Gaetani & Leven 1993, Zanchi *et al.* 1997).
Early Jurassic crustal melting in the Eastern Hindu Kush is documented by a ca. 195 Ma foliated leucogranite intruding migmatites in the upper Lutkho Gol (U-Pb on monazite, Hildebrand *et al.* 2000, Garam Chashma area, Fig. 2.3).

Hildebrand *et al.* (2000) concluded that this leucogranite intruded prior to or during the presumably regional accretion-related deformation. However, a plate tectonic interpretation remains difficult as this is the only known sign of Jurassic crustal melting along the southern Eurasian margin.

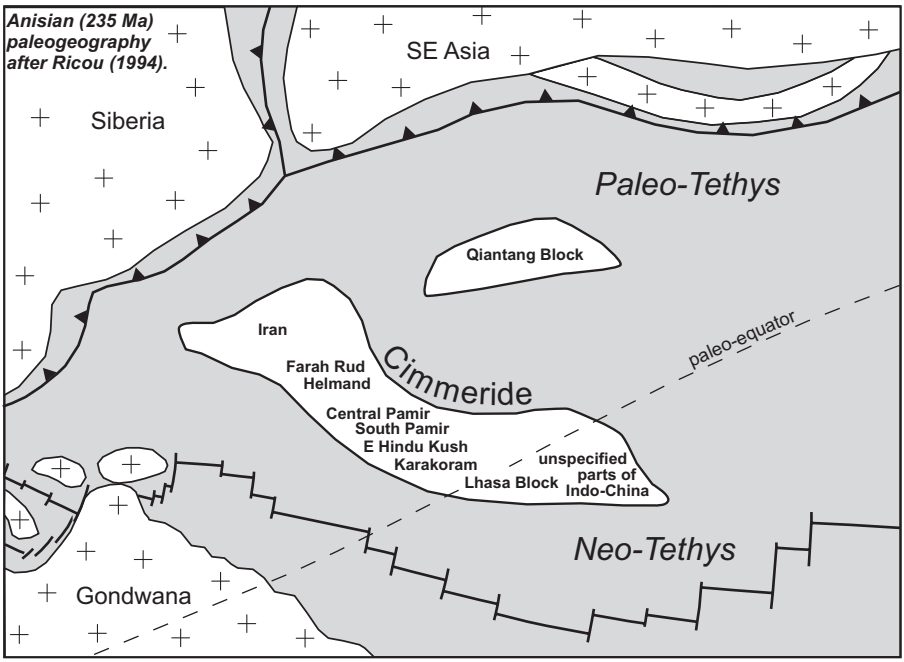

Fig. 2.4. *Simplified sketch map of the Cimmeride continent. The different microcontinents are tentatively located after Tapponnier et al. (1980), Boulin (1981) and Gaetani (1997). The heavy line with triangles represents the subduction zone at the Asian and Siberian margins, the heavy line the ridge in Neo-Tethys.*

2.2.2 Jurassic to Early Cretaceous: Ongoing convergence

Ongoing northward directed subduction along the southern side of the Cimmeride continent likely resulted in intrusions (e.g. Tirich Mir and Kafiristan plutons in the Chitral area, Fig. 2.3) forming a subalkaline to calc-alkaline granitoid belt from Chitral to central Afghanistan (Debon *et al.* 1987b). Seaways with thinned continental crust within the Cimmeride continent have been closed during ongoing convergence (Gaetani 1997).
Hildebrand *et al.* (2001) determined a U-Pb age of 135-126 Ma on metamorphic monazite in staurolite-grade meta-pelites (Garam Chashma area, Fig. 2.3) They interpreted it as a minimum age for metamorphism. The common occurrence of andalusite, and less common sillimanite during this earliest-recorded metamorphism in the Eastern Hindu Kush suggest a high

geothermal gradient (Hildebrand *et al.* 2000, 2001). Hence these authors argued that the high heat flow combined with the probable Jurassic-Early Cretaceous age of metamorphism and the abundance of subalkaline to calc-alkaline granitoid intrusions (Debon *et al.* 1987b) may be linked with an active continental margin.

2.2.3 Early to mid-Cretaceous: Subduction-related magmatism (intrusion of the Tirich Mir pluton)

Desio *et al.* (1964) published a 115±4 Ma age (Rb-Sr on biotite) for the Tirich Mir pluton. As this intrusion crosscuts the TBZ, it represents a minimum age for the suturing between the Western Karakoram and Eastern Hindu Kush terranes. However, the Rb-Sr age may be inaccurate due to pervasive alteration of biotite (Villa, pers. comm.).
Evidence for Cretaceous deformation at the southern Eurasian margin is reported mainly in the Karakoram (section 3.3.6). Metamorphic textures and structures from the Garam Chashma area suggest that Jurassic deformation in the Eastern Hindu Kush had likely ended prior to Early to mid-Cretaceous thrusting along the Tirich Boundary Zone (Hildebrand *et al.* 2000, 2001). A foliated pegmatitic dyke crosscutting staurolite-grade meta-pelites in Garam Chashma yielded an age of 114±2 Ma (U-Pb on uraninite, Hildebrand *et al.* 2001). It is considered to be synchronous with thrusting along the Tirich Mir pluton fault, the southwestern limit of the Tirich Mir pluton (Hildebrand *et al.* 2000, 2001).
Another sample of the staurolite-schists dated by Hildebrand *et al.* (2001) yielded an age of 106-102 Ma (U-Pb on monazite) documenting deformation and metamorphism in the Early to mid-Cretaceous.

2.2.4 Early Miocene: Crustal shortening and intrusion of the Garam Chashma leucogranites

There is no record of deformation or magmatism in the Eastern Hindu Kush between the mid-Cretaceous and the early Miocene (Hildebrand *et al.* 2001). It is unclear whether this lack of information reflects the geological history over 80-90 Ma, or if it is due to the missing geological information.
A 24.0±0.5 Ma undeformed leucogranite body (U-Pb on xenotime and monazite, Hildebrand *et al.* 1998) intruded garnet-staurolite schists of the Eastern Hindu Kush in the Garam Chashma area. A 24.2±0.2 Ma (U-Pb on monazite, Hildebrand *et al.* 1998) undeformed leucogranitic dyke intruded migmatites.
These ca. 24 Ma leucogranitic intrusions imply crustal melting in the Eastern Hindu Kush contemporaneous with 26-21 Ma granitic intrusions in the Baltoro

Karakoram, 400 km to the east (Parrish & Tirrul 1989, Schärer *et al.* 1990). Hildebrand *et al.* (2000) reported a deformation phase probably synchronous with the emplacement of the leucogranites. They related this deformation to 'thrusting-assisted' intrusion and crustal shortening that was accommodated by open to tight folding and thrusting in the area.

2.2.5 Middle Miocene to present: Left-lateral reactivation of major faults and recent seismicity

Hildebrand *et al.* (2000) described NNE-SSW trending sub-horizontal stretching lineations overprinting pre-Middle Miocene structures striking also NNE-SSW. These are possibly the only post-24 Ma structures reported from the Eastern Hindu Kush.

Evidence for sinistral lateral shear-movement on reactivated faults is reported in the Western Karakoram in Chitral and its bounding NE-SW striking fault zones, the Tirich Boundary Zone and the Karakoram-Kohistan Suture Zone (sections 3.3.10, 4.2 and 6.2). Hildebrand *et al.* (2000, 2001) therefore inferred a sinistral transpression tectonic regime which is attributed to the progressive indentation of India into Eurasia (Tapponnier *et al.* 1981) and a possible anticlockwise regional rotation.

The Pamir-Hindu Kush region is today one of the most active regions of deep (~70-300 km) seismicity (Pegler & Das 1998, Fig. 2.5). This seismicity is attributed to a remnant oceanic slab likely derived from northward subduction of the Neo-Tethys basin at the Eurasian margin after the collision of India with Kohistan (Roecker 1982, Pegler & Das 1998, Pavlis & Das 2000).

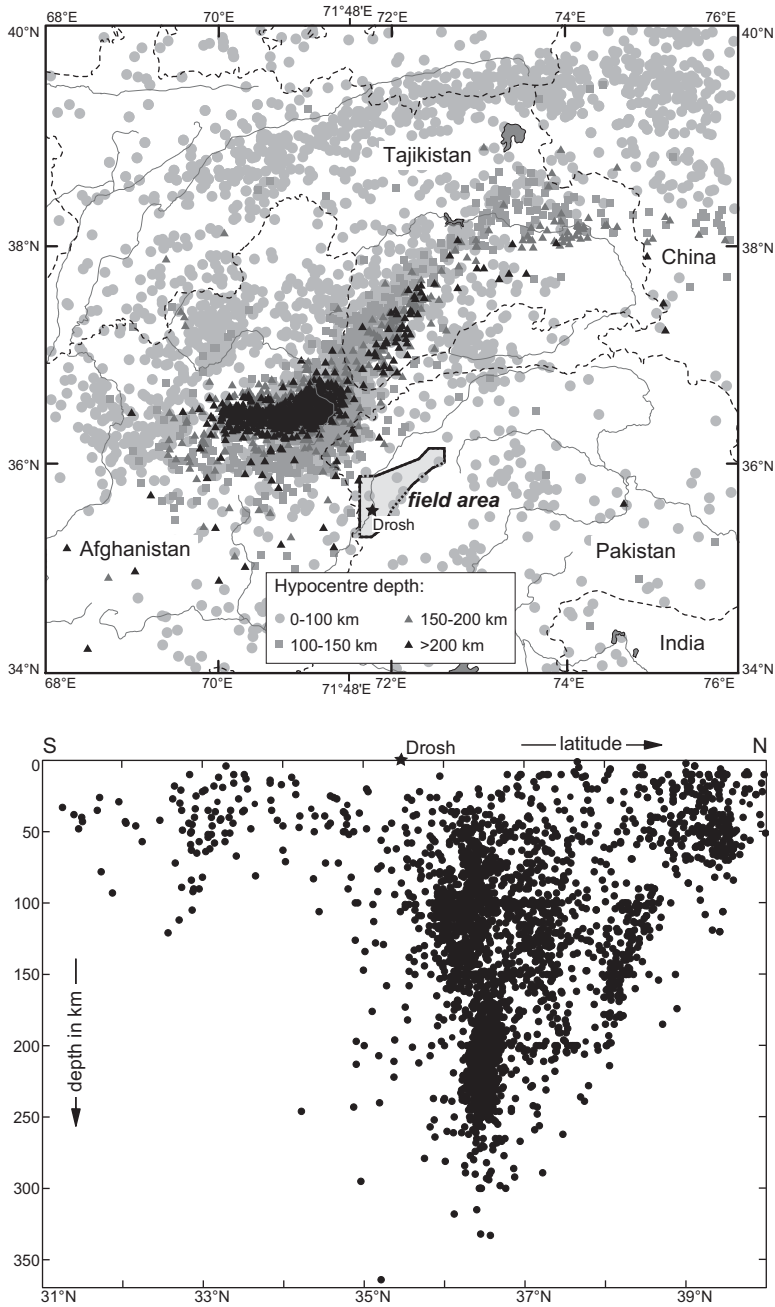

Fig. 2.5. *Top: Earthquake hypocentres distribution map; bottom: data projected onto N-S section at 71°48'E, Eastern Hindu Kush-Pamir region. Data from the NEIC (2004).*

2.3 Summary and discussion

The Jurassic to Late Cretaceous Eastern Hindu Kush represents a magmatically and tectonically thickened active continental margin. The mid-Cretaceous Tirich Mir pluton likely represents a western continuation of the ca. 120-100 Ma intrusions of the subduction-related Karakoram Axial Batholith (section 3.2.2). It also marks an upper age limit for high-grade regional metamorphism in the Eastern Hindu Kush and the formation of the Tirich Boundary Zone.
Late Oligocene-Early Miocene (26-21 Ma) crustal melting-derived leucogranites may represent post-India-Asia-collision magmatism in the Eastern Hindu Kush.

The role of the Eastern Hindu Kush as part of the Cimmeride continent is still ambiguous. It is unclear whether the Hindu Kush was a continental block separated by oceanic basins from the South Pamir (to the north) and the Karakoram (to the south). Furthermore, there is no chronological evidence for the accretion to the southern Eurasian margin.

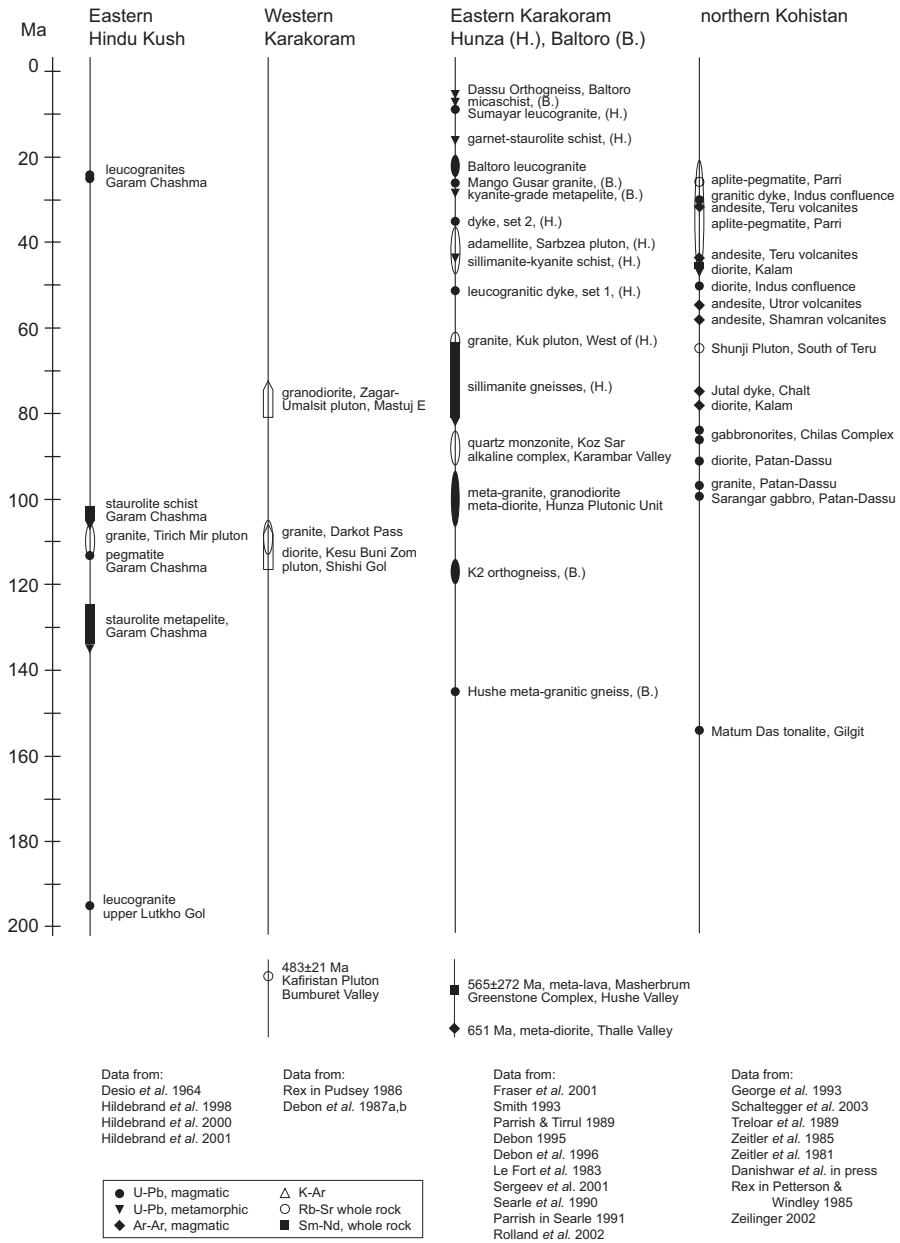

Table 2.1. *Geochronological ages of magmatic and metamorphic rocks in the Eastern Hindu Kush, the Karakoram and the northern Kohistan arc.*

3. Western Karakoram

3.1 Introduction

The elongate Karakoram terrane is squeezed between the composite Eurasian margin to the north and the Kohistan paleo-island arc to the south. In the west, the southern geological boundary is formed by the Karakoram-Kohistan Suture; and the northern boundary was set at the Tirich Boundary Zone (Gaetani *et al.* 1996, Zanchi *et al.* 2000). The Tirich Mir Fault (Buchroithner and Gamerith 1986, section 4.1), the northern limit of the Tirich Boundary Zone, may be linked eastwards with the Kilik Fault (Gaetani 1997, Gaetani *et al.* 2004) in the Hunza area (Fig. 2.1). The Farah Rud and the Helmand Blocks in central Afghanistan are regarded as western continuations of the Karakoram (Boulin 1981, Tapponnier *et al.* 1981, Sengör 1984, Fig. 2.1 and section 2.2.1).
To the east, the Lhasa terrane (S Tibetan Block) may be equivalent to the Karakoram, but the large dextral offset along the Karakoram fault (~1000 km, Peltzer & Tapponnier 1988; Fig. 2.1) makes correlations across this fault hazardous (Kapp *et al.* 2003).

3.2 Geological setting

3.2.1 Western Karakoram

The term *Western Karakoram* is used in this study for the segment of the *geological* Karakoram to the west of the Ishkuman valley. Metamorphic grade in the southern Karakoram lithologies is low (Pudsey 1986) and lithologies trend NE-SW to E-W in contrast to the high-grade NW-SE trending units in the east (Hunza and Baltoro areas).
The Western Karakoram is divided by the Reshun Fault into two major units, the *northern* and the *southern units* (Pudsey *et al.* 1985). The reverse Reshun Fault brings Paleozoic sediments in the north onto Paleozoic to Mesozoic meta-sediments in the south (Fig. 2.3). It can be traced from the upper Yarkhun valley and further east to the Baroghil and Chillinji Passes in the Afghanistan-Pakistan border area (Gaetani *et al.* 2004). The fault is unconformably overlain by the probably Cretaceous Reshun Formation (Hayden 1915, Desio 1963, Pudsey *et al.* 1985) in the east. Elsewhere, the Reshun Formation is the uppermost formation of the southern unit in the footwall of the

Reshun Fault (Pudsey *et al.* 1985). Hence, some segments of the Reshun Fault have been reactivated after the deposition of the Reshun Formation.
Northern unit lithologies, interpreted as western equivalents of the *Northern Sedimentary Belt* of the Eastern Karakoram (Zanchi *et al.* 2000 and ref. therein), include mainly low-grade, shelf-type meta-pelites, -carbonates, -sandstones, -volcanites and -volcanoclastic rocks. Open to tight, outcrop-scale folds have axes trending regionally NNE-SSW to ENE-WSW. The steeply WNW to NNW dipping units are separated by faults along which subhorizontal striation lineations occur. These lithologies and structures were described by Pudsey *et al.* (1985), Gaetani *et al.* (1996), Zanchi *et al.* (2000) and Hildebrand *et al.* (2000).
The age of the southern unit shelf-type sediments is ill constrained because almost no fossils were found. There is evidence for the slates and quartzites of the Darkot Group to be Carboniferous to Uppermost Permian (Ivanac *et al.* 1956, Pudsey & Gupta 1985) and for the Krinj Limestone to be Early Cretaceous (Desio 1959). Elongate limestone pebbles of the Reshun Conglomerate contain rudists (as in underlying Karakoram carbonates) the youngest of which are Aptian-Albian (Talent *et al.* 1982, Pudsey *et al*. 1986). There is no upper age limit for this conglomerate.
Pudsey *et al.* (1985) described stretching lineations in the southern unit displaying two major orientations. The older one trends subhorizontally NE-SW and the younger, less pronounced one, plunges steeply NW.
There are no ascertained ages for the generally deformed granitoid intrusions in the Western Karakoram. The Kafiristan pluton (ca. 483 Ma), the Kesu-Buni Zom pluton (111±5 Ma), the Darkot Pass plutonic unit (109±4 Ma) and the Zagar-Umalsit pluton (77±3 Ma) were dated by Rb-Sr whole rock and K-Ar methods; but these ages may represent cooling or are the result of isotope system perturbation (Table 2.1).

3.2.2 Hunza and Baltoro Karakoram (Eastern Karakoram)

Gaetani *et al.* (1996) divided the Karakoram in the Hunza area and upper Chitral into three main belts, which are from north to south: (1) the *Northern Sedimentary Belt*, (2) the *Karakoram Axial Batholith* and (3) the *Southern Metamorphic belt*. The northern unit of the Western Karakoram corresponds to the Northern Sedimentary Belt and the southern unit can be linked to the Southern Metamorphic belt, respectively, although the metamorphic grade is lower in the Western Karakoram.
The Northern Sedimentary Belt was subdivided into 6 tectonostratigraphic sequences documenting the evolution of the northern Karakoram in a primarily marine milieu from the Ordovician to the Late Cretaceous (Gaetani 1997). These sediments were deposited on a crystalline basement that includes pre-Ordovician granitoids (Le Fort *et al.* 1994).

The Karakoram Axial Batholith includes mid-Cretaceous to Late Tertiary intrusions that are attributed to Andean-type magmatism followed by postcollisional crustal melting (Debon *et al.* 1987a, Hildebrand *et al.* 2001, Fraser *et al.* 2001 and ref. therein).

3.3 Tectonic evolution

The tectonic evolution of the Western Karakoram is described following Gaetani's (1997) stratigraphic subdivisions for the Northern Sedimentary Belt. Due to the scarcity of absolute ages, U-Pb data from the Eastern Karakoram (mainly from Fraser *et al.* 2001) are extended to describe the magmatic and metamorphic evolution of the whole Karakoram.

3.3.1 Precambrian: crystalline basement

The oldest rocks reported in the Karakoram are located in the Baltoro area, just north of the Shyok Suture Zone separating the Karakoram from the Ladakh arc. Foliated meta-diorites yielded an age of ca. 651 Ma (Ar-Ar on hornblende, Rolland *et al.* 2002). These Precambrian rocks are unconformably overlain by Lower Paleozoic meta-pelites and -sandstones (Rolland *et al.* 2002).

3.3.2 Ordovician to earliest Permian: transgression onto basement and subsequent initiation of rifting

The northwest-southeast elongate Masherbrum Greenstone Complex (Rolland *et al.* 2002), previously known as *Panmah ultramafic unit* (Searle *et al.* 1989, Searle & Tirrul 1991) in the Baltoro Karakoram, consists of a dismembered series of meta-gabbros, ultramafites, meta-volcanites and meta-pelites. This complex is folded within marbles of supposed Cambrian to Early Ordovician age (Rolland *et al.* 2002). A 565±272 Ma Sm-Nd isochrone age of arc- and back-arc-type meta-lavas and a Lower Cambrian ^{13}C age of surrounding meta-carbonates suggest that the Masherbrum Greenstone Complex is Early Paleozoic in age (Rolland *et al.* 2002). Geochemical analyses of the meta-lavas indicate different geodynamic settings such as evolved arc, back-arc and ocean island setting (Rolland *et al.* 2002). Therefore, these authors suggested 'intraoceanic piling' of these rocks. The Masherbrum Greenstone Complex may be the relict of a Lower Paleozoic ocean 'within' the Eastern Karakoram.

Le Fort *et al.* (1994) documented a marine environment through the Ordovician and Silurian in the Baroghil Pass area with a transgression onto the crystalline Karakoram basement. Early Ordovician litharenites and slates were assigned to the Peri-Gondwana biogeographic province (Le Fort *et al.* 1994). Carbonates were occasionally deposited during the Ordovician but became more frequent in the Devonian (Golonka *et al.* 1994, Gaetani 1997).
Early Ordovician graptolite-crinoid limestones (Rolland *et al.* 2002) have been reported from the Baltoro area, where lower greenschist facies marls and limestones, part of a Lower Paleozoic meta-pelite and sandstone series, unconformably cover the Precambrian basement.
Massive alkaline meta-basalts and tuffs are interlayered with Early Carboniferous dolomites (Kafarskyi *et al.* unpubl. in Gaetani *et al.* 1996) in the Tas Kupruk unit (Kafarskyi & Abdullah 1976, Buchroithner 1978, Gaetani & Leven 1993), the northernmost Karakoram formation in upper Chitral. This sequence unconformably overlies Late Devonian limestones (Gaetani *et al.* 1996). These probably rifting-related volcanites may mark an extensional event between the Middle Devonian and earliest Carboniferous, thus suggesting the existence of a rift basin north of the Karakoram terrane (Gaetani 1997).
Rifting along the Gondwana margins and the fall of the sea level related to the mid to late Ordovician glaciation presumably caused recurrence of erosion on the Karakoram part of Gondwana, resulting in a very mature detritus in the adjoining sedimentary basin (Gaetani 1997). The Devonian Lun shales in Chitral (Talent *et al.* 1982) represent this continent-derived detrital sedimentation.

3.3.3 Early Permian to earliest Jurassic: separation from Gondwana

Early Permian slates, sandstones and conglomerates, locally intercalated with carbonates, were interpreted as indicators for rifting on a passive margin in the northern Karakoram (Gaetani 1997). The Late Permian sedimentary successions are more irregular and complicated than the underlying sequences. A shallow and a deep environment are defined. The subsequent development of platform carbonates from the Late Permian to the earliest Jurassic indicates pelagic conditions throughout the Karakoram (Gaetani 1997). Seaways separating the Cimmeride continent from Gondwana began to open in the Late Permian and were established in the Early Triassic (Gaetani 1997).

3.3.4 Early Jurassic: orogenic event and magmatism

The passive margin succession in the northern Karakoram is overlain by Liassic turbiditic sandstone sequences containing lithic fragments of mafic volcanites and serpentinite (Gaetani 1997). Shallow water carbonates

continued to develop in nearby areas. These two successions are both unconformably overlain by deltaic to marginal marine red sandstones that cover most of the northern Karakoram units in the Hunza region (Gaetani *et al.* 1993). This Early Jurassic sequence is taken as evidence for an orogenic event that mainly took place in neighbouring areas like the Eastern Hindu Kush, the Wakhan and the Pamir (Gaetani *et al.* 1993, Gaetani 1997 and authors therein).
In the Eastern Karakoram, the granodioritic protolith of the Hushe gneiss of the Southern Metamorphic belt in the Baltoro region has a 145-150 Ma intrusion age (U-Pb on zircon, Parrish in Searle 1991) indicating magmatism in the Late Jurassic.

3.3.5 Middle Jurassic to Early Cretaceous: shallow marine transgression

The arenaceous Early Jurassic sequences are covered by Alenian (earliest Middle Jurassic) carbonate ramps (Gaetani 1997). Marine conditions persisted until at least the Early Cretaceous (Orbitolina-bearing Krinj Limestone, Hayden 1915, Desio 1959, Pudsey *et al.* 1985) in the Chitral area.

3.3.6 Early to mid-Cretaceous: subduction-related magmatism and collision with the Eurasian margin

Northern Sedimentary Belt
Sedimentary strata were strongly folded and/or stacked in thrust sheets (Pudsey *et al.* 1985, Gaetani *et al.* 1993, Zanchi and Gritti 1996) and were locally eroded down to the Permian (Gaetani *et al.* 1993). Deformation took place under low grade metamorphic conditions and is related to the onset of an overall convergence regime (Gaetani *et al.* 1990, 1993, Gaetani 1997). In several areas of the Western Karakoram, these units were covered by conglomerates (e.g. Tupop conglomerate, Gaetani 1990, Reshun conglomerate, Hayden 1915) above remarkable unconformities (Gaetani *et al.* 1993, section 2.2.1). These conglomerates consist of well-rounded mainly sedimentary pebbles in a red shaly matrix, some of which being derived from Early Cretaceous Orbitolina limestones and the crystalline basement. A fluvial environment and a submarine fan are probable sedimentation settings for these clastics (Gaetani *et al.* 1993).
The Tupop conglomerate was unconformably overlain by Campanian carbonates (Darband Fm.) in the Hunza area, documenting that marine sedimentation continued until the Late Cretaceous (Gaetani *et al.* 1993). This marine episode implies a marine basin or trench in (or south of?) the Karakoram, after its accretion to the Eurasian margin.

Karakoram Axial Batholith (Eastern Karakoram)
The calc-alkaline Hunza Plutonic Unit is one of the best studied Cretaceous intrusions in the Karakoram. It is composed of granodiorites and quartz diorites that were deformed by south-vergent thrusting. U-Pb ages on zircon are 105.7±0.5 Ma (Fraser *et al.* 2001), 106.1±0.1Ma and 100.1±0.1Ma (Sergeev *et al.* 2001). The K2 Orthogneiss in the Baltoro area yielded 115-120 Ma (U-Pb on zircon, Searle *et al.* 1990) further southwest.
Referring to the occurrence of pseudomorphs after andalusite in adjacent kyanite-sillimanite schists, the Hunza Plutonic Unit is interpreted as a possible heat source for pre-India-Asia collision contact-metamorphism (Fraser *et al.* 2001). Similar high-temperature, low-pressure indicators were reported from the Eastern Hindu Kush (Hildebrand *et al.* 1998, 2001, section 2.2.2) and from the Baltoro region (Searle & Tirrul, 1991, Fraser *et al.* 2001) leading to the assumption that they are related to the emplacement of subduction-related granitoids coupled with a high thermal gradient (Searle & Tirrul 1991, Hildebrand *et al.* 1999, Fraser *et al.* 2001) and subduction taking place along the southern boundary of the Karakoram.
The Koz Sar Alkaline Complex in the Karambar Valley consists of a number of granitoid bodies defining a strongly ferriferous alkaline series, unique in the Karakoram Axial Batholith (Debon *et al.* 1996). One granite body yielded 88±4 Ma (Rb-Sr whole rock, Debon *et al.* 1996). The alkaline character of this complex is thought to testify an extensional tectonic regime (Debon *et al.* 1996). Extension may also be indicated by the possibly rifting-related marine trench documented by the Campanian (84-71 Ma) marine episode (Debon *et al.* 1996).

Western Karakoram
The mid-Cretaceous Tirich Mir pluton (115±4 Ma, Rb-Sr on biotite, Desio *et al.* 1964) crosscuts the Tirich Boundary Zone and fits well in the calc-alkaline subduction-related magmatic suite (~100-120 Ma) identified in the Eastern Karakoram. Other Cretaceous intrusions are represented by the composite, mostly granodioritic Kesu-Buni Zom pluton (Pudsey *et al.* 1985), intruding the Paleozoic-Mesozoic successions south of the Reshun Fault between Mastuj and Drosh, the granodioritic to granitic Zagar-Umalsit pluton and the strongly deformed granitoids of the Darkot Pass plutonic unit (section 3.2.1).

3.3.7 Late Cretaceous to Paleocene: Kohistan-Karakoram accretion

Regional high-grade metamorphism in the Hunza Karakoram occurred before 60 Ma, with sillimanite-bearing and migmatitic meta-pelites yielding 63.3±0.3 Ma (U-Pb on metamorphic monazite, oldest monazite cores are ~83 Ma, Fraser *et al.* 2001). This metamorphic event was attributed to the accretion and collision of the Kohistan arc to the Eurasian margin during the latest Creta-

ceous by these authors. However, a non-collisional (contact) metamorphism cannot be ruled out.

3.3.8 Paleogene: Crustal thickening and ongoing magmatism

Two sets of dyke swarms in the Hunza Valley represent ongoing magmatism between 52 Ma and 35 Ma in the Eastern Karakoram (Fraser *et al.* 2001). The first set intruded the Hunza Plutonic Unit at 52-50 Ma (U-Pb on zircon, Fraser *et al.* 2001). The dykes are boudinaged and parallel to the main foliation of the host rocks. The second set intruded 44.0±2.0 Ma (U-Pb on metamorphic monazites) sillimanite-grade meta-sediments at 35.0±1.0 Ma (U-Pb on monazite and zircon, Fraser *et al.* 2001). It is not clear whether the set 1 dykes are related to crustal thickening due to accretion of Kohistan to the Eurasian margin, or to subsequent India-Asia collision at ca. 65-50 Ma (Fraser *et al.* 2001).

Evidence for crustal thickening was reported from the Northern Sedimentary Belt in the upper Hunza Valley where mainly north-dipping reverse faults represent a phase of south-directed thrusting and stacking (Gaetani *et al.* 1990, Zanchi 1993 and Zanchi & Gaetani 1994). A clear example is the Kilik fault bringing low-grade Misgar slates (Desio & Martina, 1972) onto Permo-Cretaceous sediments of the Northern Sedimentary Belt (Gaetani *et al.* 1990). Gaetani *et al.* (1997) proposed this fault to be the northern limit of the Eastern Karakoram and the Misgar slates to be the eastern equivalent of the Eastern Hindu Kush Wakhan slates.

The subalkaline and ferriferous Batura plutonic complex, at the northern edge of the Hunza plutonic unit, represents a distinct igneous association (Debon 1995). Individual plutons are predominantly granitic and adamellitic in composition and intruded granodiorites of the Hunza Plutonic Unit and Paleozoic meta-sediments. The Batura complex postdates Cretaceous folding and thrusting (Gaetani *et al.* 1990, Zanchi & Gaetani 1994, Debon 1995) but predates thrust stacking and later strike-slip faulting. Rb-Sr whole rock ages of 63.4±2 Ma were obtained on undeformed Kuk granites and 42.9±5.6 Ma for the Sarbeza adamellites (Debon 1995). Debon (1995) interpreted the Batura complex to be related to the northward subduction of the Neo-Tethys beneath the South-Karakoram (Eurasian margin).

Oligocene magmatic and metamorphic ages are reported from the Mango Gusar region in the Eastern Karakoram. The Mango Gusar granite intruded at 26.4±1.3 Ma (Th-Pb on allanite, Fraser *et al.* 2001) kyanite-grade meta-pelites dated at 28.0±0.5 Ma (U-Pb on metamorphic monazite).

3.3.9 Early Miocene: crustal melting

The huge east-west elongated Baltoro leucogranite batholith, crosscutting the southern edge of the Hunza Plutonic Unit, is dated at 26-21 Ma (U-Pb on zircon, Parrish & Tirrul 1989, Schärer *et al.* 1990). High-temperature, low-pressure contact-metamorphism overprinted sedimentary sequences north of the batholith and high-grade gneisses on its southern rim (Searle & Tirrul 1991, Searle 1991). This large leucogranitic intrusion is attributed to melting of the Karakoram lower crust (Searle *et al.* 1992).

3.3.10 Neogene: Thrusting-related metamorphism and exhumation of migmatitic domes in the Eastern Karakoram

Due to ongoing indentation of the Indian plate into the Eurasian continent, thrusting and related metamorphism continued until the Neogene. Staurolite-grade metamorphism is dated at 16.0±1.0 Ma (U-Pb on metamorphic monazite, Fraser *et al.* 2001) and is associated with southward thrusting of sillimanite-grade schists in the Hunza valley. Fraser *et al.* (2001) linked this metamorphic event to the kyanite-grade event documented in the Baltoro area.

Southeast of Aliabad, the 9.3±0.1 Ma (U-Pb on uraninite and monazite) Sumayar pluton is the youngest leucogranite in the Hunza Valley (Fraser *et al.* 2001).

Mid-crustal migmatitic rocks are exhumed in the Karakoram Southern Metamorphic Belt in the Baltoro area (Searle *et al.* 1989). Kilometre-long, sub-circular to east-west elongated migmatitic domes crosscut Late Cretaceous to early Paleogene, mainly NW-SE trending, structural patterns that were linked to SW-verging thrusting and associated crustal thickening (Rolland *et al.* 2001). Age constraints for metamorphism in these domes were reported from the 5.4±0.2 Ma Dassu Orthogneiss (U-Pb on zircon, Fraser *et al.* 2001) and a 6.7±0.5 Ma micaschist (U-Pb on zircon, Smith 1993) east of the Dassu gneiss. Fraser *et al.* (2001) concluded that the Dassu Orthogneiss originally crystallised at 1855±11 Ma (U-Pb on zircon) and experienced partial melting during sillimanite-grade metamorphism in the Early Pliocene. Rolland *et al.* (2001) suggested that these high-temperature, medium-pressure rocks, weakened by anatexis, were exhumed in the core of a crustal-scale fold formed during north-south shortening.

Youngest Karakoram fault systems were reported from the upper Hunza area, where large strike-slip faults cut E-W striking reverse faults (Zanchi 1993, Zanchi & Gritti 1996). There are two sets of strike-slip faults: E-W striking sinistral, and NW-SE striking dextral faults. These fault geometries and calculated paleostress tensors from fault slip data of the area point to a N-S to NE-SW compression (Zanchi 1993, Zanchi & Gritti 1996), attributed to tectonic

indentation of India into Eurasia (Molnar & Tapponnier 1975, Tapponnier *et al.* 1986). NW-SE dextral faulting in the Hunza area is probably related to the large NW-SE striking Karakoram fault further East in Ladakh (Zanchi 1993), which was active at least since the end of the Oligocene (Lacassin *et al.* 2004).

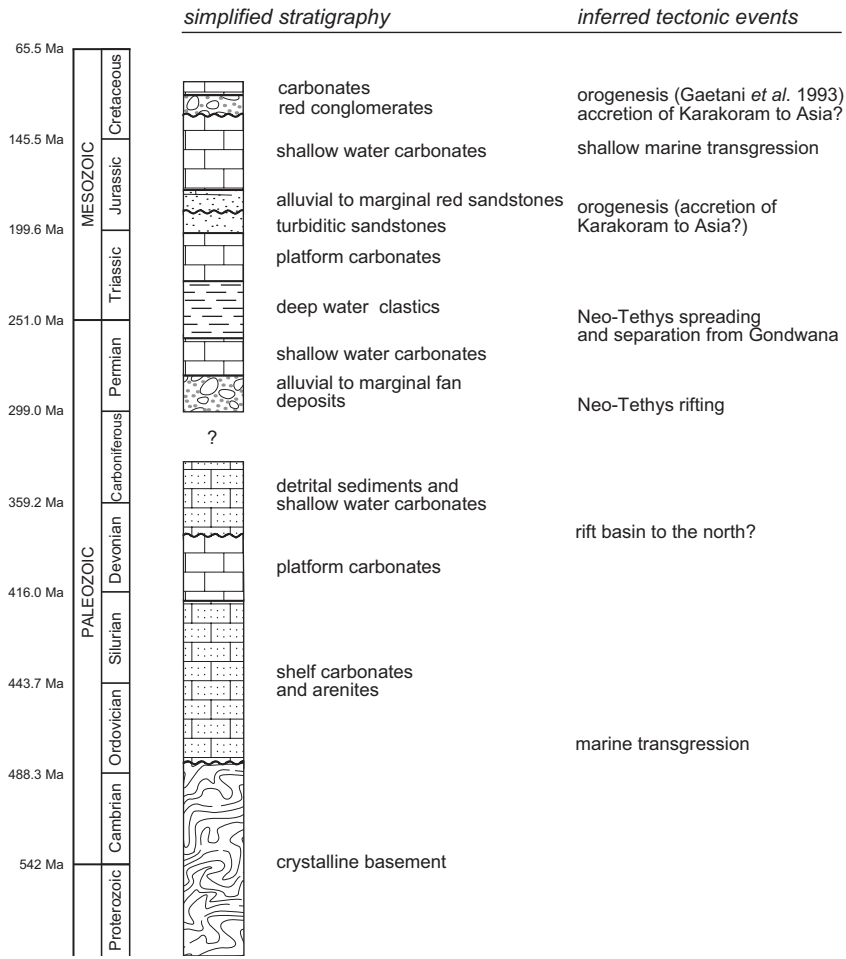

Fig. 2.6. *Stratigraphic scheme summarising main tectonic and sedimentary events. Modified after Gaetani (1997). Stratigraphic time scale after International Commission on Stratigraphy (2003), Appendix B.*

In the Hunza Karakoram, the most prominent fault of this generation is the NW-SE striking dextral Misgar fault offsetting geological units and older faults (e.g. the Kilik fault, section 3.3.8) by about 6 km (Gaetani *et al.* 1990).

3.4 Summary and discussion

The Karakoram terrane consists of a Precambrian crystalline basement unconformably covered by Paleozoic marine sediments (Fig. 2.6). Middle Devonian to earliest Carboniferous rifting is recorded along the northern Karakoram margin. In the Eastern Karakoram the Masherbrum Greenstone Complex may represent a lower Paleozoic ocean between two continental blocks.

Permian detrital sediments interlayered and overlain by late-Permian to earliest Jurassic carbonates indicate rifting from Gondwana before the northward-drift of the Karakoram terrane as part of the Cimmeride continent. Collision of the Karakoram with the Eurasian margin (Eastern Hindu Kush) is documented by the formation of the Tirich Boundary Zone and early Jurassic red sandstones. Shallow marine sedimentation was predominant during Middle Jurassic and Early Cretaceous times. The ca. 115 Ma Tirich Mir pluton, crosscutting the TBZ, gives a minimum age for that collision. Erosion and deformation at low metamorphic grade combined with intense plutonic activity is recorded between the Early and mid-Cretaceous, which is attributed to northward subduction of the Neo-Tethys underneath the Karakoram.

The timing of the accretion of the Kohistan island arc to the Karakoram margin is still disputed. Indirect indicators, such as the regional metamorphism in the Eastern Karakoram around 80-60 Ma were used to assign accretion to the Late Cretaceous. Extension in the mid-Late Cretaceous, after the collision of Kohistan with the Karakoram, is indicated by the Koz Sar ferriferous-alkaline intrusion in the Karakoram Axial Batholith and by Campanian (84-71 Ma) carbonates implying a marine basin in the Karakoram.

The later history in the Western Karakoram is poorly documented. In the Eastern Karakoram, crustal thickening was inferred from high-grade metamorphism, top-to-the-south thrusting and stacking and Oligocene and Miocene magmatism and metamorphism. N-S to NE-SW shortening during the uppermost Miocene is responsible for gneissic domes formed around 7-5 Ma and mainly dextral wrenching (Rolland *et al.* 2001).

4. Eastern Hindu Kush-Karakoram boundary: The Tirich Boundary Zone

4.1 Introduction

The Tirich Boundary Zone in northern Chitral separates the Eastern Hindu Kush, to the north, from the Karakoram to the south (Gaetani 1997, Zanchi, *et al.* 1997, 2000, Figs. 2.1, 2.3). This sinistral strike-slip fault zone contains mafic and ultramafic slices and forms a continuous NE-SW trending, 150 km long zone (Zanchi *et al.* 2000). It has not been studied in the remote Afghanistan-Pakistan border area.

The mid-Mesozoic Wasser-Panjao Suture separates the Farah Rud Block, to the north, from the Helmand Block, to the south, in Central Afghanistan (Tapponnier *et al.* 1981, Fig. 2.1). Ophiolitic sequences are associated with Upper Triassic to Jurassic 'flysch' sequences that were thrust onto the Helmand Block continental margin around the Late Jurassic-Early Cretaceous (Tapponnier *et al.* 1981, and ref. therein). The Helmand Block has strong geological affinities with the Western Karakoram (Boulin 1988, Gaetani 1997). Zanchi *et al.* (2000) tentatively linked these two terranes and speculated about a genetic link between the TBZ and the Wasser-Panjao Suture.

4.2 Geological setting

The TBZ was studied northeast of Garam Chashma in the Chitral area (Zanchi *et al.* 2000). TBZ units are cut out by south-vergent thrusts and later sinistral strike-slip faults reducing the TBZ to a single fault in the Afghanistan-Pakistan border area in upper Chitral (previously termed *Tirich Mir Fault* by Buchroithner 1980 and Buchroithner & Gamerith 1986). The TBZ can be traced along that fault between the Wakhan slates and the Northern Karakoram sedimentary units further to the east in the Wakhan corridor (Afghanistan, Gaetani *et al.* 1996). In Pakistan, further to the east-southeast, the TBZ is apparently linked with the NW-SE trending Kilik fault (Gaetani 1997).
The Tirich Boundary Zone consists of imbricate units that are, from northwest to southeast, meta-ultrabasites, a mafic igneous complex and a high-grade metamorphic complex (Zanchi *et al.* 2000). The meta-ultrabasites mainly consist of sheared serpentinites locally occurring as metasomatic talc-siderite schists in tectonic lenses along the northern limit of the TBZ (Zanchi *et al.* 2000). The ultramafites include well-preserved spinel lherzolites and harzbur-

gites amongst schistose serpentinites. The mafic igneous complex is composed of hornblende gabbros, hornblendites and quartz diorites that locally occur as strongly lineated meta-gabbroic amphibolites. The high-grade metamorphic complex is mainly made up of amphibolites, sillimanite gneisses and kyanite schists. Referring to the lack of a typical ophiolitic sequence and the close association with deep-crustal rocks Zanchi *et al.* (2000) suggested a sub-continental origin for the TBZ peridotites.
The ca. 115 Ma Tirich Mir pluton is heterogeneously foliated. It was thrust southeastwards onto very low-grade meta-pelitic Karakoram units along the Tirich Mir pluton fault (Hildebrand *et al.* 2000). This thrusting is claimed to be synchronous with the Tirich Mir pluton and pegmatites intrusion (Hildebrand *et al.* 2001, section 2.2.3).

4.3 Summary and discussion

The presence of ultramafites is a strong argument to interpret the TBZ as the Western Karakoram-Eastern Hindu Kush suture zone. The Tirich Mir intrusion marks a minimum age for metamorphism and imbrication of the Tirich Boundary Zone units and subsequent thrusting onto the very low-grade Karakoram meta-sediments. Hence, the accretion of the Karakoram to the Eurasian margin (Eastern Hindu Kush) occurred before the mid-Cretaceous (ca. 115 Ma). Zanchi *et al.* (2000) supposed that the TBZ derived from a lower crust-upper mantle sequence of either an area of thinned continental crust or a passive continental margin. The deposition of the Paleozoic to Triassic Wakhan and Misgar slates in the Eastern Hindu Kush implies the existence of a basin between the Karakoram and the South Pamir (Gaetani 1997). Therefore Zanchi *et al.* (2000) assumed the TBZ to represent either remnants of an intra-*Cimmeride* orogenic belt related to the early Mesozoic accretion of the Cimmeride continent to the southern margin of Eurasia or the eastern continuation of the mid-Mesozoic Wasser-Panjao Suture of Central Afghanistan.

5. Kohistan arc

5.1 Introduction

The Kohistan arc has been recognised as a paleo-island arc (Tahirkheli *et al.* 1979, Bard *et al.* 1980) formed within the Neo-Tethys during the Mesozoic (Bard *et al.* 1980, Bard 1983, Coward *et al.* 1986). The arc likely accreted to the Karakoram (southern Eurasian margin) before 85-75 Ma (Treloar *et al.* 1989, Searle *et al.* 1999) thus becoming an Andean-type magmatic arc, before collision with the Indian continent at 65-50 Ma (Gansser 1964, Molnar & Tapponnier 1975, Jaeger *et al.* 1989 and many later authors). The Kohistan arc is separated by the Karakoram-Kohistan Suture (also termed Northern or Shyok Suture, Bard *et al.* 1980, Pudsey *et al.* 1985, Thakur 1981) from the Karakoram terrane to the north, and by the Indus Suture (also called Main Mantle Thrust, Tahirkheli *et al.* 1979) from the Indian Plate, to the south. To the east, the Nanga Parbat syntaxis separates the Kohistan from its eastern equivalent, the Ladakh paleo-island arc (Honegger *et al.* 1982).
The Kohistan paleo-island arc is composed of uppermost Jurassic to Cenozoic, mainly calc-alkaline magmatic and volcanoclastic rocks and marine sediments. The Kohistan arc is better studied than the Western Karakoram but the northwestern and, in particular, the remote internal parts are still poorly known.

5.2 Geological setting

The subdivision of the Kohistan arc into different units, described below from north to south, is primarily adapted from Bard *et al.* (1980), Khan *et al.* (1993), Treloar *et al.* (1996) and Burg *et al.* (1998, Fig. 2.7).

5.2.1 Yasin detrital series

The Yasin detrital series form a long narrow belt just south of the Karakoram-Kohistan Suture and were first described by Ivanac *et al.* (1956) and Desio (1963). Low-grade red, green and grey shales are interlayered with volcano-clastic greenschists, turbiditic sandstone-slate sequences, volcano-lithic conglomerates, tuffs and rudist-orbitolina limestones. Yasin-type orbitolina limestones, found also south of Drosh, at Harchin and Chumarkhan, were palaeontologically dated as Upper Barremian to Albian (e.g. Hayden 1915, Rossi & Farioli 1959, Desio *et al.* 1977). Pudsey *et al.* (1985b) revised these

ages to Late Aptian to Albian. The Yasin detrital series are interpreted as a turbiditic unit that was deposited in an intra-arc or back-arc basin of the Kohistan paleo-island arc (Pudsey 1986, Khan *et al.* 1995, Treloar *et al.* 1996).

5.2.2 Volcanosedimentary groups (Chalt and Utror-Shamran)

Many volcanic units of northern Kohistan have been described and correlated (summaries in Treloar *et al.* 1996, Kazmi & Jan 1997). However, correlations are tentative because of weak field constraints. Two major groups are distinguished based on their approximate ages: the mid-Cretaceous Chalt Volcanic group and the Paleogene Utror-Shamran Group.

The Chalt Volcanic Group includes the Chalt Volcanites in the Hunza-Ishkuman area (Petterson & Windley 1985) and the Drosh Volcanites (Pudsey *et al.* 1985). The Chalt Volcanites are unconformably overlain by, and interlayered with the Yasin detrital series in the Hunza area (Matsushita & Huzita 1965) and consist of strongly deformed greenschist to amphibolite-grade meta-volcanites varying in composition from basaltic komatiite, boninite, high-Mg andesite to calc-alkaline basalt, andesite and dacite-rhyolite (Petterson *et al.* 1991). Pillowed and massive lavas, tuffs, volcanic breccias and agglomerates are common whereas the proportion of volcanoclastites increases and the metamorphic grade decreases to lower greenschists facies westwards in the Ishkuman and Yasin valleys (Petterson *et al.* 1991, Kazmi & Jan 1997). The Drosh volcanites form one of the northernmost units of the Kohistan paleo-island arc and are interlayered with Upper Aptian to Albian Yasin Group sediments (Pudsey *et al.* 1985, Pudsey 1986). In contrast to the Chalt volcanites, they are almost undeformed and display a lower greenschist facies metamorphism. Geochemistry suggests that the Chalt Volcanic Group can be subdivided into two types: the tholeiitic and high-Mg Chalt Volcanites of the Hunza valley and the calc-alkaline ‘western’ volcanites west of the Hunza valley, including the Drosh volcanites (Petterson *et al.* 1991).

The Utror-Shamran Volcanic Group includes the undeformed Utror volcanites (Jan & Mian 1971, Bard 1980) in the Dir-Kalam area and the Shamran volcanites in the Shandur-Gupis area. The Utror volcanites were thrust southward along the Dir thrust (Fig. 2.1) and comprise predominantly low-grade andesitic and rhyolitic lava flows, acid ignimbrites and volcanoclastic sediments (Sullivan *et al.* 1993). A basaltic-andesite yielded an Ar-Ar age of 55±2 Ma (on hornblende, Treloar *et al.* 1989). 45-48 Ma diorites (Ar-Ar on hornblende, Zeitler 1985, Treloar *et al.* 1989) intruded the Utror volcanites in Kalam. The Shamran volcanites (Pudsey *et al.* 1985; re-named by Danishwar 2001 as Teru volcanic formation to avoid confusion with the Shamran Volcanic Group of Treloar *et al.* 1996) unconformably overlie deformed rocks of the Chalt Volcanic group (Matsushita & Huzita 1965, Danishwar *et al.* 2001, Petterson & Treloar 2004) and the ca. 65 Ma Shunji Pluton (Rb-Sr whole rock,

Khan *et al.* 2004) to the east of the Shandur Pass. They are dominantly silicic rocks mainly comprising andesitic to rhyolitic lavas, acid ignimbrites, poorly sorted volcanoclastic conglomerates, sandstones and tuffs. They locally form an undeformed, flat-lying sequence (Matsushita & Huzita 1965, Pudsey *et al.* 1985, Danishwar *et al.* 2001, Petterson & Treloar 2004). Two andesitic basalts yielded 43.8±0.5 Ma and 32.5±0.4 Ma (Ar-Ar on hornblende, Khan *et al.* 2004). These volcanites are lithologically very similar to the Utror volcanites and basaltic andesites near Phander, which yielded an early Eocene age (58±2 Ma Ar-Ar on hornblende, Treloar *et al.* 1989).

5.2.3 Oceanic series (Dir, Kalam and Jaglot groups)

The Oceanic series (Bard *et al.* 1980, Burg *et al.* 1998) include meta-sedimentary sequences that are the non-volcanic members of the Dir, Kalam and Jaglot Groups (as summarised by Treloar *et al.* 1996). Two major units are distinguished: the Paleocene-Eocene Baraul Banda Slate Formation and the probably Early Cretaceous Jaglot-Kalam meta-sediments.
The Baraul Banda Slate Formation consists of sand- and siltstones interpreted as deep-water turbiditic sequences (Sullivan *et al.* 1993). This unit unconformably overlies meta-sedimentary and meta-volcanic rocks of the Kalam Group interpreted as arc basement, and 78-76 Ma diorites (Ar-Ar on hornblende, Treloar *et al.* 1989). Interlayered limestones yielded Thanetian (60.2-54.9 Ma, Sullivan *et al.* 1993) and Eocene (Kakar *et al.* 1971) marine faunas and shales were dated as Early Eocene (Khan 1979).
Jaglot-Kalam Group meta-sediments, described mainly south of Gilgit but also in the Dir and Swat areas, comprise greenschist to amphibolite-grade schists that predominantly are quartz-rich semi-pelites interpreted by Treloar *et al.* (1996) as turbidites deposited in a medium to deep water marine basin. Marbles occur locally. These sequences are interlayered with basic volcanites of the volcanosedimentary groups. In the Gilgit area, Jaglot-type meta-sediments conformably underlie the Chalt Group; therefore, Kazmi & Jan (1997) inferred an Early Cretaceous age for these sediments.

5.2.4 Kohistan Batholith

The Kohistan Batholith represents the principal unit of the Kohistan magmatic arc (Fig. 2.7). It is composite and comprises numerous isolated plutons, dykes and sills of calc-alkaline gabbroic to leucogranitic composition (Petterson & Windley 1986; Kazmi & Jan 1997 and authors therein). Petterson & Windley (1985) distinguished three major plutonic stages:
‘Stage 1’ is represented by predominantly deformed gabbros and diorites (Petterson & Windley 1985). These intrusions were interpreted as subduction-

related plutons based on trace element geochemistry (Petterson & Windley, 1986). A Late Jurassic age (154.0±0.6 Ma, U-Pb on zircon) for the Matum Das tonalite, north of Gilgit, represents the oldest Kohistan intrusion age (Schaltegger *et al.* 2003).
'Stage 2' intrusions include diorites, granites and leucogranites yielding Rb-Sr and Ar-Ar ages between 85 Ma and 40 Ma with a general basic to acid trend over time (Petterson & Windley 1985,1986, Debon *et al.* 1987, Treloar *et al.* 1989, 1996). A diorite south of Gilgit (Indus confluence) was dated at 50.44±0.13 Ma (U-Pb on zircon, Schaltegger *et al.* 2003). The Jutal dykes (north of Gilgit) were described by Petterson & Windley (1985) as a swarm of undeformed basic dykes intruding the Matum Das tonalite and the Chalt volcanites. Ar-Ar ages on hornblendes indicate cooling of these rocks at ca. 75 Ma (Rex in Petterson & Windley 1985 and Treloar *et al.* 1989). 'Late Stage 2' intrusions are interpreted as Andean-type plutons (Petterson & Windley 1985).
'Stage 3' intrusions are represented by composite aplite-pegmatite bodies (dykes) intruding meta-sediments at Parri (south of Gilgit) and 'stage 2' plutons at the Indus confluence. They yielded 26.2±1.2 Ma (Rb-Sr whole rock, Petterson & Windley 1985, George *et al.* 1993) and 34±14 Ma (Rb-Sr whole rock, Petterson & Windley 1985), respectively. A leucogranite from the Indus confluence area was dated at 30.4±0.6 Ma (U-Pb on zircon, Schaltegger *et al.* 2003), which confirms the Rb-Sr ages.

5.2.5 Chilas Complex

The Chilas Complex extends for almost 300 km from the Nanga Parbat Syntaxis to the Afghanistan-Pakistan border area. It is a gabbronorite with a primarily magmatic fabric and encloses mafic-ultramafic associations (Khan *et al.* 1989). The Chilas Complex intruded sediments and volcanites of the oceanic series, to the north and strongly deformed meta-volcanites and gabbros of the Southern Amphibolites to the south (Treloar *et al.* 1996). Zeitler *et al.* (1981) reported a 84±0.5 Ma (U-Pb on zircon) crystallisation age of the gabbronorite that was confirmed by Schaltegger *et al.* (2002, 85.73±0.15 Ma; also U-Pb on zircon). The ultramafic associations are interpreted as parts of mantle diapirs pointing to splitting of the Kohistan arc into a volcanic and a remnant arc (Burg *et al.* 1998).

5.2.6 Southern Amphibolites

The Southern Amphibolites (Treloar *et al.* 1996, earlier termed the Kamila Amphibolite belt by Jan & Tahirkheli 1979, Tahirkheli *et al.* 1979, Bard *et al.* 1983, Treloar *et al.* 1990) are located to the south of the Chilas Complex. They

consist of a thick stack of imbricate calc-alkaline laccoliths, meta-volcanites and minor meta-sediments variably deformed under amphibolite facies conditions Zeilinger, 2002).
Relics of pillow lavas (Upper Swat and Thak Valley, Kazmi & Jan 1997 and ref. therein) were interpreted as remnants of the Neo-Tethys oceanic crust on which the island-arc was built (Jan 1988, Khan *et al.* 1993, Treloar *et al.* 1996). Different plutonic bodies along the Indus River, between Patan and Dasu, yielded ages of 98.9±0.4 Ma for a gabbro, 97.1±0.2 Ma for a granite and 91.8±1.4 Ma for a hornblende diorite (U-Pb on zircon, Schaltegger *et al.* 2002).

5.2.7 Jijal Complex

The Jijal Complex crops out in the Indus Valley and is bounded by the Indus Suture to the south, by a zone of serpentinites along a sinistral NE-SW trending fault to the west and by intrusive contacts to diorites and gabbros to the northeast. It mainly consists of an ultramafic sequence below a garnet-rich, granulite-facies, meta-gabbro. The ultramafites (peridotites, pyroxenites, websterites and dunites) and garnet granulites represent the lowest level of the Kohistan arc and have been described by Jan & Howie (1981), Bard (1983), Miller *et al.* (1991) and Burg *et al.* (1998). The north-dipping contact between the ultramafites and the overlying meta-gabbro was interpreted as the sub-arc petrological Moho (Burg *et al.* 1998). Cooling of the granulite-facies garnet-pyroxene gabbros was dated at 91-95±6 Ma by the Sm-Nd pyroxene-garnet technique (Anczkiewicz & Vance, 2000; Yamamoto & Nakamura, 1996, 2000) which is coeval with the 92-100 Ma intrusions in the Southern Amphibolites and with the imprecise age of the collision between the Kohistan and the Karakoram (Petterson & Windley 1985, Treloar *et al.* 1996).

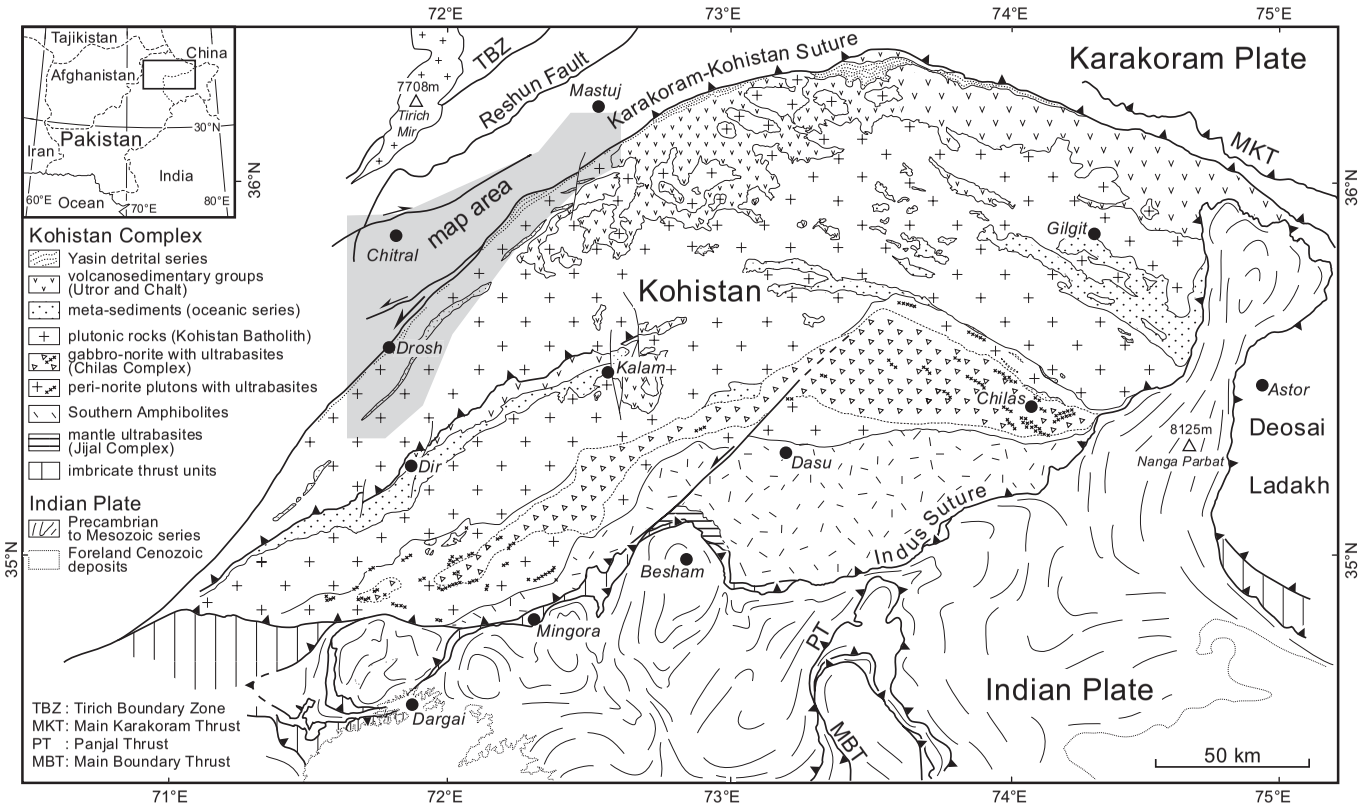

Fig. 2.7. *Structural sketch map of the Kohistan arc complex. The shaded polygon marks the map area (enclosed map).*

5.3 Tectonic evolution and discussion

5.3.1 Late Jurassic to mid-Cretaceous (Albian)

The Indian Plate began its northward motion through the Tethys sometime in the Mesozoic during intra-oceanic, northward-dipping subduction offshore of the Eurasian margin. This created the Kohistan island arc. The oldest Kohistan rock dated up to now is Late Jurassic (154.0±0.6 Ma, U-Pb on zircon, Matum Das tonalite). This tonalite was likely derived from strongly depleted oceanic lithosphere melts without any mixing with continental crust as indicated by extremely high epsilon Hf values (+21, Schaltegger *et al.* 2003). Late Jurassic ages (162-152 Ma, Ar-Ar on hornblende and U-Pb on zircon) were also reported from the Zedong Arc, a recently discovered intra-oceanic paleo-island arc now included within the Tsangpo Suture, in Southern Tibet (McDermid *et al.* 2002). These new results suggest that intra-oceanic subduction within the Tethys extended eastwards and likely started earlier than previously thought (mid-Early Cretaceous, Dercourt *et al.* 1993).
Enclaves of high-Ti tholeiitic meta-basalts within plutonic rocks of the Southern Amphibolites may represent remnants of Tethys oceanic crust. Arc magmatism is documented by low-Ti mafic rocks. No absolute geochronological age on the oceanic rocks is available yet.
Greenschist to amphibolite facies meta-volcanites and turbiditic meta-volcanosediments of the oceanic series were deposited (after Treloar *et al.* 1996), into an intra- or back-arc basin of the Kohistan arc, possibly indicate an extensional phase in or at the young island arc. This hypothesis is supported by the extrusion of back-arc type, high-Mg andesites of the Chalt Volcanites to the northeast of the arc.

5.3.2 Late Cretaceous

The intrusion of a 99 Ma gabbro at a pressure of 1.1 GPa indicates an already thickened arc crust at that time (Yamamoto 1993, Schaltegger *et al.* 2002). Shear-deformation in the Southern Amphibolites during the early Late Cretaceous may be related to northward subduction of the Neo-Tethys beneath the Kohistan arc (Arbaret *et al.* 2000).
The ultramafic associations of the Chilas Complex suggest that mantle diapirism may have played an important role in opening a Kohistan inter-arc basin, separating the volcanic from a remnant arc at about 85 Ma (Burg *et al.* 1998).
Timing of the Kohistan-Karakoram accretion is still debated. Petterson & Windley (1985) proposed the time span between the Matum Das tonalite intrusion (102 Ma) and Jutal dykes (75 Ma). Treloar *et al.* (1996) proposed

between 102 and 85 Ma, after the Matum Das intrusion and before the ‘stage 2’ and Chilas gabbronorite intrusions.

5.3.3 Paleocene-Eocene

Uplift and erosion of ‘early stage 2’ plutons and Kalam basement rocks has occurred before sedimentation of the Paleocene-Eocene turbidites of the Baraul Banda formation. Subsequent acid volcanism documented in the Utror and Shamran Volcanites took place in the early Eocene, coeval with the ‘late stage 2’ plutonism. The 50 Ma diorite at the Indus confluence, displaying an island-arc to MORB-type melt source, may represent an intra-arc rift zone that persisted since the mid-Late Cretaceous.
Subduction of Neo-Tethys beneath the Kohistan arc continued until ca. 67 Ma, when collision with, and underthrusting by continental India was initiated (Beck *et al.* 1995). Collision of the Indian continental plate with the southern Eurasian active margin (i.e. the accreted Kohistan arc) was interpreted as having occurred around 55 Ma (review in Guillot *et al.* 2003). Coesite-bearing eclogites just south of Indus Suture in the Babusar Pass area indicate deep subduction of continental India at ca. 46 Ma (O’Brien *et al.* 2001).

5.3.4 Oligocene to present

Post-collisional (‘stage 3’) magmatism at ca. 26 to 34 Ma points to ongoing magmatism after the India-Asia collision.
Indentation of India into Eurasia continues as expressed by frequent earthquakes in the whole area.

6. Karakoram-Kohistan Suture Zone

6.1 Introduction

The Karakoram-Kohistan Suture Zone (KKSZ) is the fault contact between the Kohistan paleo-island arc to the south and the Karakoram to the north.
Timing of the collision between the Kohistan-Ladakh arcs and the Karakoram has been 'bracketed' between 100 and 75 Ma (Petterson & Windley 1985, 1992; Pudsey 1986; Hanson 1989; Treloar *et al.* 1989; Treloar *et al.* 1996; Clift *et al.* 2002), but precise constraints are still lacking. Pudsey (1986) interpreted the suture zone in northwestern Pakistan as the remnant of a back-arc basin associated with a serpentinite-bearing mélange. Robertson and Collins (2002) and Rolland *et al.* (2000) described the suture further southeast in Baltistan as an imbricate zone of mainly Ladakh arc units (lateral equivalents to the Kohistan arc units) separated by faults along which lenses of meta-ultramafites occur. Brookfield & Reynolds (1981) characterised the suture in the Hushe-Saltoro river confluence area as a tectonic mélange with 'ophiolitic' units. Weinberg *et al.* (2000) reported the suture to be inaccessible in the Nubra-Shyok river confluence area (mostly in the Saltoro Range) and, based on field work, rejected Rolland *et al.*'s (2000) interpretation of 'suture mélanges' along the Shyok and Nubra rivers (Weinberg & Dunlap 2001).
The lack of convincing suture characteristics lead Thakur (1981), Pudsey *et al.* (1985), Petterson & Windley (1985), Coward *et al.* (1986), Treloar *et al.* (1989) and Hanson (1989) to the assumption that the KKSZ marks the site of an Early Cretaceous, small back arc basin offshore the Eurasian margin.

6.2 Geological Setting

The KKSZ in Pakistan was described as a fault zone that is 2-3 km wide between Drosh and Mastuj and only 150-500 m wide in the Yasin to Hunza areas (Tahirkheli *et al.* 1979, Bard *et al.* 1980, Bard 1983, Coward *et al.* 1986, Pudsey *et al.* 1985, Pudsey 1986). The suture was defined as 'mélange' comprising blocks of volcanic greenstones, limestones (some of which are fossiliferous), red shales and serpentinites in a matrix of strongly cleaved slates (Pudsey *et al.* 1985). Blocks in the 'mélange' are interpreted to be derived almost entirely from the Kohistan arc, with only a small contribution of quartzites from the Karakoram (Pudsey *et al.* 1985). Pudsey (1986) suggested a sedimentary origin for the 'mélange'.
Pudsey *et al.* (1985) defined Northern Kohistan Units to the south of the 'suture mélange'. In the Drosh-Shishi Gol area, they are from north to south:

Drosh Formation:
A sequence of porphyritic, often epidotised andesitic lava flows and minor volcanic breccias, interlayered locally with red shales, conformably overlies the Purit Formation.
Purit Formation:
Fluvial red shales, sandstones and conglomerates containing pebbles of porphyritic andesites, grey limestones, basalts and red shales. Red siltstones and sandstones overlie a 7 m thick breccia of granodiorite and andesite clasts in a red sandstone matrix that unconformably covers a granodiorite at Mirkhani (12 km south of Drosh). This granodiorite intruded the Gawuch Formation.
Gawuch Formation:
Dark green, strongly cleaved and lineated phyllites interlayered with thick limestone units. Locally, green tuffs and lavas occur at the top of the formation. These rocks are described as greenschist to amphibolite facies meta-volcanites with interlayered meta-sediments including marbles south of Drosh. The Gawuch Formation is intruded by diorites of the Kohistan Batholith to the south and faulted against the Purit Formation. The whole formation is isoclinally folded with a strong horizontal lineation.

6.3 Summary

The Karakoram-Kohistan Suture Zone marks the locus of the collision between the Karakoram active margin and the Kohistan paleo-island arc. Imbricate lenses of serpentinites are considered to be derived from the mantle lithosphere of the Neo-Tethys or an oceanic back-arc basin. Classification of the imbricate units is still tentative and needs more documentation in order to constrain the tectonic origin of each unit. Moreover, precise ages and more structural analyses are needed to better understand the kinematics of the suturing events.

Chapter 3: Tectonostratigraphy of the Karakoram-Kohistan Suture Zone in the Drosh-Shishi-Sor Laspur area

1. Introduction

The new geological map (enclosed) at a 1:100,000 scale, four cross-sections (enclosed map) and a new tectonostratigraphic subdivision of the suture zone are presented on the basis of extensive field work between 1999 and 2001 along 115 km of the western part of the Karakoram-Kohistan Suture Zone, between the Afghan border in Chitral and the Shandur Pass.

1.1 Geography of southern Chitral

The Chitral district is located at the northwestern edge of the Northwest Frontier Province (N.W.F.P.) of Pakistan and is bounded by Afghanistan to the west and to the north, the Upper Dir and Swat districts to the south and the Ghizer district in the east (Fig. 2.2 in chapter 2). The field area is located in the eastern part of the Hindu Kush mountain range. Chitral can be reached by road from April to October through the Lowari Pass (3,201 m) from Dir, the Shandur Pass (3,669 m) from Gilgit and along the Kunar River from the Kunar Province of northeastern Afghanistan. It is also entered on foot through the Dorah Pass (3,751 m) from the Badakhshan Afghan Province (Fig. 2.2 in chapter 2).
Names for valleys and localities use the local languages and expressions. ‘Gol’, for example, is a Khowar (spoken language of Chitral) word for ‘stream’, which is geographically used for ‘valley’.

1.2 Compilation of the Geological Map

Detailed field work has been carried out mainly along sections across the suture zone. Less detailed investigations were done in the valley from Drosh to Arandu (Afghanistan-Pakistan border check point) and along the road from Drosh to Chitral. The very mountainous and remote area between Madaglasht and Sor Laspur (elevations between 2,500 and 6,500 m) was mapped during a ten-day walking trip.

The field map was extended using a Landsat 7 ETM+ image (path: 151, row: 035, date of acquisition: 16.9.1999, scene ID: LE715035009925950) and published geological maps by Pudsey *et al.* (1985), Pudsey (1986) and Hildebrand *et al.* (2000) and an unpublished map by *Austrominerals*. The spectral bands of the Landsat image were used in the ArcGIS software with the b7 band for red colour, the b4 band for green and the b1 band for blue. A principal component analysis (PCA) was done on the Landsat image by Jagoutz *et al.* (2001) in order to enhance the contrast. Geology was thus mapped from the original Landsat image and the PCA modified Landsat image.

2. Lithologies

2.1 Karakoram

2.1.1 Introduction

Hayden (1915) and Tipper (in Fermor 1922 and in Pascoe 1923, 1924), reported general successions and fossil localities of the Karakoram in their pioneering work. Other mainly litho-stratigraphic publications are due to Desio (1959,1963), Ivanac *et al.* (1956), Matsushita & Huzita (1965) and Desio *et al.* (1977). Karakoram sedimentary units in Chitral were later described by Pudsey *et al.* (1985), Pudsey (1986), Gaetani *et al.* (1996), Zanchi *et al.* (2000) and Hildebrand *et al.* (2000). The northwestern edge of the geological map (enclosed) overlaps the map of Hildebrand *et al.* (2000). Some lithology names were adopted from Pudsey *et al.* (1985).
Three Karakoram lithological groups are distinguished: (1) low grade meta-sediments, (2) Gambir monzonite, granites and granodiorites and (3) meta-basites.

2.1.2 Low grade meta-sediments

Carbonates-sandstones sequences (Kk-CS)
This unit crops out in the uppermost Chitral Gol and was extended using the Landsat image. Hildebrand *et al.* (2000) termed this unit ‘brown to dark grey fine-grained phyllites’ and correlated it with the probably Devonian-Permian Lun and Owir shales (Hayden 1915, Desio 1966). Hildebrand *et al.* (2000) described strongly cleaved phyllites consisting of mainly quartz, muscovite ± carbonates.

Limestones and marbles (Kk-L)
The eastern belt of the *limestones and marbles*, southwest and northeast of Gahiret, were termed by Pudsey *et al.* (1985) ‘Gahiret limestone’. They allegedly overlie the *slates and quartzites* (Pudsey’s ‘Chitral slates’).
The western 1-2 km thick *limestones and marbles* belt, located in the footwall of the Reshun fault from the Chitral to the Birir Gol, coincides on the Landsat image with the ‘Krinj limestone’ previously mapped by Desio (1959), Pudsey *et al.* (1985) and Hildebrand *et al.* (2000). Desio (1959) dated orbitolinae and rudists from the Krinj location in the Luthko Gol as ‘probably Early Cretaceous’. These *limestones and marbles* were mapped west and northwest of Drosh at Gahiret, in the Jingeret, Swir and Dam Gol. Unpublished data from Pudsey

(pers. comm.) were used for the Rumbur Gol section. The sequence comprises snow white to greyish laminated, fine-grained marbles. The unit thins out in the Dam Gol and becomes mylonitic southwestwards towards the suture fault zone (Fig. 3.1a). White to grey marbles are laminated, isoclinally folded and locally contain interbeds of up to 2 m thick sandy limestones and black schists northwest of Madaglasht, in the upper Shishi Gol.

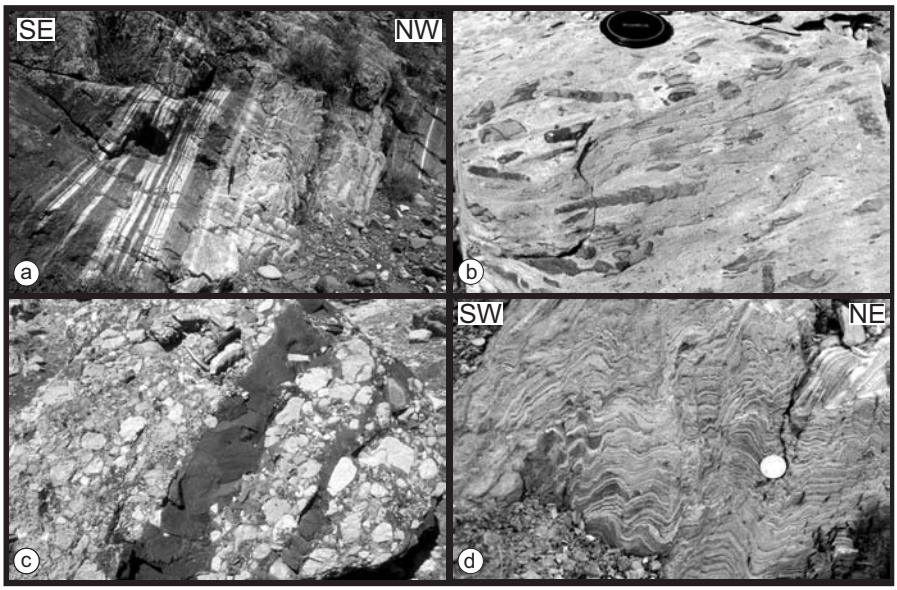

Fig. 3.1. *Karakoram units.* ***a)*** *foliated marbles (light colour layers) and greenschists (dark layers); Kk-S, Dam Gol, 8.5 km SW of Drosh.* ***b)*** *micritic limestone containing up to 10 cm long gastropods and smaller foraminiferae; Kk-VC, Manji Gol, 4 km NE of Madaglasht.* ***c)*** *almost undeformed grain-supported quartz-pebble conglomerate intruded by a basaltic sill (black) containing quartz arenite (white) and limestone pebble enclaves (grey); pebbles are angular to weakly rounded and up to 0.5 m big; minor pebbles are derived from violet shales, volcanoclastic greenstones and basaltic dykes; Kk-VC, Shachiokuh, 6.5 km N of camp III.* ***d)*** *disharmonically folded black shales (dark layers) and brown calcareous quartz arenites (light colour layers); Kk-SSQ, Angarbah Gol, 2 km N of Madaglasht.*

Slates and quartzites (Kk-S)

Black slates are the major constituent of the Karakoram terrane (Gaetani 1997). The *slates and quartzites* were first described by Hayden (1915), followed by Tipper (in Fermor 1922 and in Pascoe 1924, Desio 1963, Pudsey *et al.* 1985, Buchroithner *et al.* 1986 and Pudsey 1986). On the map, the *slates and quartzites* include the Paleozoic to Mesozoic ‘Chitral slates’ (Pudsey *et al.* 1985) west of the Golen Gol and the likely Permian to Carboniferous ‘Darkot Group’ (Pudsey *et al.* 1985 and ref. therein) in the east.

Graphitic to black slates are locally intercalated with 1-2 m thick carbonate layers in the Jingeret Gol and the valleys further southwest (Figs. 3.2a,b).

Black calcareous schists with quartz ribbons are quite common while quartzite layers occur rarely.
Greenschists, including micro-conglomerates and -breccias, of volcanoclastic origin occur locally, in particular just beneath and above the interlayered marbles between Ursun and the Jingeret Gol. These fine-grained greenschists comprise mainly quartz, epidote, muscovite, biotite, chlorite and feldspar (microscope identification). Accessory minerals are brown spinel, ores and zircon. Ribbons of recrystallised quartz define the foliation.

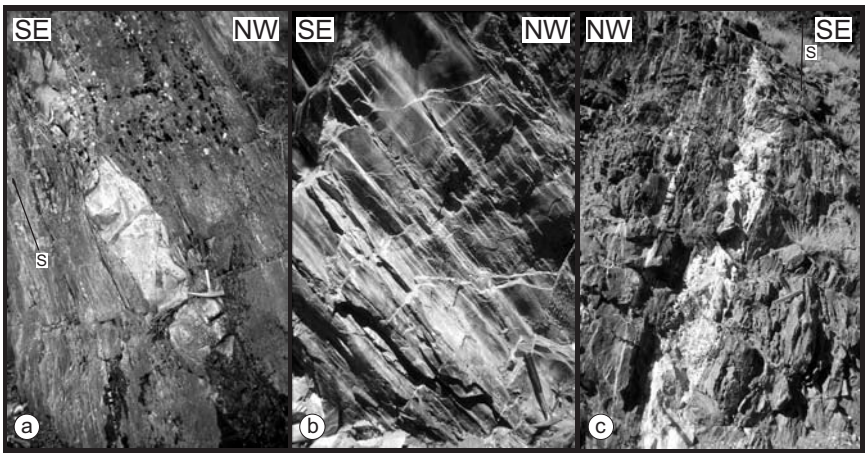

Fig. 3.2. *Karakoram units.* ***a)*** *pinched-and-swelled granitic dyke (white) crosscutting Kk-S black slates; Gambir Gol, 11.6 km SW of Drosh.* ***b)*** *kink to chevron folds in the black slates; Kk-S, Jingeret Gol, 6.5 km W of Drosh.* ***c)*** *tabular marble (white) enclave (0.5 m thick) within meta-gabbro; strongly recrystallised and stretched in the main foliation S; Kk-GD, opposite (W of) Shishi-Kunar River confluence, 3 km N of Drosh.*

Black shales and slates often display graded bedding and contain some metres thick, mainly brownish quartzite beds further northeast, in the Golen and Phargam Gol. The slates are contact metamorphosed into andalusite-biotite schists around the nearby Phargam and Buni Zom granite bodies. These schists display a porphyric schistose texture where euhedral andalusite porphyroblasts are overgrown by biotite in a fine-grained matrix of quartz and feldspar (thin section observation).
The sedimentary facies of these slates and quartzites is difficult to constrain. They may either represent a slate-dominated turbiditic sequence or mature shallow water marine platform deposits.

Volcanoclastic and calcareous sequences (Kk-VC)
These sediments comprise black limestones, grey marbles, different types of conglomerates, volcanoclastic sandstones, volcanites and shales. The sediment assemblage could not be correlated with previously defined lithologies of the southern Karakoram. Pudsey *et al.* (1985) included this unit into

their pelitic ‘Darkot Group’ or the undifferentiated ‘Northern Suture mélange’. However, in the Shishi Gol section, several different sedimentary sequences were clearly identified:

(1) Conglomerates and interlayered, calc-alkaline volcanites crop out in the Domuk Gol north of Kalas and in the Shachiokuh. The conglomerate matrix varies from dark green to black depending on its relative volcanoclastic or calcareous content. The conglomerates are grain-supported, poorly sorted and generally rich in pebbles of quartz arenite, volcanoclastic greenstones, violet shales, micritic limestones and mafic volcanites (Fig. 3.1c). The pebble size ranges between 0.5 and 25 cm. The northernmost outcrops reached in the Domuk Gol comprise deformed conglomerates with elongate quartz and volcanite pebbles in a matrix of white marble. Grey limestone beds with 0.3 m thick calc-alkaline volcanic interlayers occur locally. Impressive quartz arenite-pebble conglomerates are intruded by 10-50 cm thick basaltic sills in the Shachiokuh (Fig. 3.1c). Quartz arenite pebbles are angular to moderately rounded and 10-25 cm in diametre.

(2) Carbonate conglomerates and typically green volcanoclastic conglomerates and breccias crop out northwest of Madaglasht. These apparently undeformed conglomerates are generally matrix-supported, poorly sorted and the moderately to well-rounded pebbles mainly consist of quartz arenite. Other small pebbles are limestones, volcanites and, less frequently, cherts and paragneisses.

(3) Pebbly mudstones and laminated limestones are tectonically imbricated within meta-ultramafites in the Tar and Ustrum Gol and northeast of Ursun (Fig. 3.3a). Laminated limestones and shales are graded (where little deformed) indicating a general younging to the northwest. Sandstones and quartzites are rather rare. Green volcanic or volcanoclastic interlayers and boudins are 0.1-0.5 m thick and occur frequently within these sequences. The pebbly mudstones are mainly grain-supported, poorly sorted, and strongly deformed. The matrix is essentially carbonatic, locally volcanoclastic. Well-rounded quartz-rich pebbles are the most abundant. Other pebbles are volcanic greenstones, diorites (Fig. 3.3b) and shreds of white marble. The pebble size varies from mm up to 20 cm. The limestones occur as schistose sandy packstones containing bioclasts east of Manji Gol. Dark grey sand-bearing ‘impure’ limestones are rich in biogenic fragments such as stems of crinoids, bryozoae, calc-algae, radiolitidae (*rudist bivalves*, Cretaceous), gastropods (*nerinea, Cretaceous*), foraminifera (*orbitolinae*, Early to early Late Cretaceous) and corals (D. Bernoulli, pers. comm.), recognised in thin sections. Rudists and gastropods (up to 10 cm big), and unspecified shells are preserved in schistose and thinly laminated, black reef limestones of the Angarbah Gol and in grey micritic limestones in the Manji Gol (Fig. 3.1b).

(4) Grey massive micritic limestones are very common among the carbonate conglomerates and shaly limestones (Fig. 3.3c). They often occur as small tectonic wedges within the *serpentinites and talcschists*.

(5) Blue green, locally agglomeratic and isoclinally folded meta-volcanic greenstones, conglomerates and snow-white, very fine-grained marbles occur north and south of a quartz diorite body in the lower Domuk Gol. White, coarse-grained marbles occur as boudinaged lenses within the meta-volcanites.
Interlayered green doleritic volcanites west of Madaglasht were mapped as a separate subunit (*mafic volcanites)* of the *volcanoclastic and calcareous sequences.*
The bentic fauna in the limestones indicates deposition in a shallow water environment during the Early to early Late Cretaceous. The large amount of quartz pebbles in the conglomerates indicates a continental crust in the source region. Local volcanic interlayers point to nearby active volcanism. The combined occurrence of shallow marine fossiliferous limestones and a strongly variable clastic facies suggests deposition in a delta environment on the shelf of the Karakoram active margin.

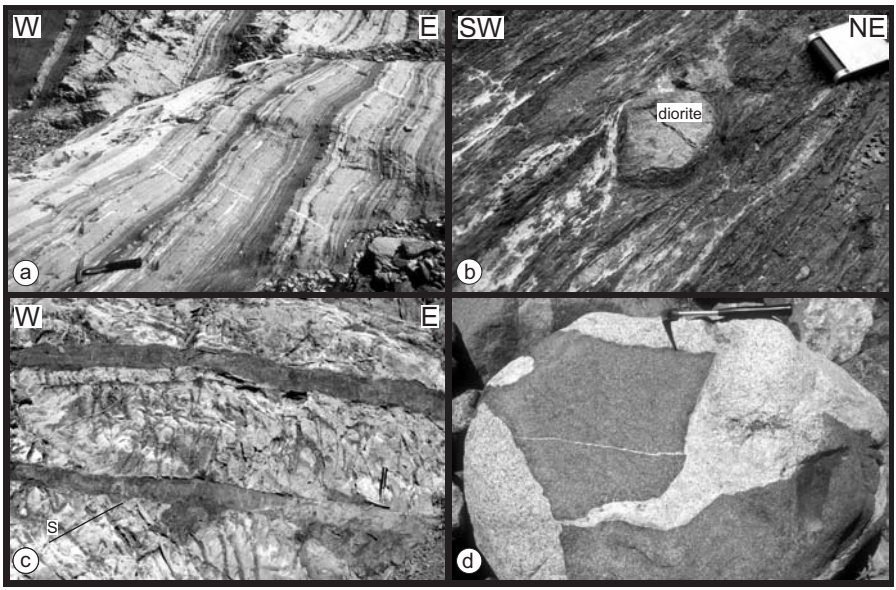

Fig. 3.3. *Karakoram units.* ***a)*** *turbiditic sequence of laminated micritic limestones with interlayered carbonatic shales and volcanoclastic sandstones (dark, to the left); Kk-VC, Tar Gol, 1.6 km NW of Gawuch.* ***b)*** *volcano-clastic greenschist containing a diorite pebble; Kk-VC, 0.7 km E of Ursun.* ***c)*** *0.2 m thick undeformed, E-W striking, mafic dykes crosscutting NE-SW striking grey limestones; S: foliation (parallel to bedding); Kk-VC & S-mD, 3.5 km SW of Madaglasht.* ***d)*** *boulder of the homogeneous medium-grained Gambir monzonite (white) containing angular mafic xenoliths (dark), Kk-M, Gambir Gol, 12 km SW of Drosh.*

Slates-siltstones-quartzites sequences (Kk-SSQ)

This formation includes three spatially distinct units. One is located in the hanging wall of the Reshun Fault and was mapped on the Landsat image. It

correlates, together with the *carbonates-sandstones sequences,* with the 'Phyllites' of Hildebrand *et al.* (2000).
The second unit crops out in the upper Shishi Gol and comprises disharmonically folded sequences of black shales and brown calcareous quartzites with a few metres thick red sandstones and deformed conglomerates at the base (Fig. 3.1d). Graded bedding indicates younging to the northwest, thus a normal sequence.
The third unit was briefly investigated in the Golen Gol. It contains calcareous quartzites with a typical rusty colour, non-calcareous white quartzites and quartz-muscovite-biotite schists. This unit has no characteristic colour on both Landsat images and its extent is therefore ill constrained.

2.1.3 Gambir monzonite, granites and granodiorites

Gambir Monzonite (Kk-M)
An essentially undeformed, medium-grained monzonite body intruded the *slates and quartzites* west of Ursun (cross-section AA', enclosed map). Metre to decametre long hornfels and marble enclaves occur locally. Minor *mafic dykes* are subvertical.
The magmatic texture is preserved, as displayed by common angular to rounded hornblende-rich, centimetre sized xenoliths (Fig. 3.3d). The magmatic minerals, determined under the microscope, are K-feldspar (35%), plagioclase (25%), amphibole (8%) and accessory apatite, zircon and unspecified ores. Alteration products are muscovite, chlorite and biotite.
A slightly deformed, foliation-parallel granitic dyke intruded the *slates and quartzites* in the lower Gambir Gol and is likely related to the nearby intrusion of the Gambir monzonite (Fig. 3.2a).

Granites (Kk-G)
This unit includes different bodies, some mapped in the field, others identified on the Landsat image.
A N-S trending granite body known as the Kafiristan pluton in the uppermost Bumburet and Chitral Gol (Desio 1964, Pudsey *et al.* 1985, Debon *et al.* 1987b, Hildebrand *et al.* 2000), was mapped using mainly the Landsat image on which it could be traced easily due to the white to yellowish-rose colour typical for granites on the ETM+ image. Hildebrand *et al.* (2000) described it as 'strongly foliated porphyric granodiorite to granite'. A Rb-Sr whole-rock age yielded ca. 483 Ma (Desio 1964, Debon *et al.* 1987b).
Another granitoid body (Austrominerals unpub.) intruded the *sheared gabbros and diorites* and *granodiorites* in the lower Golen Gol as defined from the Landsat image.
The undeformed, coarse-grained *Phargam granite* intruded the *slates and quartzites* and other volcanosedimentary sequences in the upper Golen Gol.

Elongate mafic xenoliths are common, as well as crosscutting mafic dykes and rounded dioritic enclaves. The magmatic minerals, identified in thin sections, are euhedral K-feldspar, plagioclase, quartz and less frequent green biotite and sphene. Accessory minerals are zircon, apatite and unspecified ores. Alteration products are muscovite, chlorite and epidote. A U-Pb zircon age of the *Phargam granite* yielded 103.79±0.27 Ma (chapter 5).
The *Buni Zom granite* occurs at the northeastern edge of the map and was mapped from the Landsat image. Boulders of this body were found in the moraines near Phargam. They display an undeformed, unaltered, medium-grained granite containing quartz, feldspar, biotite and epidote.

Granodiorites (Kk-Gd)
Granodiorites were identified on the PCA-modified satellite image from their blue-violet colour. They are sometimes not easy to distinguish from gabbros and diorites which have similar colours on the same image. Boulders were found in the Shachiokuh. Another granodiorite probably intruded the *slates and quartzites* prior to the intrusion of the *Gambir monzonite* in the Jingeret and Gambir Gol (cross-section AA', enclosed map). Intrusive relationships were inferred from the Landsat and PCA-modified Landsat images and therefore remain uncertain. Granodiorites likely intruded the *sheared gabbros and diorites* in the Golen Gol and were intruded by younger *granites*.

2.1.4 Meta-basites

Sheared gabbros and diorites (Kk-GD)
This unit forms a lenticular, 75 km long composite body of mainly sheared meta-gabbros and -diorites with minor quartzo-feldspathic migmatites, meta-granitic dykes and hornblendites. Its extent coincides approximately with the western part of the 'Kesu-Buni Zom pluton' mapped by Pudsey *et al.* (1985). The unit thins against the suture west of Drosh and disappears completely southwest of the Dam Gol (cross-sections AA', BB', enclosed map). Metre to decametre large enclaves of quartz-feldspar-rich migmatites make up about 10-15% of this unit (Pudsey *et al.* 1985). Foliation-parallel coarse-grained marble enclaves are 1-100 m thick and 5-500 m long (Fig. 3.2c).
The sheared gabbros and diorites are compositionally 'layered' with pale green hornblende and plagioclase-rich layers being the predominant constituents. The magmatic mineral composition was deduced from microscope observation and is represented by euhedral hornblende, brown biotite, sphene, illmenite and quartz (in meta-diorites). Accessory minerals are brown spinel, zircon and apatite. The metamorphic minerals are represented by recrystallised plagioclase, hornblende, epidote, chlorite, actinolite and garnet in some places.

Sheared leucocratic dykes, crosscutting the sheared gabbros and diorites, are composed of magmatic K-felspar, plagioclase, quartz, biotite and locally allanite and amphibole. Accessory minerals are brown spinel, zircon and sphene. The metamorphic paragenesis is expressed by muscovite, epidote and clinozoisite. Feldspar and quartz are recrystallised and muscovite occurs often as large mica fish (Fig. 3.4a). These rocks show locally an ultramylonitic texture (Fig. 3.4b). The whole unit is isoclinally folded.
A meta-dioritic amphibolite just north of the imbricate suture zone in the Kalas Gol was dated at 105.20±0.29 Ma (U-Pb on zircon, chapter 5).
The *sheared gabbros and diorites* are interpreted as greenschist to lower amphibolite facies metamorphic rocks. The leucocratic dykes have a granitic composition.

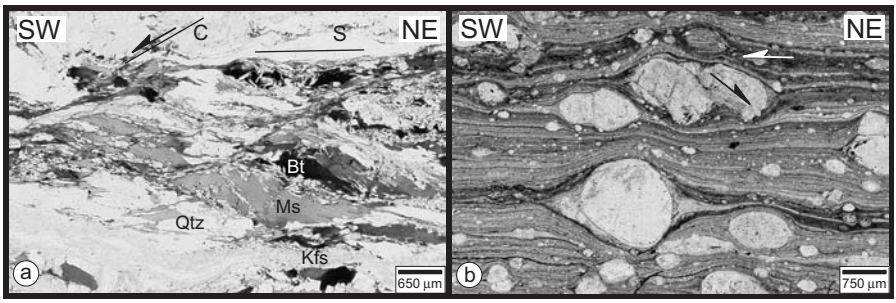

Fig. 3.4. *Thin sections of Karakoram units (sections are parallel to the lineation and perpendicular to the foliation; mineral symbols after Kretz 1983); non-polarised light:* ***a)*** *meta-granite; the foliation (S) is defined by biotite-muscovite and quartz-rich bands; shear bands (C) indicate a top-to-SW (sinistral) sense of shear (arrow); Kk-GD, Skari Gol, 4 km of SW of Madaglasht.* ***b)*** *granitic ultramylonite with rounded, altered plagioclase and minor K-feldspar porphyroclasts; the finely banded matrix consists of quartz, feldspar, biotite and muscovite; a broken feldspar porphyroclast forms a book-shelf structure (black arrow) consistent with a sinistral (SW-ward) sense of shear (white arrow); Kk-GD, Dam Gol, 8.5 km SW of Drosh.*

Amphibolites (Kk-A)
Amphibolites, occurring within the *slates and quartzites* unit, were easy to identify on the Landsat image due to their typical reddish colour. Desio *et al.* (1977) described 'pyroxene two-mica gneiss, augen gneiss, epidotic amphibolite, pyroxenite and pyroxene-amphibole-biotite diorite' as abundant rocks occurring next to the predominant 'black slates and quartzites' of his 'Laspur complex' that corresponds to the *slates and quartzites.*

Greenschists (Kk-Gr)
Greenschists display reddish colours similar to that of the amphibolites on the Landsat image, but they are clearly distinguishable from the latter on the PCA-modified image thanks to their intense pinkish-violet colour. The major greenschist unit is the so-called *Koghozi greenschist (Pudsey et al. 1985)* east of Chitral. Pudsey *et al.* (1985) described it as 'fine-grained chlorite-epidote-quartz-schists'.

2.2 Karakoram-Kohistan Suture

2.2.1 Introduction

The suture is defined as a zone of imbricate units that are derived from the marine basin between the Karakoram margin and the Kohistan island arc. The northern boundary of this zone is a fault separating the southernmost Karakoram units (*slates and quartzites* in the very southwest of the map and northeast of Madaglasht, and *sheared gabbros and diorites* and v*olcanoclastic and calcareous sequences* in the Jingeret and lower Shishi Gol area; cross-section AA', enclosed map) from the imbricate *serpentinites and talcschists*, *calcareous turbidites* and Karakoram derived *volcanoclastic and calcareous sequences*. The southern boundary of the suture zone is represented by a fault separating *calcareous turbidites* to the northwest from *Purit red clastics* and *Drosh volcanites* to the southeast.
The specific, imbricate suture units, west of Andowir Ghari, are from north to south (Fig. 3.10, cross-sections AA', BB', CC', enclosed map):

- *serpentinites and talcschists (S-ST)*
- *mafic dykes (S-mD)*
- *gabbros and diorites (S-GD)*
- *hornfelses (S-H)*
- *calcareous turbidites (S-T)*

Northeast of the Shishi Gol (NE of the Lohigal An), the Kohistan-derived *Drosh limestones and volcanites* and *Purit red clastics* are imbricate in the suture, whereas there are no Karakoram-derived *volcanoclastic and calcareous sequences*. The suture zone assemblage therefore contains from north to south (cross-section DD', enclosed map):

- *serpentinites and talcschists (S-ST)*
- *three units derived from north Kohistan*
- *calcareous turbidites (S-T)*

Duplication across a wrench-duplex is probably responsible for the three *north Kohistan units* to occur north of the *calcareous turbidites*.

2.2.2 Suture lithologies

Serpentinites and talcschists (S-ST)
Schistose serpentinites, talcschists, ophicarbonates and locally massive serpentinites crop out between Ursun and the Lohigal An. Meta-ultramafites

are very rare further east. These serpentinite slices are fault everywhere bounded, denoting the suture imbrication, and occur in four different tectonostratigraphic groups:
(1) metre to hundred metres thick lenses of ultramafites crop out within and to the southeast of the *volcanoclastic and calcareous sequences* forming a tectonic imbrication between Ursun and Madaglasht.
(2) two to five metres thick slices of serpentinites and mainly talcschists separate the *Purit red clastics* from the *Gawuch greenschists and marbles* between Mirkhani and the Birgah Gol.
(3) schistose serpentinite occurs as small 2-10 m thick tectonic lenses along the fault separating the Karakoram *volcanoclastic and calcareous sequences* from the *Purit red clastics* between the uppermost Shishi Gol to the Shachiokuh.
(4) thin tectonic slices of serpentinite separate *calcareous turbidites* from *Gawuch greenschists and marbles* between the Lohigal An and the Shachiokuh Pass.

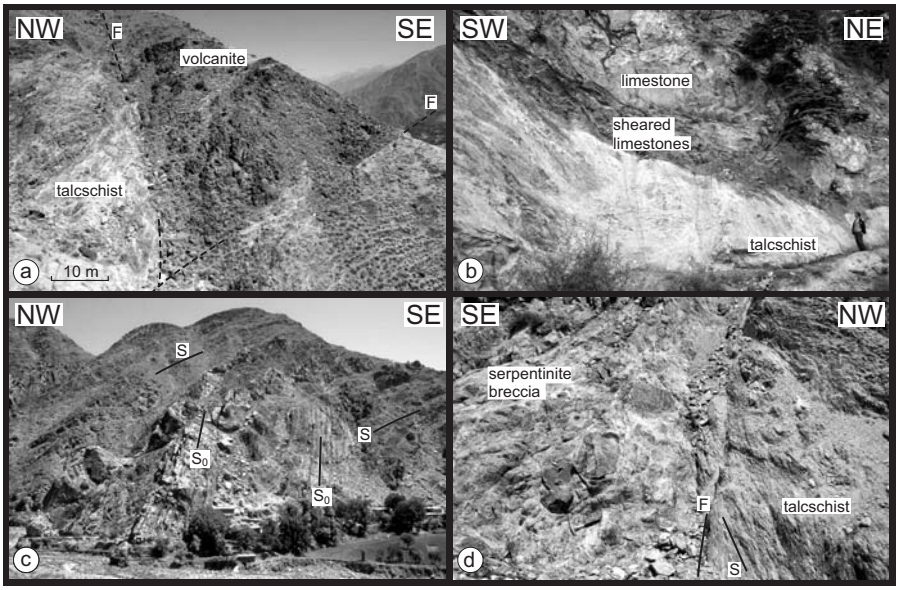

Fig. 3.5. *Imbricate suture units.* ***a)*** *low grade volcanite block squeezed between talcschists separated by anastomosing faults (F); S-ST, Swir Gol, 6 km SW of Drosh.* ***b)*** *NW dipping fault along which sheared limestones separate talcschists from limestones; S-ST, Kk-VC, Angarbah Gol, 200 m W of Madaglasht.* ***c)*** *huge block (trees for scale) of micritic limestones (S_0: bedding) within moderately NW dipping talcschists and serpentinites; note that bedding in the block is oblique to the serpentinite foliation (S); S-ST, Kk-VC; just NW of Jingeret, 5 km SW of Drosh.* ***d)*** *subvertical brittle fault (F) separating steeply NE dipping talcschists from a 4 m thick boudin of serpentinite breccia; the breccia is component-supported containing up to 1 m large blocks of massive serpentinite in a matrix of fine-grained schistose talcschist; S-ST, Kashindel Gol, 6 km NNW of Gawuch, lower Shishi Gol.*

The following descriptions will focus on group (1) ultramafites. They are tectonic wedges associated with lenses and blocks of basic volcanites and dykes, gabbros, limestones and crosscutting mafic dykes and sills (Fig. 3.5).
Thin section microscopy revealed six greenschist facies rock types: (1) antigorite-magnesite-magnetite serpentinites (Fig. 3.6a), (2) talc-chlorite felses, (3) magnesite schists (Fig. 3.6b), (4) talc-magnesite-dolomite schists, (5) chlorite-dolomite marbles and (6) strongly deformed ophicarbonates. Chrysotile and tremolite are frequent.
The original paragenesis of the ultramafites is rarely preserved and is represented by spinel, magnetite and scarce unspecified clinopyroxene relicts. The scarcity of Ca and Al-rich phases suggests a harzburgitic rather than a lherzolitic protolith. Generally, two major mineral reactions were identified: serpentinisation and carbonatisation.

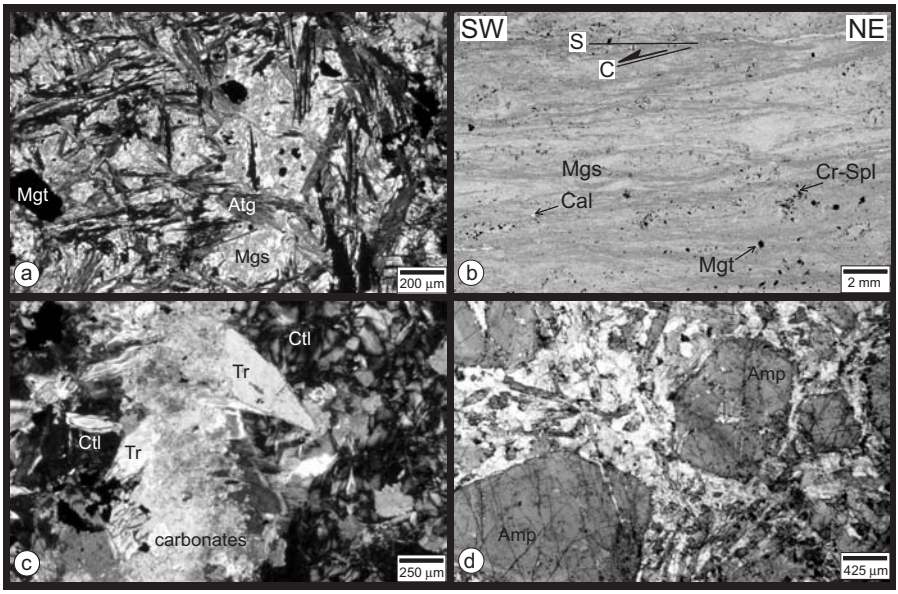

Fig. 3.6. *Thin sections of suture zone units (section c is horizontal, parallel to the lineation and perpendicular to the foliation; mineral symbols after Kretz 1983); a, c: polarised; b, d: non-polarised light.* ***a)*** *typical greenschist facies suture serpentinite; antigorite is the predominant serpentine mineral along with metamorphic magnetite and magnesite; Jingeret Gol, 5 km SW of Drosh.* ***b)*** *magnesite schist (S: foliation) with shear bands (C) indicating a sinistral (SW-ward) shear (arrow); accessory minerals shown are magnetite, spinel and calcite; S-ST, Manji Gol, 3 km NE of Madaglasht.* ***c)*** *ophicarbonate, indicating infiltration of sea water, along cracks within serpentinites where chrysotile is the dominating mineral; tremolite grew at the interface between carbonates and chrysotile; S-ST, same locality as a).* ***d)*** *magmatic texture in an undeformed 106.6 Ma basaltic sill; euhedral amphiboles occur as large phenocrysts as well as smaller grains in the matrix (see text); Chhuchhu Gol, 1 km SW of Madaglasht.*

The least deformed lens of meta-ultramafite was found in the Jingeret Gol among splintery serpentinites and talcschists (Fig. 3.7a). This lens is composed of brecciated serpentinite with a carbonate matrix. Primary ultra-

mafite minerals, e.g. spinel, are rarely preserved. The metamorphic paragenesis is represented by chrysotile, magnesite, magnetite, tremolite, dolomite and subordinate calcite (Fig. 3.6c).
Carbonates (calcite and probably dolomite) seem to have precipitated from infiltrated sea water into brecciated serpentinite. Therefore, this meta-ultramafite represents an ophicarbonate. The occurrence of ophicarbonates indicates that these meta-harzburgites were brecciated near or at the sea floor (Bernoulli & Weissert, 1985) in the Neo-Tethys.

Mafic dykes (S-mD)
Mafic dykes and sills intruded the *volcanoclastic and calcareous sequences* and were found mainly in the upper Shishi Gol (e.g. Tar, Angarbah and Manji Gol) but also occur in the Drosh area, intruding the *Drosh volcanites* (Fig. 3.9b), *sheared gabbros and diorites (*e.g. southwest Matio, Taikra*),* the Gambir monzonite (section 2.1.3), the *serpentinites and talcschists (*Fig. 3.7b, Chhuchhu Gol*)* and the *calcareous turbidites (*e.g. Tar Gol, Gashish Gol, Birgah Gol).
Two generations of dykes can be distinguished. The first generation, folded and parallelised to the foliation (Fig. 3.19a), intruded before the formation of the main foliation. The second generation is represented by 106.6 Ma (next paragraph and chapter 5) undeformed dykes and sills crosscutting ductile deformation fabrics and bedding (Fig. 3.3c). Hence, the first generation intruded before 107 Ma.
The magmatic paragenesis of an undeformed sill crosscutting talcschists in the Chhuchhu Gol (Fig. 3.7b) includes brown and possibly also green amphiboles, plagioclase, sphene and hematite (microscope determination). Accessory magmatic minerals are zircon and apatite. Alteration products are calcite, chlorite, epidote, muscovite, albite and actinolite. Brown magmatic and green euhedral amphiboles occur as porphyritic phenocrysts (Fig. 3.6d). The green amphiboles locally grew along the rims of the brown ones and are altered to calcite, muscovite and epidote. The matrix consists of brown, smaller grained amphiboles and mainly alteration products. The metamorphic paragenesis indicate greenschist facies metamorphic conditions. It is unclear whether the euhedral, unaltered amphiboles are magmatic or metamorphic.
The intrusion age of this sill, measured with the U-Pb method on zircon, is 106.64±0.35 Ma (chapter 5). The Ar-Ar method on hornblende yielded a consistent age of 106.8±2.5 Ma (chapter 5). This age represents a minimum age of the serpentinisation and deformation of the foliated serpentinites (meta-harzburgites).

Gabbros and diorites (S-GD)
Several quartz diorites and gabbros intruded serpentinites, *limestones* and the protoliths of the *hornfelses* between the Tar and Kashindel Gol (Figs. 3.8a,b).

An undeformed lens of serpentinite was intruded by a quartz monzodiorite in the Tar Gol (Fig. 3.7c). A 5-15 cm thick chilled margin and serpentinite enclaves within the gabbro prove its intrusive character. Magmatic minerals of the monzodiorite are zoned, green magnesiohastingsite (amphibole), illmenite, plagioclase, quartz, probably garnet and accessory apatite. The rock is strongly altered to fine-grained unspecified feldspar, epidote, sphene and chlorite. Plagioclase and amphibole occur as eu- to subhedral phenocrysts. A dark green amphibole was found locally in the core of the magnesiohastingsite. This strongly altered quartz monzodiorite did not yield any zircon out of a 24 kg sample. Ar-Ar dating on hornblende yielded an age of 130±7.6 Ma (chapter 5) suggesting that the meta-harzburgites were serpentinised before the Barremian (130 Ma).

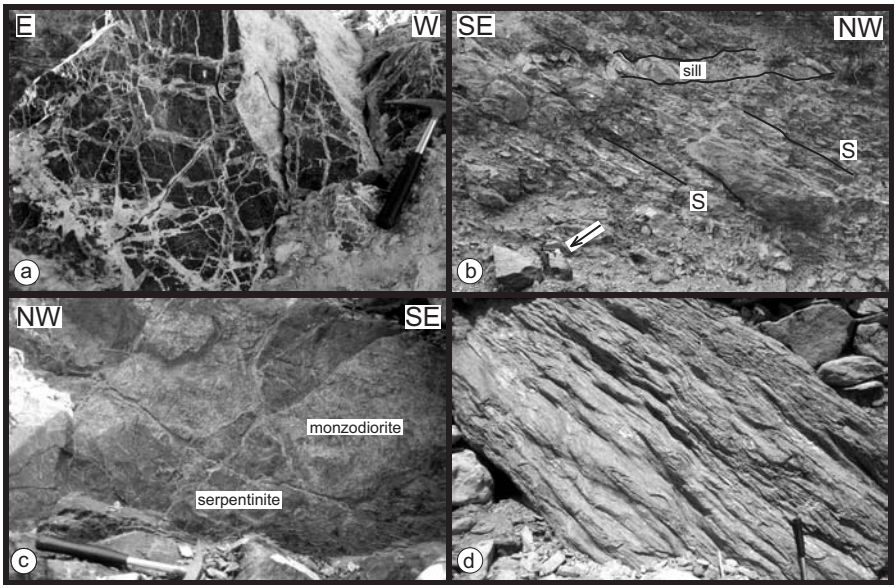

Fig. 3.7. *Imbricate suture units.* ***a)*** *cutout of a decametre big lens of brecciated, internally undeformed serpentinite/ophicarbonate (black); cracks are filled with calcite (and probably dolomite); S-ST, Jingeret Gol, 5 km SW of Drosh.* ***b)*** *subhorizontal, 106.6 Ma old, basaltic sill, that crosscuts NW-dipping, schistose (S) serpentinites; rucksack (arrow) for scale; S-ST, S-mD, Chhuchhu Gol, 0.8 km SW of Madaglasht.* ***c)*** *enclaves of black serpentinite in the ca. 130 Ma quartz monzodiorite; S-SU, Tar Gol, 1.6 km WNW Gawuch.* ***d)*** *boulder of slate-dominated, irregularly folded turbidites; S-T, lowest Shishi Gol, 7 km NE of Drosh.*

A homogeneous, medium-grained, grey quartz diorite is intruded by an undeformed granitic dyke north of Gawuch (cross-section BB', enclosed map). The quartz diorite displays a weak magmatic fabric. Thin section observation showed that magmatic minerals are quartz (15%), with undulose extinction, sub- to euhedral green hornblende, plagioclase and minor pyroxene and biotite. Plagioclase is strongly altered to white mica and chlorite. The granitic dyke comprises predominantly quartz and K-feldspar with subordinate green

hornblende. Accessory minerals are unspecified ores and zircon. Quartz is recrystallised and K-feldspar is altered to epidote and muscovite. An U-Pb age on zircon yielded an intrusion age of 107.00±0.18 Ma (chapter 5).
An isolated, 0.7 km wide and 2 km long, quartz diorite body was found at the entrance of the Domuk Gol (cross-section CC', enclosed map). It has an intrusive contact with highly deformed *volcanoclastic and calcareous sequences* to the south and northwest and is separated by sinistral faults from *serpentinites and talc-schists* to the north and to the east. The magmatic texture of this medium-grained rock is preserved in the core of the body. Stretched mafic xenoliths and subvertically oriented hornblende crystals define a weak, probably magmatic fabric. Dioritic subvertical dykes intruding the country greenstones and marbles of *volcanoclastic and calcareous sequences* are boudinaged and parallel to the regional foliation a few metres south of that contact. This indicates that the intrusion took place prior or during regional deformation. Magmatic minerals are plagioclase, green subhedral hornblende, quartz, biotite and sphene (microscope analysis). Accessory minerals are brown spinel, unspecified ores, zircon and apatite. Alteration products are white mica, epidote and chlorite. U-Pb dating on zircon of an undeformed sample from the centre of this body yielded an intrusion age of 106.95±0.97 Ma (chapter 5).

Hornfelses (S-H)
Between Gawuch and Kalas a maximum 700 m thick unit of violet to dark brown silicified hornfelses crops out. Original layering with load cast structures are locally preserved. Meta-pelitic layers are violet in colour and meta-sandstone layers are brown.
These hornfelses represent sandy meta-pelites and -sandstones that were contact metamorphosed by 10-150 m thick intrusive bodies and smaller dykes of the *gabbros and diorites* formation.

Calcareous turbidites (S-T)
Calcschists and calcareous sandstones crop out south of the imbricate *serpentinites* and *volcanosediments* between the Afghanistan-Pakistan border and Kalas. This unit appears further south, to the northeast of Andowir Ghari, separating the *Drosh limestones and volcanites* from the *Gawuch greenschists and marbles*.
The essentially finely laminated sequences of calcschists and calcareous sandstones (Fig. 3.8c) are irregularly folded (Fig. 3.7d) and often strongly deformed, as indicated by numerous veins filled with mainly quartz and minor calcite. Layers of microconglomerates occur locally. Locally preserved cross- and graded bedding indicates the younging direction to the east.
Black calcschists and well-laminated carbonate shales are interlayered with black slates in the uppermost Shishi Gol. These calcschists contain a calcite-microsparite-matrix with strongly deformed calcite crystals. Other mineral

components are locally zoned plagioclase of magmatic (likely volcanic) origin, undefined shells and echinoderm fragments. 20-200 cm thick conglomeratic interlayers contain 3-40 mm large, poorly rounded quartz pebbles in an often volcanoclastic matrix.

These turbiditic calcschists, sandstones and slates were most likely deposited in a basin close to a continent or arc with volcanic activity. From the tectonostratigraphic position and lithological correlations the calcareous turbidites may represent an equivalent to the Yasin Group turbidites. In the Yasin area, carbonate shales, slates and interlayered volcanoclastic sandstones and fossiliferous limestones are imbricated in the suture together with red conglomerates and sandstones (equivalent to *Purit red clastics*) and mafic green volcanites (possible equivalent to the *Drosh volcanites*, Desio 1963, Pudsey *et al.* 1985, 1985b).

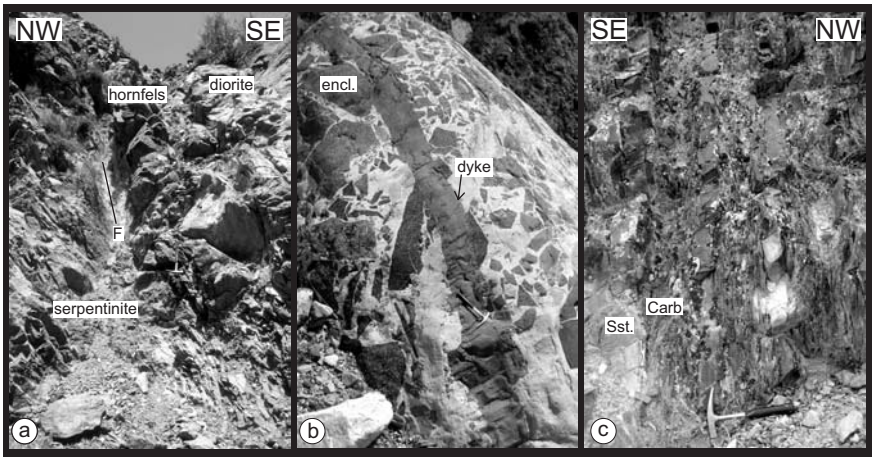

Fig. 3.8. *Imbricate suture units.* ***a)*** *brittle subvertical fault (F) separating massive serpentinites (left) from black silicified layered hornfelses (contact metamorphic meta-turbidites) that were intruded by a diorite (to the right); S-ST, S-T, S-GD; Gashish Gol, 3 km NNE of Gawuch.* ***b)*** *magmatic breccia: quartz diorite with huge (up to 1.6 m) angular mafic enclaves (encl.); all crosscut by mafic dyke; S-GD, E of the Domuk Gol, 7 km SW of Madaglasht.* ***c)*** *turbiditic sequence of carbonatic shales (Carb.) and volcanoclastic sandstones (Sst.); S-T, Tangal Gol, 8 km NE of Gawuch.*

2.3 Kohistan

2.3.1 Introduction

New lithologies are defined for the northern Kohistan units. Important differences to Pudsey *et al.*'s (1985, 1986) work are the newly specified units such as the *meta-gabbros and -diorites*, the *Mirkhani diorite* and *migmatites and paragneisses*. The *Drosh volcanites*, the *Gawuch greenschists and marbles* and the *Gawuch meta-basalts* are terms (not units) adopted from Pudsey *et al.* (1985, section 6.2 of chapter 2).
The Kohistan units are divided into three groups: (1) northern Kohistan units, (2) meta-volcanosediments and (3) plutonites, and are described from NW to SE. The northern Kohistan units (*Drosh limestones and volcanites*, *Purit red clastics* and the *Mirkhani diorite*) are separated from the meta-volcanosediments (e.g. *Gawuch greenschists and marbles*) by a fault along which lenses of serpentinites and talcschists crop out.

2.3.2 North Kohistan units

Drosh limestones (Ko-DL)
Fossiliferous micritic *Drosh limestones* crop out mainly northeast of Ghuchharsar (cross-section DD', enclosed map). There is only one, but famous, limestone outcrop southwest of Ghuchharsar, the 'Dundi Gal' locality first described by Hayden (1915) about 3 km south of Drosh (cross-section AA', enclosed map). A 100 m thick unit of grey massive limestone within the *Drosh volcanites* contains orbitolinae and up to 10 cm big rudists that were dated by Desio (1959) as 'probably Aptian'. Pudsey *et al.* (1985, 1985b) did not assign these limestones to their 'Drosh Formation' (comparable with the *Drosh volcanites*) but included them in their 'mélange' zone. However, the precise relationship of these limestones 'within' the Drosh volcanites (a lithological interlayer or a tectonic lens?) remains debated because Quaternary deposits obliterate the contacts on this outcrop.
Similarly, grey micritic limestones contain foraminiferae and are clearly interlayered in the *Drosh volcanites* in the Krui Uts area 50 km to the northeast. The limestones contain pebbles of interlayered basalts (*Drosh volcanites*) and layers of volcanoclastic sandstones with graded bedding younging towards the southeast (Fig. 3.9c). These limestone sequences with volcanic pebbles are interpreted to be derived from a volcanic arc shelf and redeposited into a deeper distal part of the marine basin.

Drosh volcanites (Ko-DV)

This unit coincides roughly with Pudsey *et al.*'s (1985) 'Drosh Formation', which they described south of Drosh and in the lower Shishi Gol. Drosh volcanites do not crop out between Gurin and Ghuchharsar.

The major rock types are weakly to undeformed anchimetamorphic, olive green to violet basaltic to andesitic lava flows, pyroclastic breccias and minor agglomerates and volcanoclastic interlayers (Fig. 3.9a). Amphibole and plagioclase phenocrysts are common.

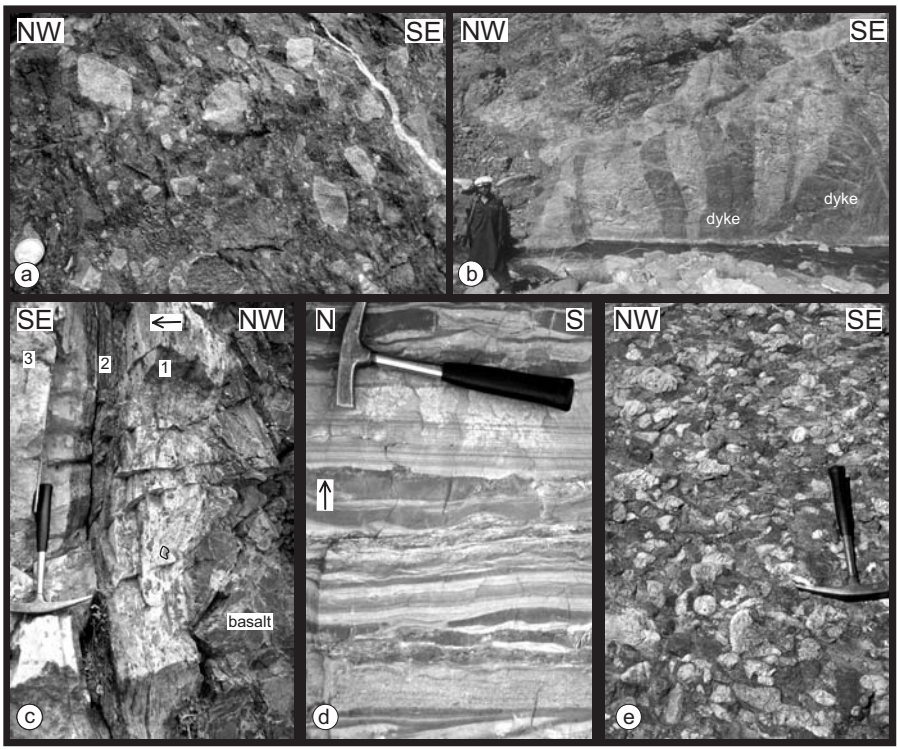

Fig. 3.9. *Kohistan arc units.* ***a)*** *volcanic breccia (Drosh volcanites) with leucocratic angular volcanic clasts (white) within a violet fine-grained andesitic matrix; Ko-DV, N of the Naghar Fort, 8.5 km SW of Drosh.* ***b)*** *subvertical mafic dykes intruding the basaltic Drosh volcanites; S-mD & Ko-DV, Ursun Gol, 11 km SW of Drosh.* ***c)*** *subvertical andesitic basalt overlain by micritic limestones containing basalt pebbles (1, one pebble is circled near the centre of the photograph), followed by volcanoclastic sandstone in a limestone matrix (2) and a pebble-free micritic limestone (3); the arrow indicates younging direction to the SE; Ko-DV, Ko-DL, uppermost Lohigal Gol, 0.6 km W of Krui Uts.* ***d)*** *graded upward (arrow) low-concentration turbidite made of red shales, siltstones and microconglomerates; Ko-PR, 9.5 km SW of Drosh.* ***e)*** *almost undeformed grain-supported Purit conglomerate; the moderately rounded pebbles comprise mainly quartz arenites (white) among minor violet shales (dark grey), volcanoclastic greenstones (dark grey) and less rounded carbonates (grey); Ko-PR, Drosh Gol, 3 km SSE of Drosh.*

At the southern limit of the unit, interlayered red to violet shales of the overlying *Purit red clastics* display the depositional transition from volcanoclastic

deposition to clastic sedimentation south of Drosh. The 111.5 Ma (see below and chapter 5) *Mirkhani diorite* and *mafic dykes* intruded the *Drosh volcanites* in the Ursun Gol and along the road from Mirkhani to Arandu (Afghanistan-Pakistan border check point, Fig. 3.9b).
To the northeast of Ghuchharsar, *Drosh volcanites* occur as frequently as *Drosh limestones* and form 20-300 m thick lens-shaped lava flows interlayered with the limestones (Fig. 3.9c). The occurrence of *Drosh volcanites* diminishes drastically northeast of the Shachiokuh Pass.
Pillow basalts were observed about 30 km SW of Drosh (off the enclosed map) along the road to Arandu (Afghan border check point). The tapered bottoms of the pillows indicate younging towards the southeast. It is possible that these pillow basalts are associated with the *Drosh volcanites* as they crop out along strike of the latter.
The *Drosh volcanites* are interpreted as island arc, effusive and explosive volcanic products. The significantly larger volume of volcanites (e.g. lava flows, agglomerates, volcanic breccias) to the southwest may point to proximity of a volcanic centre, while the smaller amounts of volcanites (e.g. lava flows, tuffs) to the northeast may reflect a more distal situation.

Purit red clastics (Ko-PR)
The red sandstones, shales and conglomerates, which crop out in the Shishi Gol, were termed 'Purit Formation' by Pudsey *et al.* (1985) referencing excellent outcrops in the Purit Gol. A 120±31 Ma detrital fission track age on zircon (Zeitler *et al.* 1985) constrains the maximum age of sedimentation. This unit is 1-3 km thick between Mirkhani and Gurin, and thins out to only a few tens of metres further northeast, where it is squeezed between two major faults (cross-sections AA', BB', enclosed map).
The sandstones are slightly calcareous with cross-bedding, ripples and graded bedding with varying upward younging directions implying an upright sequence (cross-section AA', enclosed map). Sequences of red microconglomerates, sandstones, siltstones and shales display features of low-concentration turbidites (Fig. 3.9d). Boulders and pebbles of the conglomerates are angular to well rounded consisting of quartz arenite, grey limestone, greenish volcanoclastic sandstone and andesitic basalts of the underlying Drosh volcanites (Fig. 3.9e). The matrix of the conglomerates comprises silty to sandy volcanoclastic debris and less frequent calcareous sandstones.
Red shales contain green elongated meta-lava pebbles from an underlying 2 m thick lava flow forming the base of the *Purit red clastics.* This unit unconformably overlies the *Mirkhani diorite* to the east of Mirkhani.
Red sandstones contain pebbles of green basalts (*Drosh volcanites)* and unconformably overlie the latter along an overturned erosional surface (younging to the east) southwest of Drosh. This lithological contact was locally 'reactivated' by a nearby reverse fault (cross-section AA', enclosed map).

The abundant volcanoclastic sandstones and volcanite pebbles indicate proximity of this detrital unit to an active volcanic arc. The common micritic, weakly lithified limestone pebbles indicate deposition not far from the source region. The red colour suggests subaerial deposition whereas sedimentary structures point to delta deposits. It is therefore assumed that the Purit red clastics represent alluvial fan or delta deposits in the proximity of an active (Kohistan) island arc.

Mirkhani diorite (Ko-MD)

The *Mirkhani diorite* intruded the *Drosh volcanites* south of Drosh an in the Ursun Gol. Red shales of the *Purit red clastics* unconformably overlie the diorite just east of Mirkhani. This unconformity is locally overprinted by a 10 m wide fault zone. A fault containing lenses of *serpentinites and talcschists* separates the diorite from the *Gawuch greenschists and marbles* to the south. 10-50 m sized wedges of splintery *Mirkhani diorite* within this fault were found northeast of the Drosh Gol and in the Gawuch Gol. These observations are consistent with the description of Pudsey *et al.* (1985, 1985b) reporting a 'grey diorite' underlying the 'Purit formation' and faulted against 'green phyllites' of the 'Gawuch formation'.

The grey *Mirkhani diorite* is medium to coarse-grained with its magmatic texture preserved. The magmatic paragenesis, recognised through microscope observation, is represented by plagioclase, K-feldspar, quartz, pale green hornblende and accessory spinel, apatite, zircon and sphene. Alteration products are epidote, biotite and chlorite.

A U-Pb zircon age yielded 111.52±0.40 Ma (chapter 5), which is consistent with the probable Aptian age (125-112 Ma) of the host *Drosh volcanites and limestones*.

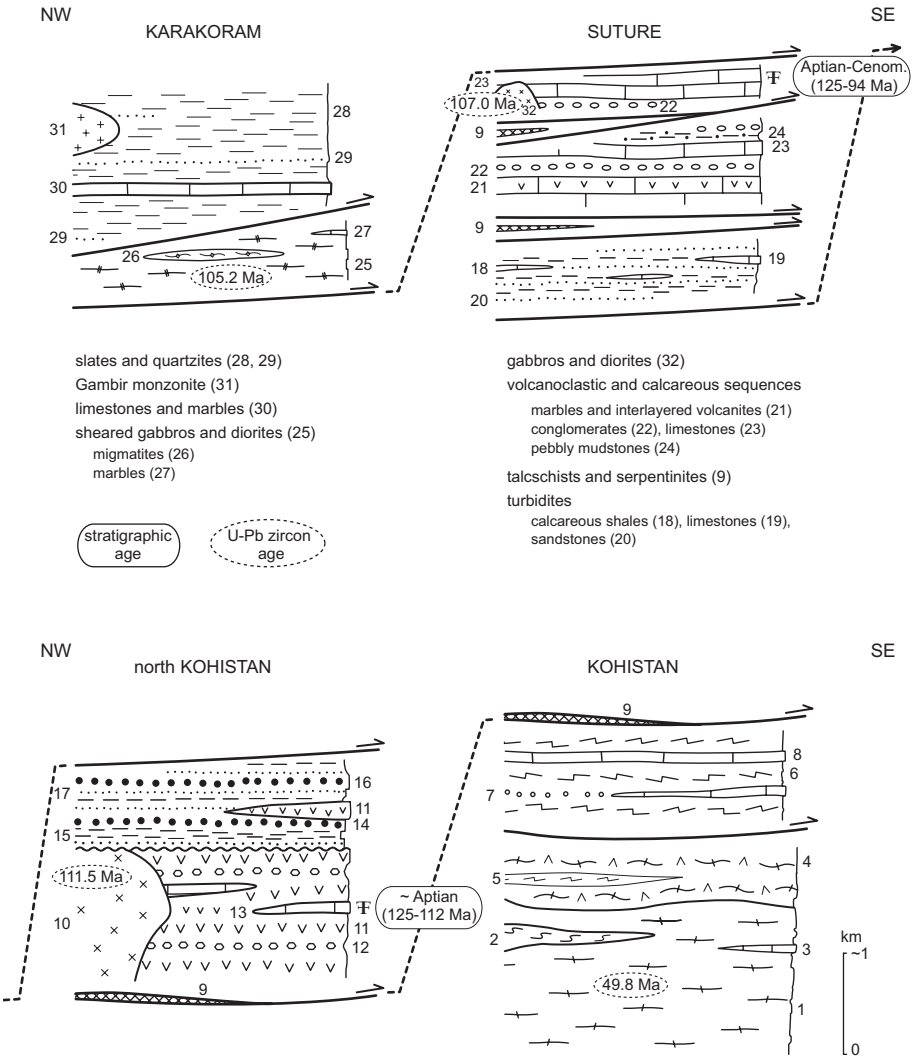

Fig. 3.10. *The Karakoram-Kohistan Suture Zone sequences with structural relationships.*

2.3.3 Meta-volcanosediments

Gawuch greenschists and marbles (Ko-GGM)
This unit, together with the *Gawuch meta-basalts,* corresponds to the 'Gawuch Formation' of Pudsey *et al.* (1985), termed after the Gawuch side valley half way along the Shishi Gol. Pudsey *et al.* (1985) described predominant 'green phyllites' with 'interbedded limestone units', 'tuffaceous meta-volcanic rocks and some andesite lavas' north of the Lowari Pass.
In this study, the 'Gawuch Formation' is redefined and divided into two tecton-ostratigraphic units: *the Gawuch greenschists and marbles* and the *Gawuch meta-basalts*.
The greenschist facies *Gawuch greenschists and marbles* are isoclinally folded and tectonically placed onto the amphibolite facies *Gawuch meta-basalts* (Fig. 3.11a, cross-sections AA'-CC', enclosed map). A fault, along which serpentinites and tectonic slices of *Mirkhani diorite* occur, separates the greenschists from the *Drosh volcanites* and *Purit red clastics* to the north. The *Gawuch greenschists and marbles* are mainly buried under Quaternary in the uppermost Shishi Gol and further northeast between the Laspur An and Sor Laspur. Black shales with quartz arenites and dark green to black volcano-clastic greenstones make up the northern half of the *Gawuch greenschists and marbles* south of Mirkhani.
Major rock types are volcanoclastic greenschists interlayered with metre to hundred metre thick, grey to white laminated, mylonitic marbles and minor greenschist facies microconglomerates, volcanoclastic sandstones, violet shales, basic lavas, tuffs and pyroclastic breccias (Fig. 3.11b). Graded bedding is locally preserved. Microconglomerates are composed of stretched, 5-10 cm large, mainly volcanoclastic pebbles in a greywacke matrix. Limestone pebbles occur rarely.
The metamorphic paragenesis of the often crenulated greenschists, deduced from microscope observation, is comprised of albite, chlorite and minor actinolite and epidote. Quartz and unspecified ores are frequent. Quartz in the quartz arenites is often broken and displays undulose extinction. Other magmatic clasts are felspar and accessory zircon and ores. The metamorphic paragenesis is represented by biotite, minor white mica and probably albite.
This unit is interpreted as a detrital, marine sequence deposited in a shelf environment with nearby volcanic activity.

Gawuch meta-basalts (Ko-GBa)
The *Gawuch meta-basalts* display an upper greenschist to amphibolite facies metamorphic grade, and are recognised by markedly steeper and higher relief in the landscape. A reverse fault between these amphibolitic *meta-basalts* and the *greenschists and marbles* was observed between the Gurin and Tangal Gol (Fig. 3.11a). Elsewhere this contact is buried under Quaternary deposits.

Meta-gabbros and -diorites intruded the meta-basalts and may be responsible for the metamorphic grade.

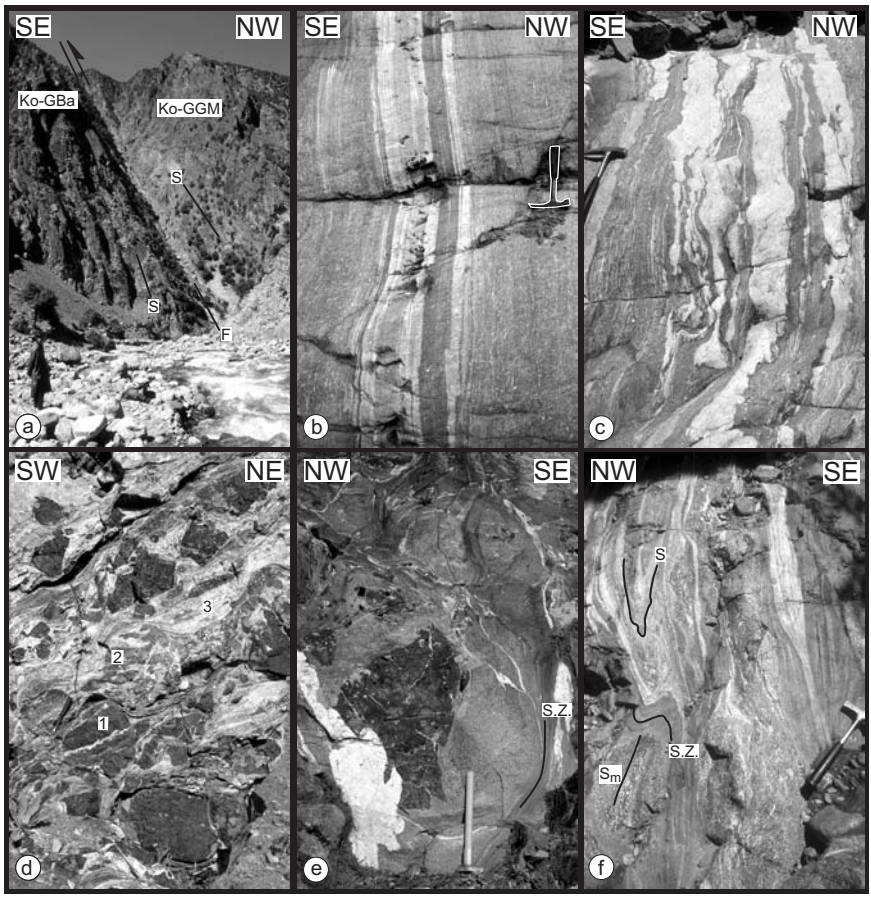

Fig. 3.11. *Kohistan arc units.* ***a)*** *reverse top-to-SE fault (F) placing the Gawuch greenschists and marbles (Ko-GGM; S: foliation) onto the Gawuch meta-basalts (Ko-GBa); note the erosion contrast of the massive amphibolitic meta-basalts with the weaker, lower-grade volcanoclastic greenschists; Tingal Gol, 2.5 km ENE of Gawuch.* ***b)*** *river polished surface of strongly foliated Gawuch greenschists (grey and dark grey) and marbles (white); Ko-GGM, entrance of Gashish Gol, 3 km NE of Gawuch.* ***c)*** *foliated garnet-sillimanite-bearing paragneisses; note the foliation-parallel leucosomes indicating partial melting; Ko-P, Tingal Gol, 5.5 km E of Gawuch.* ***d)*** *magmatic breccia containing (1) coarse-grained angular hornblendites, (2) rounded boulders of weakly deformed gabbros and diorites (grey) and (3) a leucocrate host rock; this is interpreted as derived from 3 different magma types: the intrusion of leucocrate host rock brecciated the hornblendite and the mafite whereas the gabbros and diorites behaved ductile and were only pinched and swelled; Ko-Ga, Turipilu Gol, 3 km SE of Madaglasht.* ***e)*** *ultramylonitic shear zone (S.Z.) wrapping around a lens of undeformed medium-grained gabbro; a black hornblendite enclave and a leucogranitic dyke (white); Ko-Ga, Turipilu Gol, 4.5 km ESE of Madaglasht.* ***f)*** *typical structures and textures of the sheared meta-gabbros and -diorites: isoclinal folds folding the foliation (S), boudins of undeformed, medium to coarse-grained gabbro locally displaying the original magmatic layering (S_m), and ultra-mylonitic bands (S.Z.) indicating localised shear deformation; Ko-Ga, Tingal Gol, 4 km E of Gawuch.*

Dominant rocks are meta-volcanites with a few intercalated meta-tuffs (Fig. 3.13a) and volcanoclastic meta-sediments. The meta-volcanites are dark green and usually fine-grained with a very homogeneous texture. Some layers contain up to 1 cm size hornblende porphyroclasts. Where less deformed, agglomeratic texture and/or graded bedding and cross-bedding are preserved. The very fine-grained meta-tuffs contain much epidote giving the rocks a typical pale-olive green colour. Volcanoclastic interlayers are mainly fine-grained quartz-rich sandstones with a locally calcareous matrix.
Green to pale blue, zoned magnesiohornblende, biotite, albite, plagioclase, epidote and minor actinolite, zoisite, muscovite, chlorite and red garnet represent the metamorphic mineral assemblage (Fig. 3.12a). Magmatic minerals are quartz, sphene, magnetite and accessory apatite and zircon. Quartz is mainly absent or is accessory, although it locally forms up to 15% of the rock. The predominating feldspar is plagioclase, with albite occasionally prevailing in some rocks.

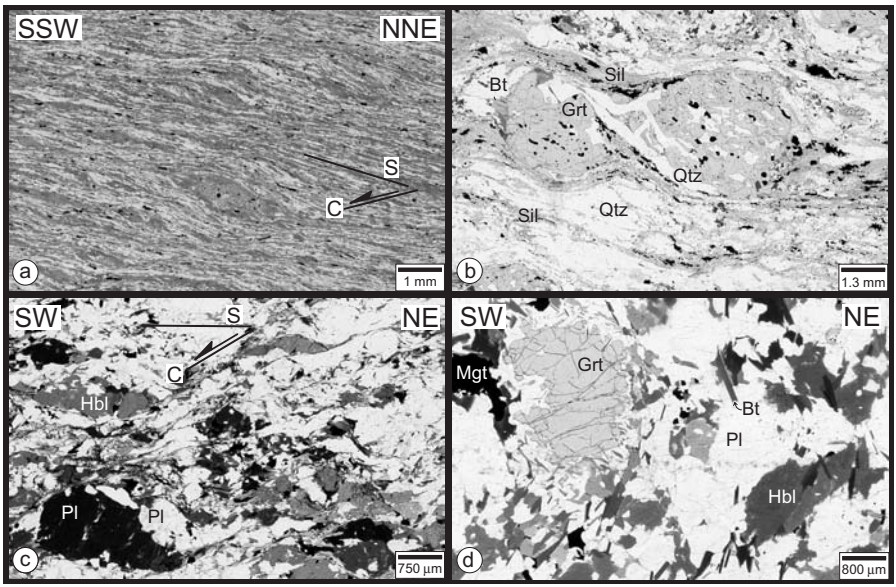

Fig. 3.12. *Thin sections of Kohistan arc units (sections are all perpendicular to the foliation and parallel to the lineation; mineral symbols after Kretz 1983); all sections non-polarised light.* ***a)*** *Gawuch amphibolite; stretched and aligned green-blue magnesiohornblende and minor biotite together with recrystallised plagioclase define the strong foliation (S); other minerals are quartz and epidote; large hornblendes are zoned (paler in the core, see middle of image); shear bands (C) indicate sinistral (SW-ward) shear (arrow); Ko-GBa, Andowir Ghari, 7 km NE of Madaglasht.* ***b)*** *garnet-sillimanite schist; poikilitic garnet overgrew aligned ores and quartz inclusions; sillimanite (fibrolite) is intergrown with biotite; Ko-P, Tingal Gol, 5.5 km E of Gawuch.* ***c)*** *meta-gabbroic amphibolite; plagioclase is locally recrystallised along thin bands defining (together with locally elongated hornblendes) the foliation (S); a weak S-C-type fabric indicates sinistral shear (arrow); Ko-GD, Purit Gol, 7 km E of Drosh.* ***d)*** *undeformed (almost eutectic) meta-gabbro; plagioclase and tschermakitic hornblendes are the dominant minerals; others are garnet, magmatic biotite, interstitial illmenite, minor quartz and chlorite; Ko-GD, Tingal Gol, 4 km E of Gawuch.*

The meta-volcanites represent mostly upper greenschist to amphibolite facies mafic volcanites. The very homogeneous texture and the small grain size suggest basaltic lava flows as protoliths. However, quartz-rich meta-volcanites and volcano-detritics, may have a more acid volcanic protolith.

Paragneisses and migmatites (Ko-P)
Meta-pelites and -volcanites occur as elongated, up to 2 km thick and 20 km long units intruded by the *meta-gabbros and -diorites*. Rock types are quartzo-feldspathic gneisses, garnet-sillimanite schists, migmatites and meta-volcano-clastic amphibolites (Figs. 3.11c, 3.13b). Paragneisses cropping out north of Laspur are generally more mafic than in the Shishi Gol and more difficult to distinguish from the amphibolitic *meta-gabbros and -diorites*. They are upper amphibolite facies, locally migmatitic, basic meta-volcanoclastic rocks where the original depositional layering is preserved in places. Pudsey *et al.* (1986) described 'arc volcanics' that were metamorphosed to 'garnet-amphibole gneisses' north of Sor Laspur, but these authors did not individualise the amphibolitic meta-gabbros, which are the predominating rock type.
A 1 km thick unit of garnet-bearing quartzo-feldspathic gneisses crops out north of the Ziarat check point on the Drosh-Lowari road. Microscope analysis showed that the metamorphic minerals in the medium-grained leucocratic layers are plagioclase, K-feldspar, biotite and minor garnet, chlorite and muscovite. Quartz belongs to the magmatic phase. Garnet and biotite are the dominant metamorphic minerals in the mesocratic layers.
Garnet-sillimanite schists and migmatites crop out next to quartzo-feldspathic gneisses in the Tingal Gol. The metamorphic paragenesis, inferred from microscope analysis, is garnet, biotite, sillimanite and K-feldspar. Garnet is eu- to subhedral and up to 2 cm large with K-feldspar inclusions (Fig. 3.12b). Quartz and unspecified ores represent magmatic minerals. Quartz and feldspar are recrystallised and partly aligned in ribbons. Pressure-temperature conditions were estimated by electron microprobe analyses done by E. Reusser on a Cameca SX-50 at ETH Zürich. Using the thermometry 'garnet-biotite' and the barometry 'GASP=garnet-aluminosilicate-plagioclase-quartz' a temperature of 680°C and a pressure of 9 kbar were obtained. The value of the pressure is not so sure because there are only very few grains of plagioclase and those grains are albitic. However, these garnet-sillimanite schists represent high-temperature conditions.

2.3.4 Gabbroic to granitic plutonites and ultramafic lenses

Meta-gabbros and -diorites (Ko-Ga)
The *meta-gabbros and diorites* could be reached in lower parts of the numerous side valleys from the Shishi Gol. The map further southeast was completed using the Landsat image because of the extremely difficult acces-

sibility of this glaciated area at altitudes between 4,000 and 6,500 m. Pudsey *et al.* (1985, 1986) included this unit into the 'Kohistan Batholith'.
Predominant rock types are quartz diorites, hornblende diorites, hornblende-quartz gabbros, garnet gabbros and hornblendites (Fig. 3.11d). Granitic dykes and lenses of ultramafite are described separately. Hornblendites and rare meta-carbonates (Fig. 3.13c) mainly occur in up to 10 m thick boudins. Undeformed quartz-biotite pegmatites crosscutting meta-gabbros were only found in the Sor Laspur area.

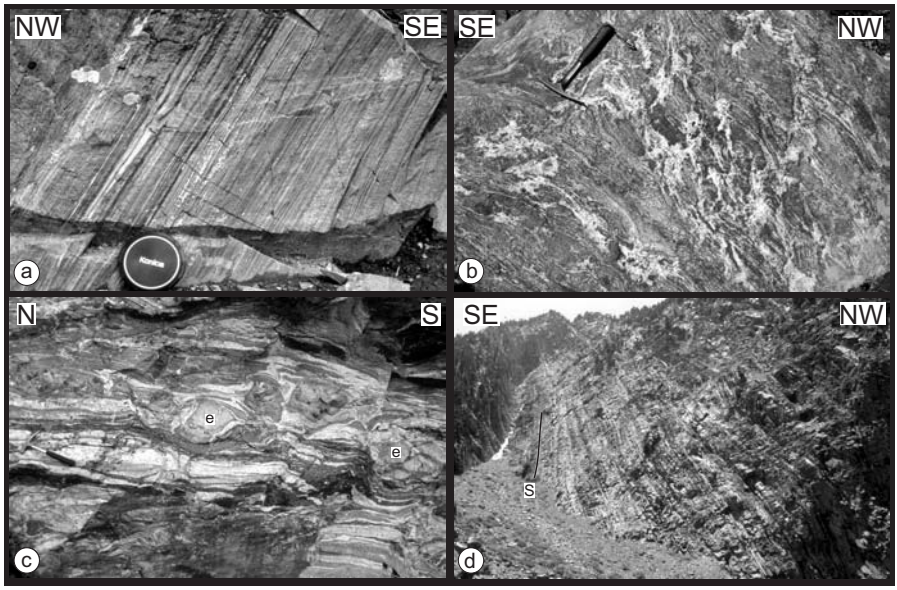

Fig. 3.13. *Kohistan arc units.* ***a)*** *finely laminated and foliated upper greenschist facies meta-tuffs of the Gawuch meta-basalts; Ko-GBa, Andowir Ghari, 7.5 km NE of Madaglasht.* ***b)*** *migmatitic quartzo-feldspathic gneisses; note the leucosome pods (white); Gurin Gol, 4.5 km SSE of Gawuch.* ***c)*** *sheared meta-diorite with enclaves (e) of garnet and quartz-rich meta-sediments; Ko-Ga, 2.5 km NNW of Sor Laspur.* ***d)*** *strongly foliated (S) meta-gabbros dipping NW just south of the contact with the Gawuch meta-basalts; Ko-Ga, Tangal Gol, 7.5 km E of Gawuch.*

Amphibolite facies metamorphism and ductile deformation overprinted many of the original intrusive relationships and mineral assemblages. The predominant texture in this unit is a gneissic banding with generally 1-20 cm thick bands. Within the northernmost 100 metres, this metamorphic banding is planar, parallel to the suture fault zone and grain size is rather small (Fig. 3.13d). There, meta-gabbros can hardly be distinguished from amphibolitic *Gawuch meta-basalts*. Deformation was localised along anastomosing, 1 to 50 cm wide mylonitic to ultramylonitic shear zones (Fig. 3.11e, cross-sections on enclosed map) and is further expressed in isoclinal folding everywhere in the unit (Fig. 3.11f). Original magmatic textures are preserved in much less

deformed layers and lenses (Fig. 3.14a). Boudinage and pinch-and-swell structures are common (Fig. 3.14b).

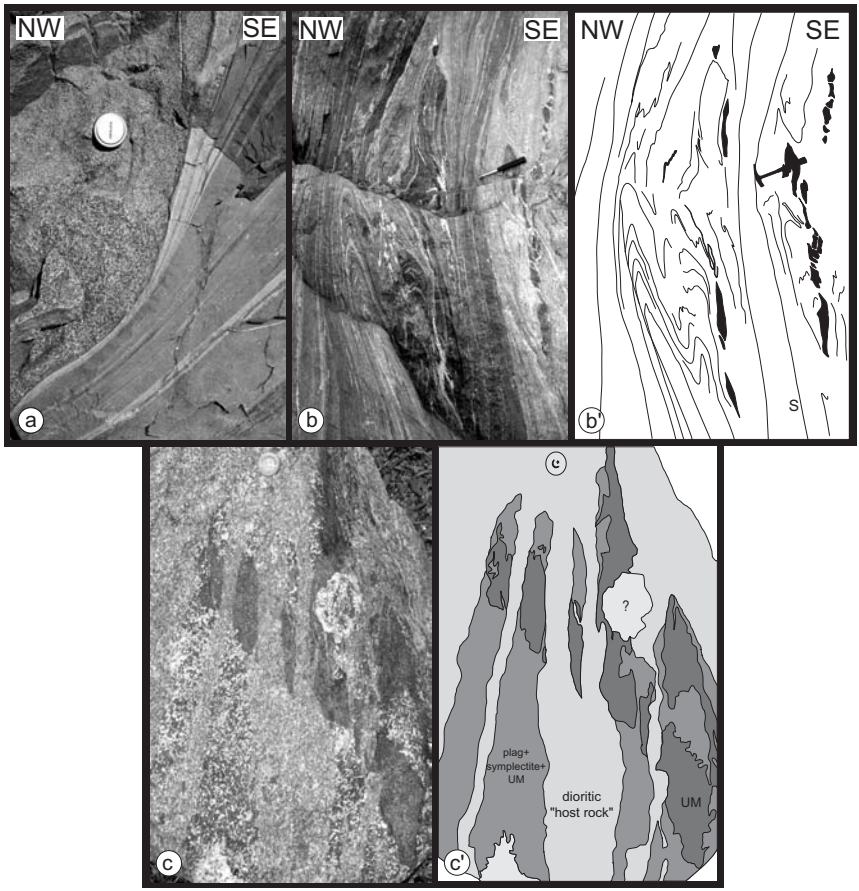

Fig. 3.14. *Kohistan arc units.* ***a)*** *mylonitic shear zone wrapping around a lens of undeformed meta-gabbro (to the left); Ko-Ga, Andowir Ghari, 9 km NE of Madaglasht.* ***b+b')*** *photo+sketch) isoclinally folded foliation (S) in meta-gabbros and -diorites (white to dark grey) with boudins of hornblendite (black); Ko-Ga, 3 km N of Sor Laspur.* ***c+c')*** *photo+sketch) ultramafite-bearing diorite boulder: the dark grey flame-like enclaves (UM) represent the 'original' ultramafite assimilated by an intruding (dioritic) plagioclase-rich melt; melt reacted with the ultramafic rock in the elongation direction resulting in clinopyroxene-amphibole-spinel symplectites around olivine grains, Purit Gol, 7 km E of Drosh.*

The metamorphic mineral paragenesis is plagioclase, biotite and minor garnet, actinolite, chlorite and epidote. Magmatic minerals are tschermakitic hornblende, biotite, plagioclase, illmenite, sphene and very rare pyroxene (<1%); spinel, apatite and zircon are accessory. Plagioclase and quartz are recrystallised and aligned in ribbons (Fig. 3.12c). Less deformed meta-gabbros preserved the magmatic texture in which plagioclase often defines a

cumulus texture with interstitial illmenite, xenomorphic to subhedral hornblende and hypidiomorphic garnet (Fig. 3.12d). Hornblende is locally replaced by biotite and sphene. Pyroxene is rare and occurs only as relicts in hornblende.
A foliated meta-gabbro, sampled south of Mirkhani along the road to the Lowari Pass, yielded a U-Pb intrusion age of 49.80±0.15 Ma (chapter 5). The Ar-Ar method on hornblende yielded a consistent age of 50.2±1.4 Ma (chapter 5). Discordant zircon microfractions possibly indicate a postcrystallisation metamorphic event around 44 Ma.

Ultramafites (Ko-Um)
A 50 m thick ultramafic lens, concordant with the sheared *meta-gabbros*, occurs in the Turipilu and Poshkari Gol. No outcrop was reached due to the steep topography of both valleys, but we approached to a few metres away so that their localisation on the map is precise. Three different rock types, sampled in fallen rocks, are distinguished based on microscope analysis:
(1) *troctolites* represent a coarse-grained cumulate with an olivine cumulus and plagioclase intercumulus. A reaction-rim around olivine grains contains symplectites of pyroxene, or amphibole and spinel. Green spinel (hercynite), clinopyroxene and brown amphibole are other magmatic minerals.
(2) *meta-harzburgites* display an equigranular cumulate texture. Magmatic minerals are represented by orthopyroxene, olivine and chromite. The metamorphic paragenesis is represented by Mg-chlorite and probably orthopyroxene. Orthopyroxene grew magmatically over olivine and shows kink bands and undulose extinction. Small (metamorphic?) orthopyroxene grano-blasts grew around primary orthopyroxene crystals.
(3) *amphibole-quartz pyroxenites* occur as very coarse-grained veins cross-cutting the meta-harzburgites. They comprise mainly clinopyroxene, orthopyroxene and amphibole with minor phlogopite forming a cumulate texture. A significant amount of undeformed quartz, containing fluid inclusions, was observed.
A meta-diorite boulder containing ultramafic ‘enclaves’ was found in the Gurin Gol (Fig. 3.14c). The ultramafites were assimilated by the intruding dioritic plagioclase-rich melt. We do not have enough information to make any statement on the origin of these rocks. They may represent mantle rocks or could be cumulates of crustal origin.

Diorite (Ko-Di)
A diorite body, approximately 6 km across, was mapped from the satellite image between the Aski and Turipilu Gol. Its yellowish-greenish colour on the PCA-modified Landsat image distinguishes it from the surrounding meta-gabbros and -diorites occurring in blue-violet colours. This body appears oblique to the regional foliation.

Granitic dykes (Ko-Dy)

Meta-gabbros and -diorites and *paragneisses and migmatites* are intruded by *granitic dykes* and sills (Fig. 3.15a) some of which have been deformed (Fig. 3.15c).

A series of fine-grained dykes crosscuts meta-gabbroic amphibolites 200 m south of the contact to the *Gawuch meta-basalts* in the Beorai Gol. These dykes display a weak foliation parallel to that of the meta-gabbros. The magmatic minerals, deduced from microscope analysis, are quartz, K-feldspar, plagioclase and biotite. Accessory minerals are epidote, zircon, apatite, sphene and illmenite. Metamorphic minerals are garnet, muscovite and chlorite. The weak foliation is defined by subhedral biotite and ribbons of recrystallised feldspar and quartz. Zircons of one dyke yielded an intrusion age of 47.4±0.5 Ma (U-Pb on zircon, chapter 5).

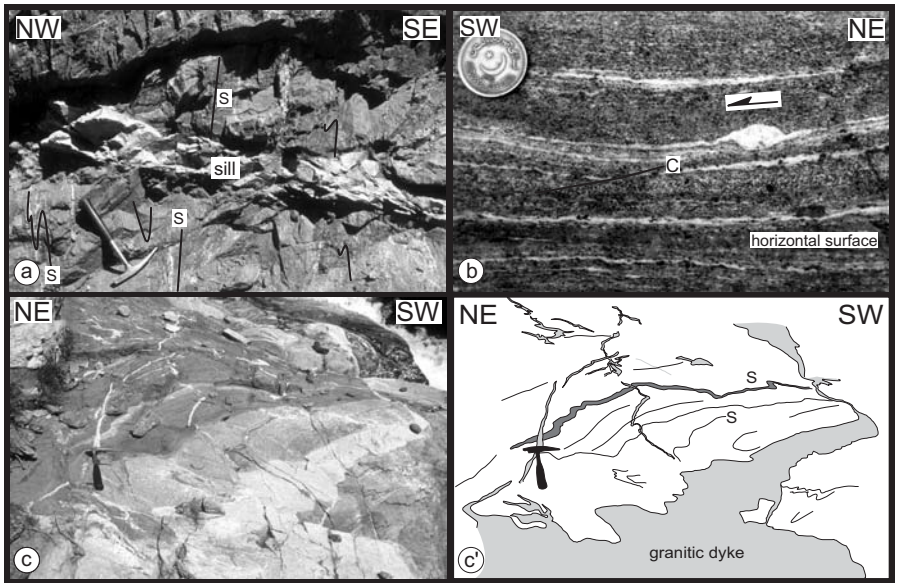

Fig. 3.15. *Kohistan arc units:* ***a)*** *0.3 m thick fine grained, almost undeformed granitic sill (white) intruding isoclinally folded meta-gabbros; Ko-Dy & Ko-Ga, Beorai Gol, 8.5 km S of Drosh.* ***b)*** *mylonitic gabbros with white plagioclase and quartz-rich banding along one of which a sigma-clast indicates, together with weakly developed shear bands, sinistral (SW-ward) shear (arrow); Ko-Ga, Beorai Gol, 9.5 km S of Drosh.* ***c+c')*** *photo+sketch) garnet-bearing paragneisses intruded by a granitic dyke; note the less deformed leucocratic veins (dykes?) oblique to the main foliation (S); Ko-P & Ko-Dy, upper Gawuch Gol, 4.5 km SE of Gawuch.*

An undeformed, 1 m thick granitic dyke intruded the meta-gabbros about 1.8 km south of the contact with the *Gawuch meta-basalts* in the Beorai Gol. It displays sharp, undeformed boundaries and contains angular xenoliths of the host rocks. Magmatic minerals are quartz, K-feldspar (microcline), plagioclase, minor biotite and sphene (microscope identification). Accessory

minerals are abundant zircon, apatite and illmenite. Muscovite appears as an alteration product from feldspar. The texture is primarily magmatic with interstitial illmenite, locally euhedral K-feldspar and mirmekite. U-Pb dating on zircons of this dyke yielded an intrusion age of 38.73±0.20 Ma (chapter 5).

Tonalite (Ko-T)
A foliated, medium-grained tonalitic body crops out south of the *meta-gabbros and -diorites* on the Lowari Pass. This body appears in the section of Bard *et al.* (1980, Fig. 2-1) as 'late-kinematic heterogeneous quartz diorite'. It was mapped mainly from the PCA-modified Landsat image on which it could be distinguished from the *meta-gabbros and -diorites* by its pale blue-violet colours.
Microscope determination showed that the tonalite is comprised of magmatic plagioclase, quartz, green hornblende with minor sphene and biotite. Accessory minerals are apatite, zircon and unspecified ores. Chlorite occurs as an alteration of hornblende.

3. Structures

3.1 Introduction

Deformation features of the Karakoram-Kohistan Suture Zone, between Chitral and Hunza, were first described by Pudsey *et al.* (1985) and Pudsey (1986). This study is focused on the western segment of the suture zone in the Chitral district. A general structural interpretation is illustrated by four cross-sections and a structural sketch map (enclosed map and Fig. 3.10). It can be readily seen that most contacts are faults (Fig. 3.20a). Both fault and lithological contacts generally dip steeply towards the northwest but a general normal position of all units (younging direction) is preserved. The suture fault zone is defined by the imbrication of meta-ultramafites, turbidites, gabbros and diorites, Karakoram and Kohistan shelf-type sediments and volcanites. Most of the faults display a sinistral and/or a reverse sense. Although faults were generally easy to identify, determination of the relative movement was hampered by inaccessability, due to a very steep topography and/or Quaternary deposits obscuring the fault contacts.

The suture fault zone is followed by major valleys and passes (Landsat ETM+ image on the enclosed map). It strikes along the Pathasun Gol from the Afghan border through Ursun, then joins the Kunar Valley in the Drosh area, follows northeastward the Shishi Gol and crosses the three passes - Lohigal An, the Shachiokuh Pass and the Laspur An. The suture fault zone is buried under moraines and alluvium between the Laspur An and the upper Rizhun Gol.

The suture-related NE-SW trending faults mainly show a sinistral sense of shear. South-vergent, steep reverse faults occur outside the imbricate zone in both Karakoram and Kohistan units (cross-section DD', enclosed map). The NE-SW trending Kohistan units are offset by subvertical N-S trending sinistral faults which do not seem to propagate across the suture into Karakoram units. A sinistral offset of the suture is inferred in the Laspur-Mastuj area from apparently offset lithologies on both sides of the Mastuj river (enclosed map).

WSW-ENE dextral faults offset Karakoram units and the Reshun fault by 0.3-1 km north of Chitral. The NE-SW trending sinistral faults and the WSW-ENE dextral faults are conjugate, suggesting a bulk NW-SE-directed compression.

The main, regional foliation plane (S) results from the superposition of several deformation phases. However, the succession of these planes could not be ascertained because of the lack of continuity and crosscutting fabrics, except in the *slates-siltstones-quartzites sequences*. The orientation of the steep foliation plane is, on the one hand, a result of the suture-parallel sinistral strike-slip faulting. On the other hand, it may have been rotated (steepened) from a

originally flat orientation, as indicated by the acute angle between bedding and foliation in e.g. suture zone *calcareous turbidites*.
Structural data are presented separately for the three main tectonic domains, namely the Karakoram, the Suture and the Kohistan (cross-sections). In the following paragraphs, penetrative foliations, folds and lineations are discussed. A separate section deals with brittle faulting at the end of this chapter.

3.2 Karakoram

The Karakoram units trend N-S to NNE-SSW and turn towards the east to NE-SW. The regionally dominant foliation generally dips moderately to steeply towards NW (Fig. 3.16a). The scattering of the foliation data can be explained by the lens-shaped units (e.g. *sheared gabbros and diorites*). Fold axes are parallel to the regional trend and therefore parallel to the suture zone, suggesting a transpressional tectonic regime (Fig. 3.16b).

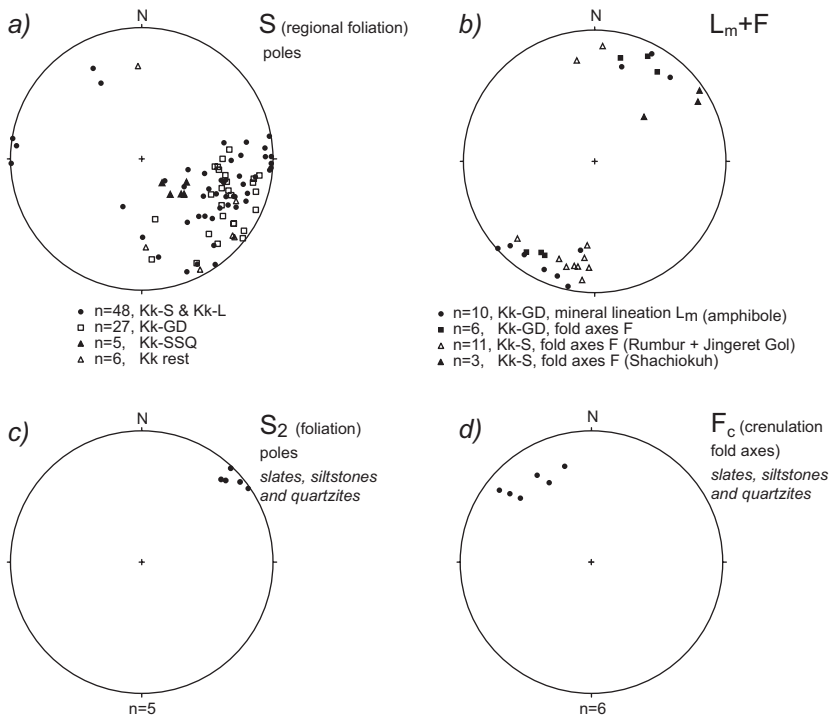

Fig. 3.16. *Orientation data of structures in the Karakoram units (all equal area projection, lower hemisphere; n=number of measurements).*

Structural data of the Rumbur and Bumburet Gol, 20 km NW of Drosh, were provided by C. Pudsey (pers. comm.).

Slates and quartzites (Kk-S)
The dominant foliation strikes N-S in the Rumbur Gol, but turns to NE-SW approaching the suture to the south, where the slates and greenschists are strongly mylonitised. This suggests increasing strain towards the suture. Isoclinal folds, folding the bedding, produced an axial plane cleavage subparallel to bedding in the limbs. The axes plunge towards N and S in the Rumbur and Bumburet Gol (Fig. 3.16b), where Pudsey *et al.* (1985) mapped a large isoclinal antiform with a N-S trending axial plane. Large folds trend parallel to the suture and plunge shallowly towards SW in the Shachiokuh (Fig. 3.16b). Sigmoidal marble clasts within the slates indicate sinistral shear (Fig. 3.17a).

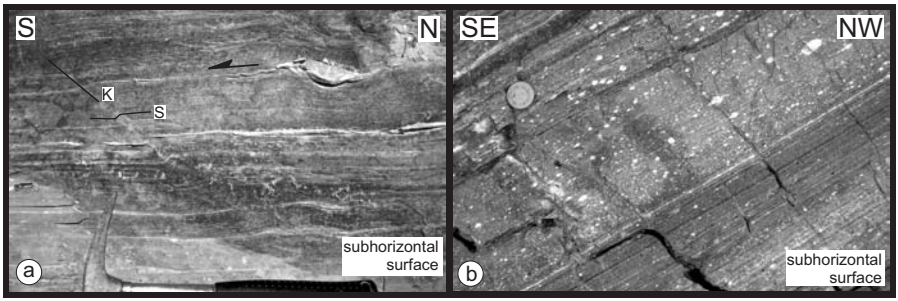

Fig. 3.17. *Karakoram units. Photos are parallel the lineation.* ***a)*** *black slates interlayered with recrystallised carbonates (white); the marble sigma-clast indicates sinistral shear (arrow); the kink-band (K) has folded the foliation (S) and is consistent with sinistral shear; Kk-S, Jingeret Gol, 6.5 km W of Drosh.* ***b)*** *ultramylonitic meta-gabbro with plagioclase porphyroclasts; Kk-GD, Jingeret Gol, 6 km SW of Drosh.*

A minimum age for the deformation of this unit, as well as for the associated *volcanoclastic and calcareous sequences*, is given by the 103.8 Ma (U-Pb on zircon, chapter 5) *Phargam granite*. This undeformed body crosscuts the foliation and folds of these two Karakoram sedimentary units 3 km north of the suture.

Slates-siltstones-quartzites sequences (Kk-SSQ)
Disharmonic folding was observed in this unit investigated to the north of Madaglasht (Fig. 3.1d). The axial plane foliation dips 40° towards NW (Fig. 3.16a). It is parallel to bedding in limbs, which suggests, that the foliation may have been subhorizontal during its formation and turned later to its present attitude. Today's shallow dips are probably due to recent soil sliding in the northern slopes of the upper Shishi Gol.
The main foliation is crenulated by fold axes plunging 25° NW (Fig. 3.16d). The associated subvertical axial plane cleavage (S_2), strikes NW-SE, perpendicular to the regional NE-SW striking regional foliation (Fig. 3.16c). These

folds indicate a (local?) NE-SW-directed shortening possibly related with NE-SW sinistral strike-slip faulting along the suture.

Sheared gabbros and diorites (Kk-GD)
The metamorphic foliation strikes NE-SW and dips steeply towards NW (Fig. 3.16a). The unit is lens-shaped and thins out SW of Drosh resulting in mylonitic to ultramylonitic textures, compared to gneissic textures further N and NE (Fig. 3.17b). Mineral lineations are defined by aligned hornblendes on the foliation plane and plunge 5 to 20° towards NE or SW (Fig. 3.16b). The part of this unit adjacent to the suture zone is isoclinally folded with fold axes plunging shallowly, towards NE and SW, parallel to the mineral lineation (Fig. 3.16b). This suggests an increasing strain towards to the suture zone. Shear bands, mica fish and book-shelf structures indicate a sinistral sense of shear on a microscopic scale (Fig. 3.4a).
The intrusion age of an 105.2 Ma (U-Pb on zircon, chapter 5) meta-diorite represents a maximum age for the ductile deformation adjacent to the suture.

Discussion
The southeastward increasing strain towards the suture in the southernmost Karakoram units (e.g. *sheared gabbros and diorites*, *slates and quartzites*) indicates a suture-related deformation younger than 105 Ma. However, older, pre-suturing deformation is preserved in Karakoram sediments a few kilometres away from the suture. These ‘old’ structures represent subduction-related deformation at the southern Karakoram active margin.

3.3 Karakoram-Kohistan Suture

The dominant, steeply NW dipping regional foliation is present in all lithologies (Fig. 3.18a). Moderately dipping to almost subhorizontal foliations occur rarely and are explained by soil sliding and tilting of preferentially schistose units (e.g. talcschists, calcschists, schistose sandstones).

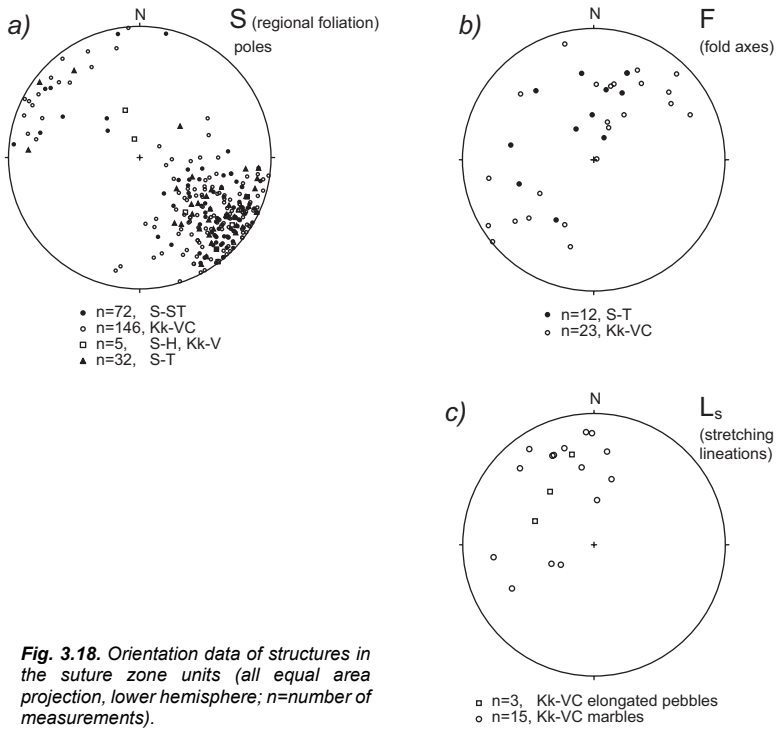

Fig. 3.18. *Orientation data of structures in the suture zone units (all equal area projection, lower hemisphere; n=number of measurements).*

Volcanoclastic and calcareous sequences (Kk-VC) and *calcareous turbidites (S-T)*

The structures of the Karakoram *volcanoclastic and calcareous sequences* were investigated mainly in the suture, where parts of this unit occur as tectonic wedges. Therefore, the structures of this unit are described in this chapter.

The foliation in the marbles is generally parallel to the bedding and dips 30-40° NW. This suggests an originally subhorizontal foliation that was steepened after its formation. Graded bedding in laminated limestones and turbidites indicate younging to the NW, with bedding planes dipping 50-70°NW. The slaty cleavage in pelitic layers dips steeper than bedding towards NW which is consistent with a normal (younging upward) sequence. Stretching lineations

plunge 10 to 65° towards SW, W and NW to N displaying a considerable scatter (Fig. 3.18c). This scatter may be explained by the lens-shape of these imbricate units. Bookshelf structures, parallel to the lineation, indicate sinistral ductile shear (Fig. 3.19b). Isoclinal folds, folding the foliation, plunge steeply to subhorizontally towards SW or N to NE (Figs. 3.18b, 3.19c). This orientation distribution of fold axes, lying approximately on a great circle parallel to the foliation, is consistent with sinistral shear-related folding.

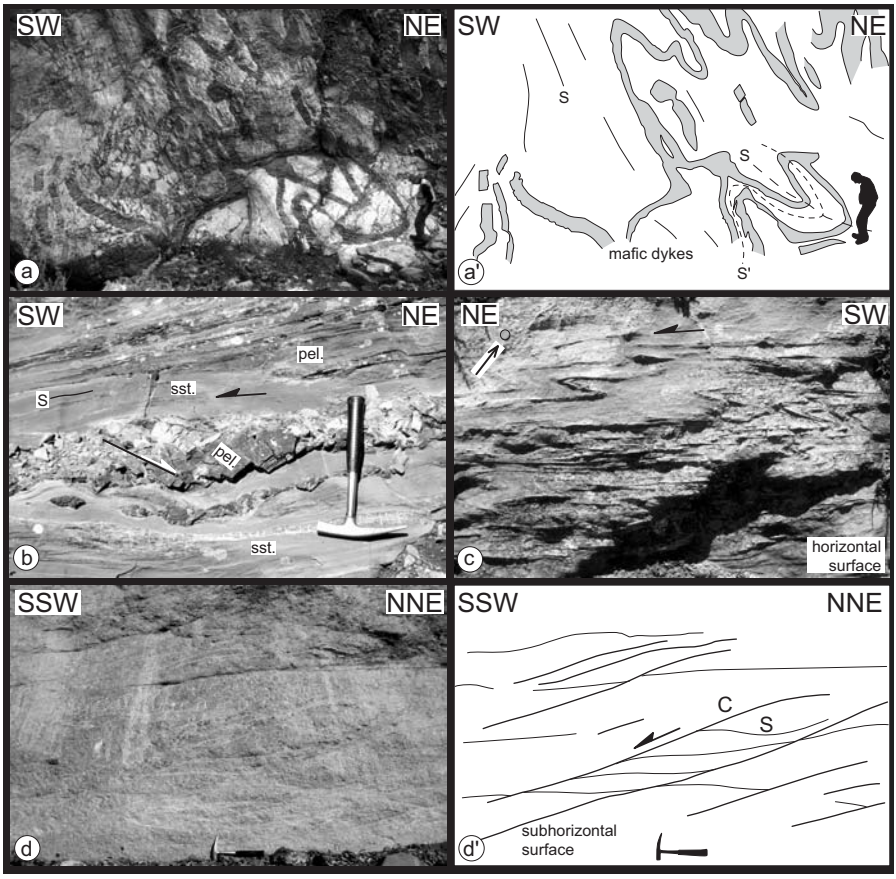

Fig. 3.19. *Imbricate suture zone units.* ***a+a')*** *photo+sketch) isoclinally folded and boudinaged mafic dykes that intruded into limestones; S': axial plane cleavage of folds older than S; S-mD & Kk-VC, Angarbah Gol, 0.3 km W of Madaglasht.* ***b)*** *calcareous sandstones (sst.) with more competent pelitic interlayers (pel., dark grey) one of which displays a sinistral (arrow), top-to-the-SW book-shelf structure (with dextrally offset pelitic blocks (white arrow); Kk-VC, Angarbah Gol, 1 km N of Madaglasht.* ***c)*** *micritic limestones with isoclinal folds whose asymmetry suggests sinistral (half-arrow) shear-related folding; coin (arrow) for scale; Kk-VC, entrance of Shishi Gol, 3.5 km NE of Drosh.* ***d+d')*** *photo+sketch) river-polished surface of talcschist (S: foliation) displaying sinistral shear bands (C); S-ST, Dam Gol, 8 km SW of Drosh.*

A first deformation phase is thus represented by the main, bedding-parallel foliation that carries a stretching lineation indicating transpression. Isoclinal folds are systematically asymmetric and likely represent drag folding during a second phase of sinistral transpression. Later, calcite-filled tension gashes are oblique to the foliation and strike NW-SE, suggesting a NW-SE compression direction.

Talcschists and serpentinites (S-ST)

The talcschists and schistose serpentinites display generally a NE-SW trending foliation dipping moderately to steeply towards NW (Fig. 3.18a). Widespread shear bands (microscopic and macroscopic) indicate sinistral (Figs. 3.6b, 3.19d) to top-to-the-SE reverse shear, as indicated also by sigmoidal lenses and boudins of serpentinites, green volcanites and mafic dykes (Fig. 3.20b). The deformation, that produced the foliation in the talcschists and serpentinites (parallel to the regional foliation), is older than 106.6 Ma (U-Pb on zircon, chapter 5), as indicated by the undeformed (second generation) crosscutting basaltic sill in the Chhuchhu Gol. Thrusting seems to be younger than 106.6 Ma, because it offsets the regional foliation and first generation dykes (Fig. 3.20b).

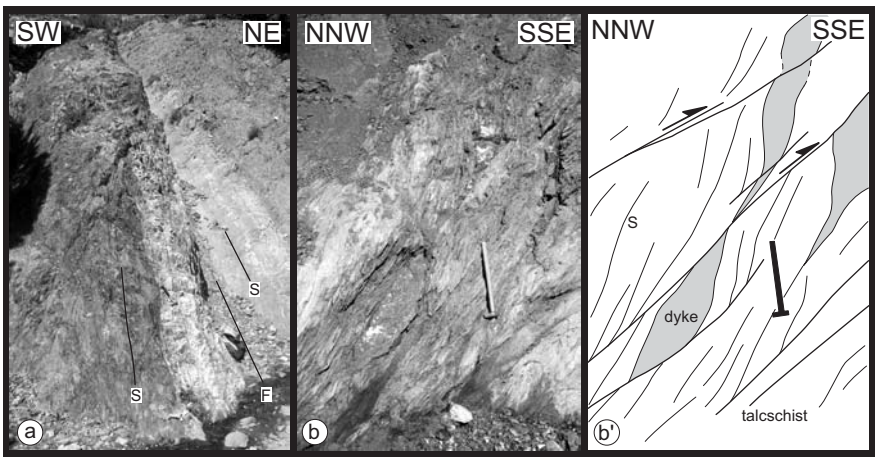

Fig. 3.20. *Imbricate suture zone units.* ***a)*** *fault contact (F) between Karakoram meta-gabbros to the left and subvertical quartz arenites to the right; note that the original intrusive contact (boundary between dark and light grey rocks) is still preserved left of the fault (F); S: foliation; Kk-GD, Kk-VC, Ustrum Gol, 3.5 km W of Gawuch.* ***b+b')*** *photo+sketch) steeply NW dipping talcschists containing sheared boudins of mafic dykes (first generation mafic dykes: older than 107 Ma) offset along top-to-SSE thrusts; S-ST, Chhuchhu Gol, 0.8 km SW of Madaglasht.*

Discussion

The suture is a 1-4 km wide zone, where units are internally coherent and bounded by brittle, anastomosing faults. There are no high-pressure rocks (blueschists) and only scarce, ultramafite blocks possibly representing olisto-

liths in a sedimentary matrix. A derivation from an accretionary wedge only is therefore unlikely. Few remnants of the marine basin (e.g. serpentinites, turbidites), between the Karakoram margin and the Kohistan island arc, are preserved in the suture. The deformation and serpentinisation of the schistose serpentinites (meta-harzburgites) occurred before 107 Ma, i.e. before the end of subduction-related magmatism along the active Karakoram margin. Thrusting is younger (<107 Ma) and may be associated with suture-related or younger deformation.

3.4 Kohistan

The main structurally investigated Kohistan units are, from north to south, the *Purit red clastics*, the *Gawuch greenschists and marbles*, the *Gawuch meta-basalts,* the *meta-gabbros and -diorites* and the *granitic dykes*. Their foliations trend NE-SW parallel to the suture (Fig. 3.21a). Mesoscopic fold axes are subhorizontally trending NE-SW, parallel to amphibole and stretching lineations in the amphibolitic units. Local drag adjacent to the N-S striking sinistral shears is essentially responsible for scattering of the foliation.

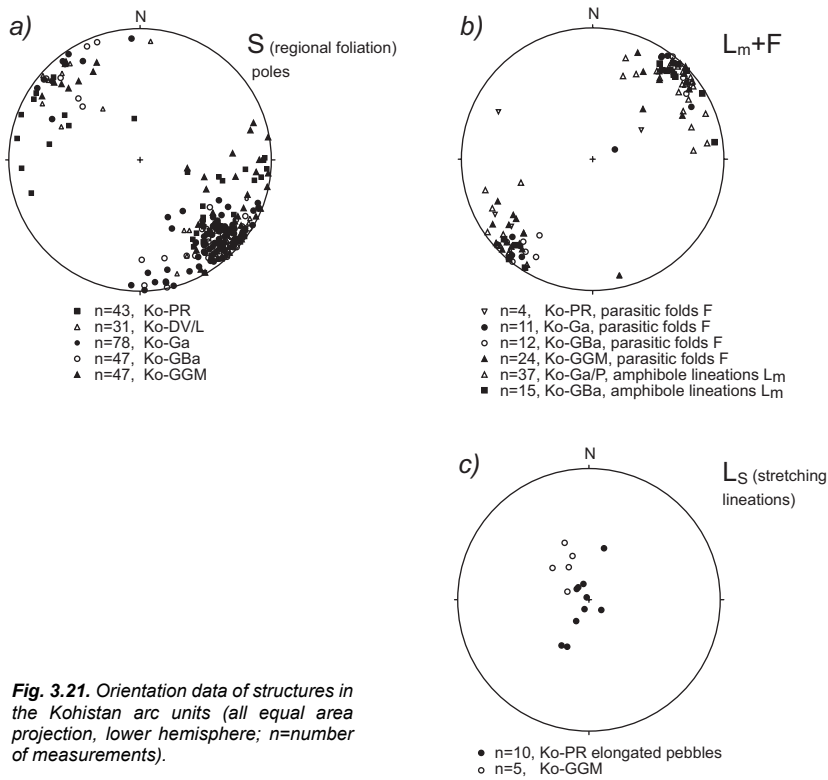

Fig. 3.21. *Orientation data of structures in the Kohistan arc units (all equal area projection, lower hemisphere; n=number of measurements).*

Purit red clastics (Ko-PR)

Red sandstones, conglomerates and shales are tightly folded with a well developed axial plane cleavage east of Naghar (Fig. 3.22a). Fold axes plunge moderately to shallow towards NE or SW (Fig. 3.21b). In the Beorai Gol and further to the northeast, the unit is fault bounded and the regional foliation is mainly parallel to the bedding dipping steeply towards NW. Elongate conglomerate pebbles define a subvertical stretching lineation in the Gurin, Purit and Tangal Gol oblique to fold axes (Figs. 3.21c, 3.22b).

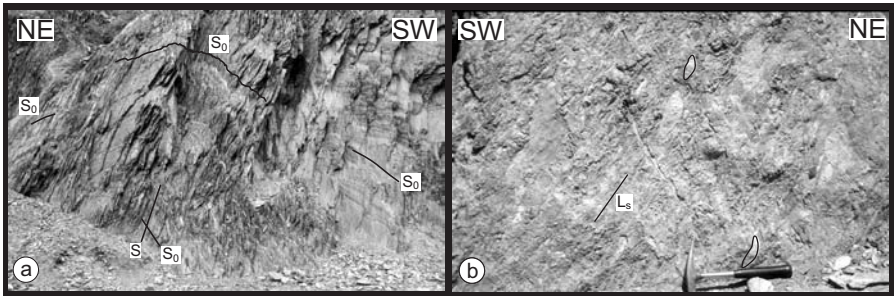

Fig. 3.22. *Kohistan arc units.* ***a)*** *open folds in Purit red shales and sandstones; graded bedding (S_0) indicates a normal sequence; note the axial plane cleavage (S); Ko-PR, 9.5 km SW of Drosh.* ***b)*** *view onto subvertical foliation surface of Purit conglomerate containing up to 0.2 m large elongated limestone pebbles (two of them are circled), among minor smaller angular to rounded quartz arenite pebbles, defining a subvertical stretching lineation; Ko-PR, Tangal Gol, 8 km NE of Gawuch.*

Gawuch greenschists and marbles (Ko-GGM)

This unit strikes NE-SW and displays a very planar foliation dipping 75-85° towards NW (Fig. 3.21a). Isoclinal, parasitic folds, folding the foliation, have subhorizontal axes trending NE-SW (Fig. 3.21b). A stretching lineation was found locally on the marble foliation planes and plunges moderately to steeply NNW, at a high angle to the fold axes (Fig. 3.21c). This stretching lineation, together with the subvertical *Purit red clastics* stretching lineation, may be linked to the transpressional deformation along the suture or may represent an older (thrusting-related?) deformation phase.

Thrusting of this unit onto the *Gawuch meta-basalts* was observed at the fault contact in the Tingal Gol where shear bands and slickenside lineations indicate a top-to-the-SE sense of relative movement (Fig. 3.11a).

Gawuch meta-basalts (Ko-GBa)

The meta-basalts display a very planar, steeply NW dipping foliation parallel to the regional foliation (Fig. 3.21a). Isoclinal folds, folding the foliation, have subhorizontal fold axes trending NE-SW (Figs. 3.21b, 3.23a). A mineral lineation on the foliation plane is represented by subhorizontally aligned hornblendes parallel to the fold axes (Fig. 3.21b). This lineation can be observed at a landscape-scale on foliation planes (Fig. 3.23b). On a microscopic scale, shear bands with aligned and deformed hornblendes indicate a sinistral shear parallel to the lineation (Fig. 3.12a).

Meta-gabbros and -diorites (Ko-Ga) and granitic dykes (Ko-Dy)

Meta-gabbros show a large range of structures from undeformed textures in boudins to ultramylonites in anastomosing shear zones (e.g. Figs. 3.11e,f, 3.14a,b). The predominant texture is the gneissic, isoclinally folded regional foliation (Fig. 3.21a). Folds, lineations and shear bands are identical to those of the *Gawuch meta-basalts*: Subhorizontal fold axes trend NE-SW (Figs.

3.21b, 3.23c), the mineral lineation, defined by aligned hornblendes, plunges shallowly NE or SW (Fig. 3.21b). The meso- and microscopic shear bands indicate sinistral shear parallel to the lineation (Figs. 3.12c, 3.15b).

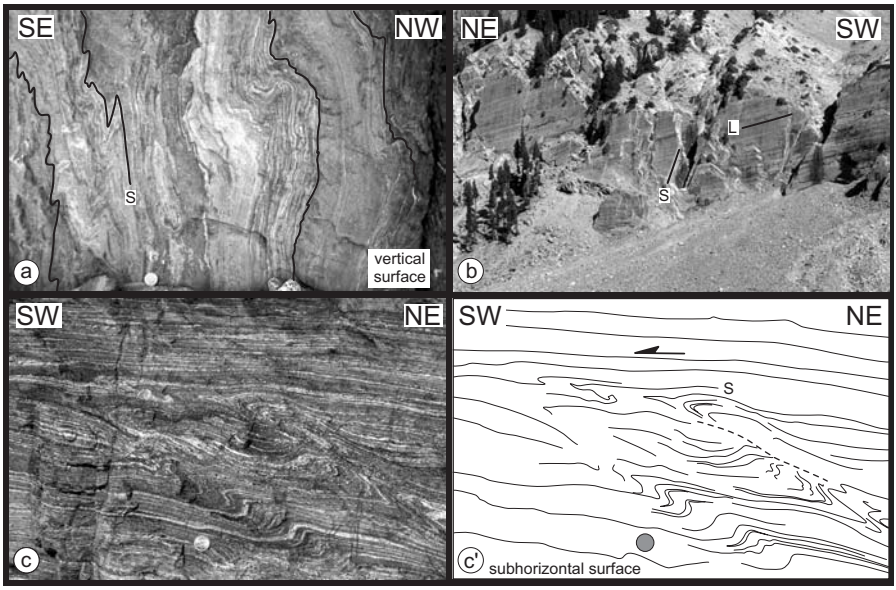

Fig. 3.23. *Kohistan arc units.* ***a)*** *tightly folded meta-volcanic greenstones containing white quartz-rich inter-layers; view of a vertical surface, perpendicular to the subhorizontal fold axes; Ko-GBa, Tangal Gol, 7.5 km NE of Gawuch.* ***b)*** *steeply NW dipping foliation (S) in meta-basalts bearing the mineral and stretching lineation (L); Ko-GBa, 3 km ENE of Madaglasht.* ***c+c')*** *photo+sketch) mylonitic meta-gabbros with drag folds folding the foliation (S) and indicating sinistral (SW-ward) shear (arrow); photo is parallel to the stretching lineation; Ko-Ga, Purit Gol, 7 km E of Drosh.*

The suture-parallel structures are again indicative of a transpressional tectonic regime along the suture zone. The 49.8 Ma (U-Pb on zircon, chapter 5) foliated meta-gabbro, together with the 47.4 Ma (U-Pb on zircon, chapter 5) foliated granitic dyke represent a maximum age of deformation in this unit. A metamorphic event is inferred at ca. 44 Ma (U-Pb on zircon, chapter 5). The undeformed granitic dyke, that intruded the *meta-gabbros and diorites* at 38.7 Ma (U-Pb on zircon, chapter 5), marks the cessation of that deformation phase.

Discussion

Ductile deformation in the *meta-gabbros and -diorites* and *Gawuch meta-basalts*, adjacent to the suture, is documented between 50 and 39 Ma. This suggests that suture-related ductile deformation occurred also after Karakoram-Kohistan collision. It possibly reached peak metamorphic conditions around 44 Ma and ended before 39 Ma. There is no age constraint for

the subvertical stretching lineation in the other Kohistan units (*Purit red clastics* and *Gawuch greenschists and marbles*) further to the northwest. This lineation may represent the thrusting component of the transpressional strike-slip faulting along the suture, or may be preserved from an older, thrusting-related N-S-directed compression.

3.5 Brittle faulting

Brittle faulting is dominated by anastomosing sinistral strike-slip faults and top-to-the-SE thrusts. A few crosscutting relationships, appearing on the map (e.g. south of Drosh), reveal that sinistral faults crosscut the reverse faults and are thus younger. Shear band fabrics in suture zone faults (e.g. within serpentinites or separating serpentinites from limestone blocks) indicate a predominant sinistral sense of movement (Fig. 3.24a). These anastomosing faults are generally steeply, mainly NW dipping, parallel to the regional foliation.

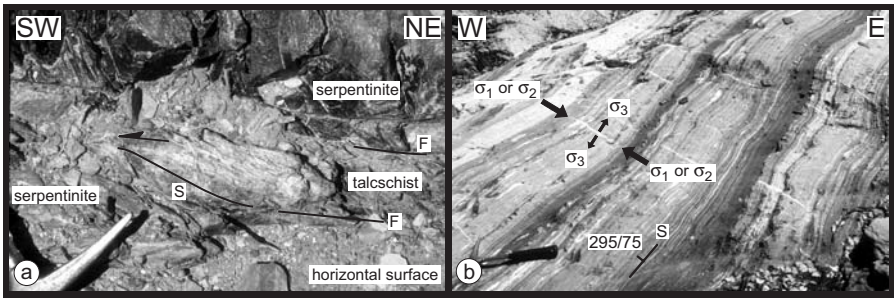

Fig. 3.24. a) *sinistral fault zone within massive serpentinite; the 0.2 m wide fault zone (F-F) is defined by white talcschists the foliation (S) showing dragging adjacent to the massive serpentinites on both sides of the fault zone; S-ST, Tar Gol, 1.6 km NW of Gawuch.* ***b)*** *laminated micritic limestones (same photo as Fig. 3.3a); the orientation of calcite-filled tension gashes (white) indicates a NNE-SSW extension direction (σ_3).*

Fission track ages on apatite and zircon from the north of the suture are 11 Ma and 20 Ma respectively, and south of the suture, they are 13 Ma (apatite) and 20 Ma (zircon, V.Gubler 2001 unpubl.). Similar zircon and apatite ages on both sides of the suture suggest that the rocks on either side passed the zircon and apatite partial annealing zones together, between 20 and 13 Ma; accordingly, no or little vertical differential movement has taken place along this fault zone since the early-mid Miocene. This does not exclude strike-slip faulting.
N-S striking vertical strike-slip faults offset Kohistan and southernmost suture units by up to 1.2 km. There is no clear field evidence for these faults to crosscut the whole suture zone. However, one such fault was interpolated from offset units on either side of the valley in the Sor Laspur-Harchin area.

Another may exist, masked by Quaternary deposits of the Kunar River in the Drosh-Kesu area. These strike-slip faults have an angle of 45 to 55° to NE-SW trending suture zone. Nonetheless they may represent R-Riedel splays out of the sinistral suture zone. The angle of R-Riedels to the main shear zone is a function of the internal friction of the material. The material contrast between ‘soft’ suture zone rocks and ‘hard’, mainly amphibolitic Kohistan rocks may therefore explain the uncommon high angle between the R-Riedel splays and the main shear zone.

Discussion

S to SE-ward thrusting occurs north of, and within the suture zone together with dominant sinistral NE-SW strike-slip faulting. The N-S striking sinistral R-Riedel shears are related to the sinistral NE-SW striking suture faults and thus seem to belong to the same deformation event as the latter. A transpressional stress regime is therefore inferred with a WNW-ESE striking compression direction, consistent with extensional calcite cracks in the suture zone (Fig. 3.24b).

Chapter 4: Paleostress regimes from brittle faults of the Karakoram-Kohistan Suture Zone

1. Introduction

The Karakoram-Kohistan Suture Zone (KKSZ) is a fault zone resulting from both ductile and brittle deformation. Ductile fabrics are polyphase with predominating subhorizontal NE-SW trending mineral lineations, fold axes and, less common, subvertical stretching lineations. Shear bands and other sense of shear criteria indicate a sinistral sense of shear parallel to the subhorizontal stretching lineations.
Brittle faults can be classified into three major populations: (1) suture parallel (NE-SW striking), mainly sinistral strike-slip faults, (2) vertical, N-S striking sinistral strike-slip faults offsetting Kohistan and suture zone units, and (3) NE-SW striking, top-to-the-SE reverse faults.
Paleostress tensors were calculated from measured fault planes and striations to clarify the chronology and the orientation of recorded stress fields along the suture zone.

2. Method and data

458 fault-slip data were collected at 22 outcrop localities (Table 4.1, Fig. 4.2). The fault sites are mainly located in the *serpentinites and talcschists* unit and are not longer than 0.5-1 km. Slickenside striations were measured on mesoscopic fault planes with orientations as various as possible (Fig. 4.1). The shear sense was determined using the growth direction of slickenside fibres. Most of the measurements were made in serpentinites and sheared ophicarbonates; therefore the fibres are mainly composed of calcite and serpentine. No superposition of striae was found at any of the investigated sites. Seven to forty measurements were made at each site.
Taken all together, the fault planes predominantly dip steeply 65-85° NW (Fig. 4.2). The rake is according to the slip direction of the hanging wall with respect to the footwall. It is measured from the strike direction and is positive counter-clockwise (e.g. sinistral movement has a rake value of 0, dextral + or -180, normal -90, reverse +90). The rake distribution displays two maxima, one at

normal (rake ~ -90°) and one at reverse faults (rake ~ +90°). The rake also shows a significant amount of strike slip, especially sinistral with a reverse component (rake ~0-30°). However, about 18% of the data have a dextral component (rake ~ +180°).

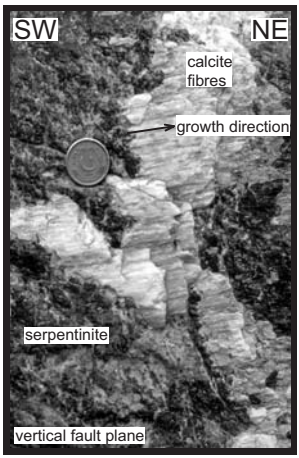

Fig. 4.1. *Calcite slickenside striations (white) on a vertical, NW dipping fault plane in serpentinites. The calcite fibres grew from the host serpentinite towards the right. Thus, (the photographed block moved towards SW with respect to the camera) a sinistral sense of shear is deduced.*

Data processing was carried out with the Fault Slip Analysis (FSA) software written by B. Célérier (1999). An effective stress tensor T was considered with principal stress directions s_1, s_2 and s_3 (Eigenvectors of T) and corresponding principal stress magnitudes $\sigma_1>=\sigma_2>=\sigma_3$ (Eigenvalues of T) with positive compression and magnitude ratios $r_0=(\sigma_1-\sigma_2)/(\sigma_1-\sigma_3)$. Tensors were sought by the inversion method (Etchecopar *et al.* 1981). It is assumed that the shear stress orientations are as close as possible to the measured slickenside striations on the related fault planes.

In a first processing step an effective stress tensor T, with principal orientations s_1, s_2 and s_3 was calculated for each locality, separately. This tensor had to explain 30-50% of the local fault-slip data with an angular error smaller than 30°. It was selected by a random search trying 10’000 tensors. The unexplained fault data were put aside.
In a second step, another (second) random tensor search was performed whereby the best tensor had to explain 95-100% of the reduced fault-slip data set with an angular error smaller than 30°. A third step (analogue to step 2) was done only if results from set 2 were not conclusive.
An alternative, second tensor was identified at four sites by applying a random tensor search on the fault data put aside during the first tensor search.

locality	long. (E)	lat. (N)	unit	S_1-az	S_1-plunge	S_2-az	S_2-plunge	S_3-az	S_3-plunge	r_0	Azshmax	Sv	label	n	select.	explained err.<15°	explained err.<30°	av. err. select.	qual.
Mirkhani	71.725	35.467	Ko-Md	153	9	63	4	312	80	0.8	332	3	14	23	14	9	11	15°	s
Ursun_1	71.708	35.492	S-ST	107	42	351	25	240	38	0.77	171	1	18	33	13	10	13	10°	s
Ursun_2	71.708	35.492	S-ST	260	6	358	54	165	36	0.53	260	2	19	33	11	6	9	11°	p
Dam	71.73	35.512	S-ST	144	11	242	37	40	51	0.81	144	3	12	17	9	5	7	11°	p
Beorai	71.775	35.525	Ko-DV	168	29	264	11	14	59	0.73	354	3	25	9	6	5	6	6°	p
Jingeret	71.752	35.531	S-ST	124	23	346	61	222	18	0.78	312	2	7	28	19	14	19	9°	w
Drosh_south	71.791	35.549	Ko-DV	128	0	218	59	38	31	0.9	128	2	9	30	18	12	18	10°	w
Shishi	71.853	35.6	Ko-DV	132	20	273	64	37	15	0.98	127	2	16	11	9	5	8	14°	p
Tar	71.883	35.638	S-ST	135	30	28	26	265	48	0.81	298	3	15	17	8	6	8	11°	p
Gashish	71.904	35.664	S-ST	265	4	172	41	360	49	0.36	265	3	21	7	5	3	5	9°	p
Lao	71.918	35.658	Ko-DV	102	54	329	26	227	23	0.44	317	1	13	16	12	10	12	11°	s
Birgah	71.912	35.672	S-ST	135	16	44	3	302	74	0.93	314	3	11	12	8	6	8	10°	p
Kalas	71.942	35.719	S-ST	205	70	352	17	85	11	0.25	175	1	4	15	12	8	11	12°	s
Domuk	71.976	35.721	S-GD	156	27	250	8	355	62	0.8	340	3	20	7	6	5	5	9°	p
Taikra	71.98	35.736	S-ST	236	73	52	17	143	1	0.64	233	1	3	14	12	10	12	8°	s
Skari_1	71.992	35.742	S-ST	149	46	243	4	337	43	0.79	243	1	17	28	12	8	11	12°	s
Skari_2	71.992	35.742	S-ST	96	28	289	61	189	6	0.88	279	2	23	28	7	5	7	11°	p
Matio	72.017	35.764	S-ST	265	29	2	11	111	58	0.88	92	3	22	12	9	7	9	9°	p
Chhuchhu_1	**72.023**	**35.774**	S-ST	107	66	196	0	286	24	0.82	196	1	5	39	19	14	18	11°	w
Chhuchhu_2	72.023	35.774	S-ST	279	17	17	26	160	59	0.38	279	3	8	39	24	20	24	8°	w
Angarbah	72.027	35.779	S-ST	116	30	333	54	216	18	0.84	306	2	10	17	11	8	11	11°	s
Saritari	72.037	35.788	S-ST	72	46	258	44	165	3	0.81	255	1	24	13	9	5	7	15°	p
Manji	72.048	35.801	S-ST	126	51	277	35	18	15	0.47	108	1	2	25	15	8	13	14°	s
Shalodok	72.071	35.815	S-ST	129	74	300	16	31	3	0.99	121	1	1	21	15	11	15	9°	w
Ando.-Turi._1	72.08	35.8	Ko-Ga	65	83	156	0	246	7	0.87	155	1	6	29	16	10	13	14°	s
Ando.-Turi._2	72.08	35.8	Ko-Ga	173	11	306	74	81	12	0.3	173	2	26	29	13	8	13	11°	s

Table 4.1. *Results of paleostress calculations. Az: azimuth; shmax: maximum horizontal stress axis; Sv: index of the vertical stress axis; n: number of measured fault data; select.: number of selected fault data used for final tensor calculation; explained: number of selected faults explained by stress tensor with angular error smaller than 15° (err.<15°) and smaller than 30° (err.<30°), av.err.select.: average angular error between the predicted rake of the stress tensor and the observed rake of the slickenside striations; qual.: quality of fit of stress tensor (see text).*

The used and explained fault-slip data and their quality are listed in Table 4.1. The two columns ‘explained’ are a measure of the quality of the calculated stress tensor. They represent the amount of faults with an angular error, between each fault and the stress tensor, smaller than 15° and 30°, respectively. A quality label (‘qual.’) is assigned to the stress tensor based on the amount of data measured at the location and the obtained quality of fit of the calculated stress tensor. For a well constrained tensor ‘w’, more than 14 faults fulfil this constraint whereas for a poorly constrained tensor ‘p’, there are less than 10 faults; ‘s’ indicates a sufficiently constrained tensor with 10-14 faults having an angular error smaller than 30°. Tensors obtained from less than 5 fault data were not accepted.

3. Results

3.1 Overview

Twenty six stress tensors were obtained for the 22 locations, with two different tensors being calculated for locations Ursun, Skari, Chhuchhu and Andowir-Turipilu (Fig. 4.2).
The maximum principal stress direction s_1 is scattered. The majority of s_1 plunges shallowly towards SSE to E, whereas four tensors plunge at shallow angles towards W (Fig. 4.3a). The intermediate and minimum principal stress directions s_2 and s_3 scatter more than s_1.
The triangular diagram of Fröhlich (1992) shows that only few principal stress directions are vertical (Fig. 4.3b). This could be due to rotation of the measured fault planes after they were activated by the calculated stress tensor. The tectonic regime plot (Armijo *et al.* 1982, Philip 1987, Célérier 1995) shows that the locations recorded two different regimes: some in an extension (vertical maximum principal stress), the others in a compression (vertical minimum principal stress) to wrench regime (Fig. 4.3c).
A horizontal principal stress direction map (Fig. 4.2) was produced by projecting two of the principal stress axes s_1, s_2 and s_3 on a horizontal plane and approximately fitting the Anderson assumption (Anderson 1905), for which one stress axis is vertical, orthogonal to the earth’s surface.
Based on all these graphical illustration methods, two major different stress tensors yielding (1) a compression to wrench and (2) an extension tectonic regime, are distinguished. Examples of these two regimes are discussed in the following sections.

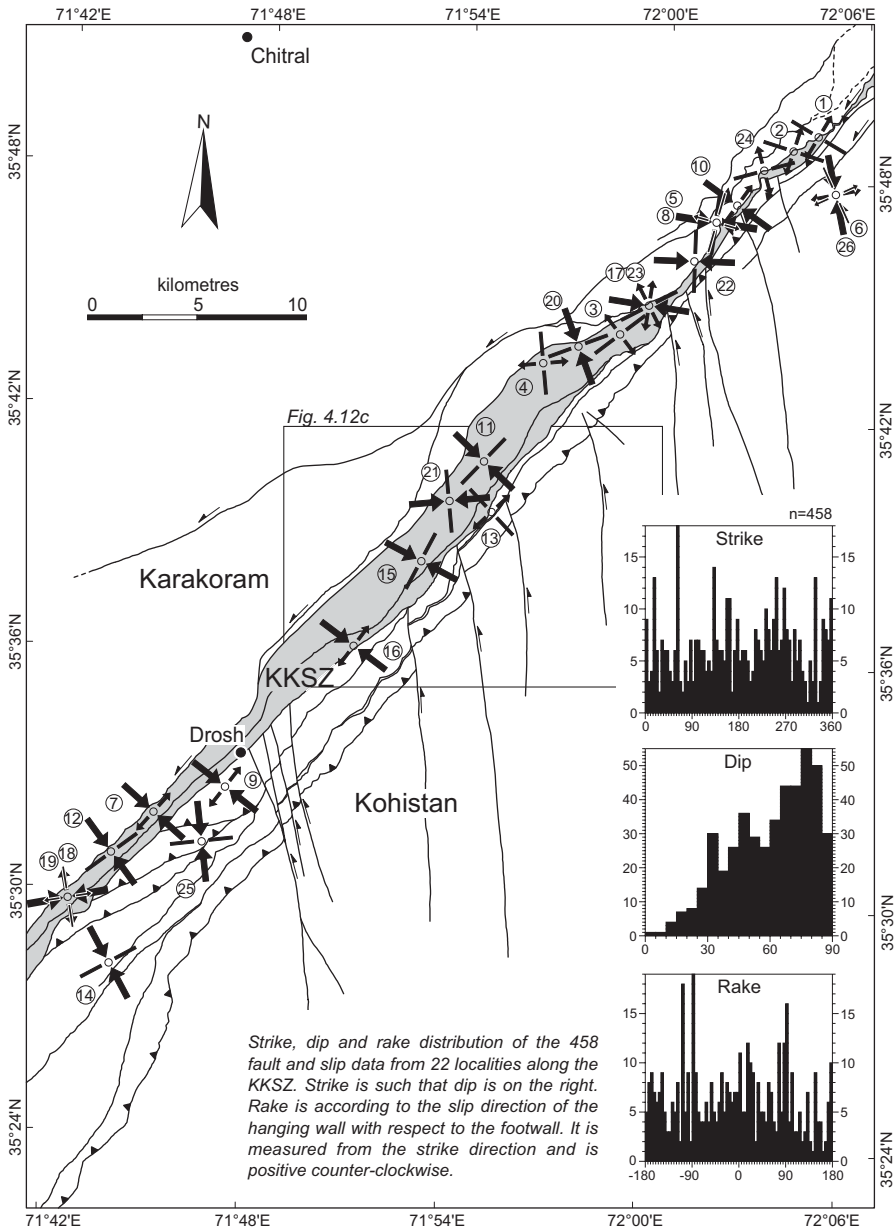

***Fig. 4.2**. Horizontal principal stress axes and main faults within the studied area; locations (circled numbers) are given in Table 4.1. Inward and outward pointing arrows: maximum and minimum principal stress direction, respectively; bar: intermediate principal stress direction; arrows and bars for locations 5, 6 and 18 are drawn with a white outline to visually separate them from the arrows and bars of the second recorded tensor at the same sites. Grey shaded area: Karakoram-Kohistan Suture Zone (KKSZ).*

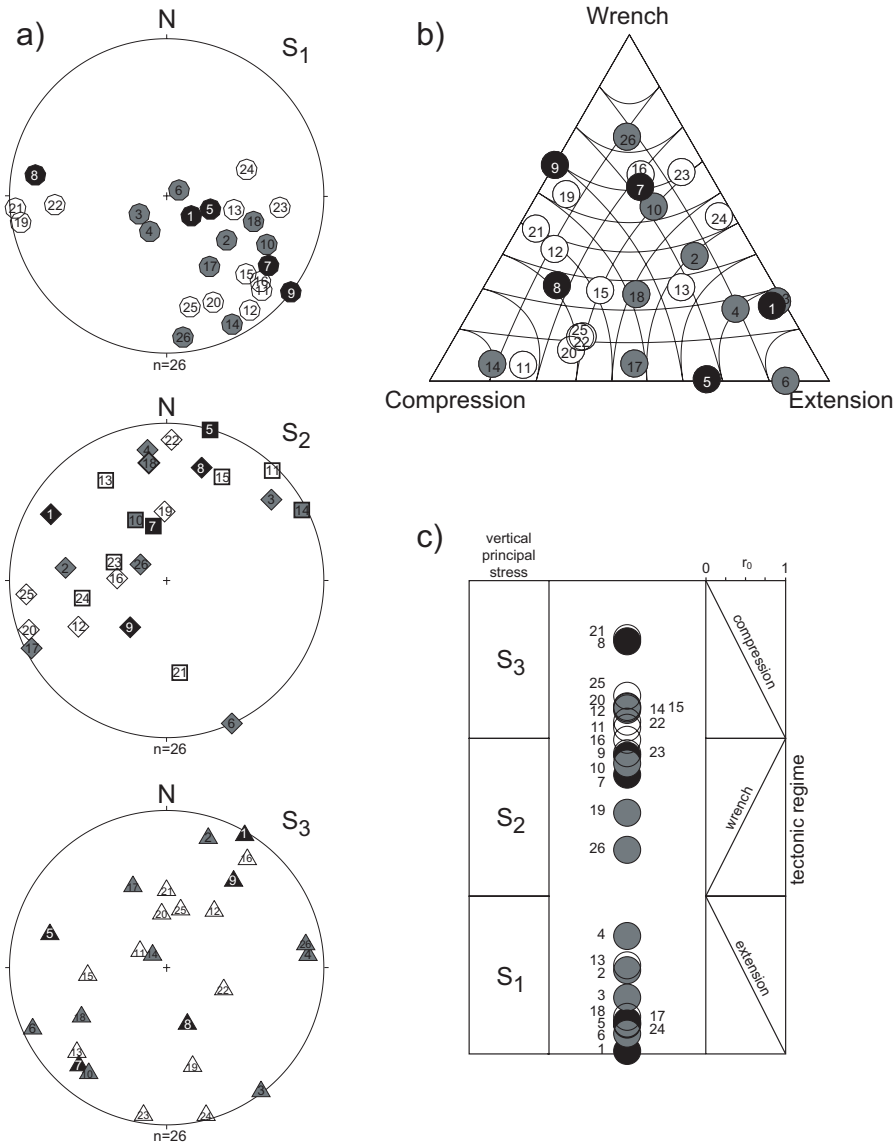

Fig. 4.3. *Stress tensor data from all locations, symbol fillings (after Table 4.1): black: well constrained, grey: sufficiently constrained, no fill: poorly constrained.*
a) *equal area, lower-hemisphere projection of the principal stress axes, squares in* s_2*: up-going directions for which the opposite (down-going) direction is plotted;* ***b)*** *triangular classification (Fröhlich 1992) of stress axes;* ***c)*** *Tectonic regime plot of stress tensors,* s_1*,* s_2 *and* s_3 *are principal stress axes (unit vectors) without their magnitudes;* $r_0=(\sigma_1-\sigma_2)/(\sigma_1-\sigma_3)$ *where* σ_i *stand for principal stress magnitudes;*

3.2 Compression and wrenching

Two different s_1 directions in two stress regimes are distinguished (Fig. 4.2): NW-SE wrenching and E-W compression, both with subhorizontal stress components s_1.

3.2.1 NW-SE directed subhorizontal s_1

A compression to wrench stress field with a NW-SE directed subhorizontal s_1 is displayed at 11 localities (Fig. 4.4).

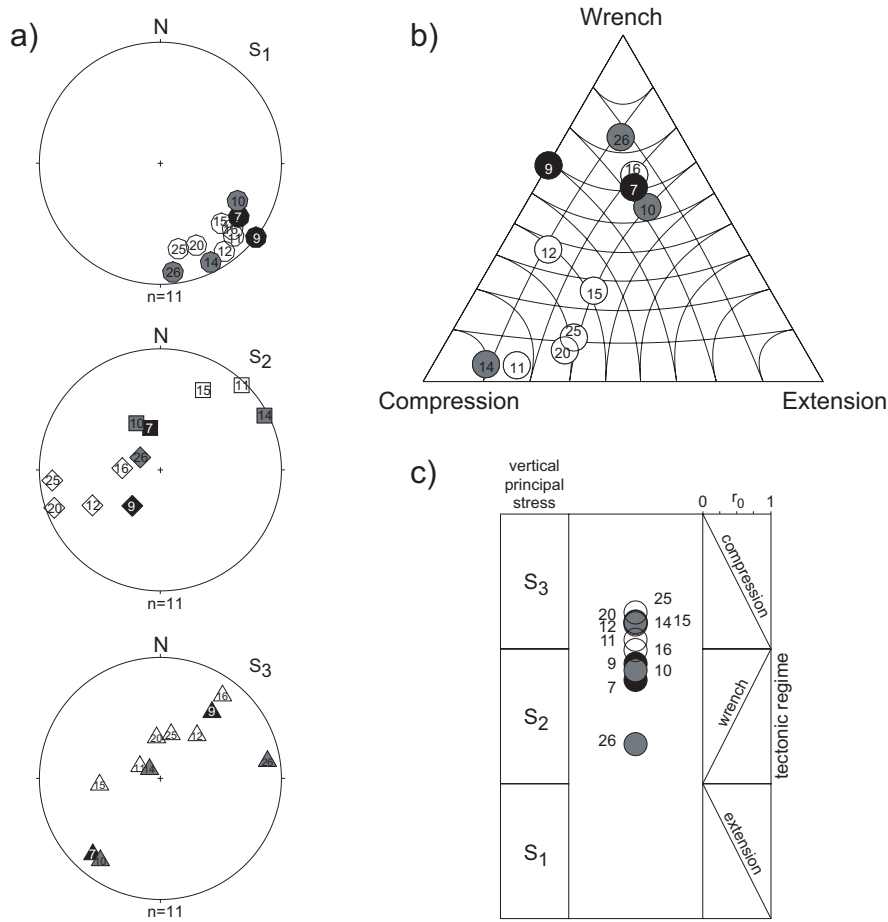

Fig. 4.4. *Stress tensor data for the NW-SE compressional to wrenching stress field. Plot explanations like in Fig. 4.3. Data are listed in Table 4.1.*

Stress components s_2 and s_3 scatter along a NE-SW trending subvertical plane perpendicular to s_1 (Fig. 4.4a). A 'well' and a 'sufficiently' constrained site are chosen to illustrate the wrenching tectonic regime and discussed in the following two sections.

Wrenching with NW-SE directed s_1 (Jingeret, site n. 7)

Twenty-eight fault-slip measurements were made at the *Jingeret* site, of which 19 are finally kept to calculate a paleostress tensor. The conjugate set of faults consists of mainly steeply east-dipping sinistral faults and steeply north-dipping dextral faults (Fig. 4.5a). The best tensor retained after slip inversion yields maximum (s_1) and minimum (s_3) principal stress axes plunging subhorizontally towards SE and SW respectively (Fig. 4.5b). The horizontal principal stress axis s_1 is nearly perpendicular to the regional fault zone (Fig. 4.2, location 7).

A measure of how well this tensor explains the fault-slip data is illustrated by the Mohr and angular error diagrams (Figs. 4.5c,d). The stress state of each fault is plotted in the Mohr diagram together with the Mohr circles of the considered stress tensor and the friction lines s_0 (considering a friction coefficient μ=0.6, $s_0=(\sigma_1-\sigma_2)/\sigma_1$). The slope of the friction lines is defined by $s_0=\mu/(\tau_r-\mu(\sigma_{nr}-1))$, the required stress difference ratio to activate a fault plane. τ_r is the shear stress, σ_{nr} the normal stress computed from the reduced stress tensor. The calculated best stress tensor can reactivate 11 out of 19 fault planes with a stress difference ratio $0.68 \leq s_0 \leq 0.8$. These 11 faults lie between the two friction lines s_0=0.68 and s_0=0.8 (Fig. 4.5c). The angular error plot (Fig. 4.5d) illustrates that this tensor explains all the 19 faults with an angular error smaller than 30°: all values of angular error, plotted for each fault, plot below the 30° line. 14 faults have an error smaller than 15° and plot below the 15° line.

Another way to prove that the tensor is a well-fitting solution, is to look at the hundred best results of the randomly searched tensors (Fig. 4.5e). The three principal stress axes show individually a small scattering. The r_0 value (0.77) suggests σ_2 being close to σ_3. This difficult identification explains scattering of calculated s_2 and s_3 in the vertical, NE-SW trending plane perpendicular to s_1. Thus, the *Jingeret* site yields a well constrained stress tensor revealing a NW-SE compression in a predominantly wrenching tectonic regime.

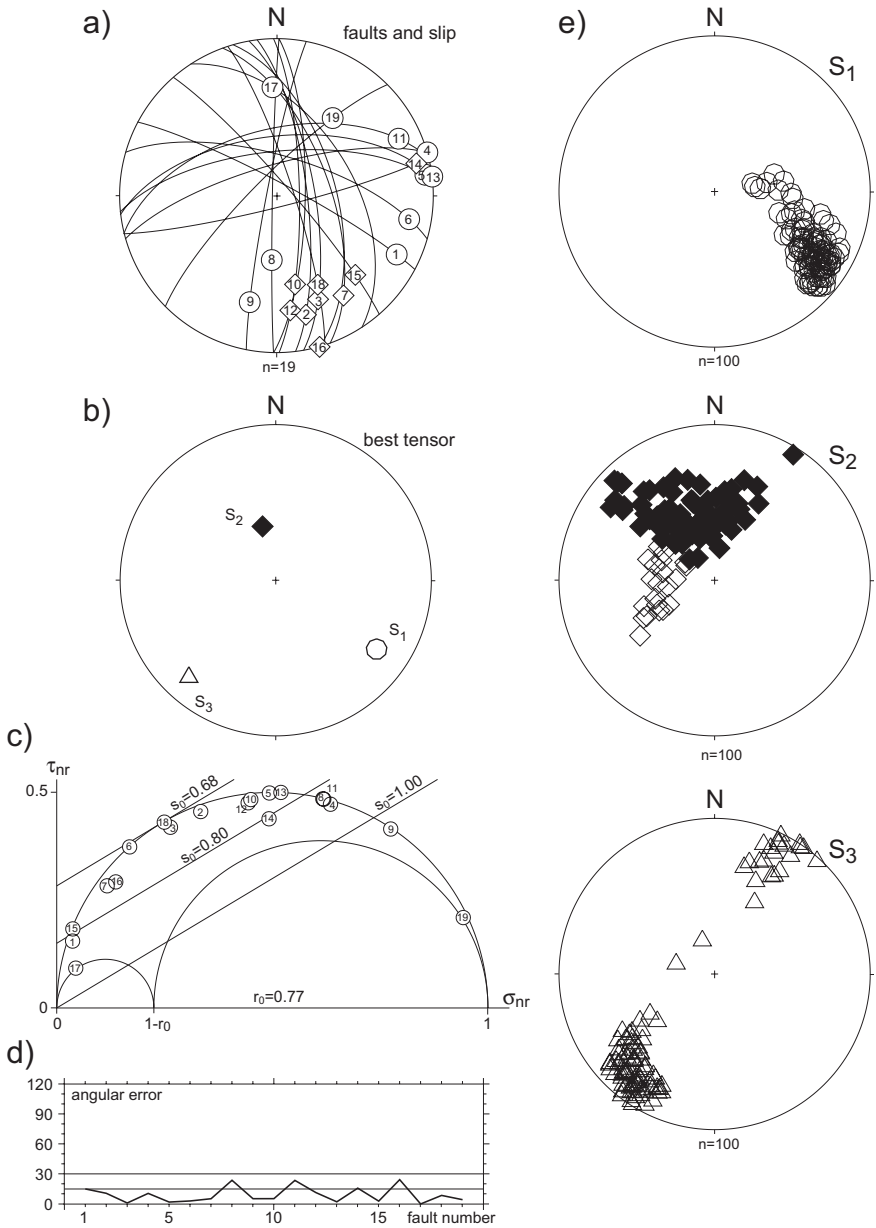

Fig. 4.5. *Fault and tensor data of the Jingeret location (**label 7** on Figs. 4.2 and 4.3). Stereographic, equal area lower-hemisphere projections of **a)** fault-slip data (circles: normal slip, diamonds: reverse slip for which the opposite down-going direction is plotted). numbers are fault data identifications. **b)** principal stress axes of the best tensor solution. **c)** Mohr-diagram (explanation in text). **d)** angular error plot (explanation in text). **e)** principal stress axes of the best 100 tensor solutions. Filled diamonds: up-going directions for which the opposite down-going direction is plotted.*

Wrenching with N-S directed s_1 (Andowir_Turipilu_2, site n. 26)
Thirteen fault slip data out of 29 from the Andowir-Turipilu site were assigned to the *Andowir-Turipilu_2* set. These are predominantly NW- and W- dipping normal and sinistral faults (Fig. 4.6a). The best tensor yields subhorizontal s_1 and s_3 plunging towards S and E, respectively, and a subvertical s_2 (Fig. 4.6b). It is well constrained as displayed in the Mohr diagram (Fig. 4.6c) and the angular error plot (Fig. 4.6d). All faults yield an angular error smaller than 30°, with 8 of them yielding an error smaller than 15°. However, only 5 out of 13 faults can be reactivated by the obtained tensor with a stress difference ratio $0.68 \leq s_0 \leq 0.8$ (five faults plot between the two friction lines s_0=0.68 and s_0=0.8 in Fig. 4.6c).
Two of the principal stress axes of the 100 best tensors display a significant scattering (s_1 and s_2 in Fig. 4.6e): s_1 and s_2 variously plunge along a N-S oriented plane, whereas strongly concentrated s_3 trend E-W. Scattering of s_1 and s_2 can be explained by the r_0=0.3 inferring a σ_1 close to σ_2. This site reveals a wrenching tectonic regime with a well defined E-W directed extension direction and a less well-defined, N-S directed s_1.

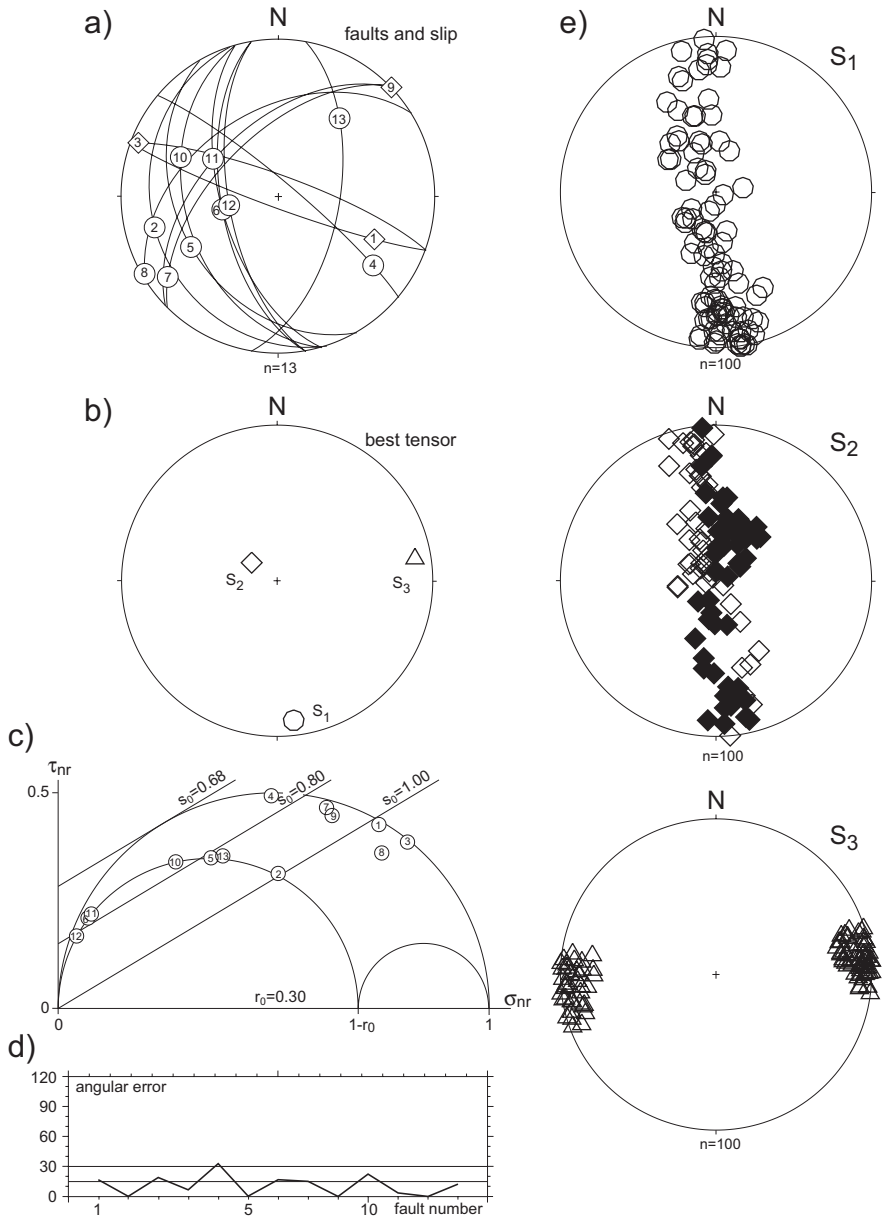

Fig. 4.6. *Fault and tensor data of the Andowir-Turipilu_2 location (**label 26** on Figs. 4.2 and 4.3). Stereographic, equal area lower-hemisphere projections of **a)** fault-slip data (circles: normal slip, diamonds: reverse slip for which the opposite down-going direction is plotted). numbers are fault data identifications. **b)** principal stress axes of the best tensor solution. **c)** Mohr-diagram (explanation in text). **d)** angular error plot (explanation in text). **e)** principal stress axes of the best 100 tensor solutions. Filled diamonds: up-going directions for which the opposite down-going direction is plotted.*

3.2.2 E-W directed subhorizontal s_1

A compression to wrench stress field with an E-W directed, subhorizontal s_1 is obtained at 5 localities (Fig. 4.7). Stress components s_2 and s_3 scatter along a N-S trending subvertical plane perpendicular to s_1 (Fig. 4.7a).

Compression with E-W directed s_1 (Chhuchhu_2, site n. 8)
Thirty nine fault slip measurements were made at the Chhuchhu location. Two fault populations could be distinguished resulting in a *Chhuchhu_1* and a *Chhuchhu_2* data set.

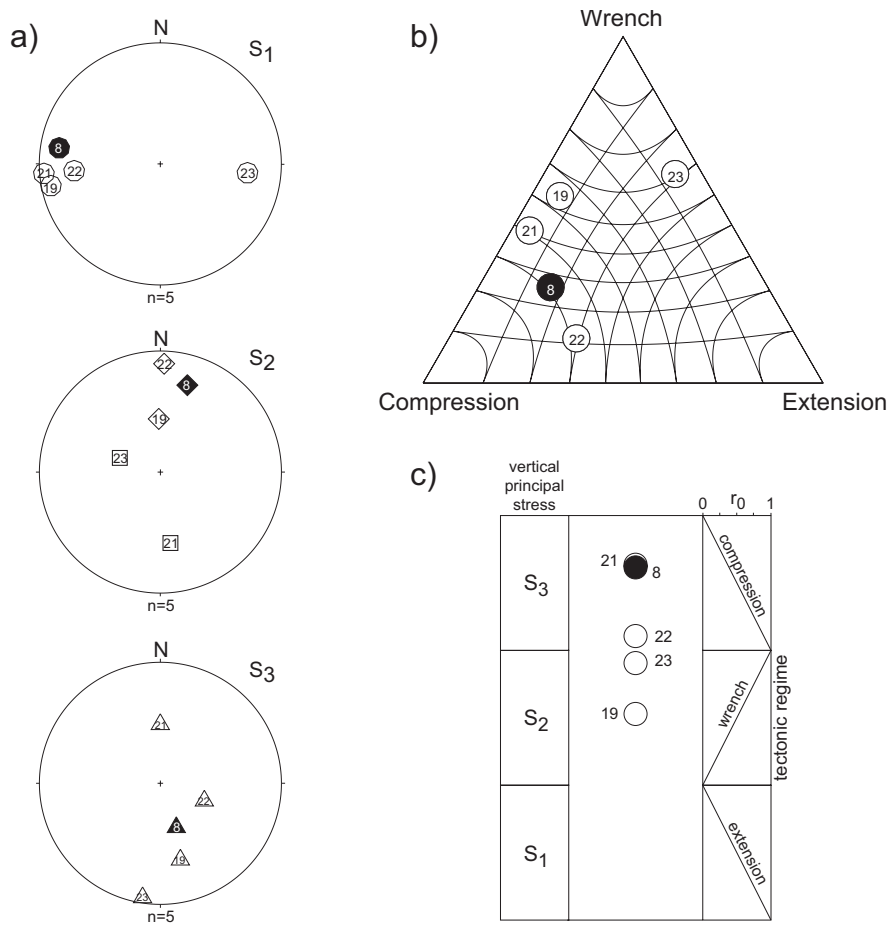

Fig. 4.7. *Stress tensor data for the E-W compressional stress field. Plot explanations like in Fig. 4.3. Data are listed in Table 4.1.*

The site *Chhuchhu_2* contains 24 measurements and is dominated by 20-50° ESE-dipping reverse faults (Fig. 4.8a). The best tensor yielded subhorizontal maximum and intermediate principal stress directions with s_1 plunging to the west and s_2 plunging to the north (Fig. 4.8b). The minimum principal stress direction s_3 plunges 59° SE (Fig. 4.8b). The resulting horizontal principal stress axis s_1 is oblique (~55°) to the regional NE-SW fault trend (Fig. 4.2, location 8).
The Mohr diagram shows that this stress tensor can only reactivate 7 of the 24 measured fault planes with a stress difference ratio $0.68 \leq s_0 \leq 0.8$ (Fig. 4.8c). But the angular errors are smaller than 30° for all the faults and smaller than 15° for 20 faults (Fig. 4.8d). The scattering of the principal stress axes of the 120 best tensors is small, indicating good consistency between measured fault slip data and the calculated tensor (Fig. 4.8e).
The *Chhuchhu_2* paleostress tensor therefore represents an E-W compressional tectonic regime.

3.2.3 Discussion

The maximal principal stress direction s_1 is subhorizontal for the three example locations and trends NW-SE, E-W and N-S at the *Jingeret*, *Chhuchhu* and *Andowir_Turipilu_2* sites, respectively. A compressional regime is inferred at the *Chhuchhu_2* site, whereas a wrenching regime is indicated at the *Jingeret* and *Andowir_Turipilu_2* sites. S_3 is subvertical and s_2 horizontal at the *Chhuchhu_2* location whereas it is the contrary at the *Jingeret* site. The azimuths of the projected horizontal maximal principal stress ('Azshmax' in Table 4.1.) differ by 74°. This variation may be explained by different orientations of the main faults at correspondent locations and/or by a local perturbation of the regional main stress direction.
Our calculations do not reveal a clear compression or wrench tectonic regime, but a combination of both. Thus, a sinistral transpression tectonic regime is inferred. This brittle, sinistral transpression is demonstrated by sinistral, NE-SW and N-S trending, strike-slip faults and top-to-the-SE thrusts. Fission track ages indicate that no or little vertical differential movement has taken place along this fault zone since the early-mid Miocene (20-13 Ma, chapter 3).

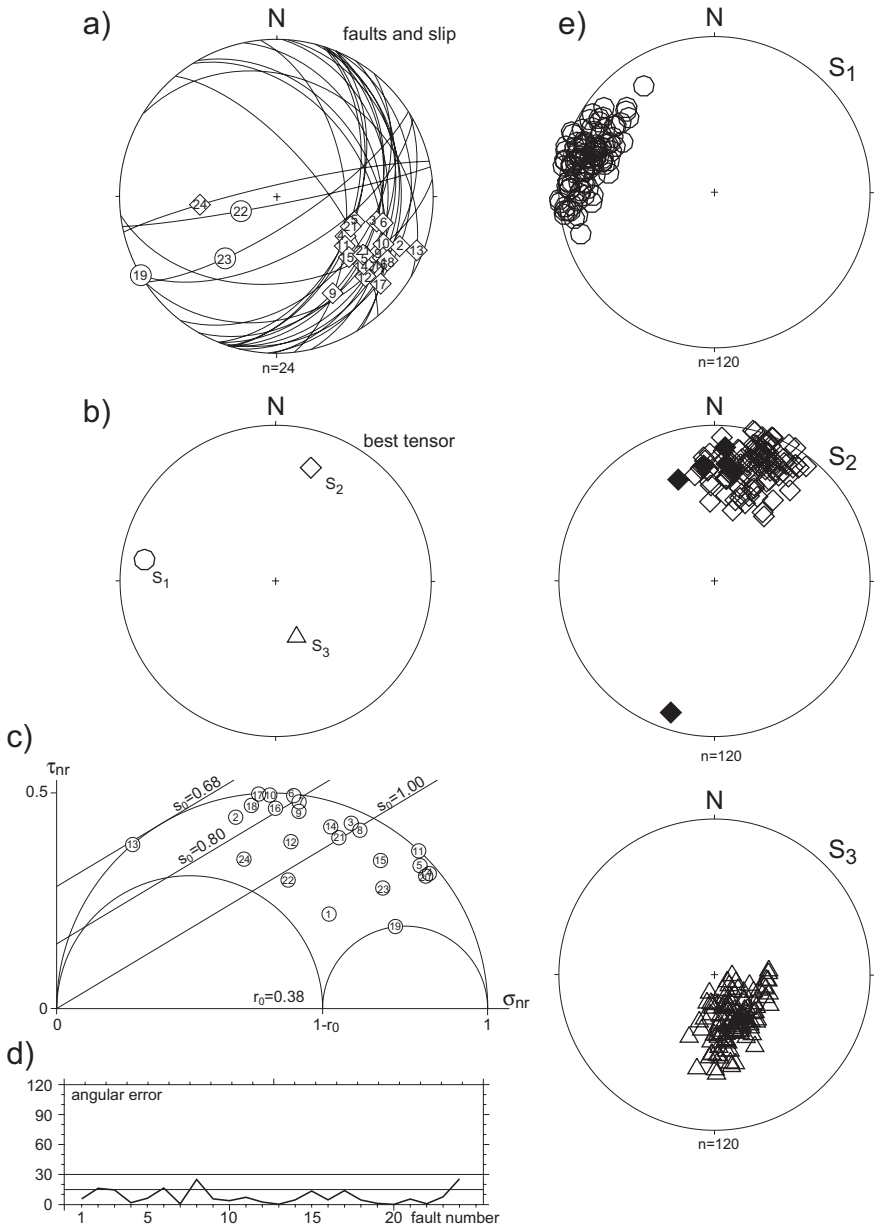

Fig. 4.8. *Fault and tensor data of the Chhuchhu_2 location (**label 8** on Figs. 4.2 and 4.3). Stereographic, equal area lower-hemisphere projections of **a)** fault-slip data (circles: normal slip, diamonds: reverse slip for which the opposite down-going direction is plotted). numbers are fault data identifications. **b)** principal stress axes of the best tensor solution. **c)** Mohr-diagram (explanation in text). **d)** angular error plot (explanation in text). **e)** principal stress axes of the best 100 tensor solutions. Filled diamonds: up-going directions for which the opposite down-going direction is plotted.*

3.3 Extension

One third of the investigated sites yielded stress tensors with predominantly steep (plunge >50°) stress components s_1 indicating an extensional stress regime (Fig. 4.9). The *Andowir_Turipilu_1* and the *Chhuchhu_1* data sets revealed 'sufficiently' to 'well' constrained stress tensors yielding an almost radial extension.

3.3.1 E-W extension

Andowir-Turipilu_1 (site n. 6)
Sixteen fault slip data were attributed to the *Andowir_Turipilu_1* set. They are, like the *Andowir-Turipilu_2* set, NW- and W-dipping normal and sinistral faults (Fig. 4.10a). The best tensor yields a vertical s_1 (Fig. 4.10b). The stress components s_2 and s_3 are subhorizontal and plunge towards SSE and WSW, respectively (Fig. 4.10b). Seven out of 16 faults can be reactivated by this tensor. Thirteen faults yield an angular error smaller than 30°, 10 faults have an error smaller than 15°, constraining the acceptable quality of the tensor (Figs. 4.10c,d).
The s_1 direction of the plotted 120 best tensors scatters a little whereas s_2 and s_3 slightly scatter subhorizontally (Fig. 4.10e). The r_0 value is 0.87 and implies σ_2 to be close to σ_3. This explains the subhorizontal scattering of s_2 and s_3. The subvertical s_1 suggests an extensional tectonic setting as shown by the Fröhlich and tectonic regime plots (Figs. 4.9b,c).

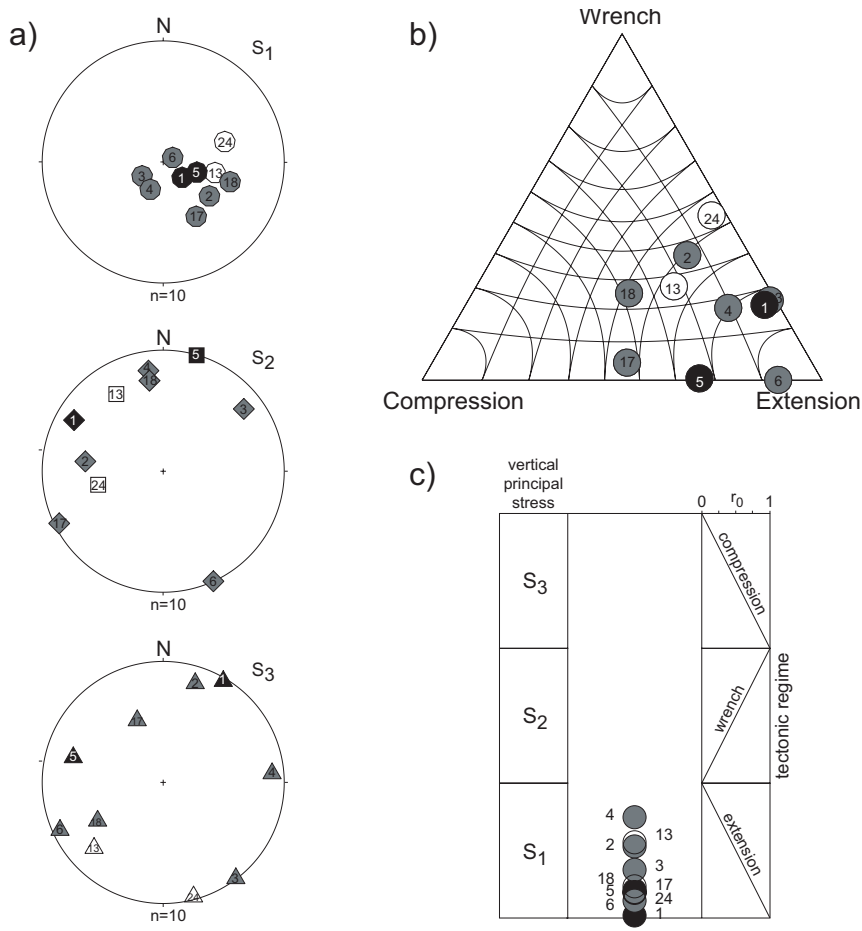

Fig. 4.9. *Stress tensor data for the extensional stress field. Plot explanations like in Fig. 4.3. Data are listed in Table 4.1.*

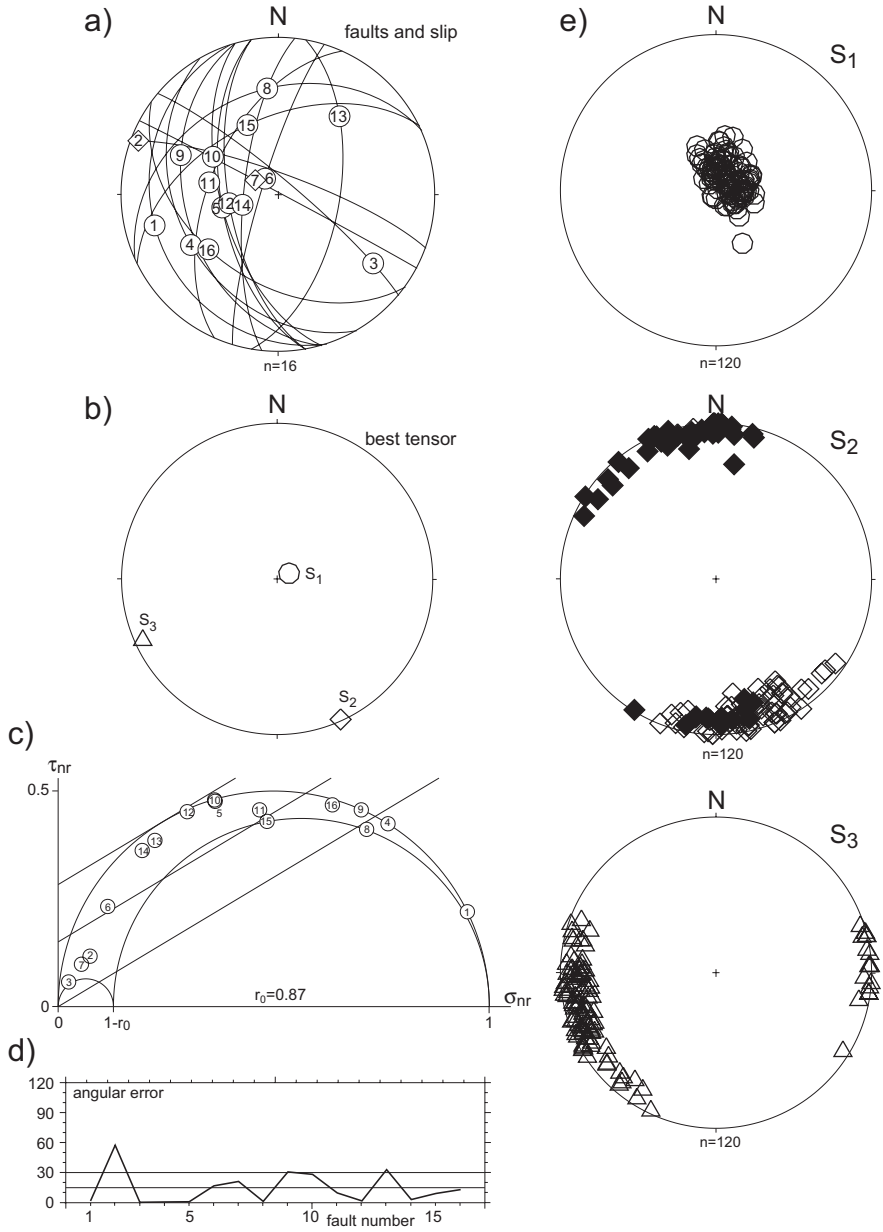

Fig. 4.10. *Fault and tensor data of the Andowir-Turipilu_1 location (**label 6** on Figs. 4.2 and 4.3). Stereographic, equal area lower-hemisphere projections of **a)** fault-slip data (circles: normal slip, diamonds: reverse slip for which the opposite down-going direction is plotted). numbers are fault data identifications. **b)** principal stress axes of the best tensor solution. **c)** Mohr-diagram (explanation in text). **d)** angular error plot (explanation in text). **e)** principal stress axes of the best 100 tensor solutions. Filled diamonds: up-going directions for which the opposite down-going direction is plotted.*

3.3.2 Radial extension

Radial extension (Chhuchhu_1, site n. 5)
Nineteen fault slip data out of 39 were attributed to *Chhuchhu_1* set. They represent a conjugate set of NW and SE dipping normal faults (Fig. 4.11a). The best calculated tensor yields a subvertical s_1 and subhorizontal s_2 and s_3 plunging towards S and W, respectively (Fig. 4.11b). Thus, s_2 is subparallel to the s_2 calculated from the *Chhuchhu_2* data set, whereas the s_1 direction of *Chhuchhu_1* is close to the s_3 direction of *Chhuchhu_2* and vice versa (Figs. 4.8b, 4.11b).
The calculated tensor is well constrained and can reactivate 11 of 19 faults with a stress difference ratio $0.68 \leq s_0 \leq 0.8$ (Fig. 4.11c). For 18 faults the angular error is smaller than 30°, for 15 faults it is smaller than 15° (Fig. 4.11d). The stress component s_1 is well constrained for the 120 best tensors, whereas s_2 and s_3 display a significant scattering plunging subhorizontally towards NE over W to S (Fig. 4.11e). This distribution of the principal stress axes together with the high r_0 value (r_0=0.82) represent an almost radial extension (Figs. 4.3b,c).

3.3.3 Discussion

The stress tensors obtained at the *Andowir-Turipilu_1* and the *Chhuchhu_1* sites are almost identical and well defined. The r_0 values of these two data sets are close to 1 (0.87 and 0.82) and suggest a flattening-type stress ellipsoid with a vertical σ_1. This shape of stress ellipsoid is also found for the majority of the extension stress tensors at other sites where s_1 is the 'vertical' stress direction (Table 4.1). An extensional stress regime is thus inferred with well defined s_1 direction, but a weakly defined extension direction s_3 with a slight tendency to E-W.
Note that the *Andowir_Turipilu_2* data set (section 3.2.1) yielded a best tensor with a subhorizontal N-S trending s_1. As the r_0 value there is 0.3, s_1 is poorly constrained and scatters, together with s_2, in a N-S trending vertical plane. But the E-W extension is well constrained. Therefore it is suggested that the Andowir-Turipilu site should not be split into two different tensors. They represent together one stress tensor with a vertical s_1 and an E-W trending s_3.

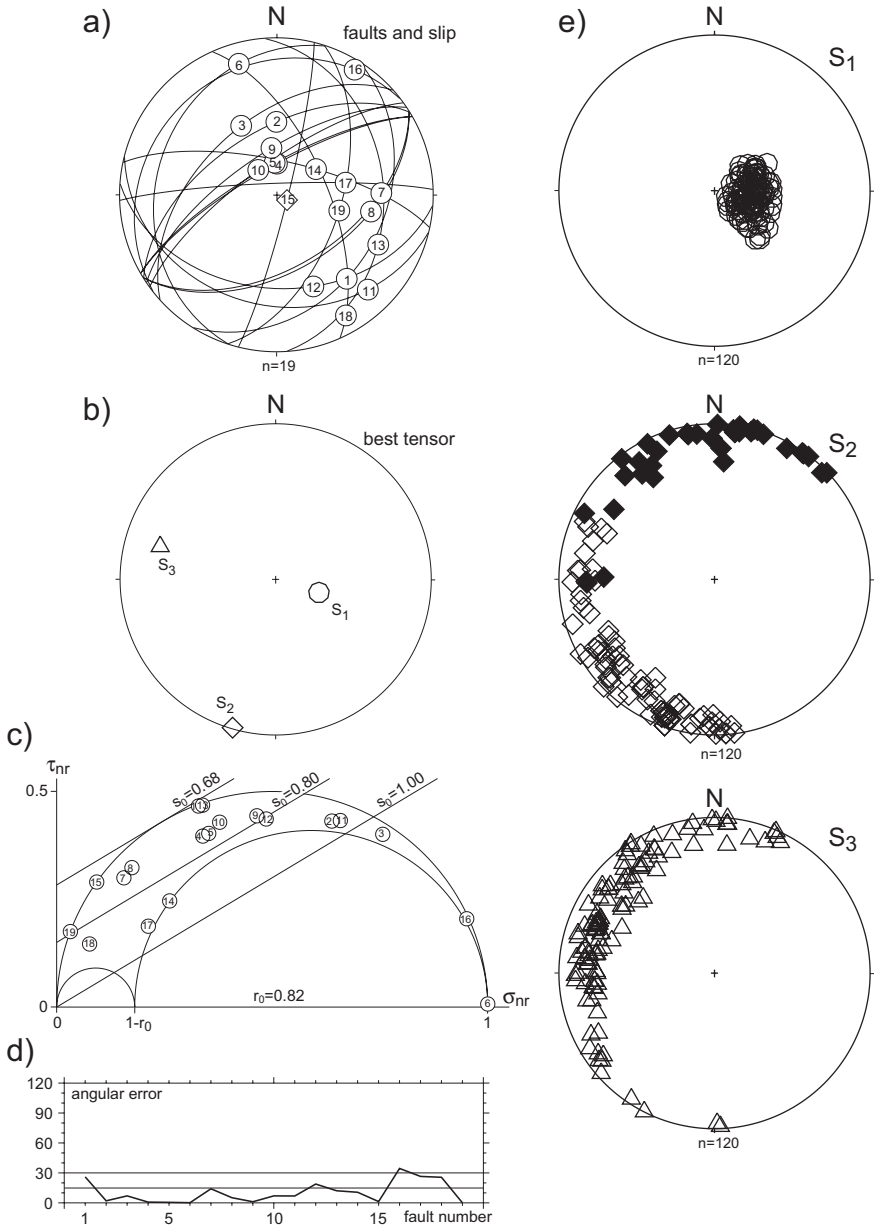

Fig. 4.11. *Fault and tensor data of the Chhuchhu_1 location (**label 5** on Figs. 4.2 and 4.3). Stereographic, equal area lower-hemisphere projections of **a)** fault-slip data (circles: normal slip, diamonds: reverse slip for which the opposite down-going direction is plotted). numbers are fault data identifications. **b)** principal stress axes of the best tensor solution. **c)** Mohr-diagram (explanation in text). **d)** angular error plot (explanation in text). **e)** principal stress axes of the best 100 tensor solutions. Filled diamonds: up-going directions for which the opposite down-going direction is plotted.*

4. Comparison with tension gashes

4.1 Method

Calcite-filled tension gashes were recorded to further constrain regional consistency of the calculated stress tensors at two, subhorizontal river polished outcrops, in the Tar and the Gashish Gol (Fig. 4.12). It is assumed that the long axis of a gash is parallel to the largest horizontal stress component s_1 or s_2 and that the shortest axis is parallel to s_3 (Ramsay & Huber 1987). Since the vertical dimension of tension gashes is not known, it is not possible to tell a priori whether the long axis on outcrops is parallel to the projection of σ_1 or σ_2.
A chronology of different crack generations was reconstructed using cross-cutting relationships. The orientations of the long and short gash axes on the outcrop were plotted on the tectonic sketch map (Fig. 4.12c) together with the horizontal principal stress axes of the calculated tensors at nearby fault sites.

4.2 Data

The Tar Gol outcrop displays one dominant generation of tension gashes (Fig. 4.12a). The long axes (σ_1 or σ_2), 30-50 cm long and 2-5 cm wide, trend NW-SE and are termed generation 1 (G1).
The Gashish Gol site exhibits two tension gash families with a well defined chronology (Fig. 4.12b). The older generation is represented by a conjugate set of tension gashes: 40-50 cm long and 5 cm wide cracks trend NW-SE (G1), and 40-70 cm long and 1-2 cm wide (G1') gashes trend WNW-ESE. A second generation (G2) crosscuts G1 and G1'. G2 gashes are 10-30 cm long and 0.5-2 cm wide, with long axes trending NE-SW.

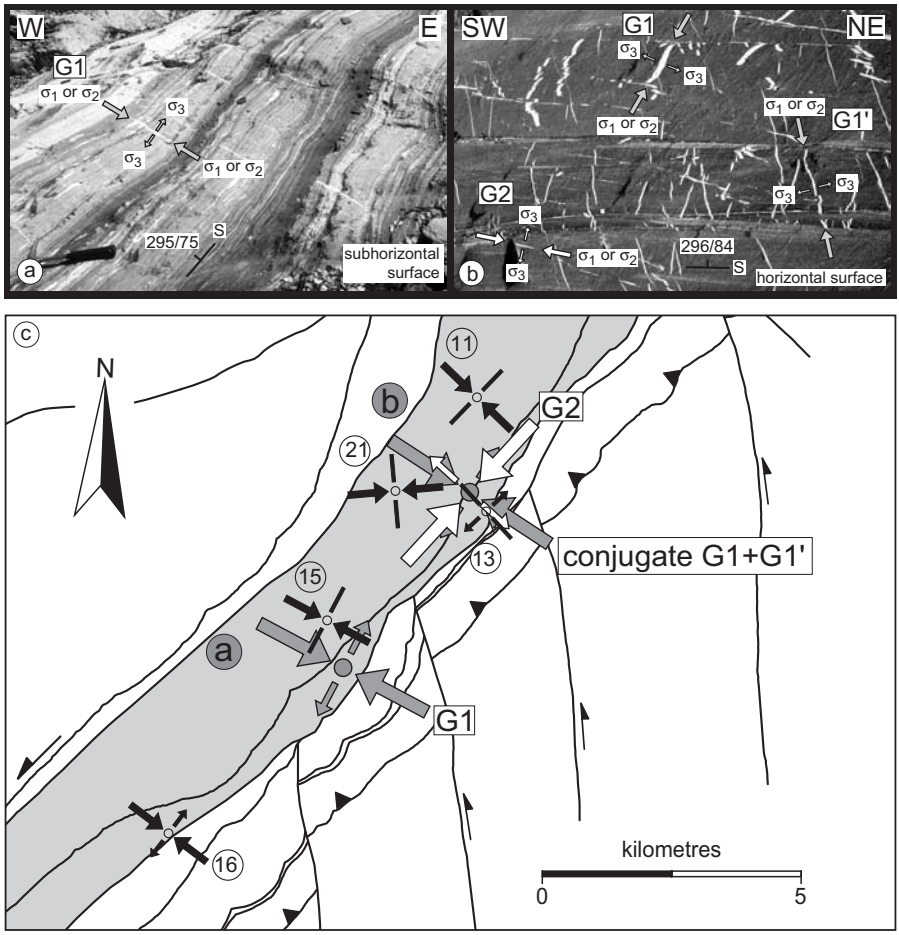

***Fig. 4.12**. Comparison of calcite-filled tension gashes observed on (sub) horizontal outcrop surfaces (photos a and b) with the calculated horizontal maximum principal stress directions (c). **a)** laminated micritic limestones in the Tar Gol. One dominant generation (G1) of calcite-filled tension gashes is observed and has NW-SE trending long axes σ_1 or σ_2. **b)** schistose Purit red shale in the Gashish Gol. Two generations of calcite-filled tension gashes are found. A conjugate set with long axes trending NW-SE (G1) and WNW-ESE (G1') and cross-cutting second generation with NE-SW trending σ_1 or σ_2 (G2). **c)** tectonic sketch map with calculated (black) and inferred, grey (G1) and white (G2) horizontal principal stress axes (cutout of, and indicated in Fig. 4.2). The grey and white arrows are inferred from a) and b). The large, inward pointing grey and white arrows represent the s_1 or s_2 direction and the small outward pointing arrows stand for s_3 (the black arrows represent s_1 and s_3 for stress tensors as in Fig. 4.2). The G1 NW-SE trend fits the calculated horizontal maximum principal stress directions from sites n. 11, 15 and 16.*

4.3 Discussion

The results are summarised in Fig. 4.12c. The older generation of tension gashes (G1 and conjugate G1+G1') at both sites are parallel and represent the same NW-SE compression, matching calculated tensors from nearby sites n. 11,15 and 16.

Comparing the G1/G1' tension gash set with the whole paleostress tensor data set from the KKSZ (Fig. 4.2), we found that the inferred σ_1 or σ_2 axes fit the majority of the horizontal principal stress axes (s_1) of the calculated stress tensors. They may therefore represent the same brittle, sinistral transpression regime with a NW-SE directed s_1.

The younger G2 generation has its long axes subparallel to the foliation and suggests a NW-SE extension. Extension with various, poorly constrained s_3, but well constrained vertical s_1 directions is observed from tensor calculations (section 3.3). The radial extension tensors (section 3.3.2) may explain the G2 tension gashes if we assume that their long axes represent σ_2.

5. Comparison with stress data from adjacent areas and with the present-day stress field

5.1 Fault slip data

5.1.1 Northern Karakoram

Zanchi (1993) and Zanchi & Gritti (1996) calculated paleostress tensors from the northern Karakoram in the northern Hunza area. E-W trending, north- and southvergent thrusts are crosscut by E-W striking sinistral, and NW-SE striking dextral strike-slip faults.
These fault geometries and calculated paleostress tensors point to a compressional to wrench tectonic regime with stress components s_1 trending N-S for thrusting ('Za1' in Fig. 4.13) and NE-SW for the subsequent strike-slip faulting ('Za2' in Fig. 4.13).
There is no absolute age for these faulting events. Thrusting was tentatively related by Zanchi (1993) to subduction-related deformation at the Andean-type Karakoram margin during the Late Cretaceous (ca. 125-100 Ma) or to crustal thickening following the India-Eurasia collision (65-50 Ma). The younger wrench faulting was linked to dextral strike-slip faulting along the Karakoram fault (Zanchi 1993), which was active at least since the end of the Oligocene (Lacassin *et al.* 2004).

5.1.2 Southeastern Kohistan arc (Jijal-Patan area)

Zeilinger *et al.* (2000) presented paleostress tensors obtained from the southeastern Kohistan paleo-island arc between Besham and Dasu. Four fault populations were separated and linked to supposedly different stress tensors.
The probably oldest fault population 1 (Z1 in Fig. 4.13) indicates a wrench tectonic regime with s_1 trending SSE-NNW and s_3 ENE-WSW. The interpreted age is late Miocene. The Z1 horizontal compression is subparallel to the Za1 compression in the northern Karakoram (Zanchi 1993) and fits approximately the NW-SE to N-S compression found in the KKSZ (section 3.2.1).
The population 2 (Z2 in Fig. 4.13) denotes E-W compression considered to be Early Pliocene in age (Zeilinger *et al.* 2000). It matches E-W compression from the KKSZ (section 3.2.2).
Zeilinger's population 3 (Z3) represents an extension tectonic regime with an inferred WNW-ESE s_3 (Fig. 4.14). r_0 is reported to be close to 1 implying that σ_2 approximately equals σ_3. Therefore, the Z3 extension direction remains ill defined. However, similar r_0 values were found for the extension regime

tensors in the KKSZ (section 3.3). Vertical s_1 is well constrained in Z3 and in the KKSZ and thus these regimes may be correlated.
There are no similarities between population 4 (Z4 of Zeilinger *et al.* 2000, Fig. 4.13) and our results.

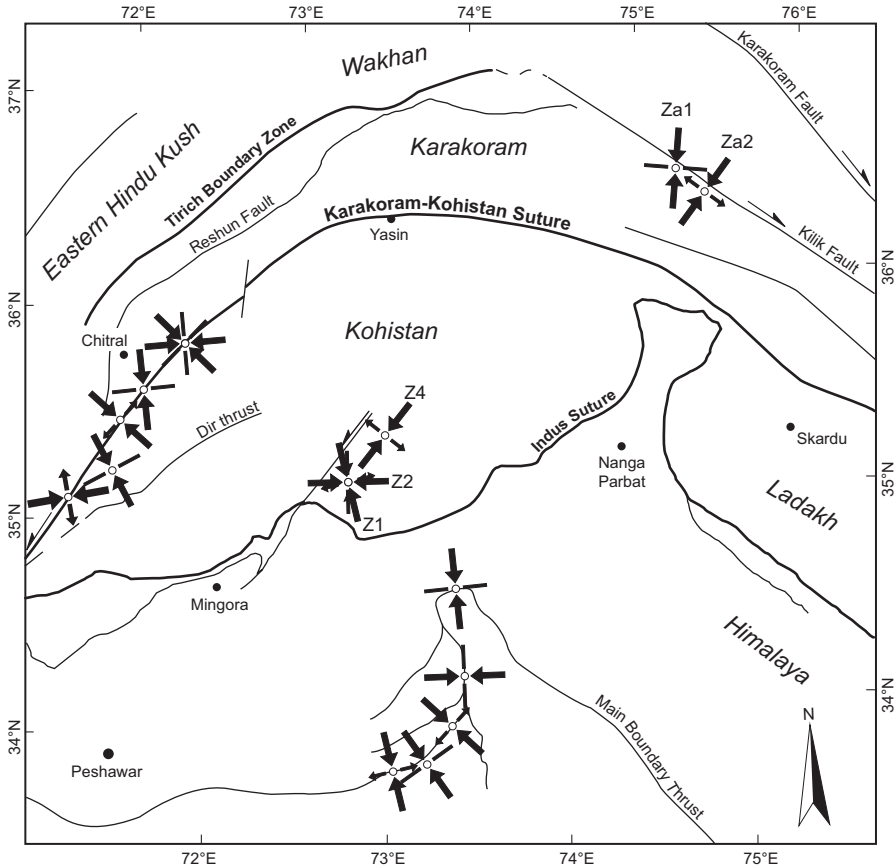

Fig. 4.13. *Tectonic sketch map of the NW Himalaya with calculated, main horizontal principal stress axes in a compressional or wrench tectonic regime in the KKSZ field area, 'northern Karakoram' (Za1 and Za2, Zanchi 1993, Zanchi & Gritti 1996), southeastern Kohistan (Z1, Z2, Z4, Zeilinger et al. 2000) and the MBT and Hazara-Kashmir Syntaxis, Burg et al. (2004); details in text. Arrows and bars are like in Fig. 4.2. Sutures (heavy lines) and major faults (thin lines) are drawn as in Fig. 2.1 in chapter 2.*

5.1.3 MBT and Hazara-Kashmir Syntaxis

Burg *et al.* (2004) documented fault slip and stress data from the Main Boundary Thrust (MBT) region, the western limb of the Hazara-Kashmir Syntaxis and the fold and thrust belt north of Murree, in northern Pakistan. The

maximum horizontal principical stress s_1 is mainly subhorizontal and generally almost perpendicular to the strike of major faults. Its direction varies regionally between NNW-SSE, E-W and N-S (Fig. 4.13).

The N-S to NW-SE compression approximately fits the NW-SE to N-S compression from the KKSZ, as well as the Za1 and Z1 compression from the northern Karakoram and SE Kohistan, respectively. The E-W compression documented from the MBT and Hazara-Kashmir Syntaxis areas may coincide with the E-W compression identified in SE-Kohistan (Za2) and the KKSZ. An extensional stress regime with an WSW-ENE directed s_3 is documented at two stations (Fig. 4.14). It may correlate with the extension phase reported from the SE Kohistan (Z3) and from the KKSZ (G2).

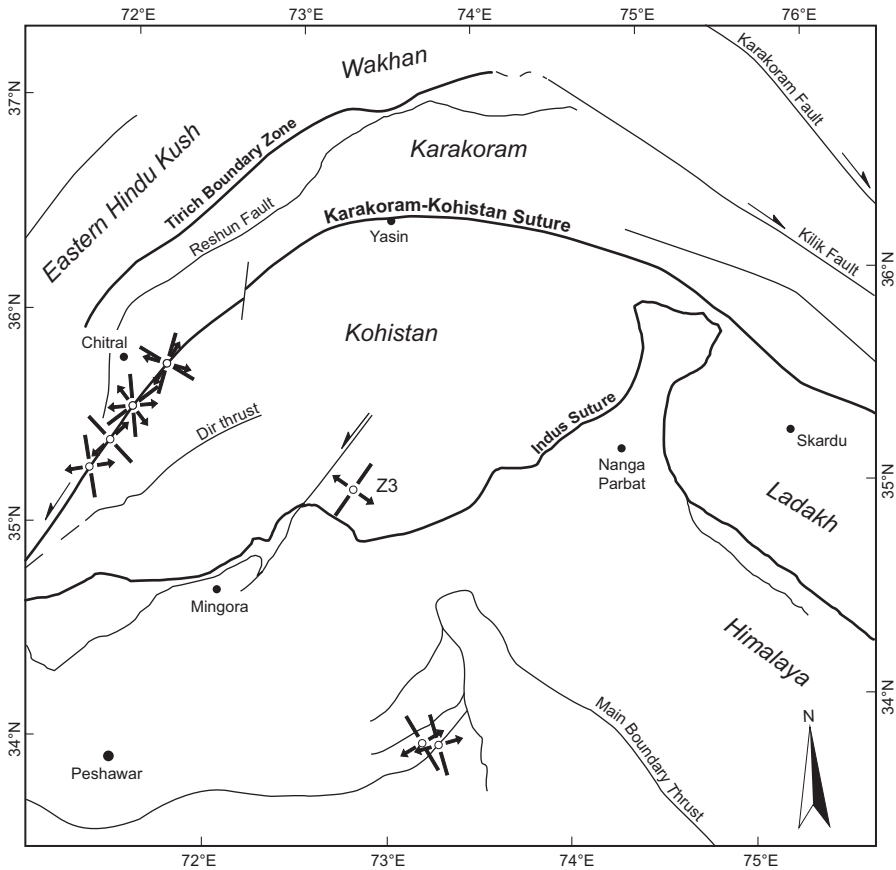

***Fig. 4.14**. Tectonic sketch map of the NW Himalaya with calculated, main horizontal principal stress axes in an extensional tectonic regime in the KKSZ field area, southeastern Kohistan (Z2, Zeilinger et al. 2000) and the MBT and Hazara-Kashmir Syntaxis, Burg et al. (2004); details in text. Arrows and bars are like in Fig. 4.2. Sutures (heavy lines) and major faults (thin lines) are drawn as in Fig. 2.1 in chapter 2.*

5.1.4 Discussion

A compressional tectonic regime with s_1 striking NW-SE to N-S is obtained in the four areas. It may represent a single regional event. Zeilinger *et al.* (2000) suggested it is late Miocene, in accordance with Zanchi (1993) who suggested an open post-mid-Cretaceous age.
E-W compression is obtained in all, but not the northern Karakoram, areas. Burg *et al.* (2004) assumed that the Pliocene, E-W shortening is a general feature in the NW Himalaya probably related to the building of the Nanga Parbat and Hazara-Kashmir syntaxes. However, our data set does not enable us to undeniably link the E-W compression along the KKSZ to that distinct regional, Pliocene phase. We interpret the E-W s_1 directions along the studied part of the KKSZ as a component of a sinistral transpression, together with NW-SE s_1 directions.
The reported extension regimes may represent the same event. In particular, the KKSZ and SE Kohistan data show the same chronology, with extension postdating both N-S to NW-SE compression and E-W compression. However, extension may also represent local lateral collapse and thus does not need to reflect a regional, contemporaneous stress regime.

5.2 Recent stress field

Earthquake focal mechanisms were used to constrain the present-day and recent stress field between longitude 71°E and 72.6°E and latitude 35°E and 36.2°N (Fig. 4.16). Fifteen focal mechanisms were taken from Mostrioukov and Petrov (1994, Table 4.2) and 177 events were extracted from the NEIC database (Table 4.3). No epicentre was found within the searched rectangle in the databases of Ekström *et al.* (2003) and Chandra (1978).

n.	long. (E)	lat. (N)	depth (km)	Paz	Ppl	Baz	Bpl	Taz	Tpl	azshmax	Sv	date
1	71.06	35.54	82	112	46	204	2	295	44	204	1	09.05.1971
2	71.46	35.48	97	297	6	30	25	195	64	297	3	30.07.1974
3	71.19	36.02	90	210	40	332	33	87	33	332	1	18.05.1975
4	71.08	36.01	73	261	19	354	7	102	70	83	3	25.10.1975
5	71.33	36.15	107	148	48	298	38	40	16	130	1	01.09.1976
6	71.01	35.65	74	125	86	231	1	321	4	231	1	13.03.1979
7	71.08	35.46	86	201	18	304	33	87	51	201	3	29.04.1979
8	72.06	35.69	4	171	37	357	53	263	3	353	2	10.07.1980
9	71.20	36.01	75	122	16	313	73	213	3	304	2	28.09.1983
10	71.19	36.2	103	331	20	216	50	75	33	331	2	25.10.1984
11	71.56	36.19	79	136	11	33	47	236	40	136	2	26.10.1984
12	72.00	36.14	87	152	0	61	60	242	30	152	2	19.08.1985
13	71.21	36.2	99	116	10	18	39	218	49	116	3	02.04.1987
14	71.19	36.19	101	226	80	334	3	64	10	334	1	21.04.1987
15	71.10	36.1	95	165	24	51	43	274	38	165	2	24.07.1989

Table 4.2. *Earthquake focal mechanisms with defined P, B and T axes. Az: azimuth, azshmax: maximum horizontal stress axis; Sv: index of vertical stress axis; data from Mostrioukov and Petrov (1994).*

The P, B and T axes of focal mechanisms provide an acceptable indication of the principle stress directions (Célérier 1988; Burg *et al.* 2004, Fig. 4.15) with P axes reflecting s_1, and T axes reflecting s_3 directions. The resulting P axes are scattered but show a concentration along directions plunging moderately to subhorizontally NW-SE. Two events display vertical P axes. The projection of the shallowest of the three principal axes into the horizontal plane may include a significant distortion. This distortion can be neglected if the steepest principal stress axis plunges more than 70° (Burg *et al.* 2004). This is the case for only 4 out of the 15 events (n. 4, 6, 9, 14 in Table 4.2 and Fig. 4.16). The tectonic regime varies from compressional to wrench, whereas two events (n. 6, 14) clearly indicate extension, as plotted in the Fröhlich triangular diagram (Fig. 4.15).

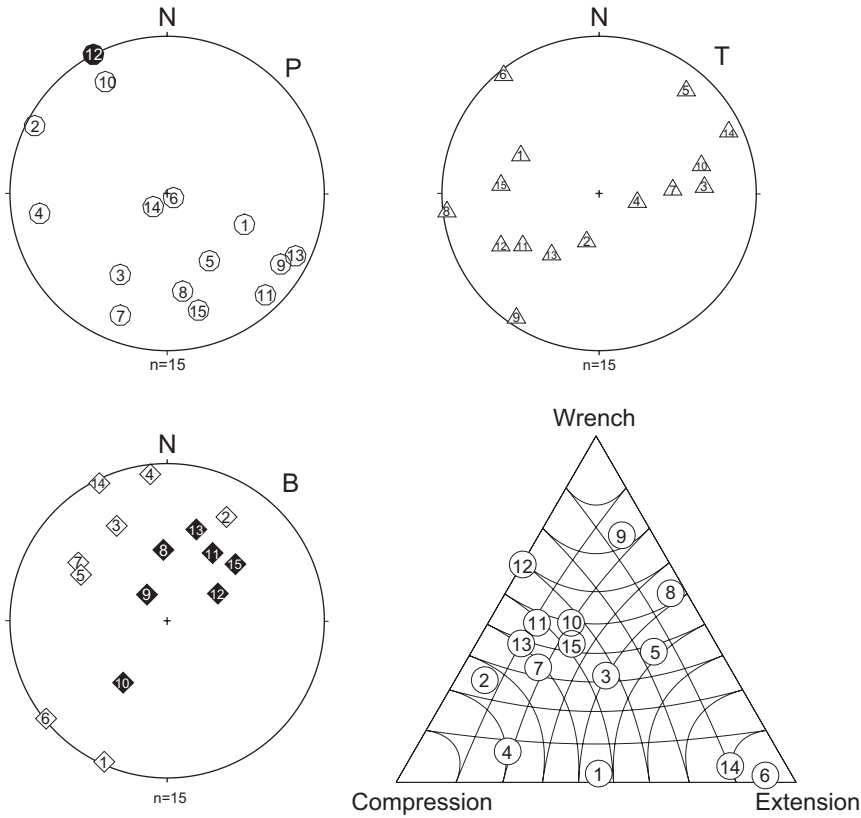

Fig. 4.15. *Equal area lower hemisphere stereographic projection of P (equivalent to s_1), B (equivalent to s_2) and T (equivalent to s_3) axes, calculated from earthquake focal mechanisms listed in Table 4.2. Filled symbols represent up-going directions for which the opposite down-going direction is plotted. Lower right: The same data in the triangular classification of Fröhlich (1992).*

date	long. (E)	lat. (N)	depth (km)	mb
02.01.1973	71.308	36.085	137	4.8
09.02.1973	71.013	35.544	75	4.5
19.02.1973	71.129	36.184	114	4.4
27.08.1973	71.074	35.944	142	3.6
17.01.1974	71.538	35.508	101	4.8
07.02.1974	71.663	36.045	132	4.4
05.05.1974	71.243	36.072	152	4.2
11.05.1974	72.109	35.652	38	4.7
14.07.1974	71.477	36.138	118	4.4
30.07.1974	71.512	35.543	70	5.3
07.08.1974	71.001	36.161	144	4.8
15.04.1975	71.179	36.097	117	4.6
18.05.1975	71.132	36.072	94	4.8
23.06.1975	71.25	36.068	161	3.7
12.10.1975	71.206	35.898	165	3.3
25.10.1975	71.039	36.066	82	4.9
30.12.1975	71.195	36.105	95	4.5
09.01.1976	71.031	35.996	148	4
09.02.1976	71.116	36.17	136	3.8
13.02.1976	71.366	36.175	169	3.1
14.05.1976	71.284	36.075	133	4.4
25.07.1976	71.275	36.166	160	
15.12.1976	71.225	35.368	222	4.1
17.03.1977	71.075	35.648	104	
12.11.1977	71.331	35.757	167	
29.01.1978	71.164	36.105	142	4
21.03.1978	71.207	36.137	123	4
28.06.1978	71.049	36.127	171	4
13.08.1978	71.041	36.142	139	4.1
13.08.1978	71.294	36.148	134	3.8
21.08.1978	71.33	35.964	197	3.5
17.10.1978	71.618	35.818	207	4.1
22.10.1978	71.307	36.197	142	4.5
29.04.1979	71.037	35.569	95	4.7
17.01.1980	71.111	35.027	20	4.7
10.07.1980	72.145	35.719	33	4.6
12.10.1980	71.26	36.011	106	4.3
18.02.1981	72.402	35.089	33	4.7
17.04.1981	71.069	36.09	142	4.4
21.09.1981	71.446	36.092	102	4.5
28.06.1982	71.152	35.96	93	4.7
09.12.1982	71.474	35.81	116	4.4
18.01.1983	71.022	35.946	67	4.8
28.09.1983	71.376	36.183	33	5
14.09.1984	71.588	35.68	33	4.7
17.10.1984	71.138	36.097	46	4.4
04.08.1985	71.052	36.138	94	5
04.08.1985	71.08	36.123	100	4.4
05.08.1985	71.501	35.982	145	4.6
14.08.1985	71.152	36.101	123	4.3
19.08.1985	71.984	36.135	51	5.2
24.08.1985	71.638	36.057	104	4.5
11.09.1985	71.143	35.906	129	3.8
20.09.1985	71.355	36.183	131	4.5
15.12.1985	71.039	36.188	119	4.5
07.01.1986	71.828	35.232	33	
05.05.1986	71.173	36.102	128	4.5
12.07.1986	71.088	35.962	33	
09.09.1986	71.42	36.135	141	4.6
01.01.1987	71.338	35.195	240	3.9
18.01.1987	71.28	36.192	94	4.8
02.04.1987	71.156	36.104	102	5.7
03.07.1987	71.214	36.051	111	5
28.07.1987	71.169	35.921	106	4.5
17.11.1987	71.084	36.169	87	4.6
21.11.1987	71.346	36.192	129	4.6
12.04.1988	71.006	36.185	33	4.2
24.07.1989	71.069	36.085	95	5.8
24.07.1989	71.121	36.118	83	4.4
10.08.1989	71.186	36.127	121	4.8
31.12.1989	71.128	36.088	155	4.5
05.01.1990	71.203	36.006	79	4.6
06.02.1990	71.349	36.186	117	5
06.03.1990	71.377	36.168	33	
02.05.1990	72.072	35.85	33	4.2
10.11.1990	71.587	35.329	33	5.3
20.12.1990	71.364	35.864	237	4.1
24.05.1991	72.03	35.589	33	4
07.01.1992	71.001	36.125	175	4.6
27.03.1992	72.548	35.997	35	4.9
30.03.1992	72.374	35.855	55	4.4
16.04.1992	72.045	35.519	33	3.9
12.06.1992	71.397	36.041	33	4.2
11.09.1992	71.026	35.84	66	5
25.03.1993	71.11	36.013	93	5.3
13.04.1993	71.069	35.915	109	4.4
02.05.1993	71.461	36.035	33	4.5
17.06.1993	71.236	36.168	104	5.2
02.07.1993	71.191	36.14	87	4.5
06.12.1993	71.027	35.748	130	4.1
25.05.1994	71.344	35.56	33	4.2
01.01.1995	71.625	36.057	84	4.2
17.01.1995	71.266	36.199	33	4.1
26.01.1995	71.255	36.147	106	5.2
15.02.1995	71.364	36.167	119	4.7
07.04.1995	71.527	35.866	135	4.4
28.04.1995	71.279	35.913	33	4.4
11.07.1995	71.253	35.927	101	4.3
24.08.1995	71.399	36.175	33	4
22.10.1995	71.339	35.29	63	4.4
28.11.1995	72.023	35.025	48	4.9
29.11.1995	71.23	36.136	130	4.6
03.12.1995	71.37	35.998	200	3.7
10.01.1996	71.053	36.022	100	4.1
17.01.1996	71.026	36.035	100	4.3
10.02.1996	71.279	35.953	100	4
13.02.1996	71.267	35.629	150	3.9
23.02.1996	71.086	35.696	33	3.9

Table 4.3. *Earthquake data from the NEIC (2004). mb: body wave magnitude.*

date	long. (E)	lat. (N)	depth (km)	mb
09.03.1996	71.6	36.035	33	3.7
18.04.1996	71.449	36.162	150	3.8
08.05.1996	72.588	35.015	33	4.1
13.08.1996	71.343	35.868	111	3.6
23.08.1996	71.183	36.025	33	
02.09.1996	71.018	36.048	106	4.3
04.11.1996	71.093	35.948	33	
07.11.1996	71.664	36.052	200	
12.01.1997	71.014	35.985	100	3.7
10.04.1997	71.219	36.184	134	
22.04.1997	71.655	35.57	33	
10.05.1997	71.051	35.592	33	3.3
13.08.1997	71.195	36.153	150	
23.10.1997	71.37	35.939	153	3.9
21.12.1997	71.338	35.143	128	4
31.12.1997	71.271	35.265	33	4
16.01.1998	71.178	36.17	100	4.1
18.02.1998	71.524	36.113	200	3.5
07.03.1998	71.528	35.174	92	3.4
18.03.1998	71.215	36.067	110	4.1
10.08.1998	71.916	36.157	168	3.5
09.11.1998	71.615	35.168	64	
12.12.1998	71.747	35.681	33	4.5
12.01.1999	71.769	36.002	33	
23.01.1999	71.099	35.851	33	3.9
23.01.1999	71.439	35.456	33	3.8
27.01.1999	71.432	35.435	33	3.4
22.02.1999	71.2	35.987	33	4
13.04.1999	71.199	36.188	106	4.4
19.04.1999	71.709	35.901	33	4.2
20.04.1999	71.034	35.067	226	
04.08.1999	71.521	36.153	149	4.3
26.08.1999	71.201	36.112	108	4.3
24.10.1999	71.094	36.19	114	4.6
23.11.1999	71.051	36.192	109	4.7

date	long. (E)	lat. (N)	depth (km)	mb
29.02.2000	72.13	35.073	33	4.3
28.05.2000	71.346	35.87	33	3.7
02.06.2000	71.638	36.195	167	4.4
05.06.2000	71.757	36.059	188	4.7
01.11.2000	71.293	36.13	33	4.8
19.12.2000	71.723	35.094	33	
24.01.2001	71.902	36.124	100	3.8
08.02.2001	71.271	36.167	33	
23.02.2001	71.166	36.121	115	
01.09.2001	71.492	36.116	127	4.6
14.09.2001	71.415	36.034	182	3.8
05.12.2001	71.043	36.131	200	3.7
01.02.2002	71.413	35.836	33	4.1
14.02.2002	71.147	36.173	178	4
07.04.2002	72.139	35.638	60	4.2
06.05.2002	71.451	36.182	100	
13.05.2002	71.064	35.973	33	3.6
26.05.2002	71.17	35.225	33	4.2
04.06.2002	71.071	36.068	33	
10.06.2002	72.124	35.86	100	4
24.06.2002	71.584	36.073	100	3.8
21.10.2002	71.116	36.128	100	3.7
23.12.2002	71.287	36.1	102	4.7
29.12.2002	71.365	36.188	33	4
07.01.2003	71.543	36.187	100	3.9
17.01.2003	71.097	35.943	33	3.9
08.03.2003	71.136	35.915	33	3.9
09.03.2003	71.303	36.166	100	3.9
24.03.2003	71.056	35.716	33	3.8
11.12.2003	71.114	36.092	33	4.2
04.01.2004	71.097	36.15	150	3.9
01.03.2004	71.212	36.133	102	4
21.03.2004	71.082	35.869	53	3.9
05.04.2004	71.266	36.124	92	

Table 4.3ff. *Earthquake data from the NEIC (2004). mb: body wave magnitude.*

Only one earthquake (n. 8 in Table 4.2) from that data set represents a crustal event that occurred at a shallow depth (4 km). The principal stress axes of this event, located beneath the KKSZ (epicentre: 72.06°E, 35.69°N on Fig. 4.16) are s_1 plunging 37°S with a horizontal, E-W trending s_3 in a wrench to extension tectonic regime (Fig. 4.15). The calculated horizontal principal stress axes (Fig. 4.16) match with those of the calculated tensor at the *Andowir_Turipilu* site (72.08°E, 35.8°N, Fig. 4.2, labels 6 and 26).
Another epicentre (n. 2 in Table 4.2) is located to the west of Drosh, not far from the KKSZ (Fig. 4.16). Its hypocentre was 97 km deep. The calculated principal stress axes reveal a subhorizontal, NW-SE directed s_1 and a subvertical s_3 in a compression tectonic regime (Fig. 4.15), which coincides with several of our calculated tensors (n. 7, 9, 10, 11, 12, 15, 16 in Fig. 4.4).
This implies that the N-S to NW-SE compression calculated from fault slip data along the KKSZ are reflected by recent seismicity in the area. Furthermore, the fact, that the majority of seismic events are deep earthquakes (>70 km), may

explain the weak correlation between seismic data representing subcrustal faulting and calculated tensors representing crustal faulting.

.

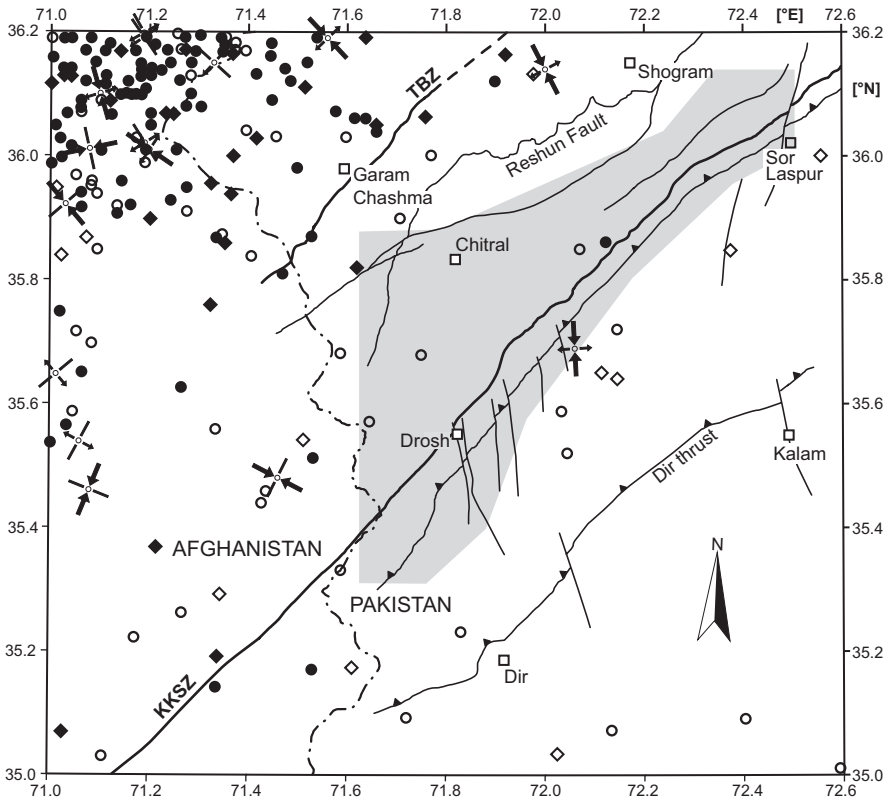

Fig. 4.16. *Earthquakes and major faults in the study area. Open circles: hypocentres at 0-33 km depth, open diamonds: 33-70 km, filled circles: 70-150 km, filled diamonds: 150-300 km; data from the NEIC database listed in Table 4.3. Open circles with horizontal principal stress axes inferred from P, B and T projection; inward and outward pointing arrows: maximum and minimum stress directions, respectively; bar: intermediate stress direction; data listed in Table 4.2. The shaded box marks the field area as shown in Fig. 4.2.*

Another set of stress data was compiled from the World Stress Map (release 2004) in a rectangle between the longitude 70°E and 82°E and latitude 30°N and 39°N (Fig. 4.17). No data were available close to our field area. NNE-SSW directed normal and thrust faulting predominates in northern Pakistan. In eastern Afghanistan (70-71°E, 34-35°N), NNW-SSE *Azhmax* directions predominate. These events are mainly deep earthquakes and thus do not necessarily reflect upper crustal faults.

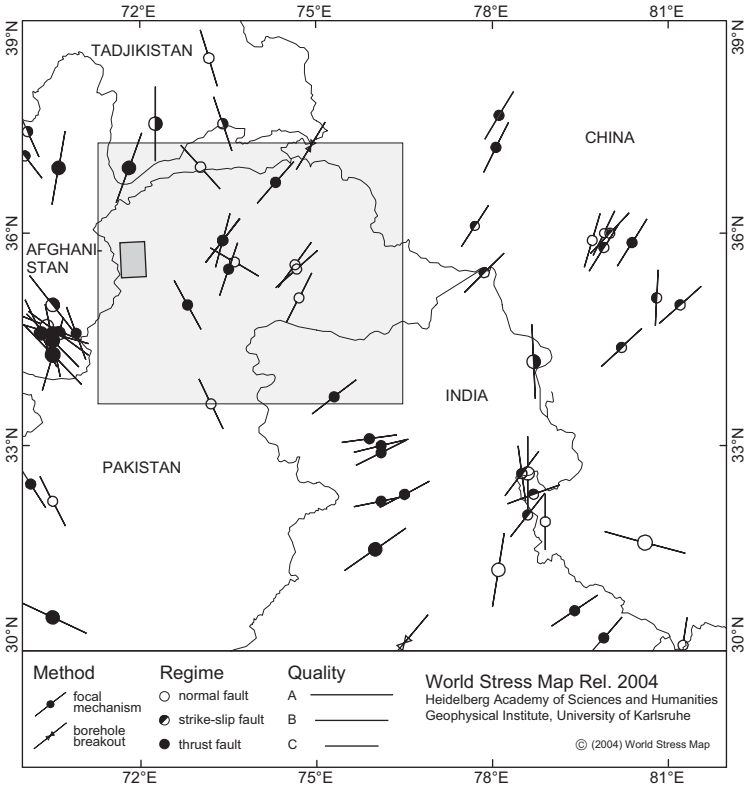

Fig. 4.17. *Recent stress field in northern Pakistan and adjacent countries (World stress map, release 2004, http://www-wsm.physik.uni-karlsruhe.de). The small, dark grey box marks the extent of study area as shown in Fig. 4.2; the large, light grey box corresponds to the extent of the figures 4.13/14.*

6. Discussion and conclusions

Fault slip analysis yielded two sets of paleostress regimes along the KKSZ. (1) a compression-wrench tectonic regime with a NW-SE to E-W compression direction and (2) an extension tectonic regime.
The set 1 is explained by brittle, sinistral transpression with strike-slip faulting and top-to-the-SE thrusting in the KKSZ (chapter 3). The set 2 may represent the same extension as recorded in the southeastern Kohistan, post-dating the N-S to NW-SE compression. But it may also represent local lateral collapse due to a likely oversteepened topography of overthrust suture units in the hanging wall of the KKSZ and thus does not necessarily reflect a regional stress regime contemporaneous with other (local?) extensions.
As fission track data (section 3.2.3) imply that no or only little vertical movement took place along the KKSZ since the early mid-Miocene (20-13 Ma), the sinistral transpression indicated by the set 1 tensors is either younger than 13 Ma and included only little vertical movement, or it is older than ca. 20 Ma.
However, the present day stress field in the NW Himalaya indicates (1) a crustal compression to wrench stress field with predominantely NW-SE, N-S and NE-SW directed compression directions, and (2) extension regimes with various extension directions. Thus, the stress tensors from the KKSZ could be more or less explained by that recent stress field.

Chapter 5: Age and isotopic constraints on magmatism along the Karakoram-Kohistan Suture Zone

1. Introduction

Detailed geological mapping was combined with high-precision U-Pb dating on zircons to constrain the timing of magmatism and associated deformation phases, related to the Karakoram-Kohistan convergence and collision. Ar-Ar dating on hornblende was performed on three samples in which zircons were absent or did not yield clear concordant ages. Initial hafnium isotope ratios were measured on the dated zircons to constrain the type of melt source of the dated plutonites.
The samples were taken along major valleys and roads in the Drosh-Shishi area in southern Chitral (Fig. 5.1) and sample locations were specified by GPS measurements (Tables 5.1 and 5.2).

2. Methods

Samples were collected from magmatic rocks for U-Pb dating in order to constrain intrusion ages. Petrographic and structural descriptions of these samples are given in chapter 3. Analytical procedures that were used include isotope dilution thermal ionisation mass spectrometry (ID-TIMS, details in appendix). The U-Pb data are given as weighted mean $^{206}Pb/^{238}U$ ages and are summarised in Table 5.1 and illustrated in the concordia plots in the Figs. 5.2 to 5.10 (errors are shown at the 2σ level). The framed numbers in the concordia plots correspond to analysis numbers in the Tables 5.1 and 5.2. Additional Ar-Ar dating on magmatic hornblende was performed on the *basaltic sill* (Fig. 5.11) and the *meta-gabbro* (Fig. 5.13) to corroborate their U-Pb age. A *quartz monzodiorite* was dated only by the Ar-Ar step heating technique because of the lack of zircon (Fig. 5.12). The Ar-Ar data are listed in Table 5.3 and technical details described in the appendix. Hafnium isotopic compositions were determined from the same zircon microfractions as those used for the U-Pb dating (Table 5.2).

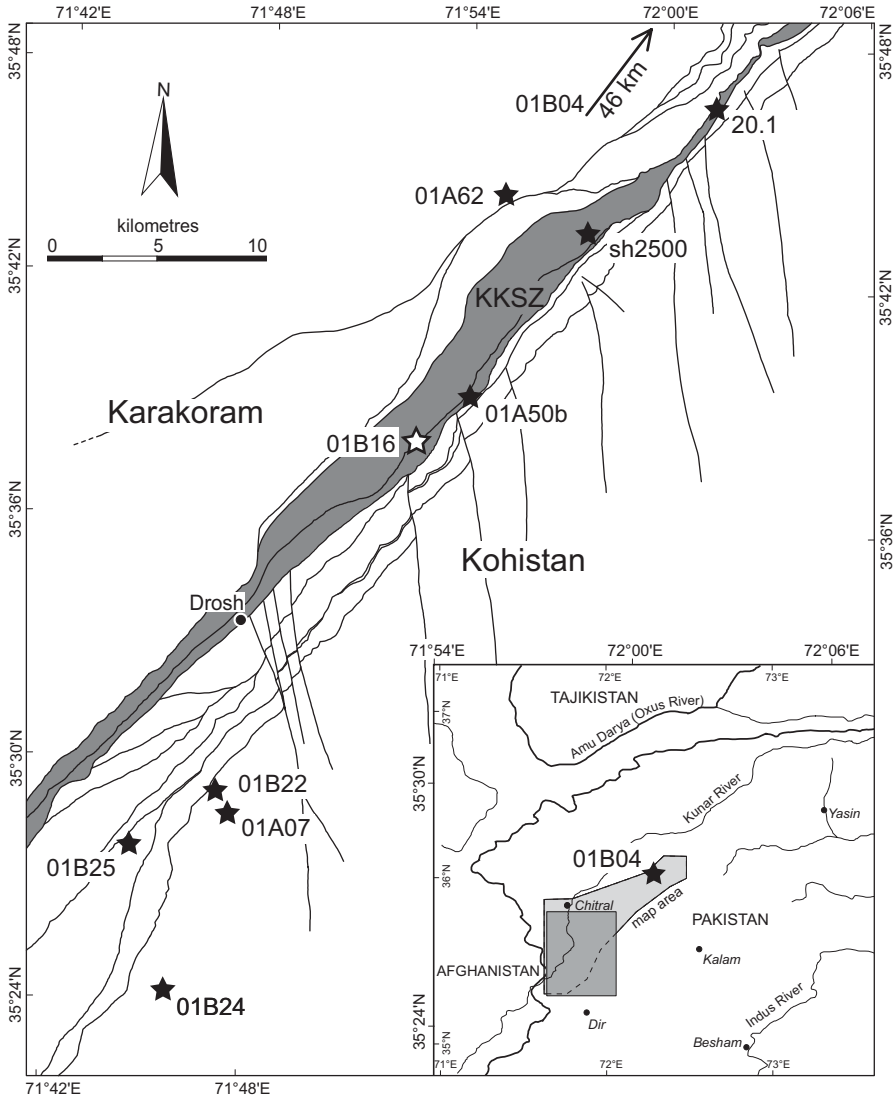

Fig. 5.1. *Structural sketch map of the Karakoram-Kohistan Suture Zone (KKSZ, shaded) in the Drosh area. Stars mark locations for the samples dated with the U-Pb method. The white star marks the site of the Ar-Ar sample. The light grey polygon inset represents the map area; the darker grey box covers the outline of this figure.*

3. Isotope results

The U-Pb dating results are first described, and complemented by the Ar-Ar results. The samples are described from northwest to southeast and separated into the three tectonostratigraphic units defined in chapter 3: Karakoram, Suture and Kohistan.

3.1 U-Pb ages

3.1.1 Karakoram intrusions

Phargam granite (01B04)
The *Phargam granite* intruded *slates and quartzites* and other volcanosedimentary sequences in the upper Golen Gol 14 km west of Sor Laspur. It forms an isolated, undeformed pluton that is 10 km in diametre and is located 3-5 km to the northeast of the KKSZ. It is younger than the deformation of the Karakoram volcanosedimentary sequences as it crosscuts their deformation structures.
The granite sample was taken northeast of the Phargam An, the Pass connecting the Golen with Phargam Gol. It displays a magmatic, undeformed and porphyric texture. Magmatic minerals are K-feldspar, plagioclase, quartz, biotite ± sphene. Alteration products are muscovite, chlorite and epidote. Accessory minerals are zircon, apatite and unspecified ores. Cathodoluminescence (CL) images on zircons reveal undisturbed oscillatory zoning patterns (Fig. 5.2a).
Four microfractions and two single grains were analysed (Table 5.1, Fig. 5.2b). Three zircon microfractions yielded $^{206}Pb/^{238}U$ ages between 103.5 and 104.0 Ma (numbers (n.) 1, 3 and 6 in Table 5.1). The analyses n. 1 and 3 are concordant whereas microfraction n. 6 displays slightly higher $^{207}Pb/^{235}U$ ratios probably due to insignificant lead loss combined with inheritance. Analysis number 3 represents a single zircon with low U (55 ppm) and radiogenic Pb (1.01 ppm) concentrations, resulting in an enhanced $^{207}Pb/^{235}U$ uncertainty. The three other microfractions (n. 2, 4, 5) yielded $^{206}Pb/^{238}U$ ages between 132 and 634 Ma and were used to calculate upper intercept ages. Three upper intercept ages were calculated by combining the analyses (a) n. 1, 3, 5 and 6 (725±39 Ma), (b) n. 1, 2, 3 and 6 (1028±180 Ma) and (c) n. 1, 3, 4 and 6 (1620±6 Ma).
The mean $^{206}Pb/^{238}U$ age calculated from zircon analyses n. 1, 3 and 6 is 103.79±0.27 Ma (Fig. 5.2b) and is interpreted as intrusion age of the *Phargam granite*. The other microfractions with Proterozoic upper intercept ages are

due to inherited zircons or to inherited old (Proterozoic) cores within the 104 Ma zircons.

a)

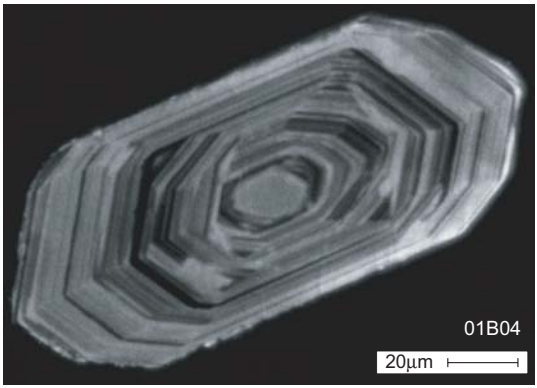

b)

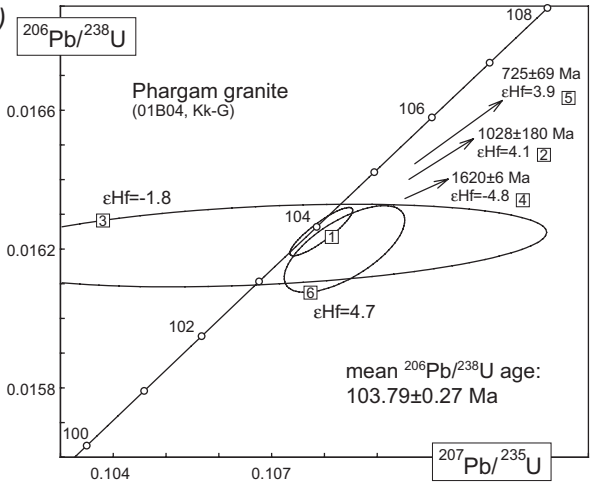

Fig. 5.2. *U-Pb zircon results of the Phargam granite (01B04). (**a**) cathodoluminescence (CL) image of a representative, non-abraded zircon. (**b**) concordia diagram with ellipses showing the analytical uncertainty at the 2 sigma level of the individual analyses.*

Meta-dioritic amphibolite (01A62)

The 75 km long Karakoram *sheared gabbros and diorites* unit is mainly composed of sheared meta-gabbros and -diorites with minor quartzo-feldspathic migmatites, meta-granitic dykes and hornblendites. The *gabbros and diorites* intruded (Fig. 3.20a in chapter 3) Karakoram volcanosedimentary sequences and display an increasing strain southeastwards, towards the suture (chapter 3). As we related this strain gradient to the suturing and/or post-suturing deformation between the Kohistan island arc and the Karakoram margin, the intrusion age of this sample sets a maximum age of that deformation phase(s).

The *meta-dioritic amphibolite* sample was taken from the southeasternmost outcrop of this unit in the Kalas Gol, 1.5 km northwest of the suture zone. The

rock is strongly foliated, but the magmatic texture is locally preserved. Magmatic minerals are represented by magnesiohornblende, biotite, sphene, illmenite ± quartz. The metamorphic paragenesis is made of plagioclase, hornblende, epidote, chlorite, actinolite ± garnet. Accessory minerals are brown spinel, zircon and apatite.
The analysed sample weighted 0.7 kg and yielded only 25 zircons. 5 of them were selected for CL analysis but were lost during the procedure. Under the binocular, we selected for further analyses, small, idiomorphic zircons containing local melt-inclusions of likely magmatic origin. Therefore we assume the zircons to be magmatic.
Three zircon microfractions (n. 7, 8 and 9) containing 2 to 3 grains were analysed (Table 5.1, Fig. 5.3). The $^{206}Pb/^{238}U$ ages range between 105.1 and 105.4 Ma. The microfraction n. 7 is concordant whereas n. 8 and 9 display slightly higher $^{207}Pb/^{235}U$ ratios.
The intrusion age of this *meta-dioritic amphibolite* is represented by the mean $^{206}Pb/^{238}U$ age yielding 105.20±0.29 Ma (Fig. 5.3).

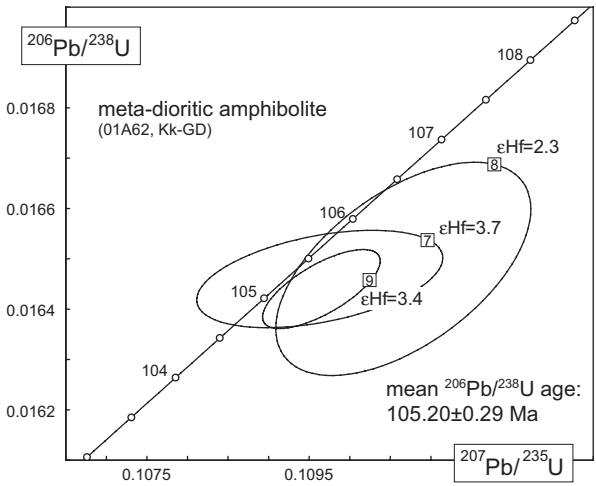

***Fig. 5.3**. U-Pb zircon results of the meta-dioritic amphibolite (01A62). Concordia diagram with ellipses showing the analytical uncertainty at the 2 sigma level of the individual analyses.*

3.1.2 Suture intrusions

Quartz diorite (sh2500)
This mainly undeformed, isolated body intruded *volcanoclastic and calcareous sequences* in the Domuk Gol, but is faulted against *serpentinites and talcschists* along its northern boundary. The magmatic texture of this medium-grained rock is preserved in the core of the body. Flattened mafic xenoliths and subvertically oriented hornblende crystals define a weak, probably magmatic fabric.

The sample was taken 500 m upstream in the Domuk Gol. Magmatic minerals are plagioclase, hornblende, quartz, biotite and sphene. Alteration products are muscovite, epidote ± chlorite.
Zircons display undisturbed growth textures on CL images (Fig. 5.4a) and thus are magmatic. Three zircon microfractions containing 2 to 3 grains were analysed (Table 5.1, Fig. 5.4b). The $^{206}Pb/^{238}U$ ages range between 106.7 and 107.2 Ma. The microfraction n. 12 is concordant whereas n. 10 displays slightly higher $^{206}Pb/^{238}U$ and $^{207}Pb/^{235}U$ ratios, but also larger 2σ errors. Microfraction n. 11 lies slightly to the left of the concordia, thus having a smaller $^{207}Pb/^{235}U$, but identical $^{206}Pb/^{238}U$ ratio than the concordant microfraction. This is considered to be an artefact of common lead correction, since the Stacey & Kramers (1975) values are too radiogenic for a continental arc setting.
The intrusion age of this *quartz diorite* is inferred from all the three microfractions yielding an average $^{206}Pb/^{238}U$ age of 106.95±0.97 Ma (Fig. 5.4b).

a)

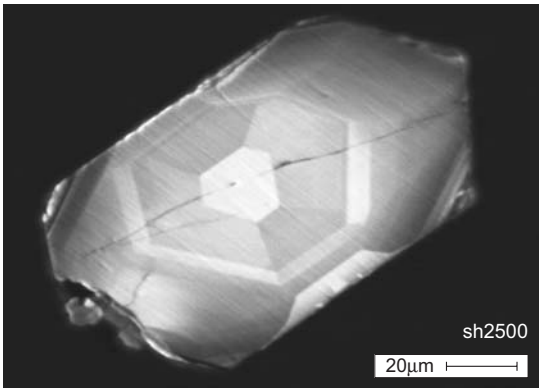

b)

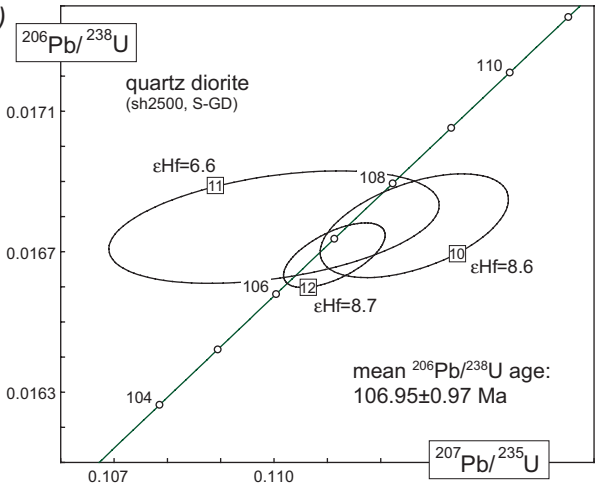

Fig. 5.4. *U-Pb zircon results of the quartz diorite (sh2500). (**a**) cathodoluminescence (CL) image of a representative, non-abraded zircon. (**b**) concordia diagram with ellipses showing the analytical uncertainty at the 2 sigma level of the individual analyses.*

Granitic dyke (01A50b)

A *quartz diorite* body pertaining to the Suture *gabbros and diorites* unit (chapter 3) was intruded by a *granitic dyke,* 1.5 km north of Gawuch. The host *quartz diorite* intruded calcareous turbidites represented today as a thrust wedge of *hornfelses* within the *serpentinites and talcschists* (Fig. 3.8a in chapter 3). The granite was sampled 1.7 km N of the village Gawuch, 350 m above (NW) the Shishi Gol jeep road.

Quartz, hornblende, plagioclase ± pyroxene ± biotite are the magmatic minerals. Plagioclase is strongly altered to muscovite and chlorite. Accessory minerals are unspecified ores and zircon. Zircons display undisturbed oscillatory patterns, with local sector zoning patterns on CL images (Fig. 5.5a).

a)

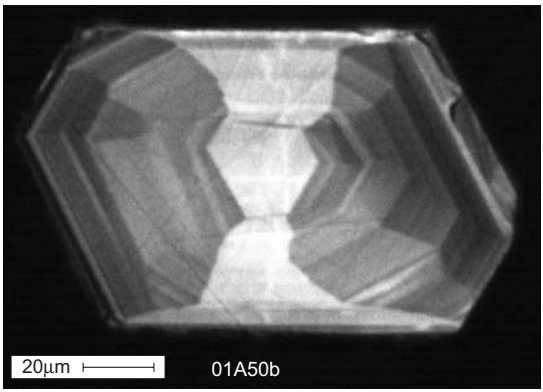

b)

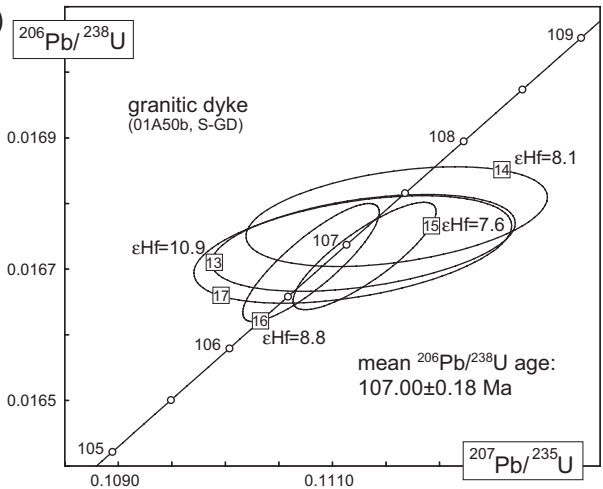

Fig. 5.5*. U-Pb zircon results of the granitic dyke (01A50b).* (***a***) *cathodoluminescence (CL) image of a representative, non-abraded zircon.* (***b***) *concordia diagram with ellipses showing the analytical uncertainty at the 2 sigma level of the individual analyses.*

Thus, they are magmatic in origin and their age represents the time of intrusion of the rock. Five zircon microfractions with 2 to 4 zircons were analysed (Table

5.1, Fig. 5.5b) all of which are lying on the concordia curve. The $^{206}Pb/^{238}U$ ages vary little between 106.8 and 107.3 Ma.
Therefore, this *granitic dyke* yielded a very well constrained mean $^{206}Pb/^{238}U$ intrusion age of 107.00±0.18 Ma (Fig. 5.5b).

Basaltic sill (20.1)
An undeformed, altered *basaltic sill* crosscuts imbricate *serpentinites and talcschists* in the Chhuchhu Gol 1 km southwest of Madaglasht (Fig. 3.7b in chapter 3). Its age therefore is a minimum age of the deformation in the serpentinites (meta-harzburgites). But it is not clear whether this sill also crosscuts faults separating the imbricate serpentinites from other suture units, and thus the sill does not give an age constraint on the suturing-related brittle imbrication.

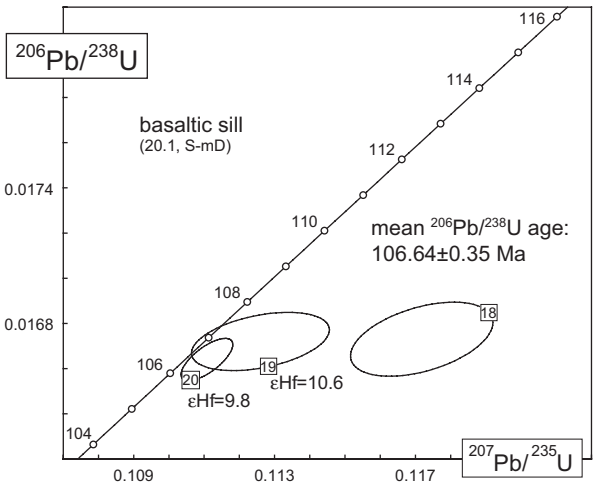

Fig. 5.6. *Concordia diagram with age determinations for the basaltic sill (20.1). Ellipses show the analytical uncertainty at the 2 sigma level of the individual analyses.*

The small (0.85 kg) sample was taken at the entrance of the Chhuchhu Gol just N of the Shishi Gol jeep road.
The magmatic paragenesis is represented by brown ± green amphibole, sphene and hematite. Greenschists facies alteration products are calcite, chlorite, epidote, muscovite, albite and actinolite. Accessory minerals are zircon, apatite and unspecified ores. The sample yielded 12 zircons, nine of which were grouped into three analytical fractions containing 1 to 5 zircons. The three zircons left were not used for further analyses because they were broken and had a brown colour (indicating possible Pb loss) or contained inclusions. The zircons were not abraded and not prepared for cathodoluminescence imaging to avoid any loss of material during the procedure.
We assume the zircons to be magmatic because there is no high-grade (>amphibolite facies), post-crystallisation metamorphic event recorded in the mineral paragenesis. However, fluid alteration is indicated by the greenschists

facies alteration products with the abundance of post-magmatic Ca-phases (chapter 3) and therefore recrystallisation at the rim of the zircons cannot definitely be ruled out.
The three analyses lie slightly to moderately to the right of the concordia line (Table 5.1, Fig. 5.6). The $^{207}Pb/^{235}U$ discontinuity may be explained by a deviation of the common lead from the accepted model (Stacey & Kramers 1975) value or possibly point to unsupported ^{207}Pb due to ^{231}Pa excess (Anczkiewicz *et al.* 2001). There is no indication for a mixing age due to a younger, post-crystallisation event. Thus the zircons give the intrusion age of the sill, a mean $^{206}Pb/^{238}U$ age of 106.64±0.35 Ma (Fig. 5.6).

3.1.3 Kohistan intrusions

Mirkhani diorite (01B25)
This undeformed, altered diorite intruded basaltic to andesitic lavas (*Drosh volcanites*) and shallow water, Aptian (125-112 Ma) limestones (*Drosh limestones*) and is faulted against the *Gawuch greenschists and marbles* 10 km southwest of Drosh.
The sample was taken on the Chitral-Lowari Pass road, 1 km SW of the Mirkhani junction. Plagioclase, K-feldspar, quartz, hornblende ± sphene represent the magmatic minerals. Alteration products are epidote, biotite and chlorite. Cathodoluminescence images show euhedral zircons with undisturbed oscillatory zoning patterns (Fig. 5.7a) indicating that the zircons are magmatic. Two white to grey, homogeneous zones (marked with a star on Fig. 5.7a) may represent recrystallised domains. Slightly corroded rims may be explained by the strong alteration of the sample.
From five zircon analyses, containing 1 to 3 grains (Table 5.1ff, Fig. 5.7b), four microfractions are concordant and one (n. 24) lies to the left of the concordia curve. This microfraction has considerably lower $^{207}Pb/^{235}U$ and $^{207}Pb/^{206}Pb$ ratios but an identical $^{206}Pb/^{238}U$ ratio. This is not considered to be an artefact of the correction of slightly elevated common lead (3.1 pg) because the microfraction 25 contains more common lead (4.0 pg) but is concordant. It may rather be explained by possible low intensities during mass spectrometry.
The diorite yielded a mean $^{206}Pb/^{238}U$ intrusion age of 111.52±0.40 Ma (Fig. 5.7b) consistent with the older, Aptian (125-112 Ma) age of the host *Drosh volcanites and limestones*.

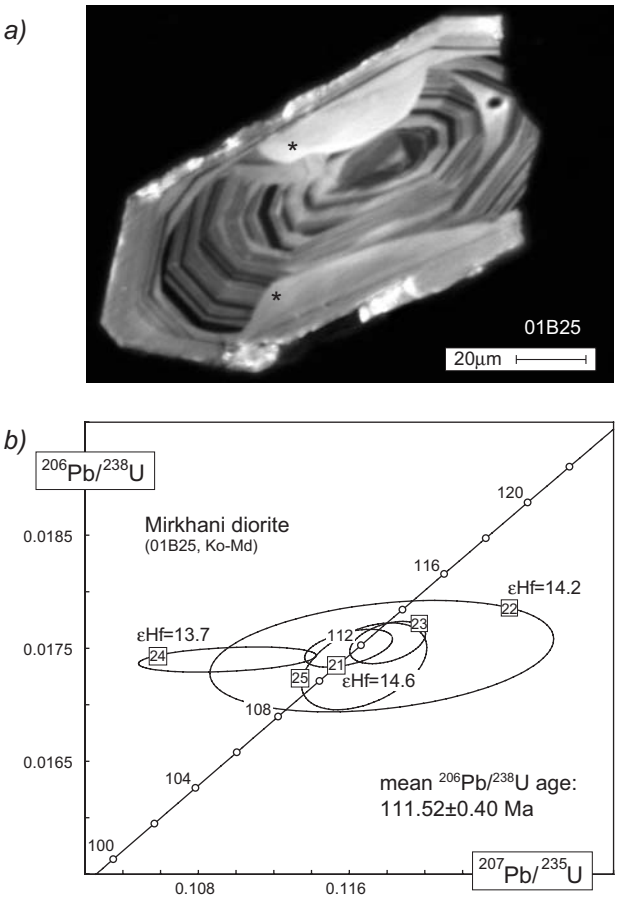

Fig. 5.7. *U-Pb zircon results of the Mirkhani diorite (01B25). (**a**) cathodoluminescence (CL) image of a representative, non-abraded zircon. (**b**) concordia diagram with ellipses showing the analytical uncertainty at the 2 sigma level of the individual analyses.*

Meta-gabbro (01B24)

Gabbros and -diorites are intrusive in mafic volcanites and volcanoclastites of the *Gawuch meta-basalts*. They are strongly deformed along shear zones with gradients from almost undeformed to ultramylonitic gabbro (Fig. 3.14a in chapter 3).

The sampled, amphibolite facies *meta-gabbro* was taken from a weakly foliated *meta-gabbro*, 17 km south of Drosh on the Chitral-Lowari Pass road. It contains magmatic tschermakite, biotite, plagioclase, illmenite, sphene ± pyroxene. The metamorphic paragenesis is represented by plagioclase, biotite ± garnet ± actinolite ± chlorite ± epidote. Zircons show either a faint, oscillatory zoning on cathodoluminescence images (Fig. 5.8a) or sector zoning combined with planar, oscillatory zoning (Fig. 5.8b); both indicate that zircons are magmatic. Thin and discordant high luminescence rims (which should have been removed by abrasion prior to analysis) represent discordant

overgrowth that may reflect recrystallisation or growth of new zircon during a post-magmatic event.
Four zircon microfractions containing 3 to 5 grains were analysed (Table 5.1, Fig. 5.8c). Two microfractions are concordant at 44.18±0.09 (n. 26) and 49.80±0.15 Ma (n. 28, $^{206}Pb/^{238}U$ ages). The two other microfractions lie on a discordia line probably together with the 44.18 Ma fraction. These three microfractions yield a lower intercept age of 44.1±8.2 Ma and an upper intercept age of ca. 409 Ma. As the lowest of these three points is concordant (at 44.18 Ma), it is appropriate to derive the lower age only from that microfraction. Possible reasons for the discordance may be lead loss and/or new zircon growth at the rims of the original zircons after intrusion (combined with a possible insufficient mechanical abrasion).

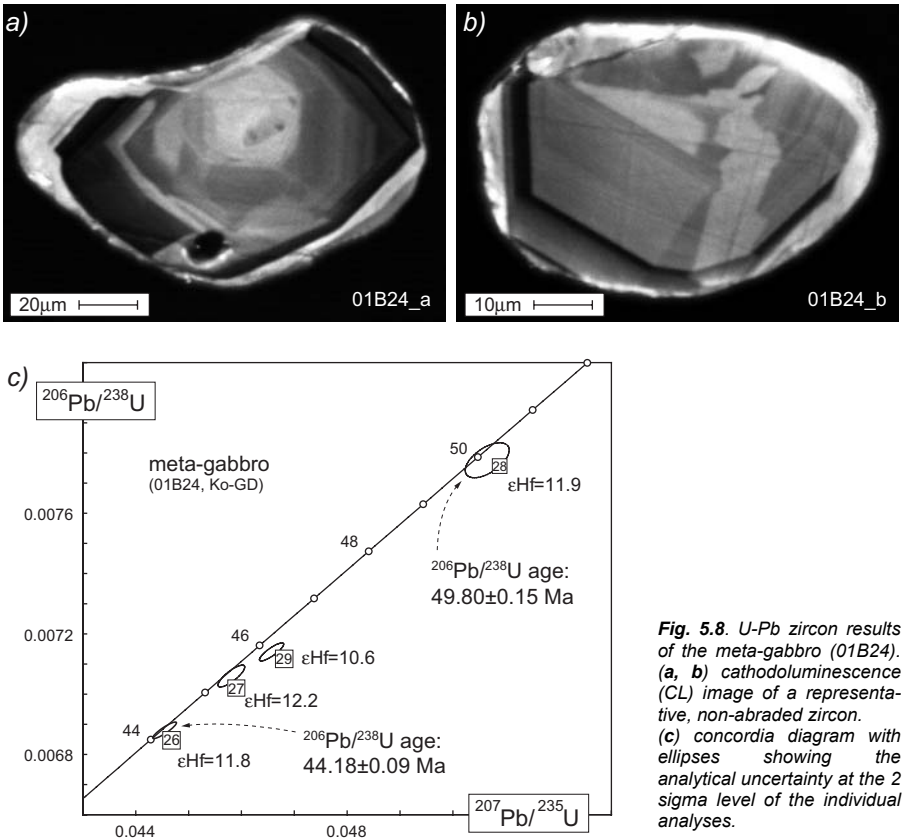

***Fig. 5.8**. U-Pb zircon results of the meta-gabbro (01B24). (**a, b**) cathodoluminescence (CL) image of a representative, non-abraded zircon. (**c**) concordia diagram with ellipses showing the analytical uncertainty at the 2 sigma level of the individual analyses.*

The intrusion age of this *meta-gabbro* is inferred from the concordant fraction at 49.80±0.15 Ma ($^{206}Pb/^{238}U$ age, Fig. 5.8c). The youngest age is interpreted as a postcrystallisation metamorphic event at 44.18±0.09 Ma ($^{206}Pb/^{238}U$). The two ages of analyses (n. 27 and 29) between the concordant points are

interpreted as mixing ages of the magmatic, 49.8 Ma zircons with younger, 44.2 Ma metamorphic zircon on the rim of the magmatic ones.

Granitic dyke (01B22)

The *meta-gabbros and -diorites* are intruded by *granitic dykes*. The sampled *granitic dyke* is folded and foliated like the host *meta-gabbro* (chapter 3).

It was taken on the Beorai Gol jeep road 8 km south of Drosh. Magmatic minerals are quartz, K-feldspar, plagioclase and biotite; the metamorphic paragenesis is represented by chlorite ± garnet ± muscovite. Zircons show polyphase growth, replacement and recrystallisation textures on cathodoluminescence images (Fig. 5.9a) as well inherited zircon cores (Fig. 5.9b, arrow), indicating a magmatic origin.

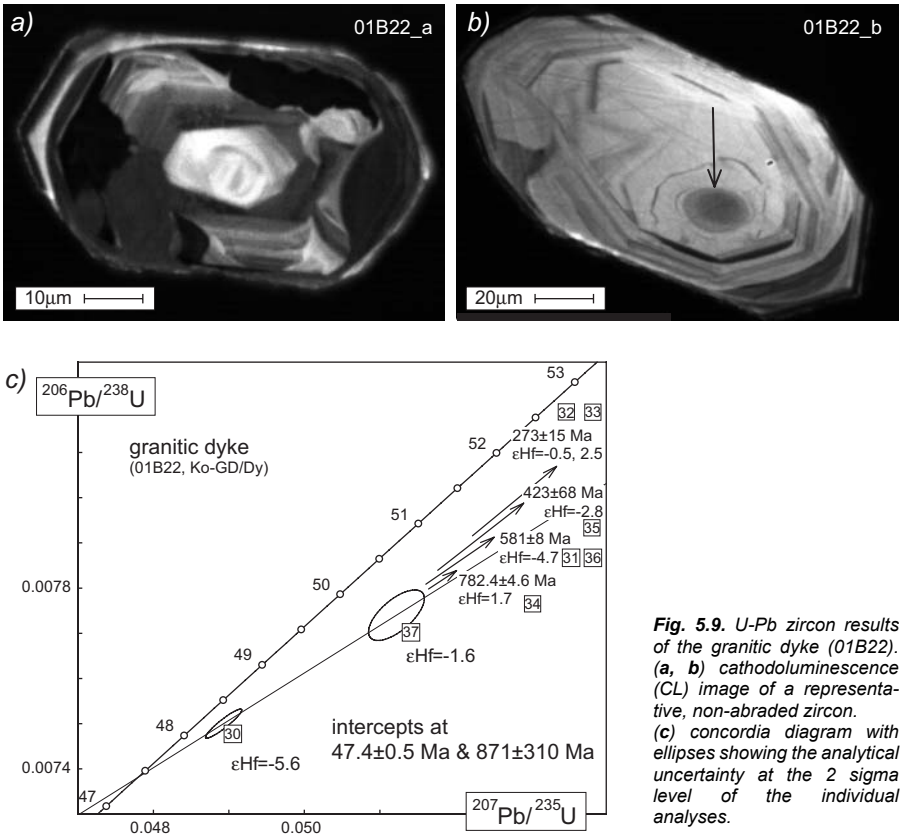

Fig. 5.9. *U-Pb zircon results of the granitic dyke (01B22).* ***(a, b)*** *cathodoluminescence (CL) image of a representative, non-abraded zircon.* ***(c)*** *concordia diagram with ellipses showing the analytical uncertainty at the 2 sigma level of the individual analyses.*

The eight analysed zircon microfractions, containing 2 to 5 grains, are discordant (Table 5.1, Fig. 5.9c). They yielded $^{206}Pb/^{238}U$ ages between 48 and 198 Ma and were used to calculate a series of upper intercept ages. Combining the microfractions n. 30, 32, 33 and 37 (model-2 fit) yielded 273±15

Ma; 30, 35 and 37 (model-2 fit) yielded 423±68 Ma; n. 30, 31 and 37 (model-2 fit) yielded 581±34 Ma and the microfractions n. 30 and 34 (model-1 fit) yielded 782±4.6 Ma. The two youngest microfractions (n. 30 and 37) yield a lower intercept at 47.4±0.5 Ma and an upper intercept age at 871±310 Ma (Fig. 5.9c).
This discordance can be explained by inheritance of Paleo- and Proterozoic zircon cores of different age within the Eocene zircons. Accordingly, the lower intercept age of 47.4±0.5 Ma is interpreted as intrusion age of this *granitic dyke*.

Granitic dyke (01A07)
This *granitic dyke* is undeformed and intrudes the *meta-gabbros and -diorites*. The sample was taken one kilometre south of the granite sample 01B22. It comprises magmatic quartz, microcline, plagioclase ± biotite ± sphene and muscovite as alteration product.

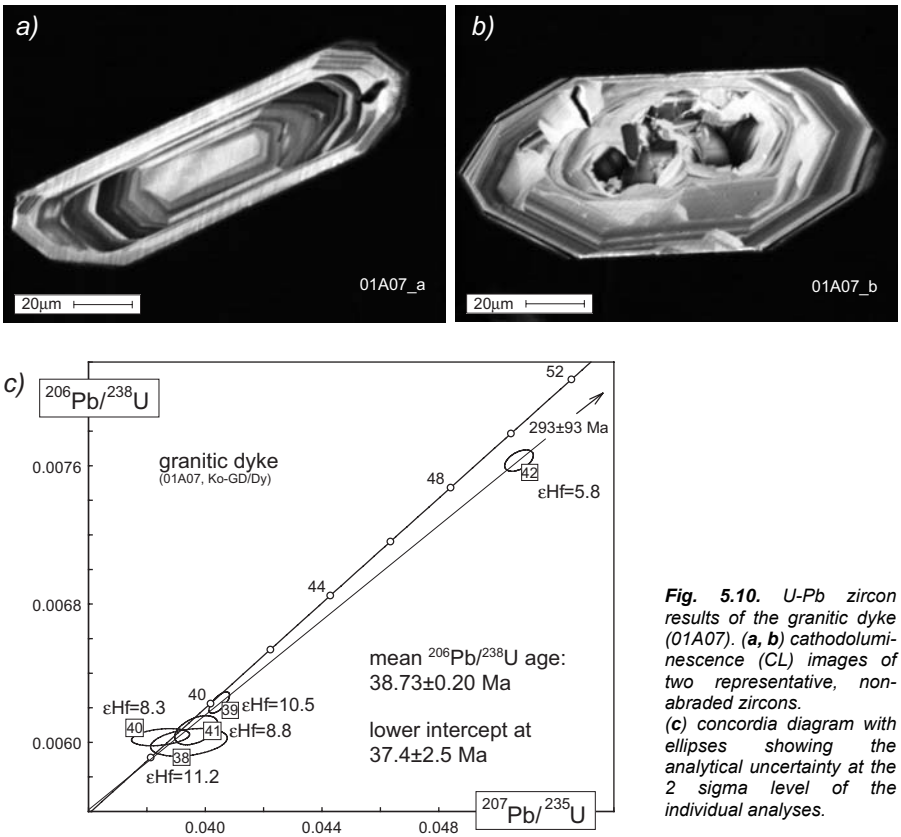

Fig. 5.10. *U-Pb zircon results of the granitic dyke (01A07). (**a, b**) cathodoluminescence (CL) images of two representative, non-abraded zircons.*
*(**c**) concordia diagram with ellipses showing the analytical uncertainty at the 2 sigma level of the individual analyses.*

Cathodoluminescence image of zircons display undisturbed, oscillatory zoning patterns (Fig. 5.10a) as well as polyphase textures in the core with quite undisturbed zoning pattern at the margins (Fig. 5.10b).
Five zircon microfractions with 2 to 4 grains were analysed (Table 5.1ff, Fig. 5.10c). Four microfractions yielded $^{206}Pb/^{238}U$ ages between 38.5 and 40.0 Ma whereas one microfraction (n. 42) was dated at 49.0 Ma ($^{206}Pb/^{238}U$ age). Intercept ages were calculated from all the microfractions yielding an upper intercept at 293±93 Ma and a lower intercept at 37.4±2.5 Ma.
A mean $^{206}Pb/^{238}U$ age of 38.73±0.20 Ma was obtained from three youngest microfractions (n. 30. 40 and 41) and is interpreted as maximum intrusion age since the points may still be biased by inheritance, despite their concordancy.

3.2 Ar-Ar ages

Basaltic sill (20.1)

As the 106.64±0.35 Ma *basaltic sill* yielded only 12 zircons and to exclude the possibility of cross-contamination by zircons of another sample during sample preparation, Ar-Ar dating was made to constrain the U-Pb results on zircon. Brown magmatic and green euhedral amphiboles occur as phenocrysts (Fig. 3.6d in chapter 3). The green amphiboles locally grew along the rims of the brown ones and are altered to calcite, muscovite and epidote. The matrix of the rock consists of brown, smaller grained amphiboles and mainly alteration products. The hand-picked amphiboles should mainly represent the brown, likely magmatic phase. However, alteration products occur mainly at/in all the separated amphibole grains and could not entirely be removed during hand picking.

The $^{39}Ar/^{40}Ar$ age data (Fig. 5.11) allows a straightforward interpretation: the four steps with a Ca/K ratio of about 11.6 to 12.0 (step numbers 10 to 13, Fig. 5.11a, b) account for 62% of the total Ar release and were interpreted to represent the magmatic (brown) hornblende. The other steps represent actinolite and alteration products (e.g. chlorite) because of their disturbed Ar release pattern and scattering of the Ca/K ratios.

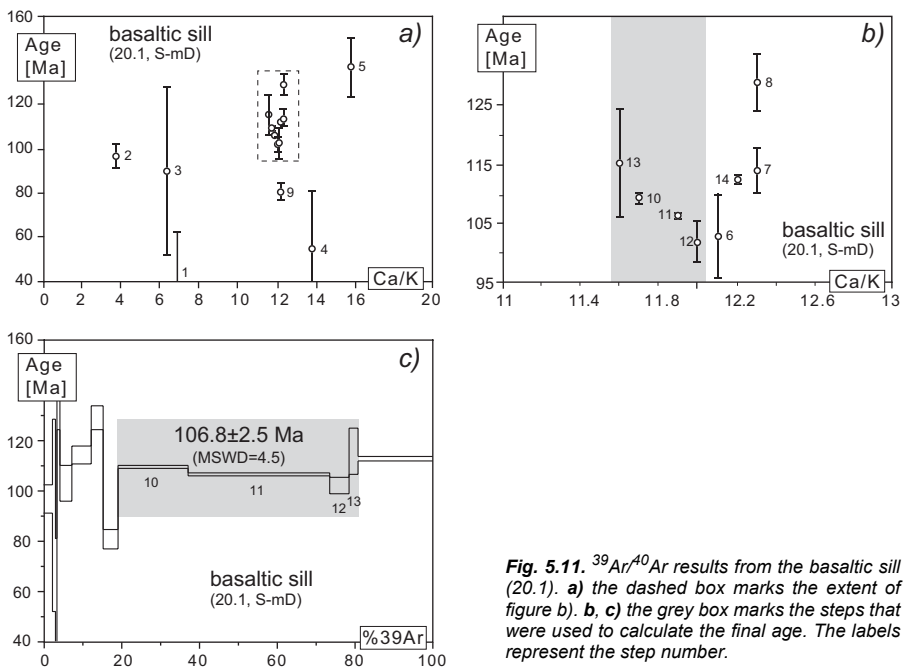

Fig. 5.11. *$^{39}Ar/^{40}Ar$ results from the basaltic sill (20.1).* ***a)*** *the dashed box marks the extent of figure b).* ***b***, ***c)*** *the grey box marks the steps that were used to calculate the final age. The labels represent the step number.*

A weighted mean age was calculated from these four steps at a 1 sigma level. The resulting age of 106.8±2.5 (2σ error) yielded an acceptable MSWD of 4.5 (Fig. 5.11c) and confirms the 106.64±0.35 Ma U-Pb zircon age.

Quartz monzodiorite (01B16)

An undeformed lens of meta-harzburgitic serpentinite was intruded by a *quartz monzodiorite* in the Tar Gol (Fig. 3.7c in chapter 3). Magmatic minerals are magnesiohastingsite, illmenite, plagioclase, quartz, probably garnet and accessory apatite. No zircon could be separated from this 24 kg sample. The rock is strongly altered to fine-grained unspecified feldspar, epidote, sphene and chlorite. The core of the magnesiohastingsite locally contains a different, dark green amphibole. The separated amphibole fraction therefore does not represent a 'pure' amphibole, but contains a significant amount of alteration products (e.g. chlorite, feldspar, sphene) and a local (different?) core that could not be removed during separation and hand picking.

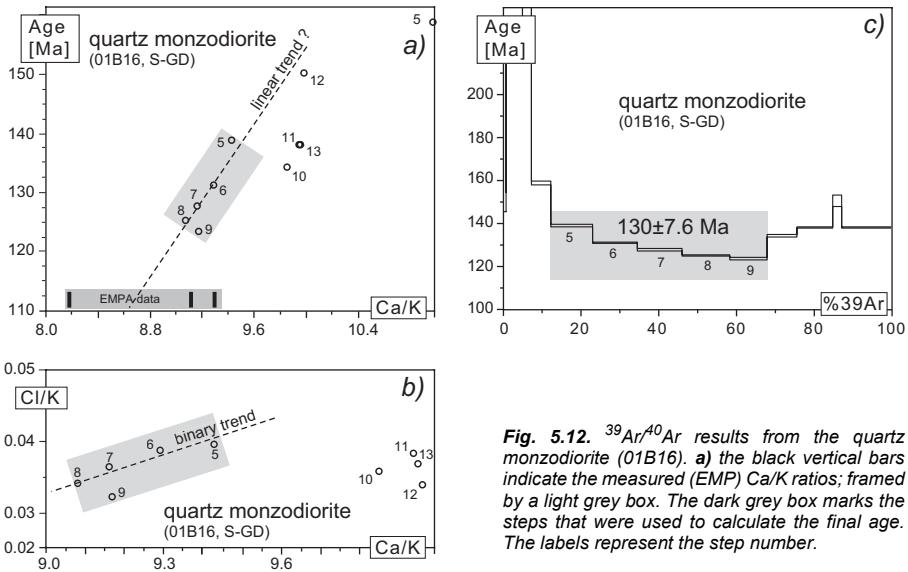

Fig. 5.12. *$^{39}Ar/^{40}Ar$ results from the quartz monzodiorite (01B16).* ***a)*** *the black vertical bars indicate the measured (EMP) Ca/K ratios; framed by a light grey box. The dark grey box marks the steps that were used to calculate the final age. The labels represent the step number.*

The $^{39}Ar/^{40}Ar$ age data is shown in Fig. 5.12. The step numbers 5 to 9 and 12 seem to define a linear trend on the age-Ca/K plot (Fig. 5.12a). This trend is confirmed by a linear relationship of Cl and Ca in the steps 5 to 9 (Fig. 5.12b). The steps 10 to 14 seem to represent an alteration product, likely chlorite, and/ or actinolite (the 'green amphibole'). The first three steps account only for 7.6% of the total Ar release at temperatures below 931°C and therefore are interpreted as representing mica and feldspar containing an excess Ar component. Three electron microprobe analyses (EMP) yielded Ca/K ratios of 8.19, 9.15 and 9.25. The measurement yielding 8.19 was measured in the

core of an euhedral magnesiohastingsite and therefore may be interpreted to represent the primary magmatic phase.
The two other measurements were done at the rims of such a mineral grain. In this respect, steps 5 to 9, having the lowest Ca/K ratios, are regarded to represent the magmatic phase best. A weighted mean age was calculated from these three steps yielding 130±7.6 Ma (Fig. 5.12c). We interpret this age as a maximum age, as it is influenced by excess Ar.
Considering the lowest obtained Ca/K ratio (=8.19) to be representative for the primarily magmatic hornblende, an Ar-Ar age of about 90 Ma would be inferred (intersection of 'trend' line with y-(age) axis in Fig. 5.12a). However, the three EMP measurements do not give a sufficient statistic amount of data and therefore remain to be confirmed.

Meta-gabbro (01B24)
The 49.80±0.15 Ma U-Pb age of the *meta-gabbro* (01B24) was inferred from only one, concordant zircon microfraction. To constrain this apparent intrusion age, Ar-Ar dating was done on tschermakitic hornblende. Metamorphic minerals such as biotite, actinolite, epidote and chlorite have locally overgrown the magmatic hornblende and could not completely be removed from the hornblende fraction.

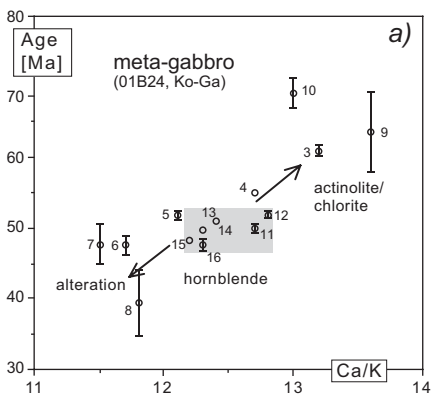

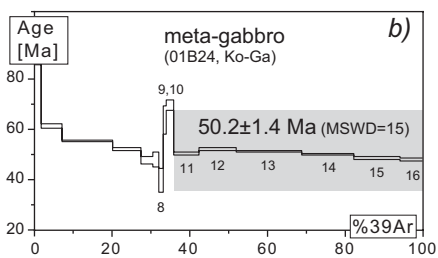

Fig. 5.13. *$^{39}Ar/^{40}Ar$ results from the meta-gabbro (01B24).* ***a)*** *arrows marks trends of increasing 'impurity' of hornblendes. The grey circle/box marks the steps that were used to calculate the final age. The labels represent the step number.*

The $^{39}Ar/^{40}Ar$ age data is shown in Fig. 5.13. The 'peak' in the ^{39}Ar-age spectra (Fig. 5.13b) is produced by the steps 8, 9 and 10. They degassed between 1023 and 1045°C and account together for only 3.7% of total Ar released and are therefore interpreted as actinolite or chlorite phases (high Ca/K; steps 9, 10) or other alteration products (step 5). Thus, all the steps to the left of that peak (degassing below 1023°C) do not seem to represent the primarily magmatic tschermakitic hornblende. Steps 11 to 16 have Ca/K ratios between 12.17 and 12.80, and their Ar spectra does not show a large variation (it is almost a plateau). Therefore these steps are interpreted to represent the magmatic, tschermakitic hornblende. A weighted mean age was calculated

from these three steps at a 1 sigma level yielding 50.2±1.4 Ma consistent with the inferred U-Pb age of 49.80±0.15 Ma. Furthermore, this age suggests that the three “discordant” microfractions reflect mixing ages of the 49.8 Ma age and a younger event at 44.2 Ma.

3.3 Hf isotopes

3.3.1 The Lu-Hf isotopic system

Terminology
The hafnium isotopic compositions were determined from the same zircon micro-fractions and single grains as those used for U-Pb dating (Table 5.2, analytical details in the appendix). The measured $^{176}Hf/^{177}Hf$ isotopic ratios (Table 5.2) were back-calculated to the time of zircon formation ($^{176}Hf/^{177}Hf$ (T) in Table 5.2) using $^{176}Hf/^{177}Hf = 0.005$. This calculation is required because zircon contains trace amounts of lutetium, and ^{176}Lu decays to ^{176}Hf with a half life of $35.7*10^9$ years. However, this correction is very minor because of the low Lu/Hf of zircon. Epsilon hafnium (εHf) represents the deviation (multiplied by 10,000) of the $^{176}Hf/^{177}Hf$ ratio from a chondritic uniform reservoir (CHUR), which is modelled from the composition of chondritic meteorites.

$$\varepsilon Hf = \frac{^{176}Hf/^{177}Hf - (^{176}Hf/^{177}Hf)_{CHUR}}{(^{176}Hf/^{177}Hf)_{CHUR}} \times 10^4$$

CHUR: **Ch**ondrite **u**niform **r**eservoir

εHf may be either positive or negative depending on the time-integrated Lu/Hf ratio of the melt from which the zircon crystallised. Values that are significantly positive (around +15 to +25, Patchett & Tatsumoto 1980, Nowell *et al.* 1998, Chauvel & Blichert-Toft 2001) suggest that the source rock(s) mainly reside in the Earth's mantle and experienced earlier periods of melt removal to form the oceanic and continental crust. Hafnium is concentrated in the melt relative to Lu during this process, yielding a residual mantle with relatively high Lu/Hf, known as the depleted mantle. On the other hand, significantly negative εHf values (around -10 to -20, Vervoort *et al*. 1996, Vervoort *et al.* 1999) indicate that pre-existing continental crust was involved in magma genesis.

Hafnium, a 'conservative' element?
The high field strength elements (HFSE) Nb, Ta, Zr, Hf and Ti, are considered to be the type example of a larger group of so-called 'conservative' elements (Pearce & Peate 1995) which are assumed to remain largely immobile during slab dehydration reactions. Thus, the HFSE provide an insight into the pre-subduction nature of the mantle-wedge, as they are believed to escape any influence from the subducting slab. The importance of the Lu-Hf decay scheme for mantle geochemistry results from the fact that during partial melting, hafnium is partitioned into the liquid phase much more strongly than rare earth elements (Erlank *et al.* 1978, rare earth elements (REE) are La, Ce,

Pr, Nd, Sm, Eu, Gd, Tb, Dy, Ho, Er, Tm, Yb, Lu, Y). Hf is distinct from Lu, Sm, Nd and Sr in that it is partitioned strongly into any available silicate liquid phase, more than Rb for example (Patchett & Tatsumoto 1980). Thus regions of mantle which have been depleted by partial melting during geologic times, like MORB sources, can show more $^{176}Hf/^{177}Hf$ variation than less depleted, pristine or enriched mantle, where Lu/Hf appears to be coherent with Sm/Nd and Rb/Sr (Patchett & Tatsumoto 1980).
However, it has been shown that hafnium, together with other HFSE, is not as 'conservative' in subduction zone settings as previously thought (Woodhead *et al.* 2001). It has been shown that sedimentary hafnium has contributed to arc lavas (Antilles and Sunda arcs, Woodhead *et al.* 2001). Furthermore, Woodhead *et al.* (2001) found that hafnium can be transferred from the subducting slab (Hf from oceanic crust or sediment load) to the mantle wedge, a behaviour that is not predicted from experimental studies on HFSE (Tatsumi *et al.* 1986).

3.3.2 Description of the isotopic results

The εHf data are summarised in Fig. 5.14 and plotted together with the corresponding ages versus their tectonic position (Karakoram, Suture or Kohistan).

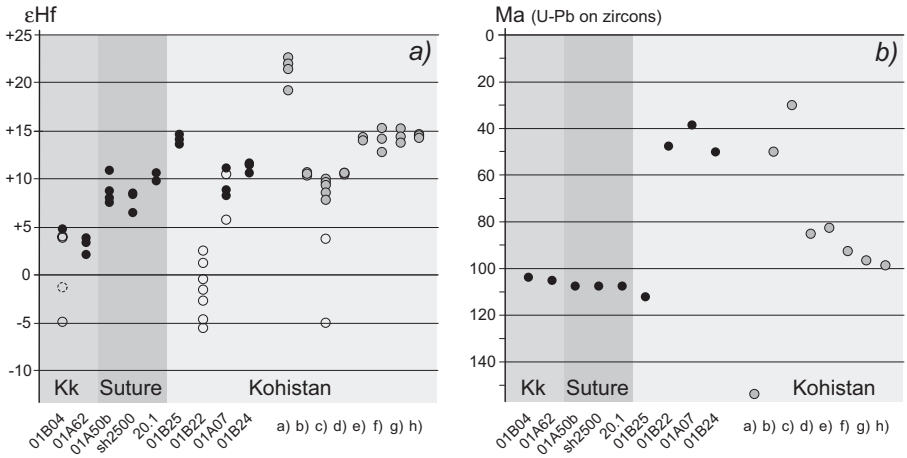

Fig. 5.14. *(**a**) Epsilon hafnium values and (**b**) U-Pb zircon ages vs. tectonic position (from N to S) of the nine samples (filled circles) from the KKSZ and the eastern and southeastern Kohistan (grey circles with black rim; **a**: Matum Das tonalite (Gilgit), **b**: diorite (Indus confluence), **c**: leucogranite (Indus confluence), **d**: Chilas gabbronorite (Swat Valley), **e**: kyanite-bearing dyke (Swat Valley), **f**: diorite, **g**: granite and **h**: Sarangar gabbro (f-h: from Pattan-Dasu area). a-c: Schaltegger et al. 2003/ data unpublished, d-h: Schaltegger et al. 2002. The open circles represent hafnium data from inherited zircons. The open dashed circle represents the analysis n. 3 of sample 01B04 that is interpreted as an analytical outlier.*

Karakoram intrusions
The 104 Ma *Phargam granite* (01B04) yielded εHf values of -1.8 and +4.7 measured on the concordant zircon microfraction (Fig. 5.2b). The negative value (-1.8) of the point n. 3 may be regarded as analytical outlier or to be due to a very unradiogenic component like n. 4 (below). The discordant $^{206}Pb/^{238}U$ ages of three microfractions with inheritance were assumed to calculate their hafnium ratios. The discordant point at 133 Ma (n. 2) yielded an εHf of +4.1, the 190 Ma (n. 5) an εHf of +3.9 and the 634 Ma point (n. 4) an εHf of -4.8 (Table 5.2). There is no correlation of the εHf values with the different degrees of inheritance suggesting that the different, polyphase zircons had different sources and/or contain cores with already different phases.
The 105 Ma *meta-dioritic amphibolite* (01A62) has εHf values of +2.3, +3.4 and +3.7 measured on the concordant microfractions yielding a mean εHf value of +3.0±1.6 (Fig. 5.3).
Both Karakoram samples have hafnium ratios between +2.3 and +4.7 (disregarding the -1.8 of sample 01B04). Similar values (-4.8 to +4.1) were obtained from the three inherited Proterozoic zircon microfractions of the *Phargam granite*.

Suture intrusions
The 107 Ma *quartz diorite* (sh2500) has εHf values of +6.6, +8.6 and +8.7 giving a mean value of +8.2±2.5 (Fig. 5.4b). Similarly, the 107 Ma *granitic dyke* (01A50b) yielded values of +7.6, +8.1, +8.8 and +10.9 with a mean of +8.9±2.3 (Fig. 5.5b); and the 107 Ma *basaltic sill* (20.1) values of +9.8 and +10.6 with a mean of 10.2±0.6 (Fig. 5.6). All these hafnium ratios were obtained from concordant zircon microfractions.

Kohistan intrusions
The 112 Ma Mirkhani diorite (01B25) yielded εHf values of +13.7, +14.2 and +14.6 with a mean εHf of +14.3±1.1 measured on three concordant microfractions (Fig. 5.7b).
The two concordant points (at 44 and 50 Ma) of the *meta-gabbro* (01B24) have εHf values of +11.8 and +11.9 respectively. The discordant $^{206}Pb/^{238}U$ ages (45 and 46 Ma) of two inherited microfractions (n. 27 and 29) were used to calculate their εHf's. They are insignificantly different from concordant points and yielded +12.1 and +10.5, respectively. This suggests that the hafnium isotopic system remained unaffected during the assumed metamorphic event between 50 and 44 Ma. The mean εHf value of all the four points is +11.6±1.1. εHf values of the inherited microfractions of the 47 Ma *granitic dyke* (01B22) were all calculated from the discordant $^{206}Pb/^{238}U$ ages. They are -5.6 (48 Ma, $^{206}Pb/^{238}U$ age of microfraction), -4.7 (192 Ma), -2.8 (164 Ma), -1.6 (50 Ma), -0.5 (198 Ma), +1.7 (169 Ma) and +2.5 (125 Ma). They vary strongly over the different degree of inheritance, and thus do not show a trend in time. However, the 48 Ma microfraction, very close to the inferred lower intercept intrusion age

of 47.4 Ma, yielded the most negative εHf value (-5.6) and is regarded as reflecting the hafnium composition best at the granite intrusion.
The 39 Ma *granitic dyke* (01A07) has εHf values of +8.3, +8.8 and +11.2 with a mean of +9.4±3.8 measured on the concordant microfractions. The discordant $^{206}Pb/^{238}U$ ages of the two inherited points were used to calculate their hafnium ratios. The 40 Ma ($^{206}Pb/^{238}U$ age) microfraction yielded an εHf of +10.5, the 49 Ma point +5.8. Thus, the 40 Ma point does not have a hafnium ratio distinct from the concordant points whereas the older, 49 Ma point has a significantly lower εHf value (+5.8) reflecting inherited zircons with a crustal hafnium signature.

3.3.3 Discussion and comparison with data from MORB and modern island arcs

In this paragraph, the hafnium isotopic data are discussed following the approach considering hafnium as a 'conservative' element, taking into account scenarios with possible hafnium mobility as described above (section 3.3.1).

Karakoram and suture zone
The εHf values of the six 112 to 104 Ma intrusions from the three distinct tectonic units (Karakoram, Suture, Kohistan) show an apparent increase from north to south (Fig. 5.15a).

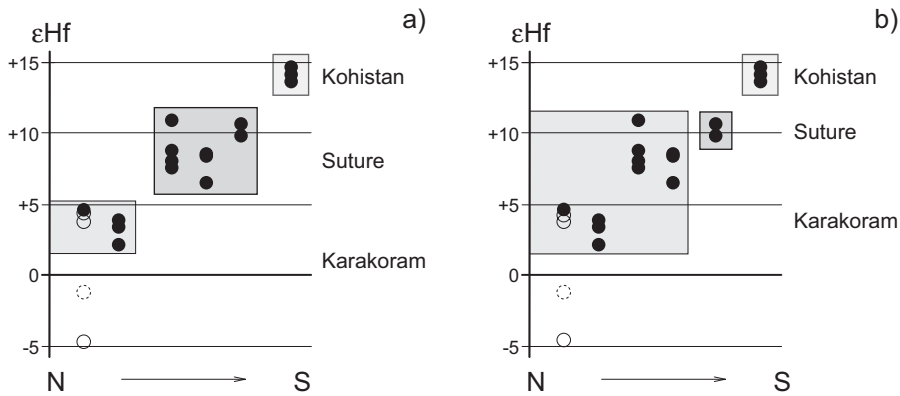

Fig. 5.15. *Epsilon hafnium values of the six 112 to 104 Ma intrusions in the Karakoram-Kohistan-Suture Zone. Sample numbers see Fig. 5.14 (the first six samples from the left).* ***a)*** *samples are grouped after their tectono-stratigraphic position.* ***b)*** *alternative presentation: samples are grouped after their inferred paleogeographic position of the host rocks. Accordingly, two suture zone intrusions that are part of an imbricate wedge of Karakoram rocks in the suture zone are attributed to the Karakoram. The (favoured) alternative representation (b) reveals that the Karakoram and the suture zone are isotopically not distinguishable with this data set. The Kohistan intrusion however, shows distinctly higher epsilon hafnium values than the Karakoram and the suture zone intrusions. Open and open dashed circles are like in Fig. 5.14.*

The 107 Ma *quartz diorite* and *granitic dyke* are tectonostratigraphically attributed to the suture zone, but they intruded Karakoram shelf-type volcano-sediments now imbricated in the suture. As suture-related deformation and imbrication is younger than 105 Ma (chapter 3), it is appropriate to reassign these two intrusions to the Karakoram. This makes the hafnium isotopic contrast between Karakoram and suture insignificant (Fig. 5.15b), but there still is a contrast between Karakoram and suture intrusions (εHf +2 to +11) and the northern Kohistan diorite (εHf +14).
The four 107 to 104 Ma, calc-alkaline (Appendix A) 'Karakoram' samples have εHf values (+2 to +11) that imply a composite melt composition. They are attributed to subduction-related magmatism at the active Karakoram margin during the Neo-Tethys subduction. The hafnium isotopic composition represents intermediate values between continental crust signature (εHf of -10 to -20, Vervoort *et al*. 1996, Vervoort *et al.* 1999) and a depleted mantle signature (εHf +15 to +25, Patchett & Tatsumoto 1980, Nowell *et al.* 1998, Chauvel & Blichert-Toft 2001).
The only 'true' suture zone sample, the 107 Ma *basaltic sill*, has an εHf value (+10) implying that there is no hafnium isotope contrast between the Karakoram and suture samples (Fig. 5.15b).

Kohistan
The Kohistan samples display strongly varying εHf values between +8.3 to +14.6 considering only the concordant microfractions (Fig. 5.14).
The *Mirkhani diorite* hafnium isotopic composition (+14.3) is very close to values of a MORB-type mantle reservoir. Present-day Indian MOR basalts generally have εHf between +11 and +22 (Nowell *et al.* 1998, Chauvel & Blichert-Toft 2001). Calc-alkaline, early to recent arc volcanites of the Izu-Bonin-Mariana system yield higher εHf ranging between +14.2 and +19.0 (Pearce *et al.* 1999). Those of the so-called Protoarc, formed during subduction initiation and tholeiitic to calc-alkaline in composition, have slightly lower values between +12.2 and +17.6 (Pearce *et al.* 1999). The calc-alkaline, 112 Ma northern Kohistan *Mirkhani diorite*, together with slightly younger (100-80 Ma) intrusions in southeastern Kohistan (Fig. 5.14) are associated with island arc magmatism above the intra-oceanic subduction zone tapping a MORB-type melt source. Possible contribution of recycled of lower island arc crust and/or a slab component (oceanic crust or sediments) in the mantle wedge may explain the hafnium ratios (εHf +13 to +15) being slightly lower than typical MORB-type values (εHf > +15).
The three Eocene Kohistan intrusions (50-39 Ma) represent magmatism post-dating India-Eurasia (Kohistan) continent-continent collision (65-50 Ma). The εHf values of the 50 Ma *meta-gabbro* (+11.6) and the 39 Ma *granitic dyke* (+9.4) denote a near-MORB-type to more enriched melt source. Inherited, Eocene to Proterozoic, discordant zircons of the 47 Ma *granitic dyke* with varying εHf (between -5.6 to +2.5) reflect the composite composition of the

zircons that underwent probably several phases of melting and crystallisation in continental crust since the Proterozoic. Thus, they are interpreted to be derived from continental Karakoram crust or subducted detrital units (e.g. turbidites) now located below the KKSZ. It is unlikely that these zircons are derived from the Kohistan island arc crust, as there is no evidence for underlying continental crust.
The two coeval, mafic Kohistan intrusions (50 Ma KKSZ *meta-gabbro* and Indus confluence diorite) have εHf around +11 whereas the three younger (47 to 30 Ma) *granitic dykes* (01B22, 01A77 and Indus confluence leucogranite) have values between +8 and +11 and/or a significant crustal inheritance with εHf between -6 to +6. Possible explanations for this εHf distribution are (1) two distinct (short?) magmatic phases with different melt sources, (2) a longer lasting single magmatic phase tapping two different melt sources at about the same time or (3) that the rising melt passed through different types (with high or low εHf) of crust that was partly assimilated.

In general, hafnium isotopic ratios in the Kohistan intrusions vary with time (Fig. 5.16).

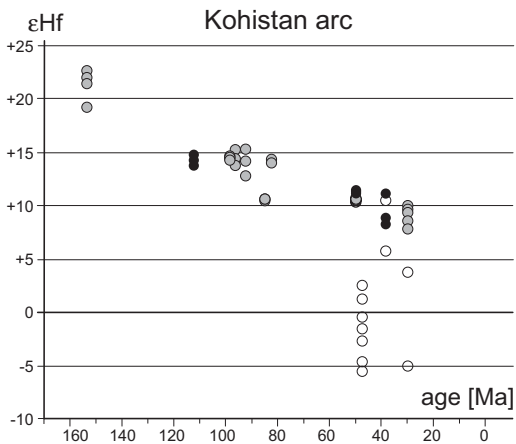

Fig. 5.16. *Epsilon hafnium values of the Kohistan arc with time. The filled, black circles represent samples from the KKSZ; the filled, grey circles are from eastern Kohistan (Schaltegger et al. 2002, 2003/ unpublished data). The open circles represent inherited zircons. For sample numbers see Fig. 5.14.*

The melts seem to have tapped an increasingly enriched mantle source evolving from εHf of +24 during initial stages of the arc at 154 Ma to around +9 at 30 Ma. However, another explanation may be the wide range (e.g the decrease) of the hafnium composition reflecting an increasing influence of slab-derived hafnium with time. Slab-derived hafnium either may come from subducted, oceanic sediments or from the subducted oceanic crust. Oceanic sediments have strongly varying hafnium isotopic ratios from +14 (deep-sea turbidites) or +6 (pelagic sediments) to extremely enriched ratios around -20 to -40 (Fig. 5.16, Vervoort *et al.* 1999, Godfrey *et al.* 1997 and Albarede *et al.* 1998). Woodhead *et al.* (2001) documented slab-derived hafnium in several

recent arcs. These authors showed, that for the New Britain arc, aqueous fluids, derived from dehydrating basaltic oceanic crust, may provide a transport mechanism of hafnium, which is responsible for the relatively low εHf values (εHf of +1 to +12, Fig. 5.17, White & Patchett 1984). Woodhead *et al.* (2001) found a sedimentary hafnium contribution to arc lavas of the Lesser Antilles arc (εHf of +4 to +16, Fig. 5.17, White & Patchett 1984). However, for that case, it is unclear whether it represents a source contamination or assimilation within the arc crust.
Another, theoretically possible source of less radiogenic hafnium in island arcs is an oceanic island basalt (OIB) type mantle source. εHf values of oceanic island basalts, possibly containing recycled sedimentary and/or continental hafnium, range from about -6 to +20 (Fig. 5.17, Nowell *et al.* 1998 and ref. therein).

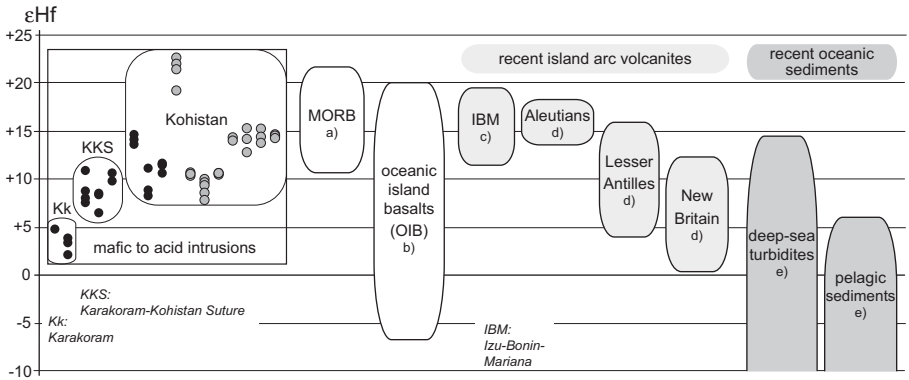

***Fig. 5.17**. Comparison of hafnium isotopic data of gabbros to granites from the KKSZ with **a)** MORB (Patchett & Tatsumoto 1980, Nowell et al. 1998, Chauvel & Blichert-Toft 2001), **b)** oceanic island basalts (Nowell et al. 1998 and ref. therein), **c)** Izu-Bonin-Mariana arc basalts and andesites (Pearce et al. 1999), **d)** Aleutian, Lesser Antilles and New Britain arc volcanites (White & Patchett 1984) and **e)** oceanic sediments (Godfrey et al. 1997, Albarede et al. 1998 and Vervoort et al. 1999). In near-arc settings, oceanic sediments can contain a significant, mantle-derived, volcanogenic hafnium component.*

To summarise, the Kohistan arc does not represent an intra-oceanic island arc since about the mid-Cretaceous (100-90 Ma), when it was accreted to the Karakoram margin to form an active continental margin until collision with India around 65 to 50 Ma. Possible reasons for the varying and the less radiogenic hafnium isotopic ratios for the intra-oceanic phase of the Kohistan arc are (1) different types of mantle wedge compositions (depleted - enriched), (2) assimilation (recycling) of lower island arc crust, (3) slab-derived hafnium from either subducted oceanic crust or oceanic sediments and (4) an OIB-type mantle source.

4. Discussion and conclusions

Mid-Cretaceous and early Eocene intrusions are documented along the KKSZ in Chitral. Four diorites and granites in the Karakoram, partly imbricated now in the suture, are 104 to 107 Ma old and represent subduction-related magmatism at the active, continental Karakoram margin. Inherited zircons of Proterozoic age (ca. 725 to 1620 Ma) are interpreted to be derived from the Karakoram crust that formed a part of the Gondwana supercontinent before the Late Paleozoic. As a regional comparison, gneisses in the northern Indian plate, in the footwall of the Indus Suture, yield U-Pb ages of 1864 Ma (DiPietro *et al.* 2001) and 1858 Ma (Zeilinger 2002). Hafnium isotopic ratios show a varying melt composition somewhere between a crustal end member and a depleted (MORB-type) mantle source and thus fit a continental margin setting. They further confirm lithological and petrological interpretations that two intrusions (01A50b and sh2500) in the suture zone are Karakoram-related as they have εHf values in the same range of +2 to +11.

Almost contemporaneous island arc magmatism in the northwestern Kohistan is documented by the Aptian (125-112 Ma) andesites that were intruded by the 112 Ma Mirkhani diorite. A melt source close to MORB-type is inferred for that diorite, as well as for younger (100-80 Ma, Schaltegger *et al.* 2002) Kohistan intrusions, which are distinctly different (i.e. more radiogenic) from the Karakoram melts.

The only ‘true’ suture zone sample, the 107 Ma basaltic dyke (20.1), has a hafnium isotopic composition (εHf of +10) similar to the imbricated Karakoram samples, and thus seems to represent the same subduction-related magmatism at the Karakoram margin.

The 50 Ma Kohistan, tholeiitic meta-gabbro is thought to represent a partial melting of depleted mantle (near-MORB-type). This melting must have occurred in the mantle wedge below Kohistan and KKSZ, which is assumed to be very thin due to the underthrusted Indian crustal slab; following tectonic models of the post-India-Kohistan collision setting (e.g. Kaneko *et al.* 2003).

The slightly younger, 47 Ma granitic dyke intruding this meta-gabbro is derived from a completely different, crustal source. The inferred youngest upper intercept age of 273±15 Ma (Fig. 5.9c) for the inherited zircons fit the 269 Ma U-Pb zircon age of Indian Plate Kaghan eclogites in NE Pakistan (Tonarini *et al.* 1993, Spencer & Gebauer 1996). The Paleozoic and Proterozoic zircons are likely derived from Gondwana crust or detrital, subducted sediments underlying the KKSZ and northernmost Kohistan in the early Eocene.

5. Appendix

5.1 Analytical techniques

5.1.1 U-Pb age determinations

Samples of 1 to 24 kg of fresh rock were collected. Zircons were separated from a fraction smaller than 350 μm using conventional mineral concentration procedures and equipment including a jaw-crusher, disk mill, Wilfley table and heavy liquids (methylene iodide). The non-magnetic zircon fraction, separated by a Frantz magnetic separator, was hand-picked under a binocular microscope (Krogh 1982a). According to morphological criteria, colour and the presence of cracks, cores and impurities, single grains or microfractions were selected. The zircons were air-abraded (if not, mentioned in Table 5.1) to eliminate zones of marginal lead loss (Krogh 1982b). The removal of the zircon margins reduced the common Pb contents and improved concordance. The selected zircons were then washed in 4 N nitric acid and rinsed several times with distilled high-purity water and distilled acetone in an ultrasonic bath. Dissolution in HF-HNO_3, chemical separation on anion exchange resin and mass spectrometry followed standard techniques (Krogh 1973) but with ion-exchange columns downsized at 1/10 of the original columns. U and Pb were loaded on a single Rhenium filament with H_3PO_4 and silica gel. Isotopic ratios were measured on a Finnigan MAT 262 system (at ETH Zürich) equipped with an ion counting system. The accuracy of the ion counting system was monitored by repeated measurements of the NBS 982 standard and corrected for fractionation with 0.09%/amu. The procedural lead blank was estimated at 0.6±0.3 pg. Common lead concentration in excess of the blank lead were corrected using crustal lead isotopic compositions (Stacey and Kramers 1975). The error ellipses for individual analyses in the concordia diagrams are given at the 2σ level; intercept ages, concordant ages and average values are given at the 95% confidence level (Ludwig 2001).

5.1.2 Hf isotopes

The Hf-Zr-REE fraction from the U-Pb separation protocol was redissolved and the hafnium was isolated using Eichrom™ Ln-spec resin and measured in static mode on a NuPlasma multi-collector ICP-MS (at ETH Zürich) using a MCN-6000 microconcentric nebulizer for sample introduction. Zircons are commonly characterised by extremely low $^{176}Lu/^{177}Hf$ ratios of less than 0.005 and the $^{176}Hf/^{177}Hf$ were corrected for in-situ radiogenic ingrowth using

this ratio. The hafnium ratios were corrected for mass fractionation using a $^{179}Hf/^{177}Hf$ value of 0.7325 and normalised to $^{176}Hf/^{177}Hf$ = 0.282160 of the JMC-475 standard (Blichert-Toft *et al.* 1997), which was repeatedly measured during analytical sessions. Mean isotopic values are at the 95% confidence level. Epsilon hafnium values were calculated with $^{176}Hf/^{177}Hf_{CHUR}$ = 0.282772 (Blichert-Toft and Albarède 1997).

5.1.3 Ar-Ar age determinations

Amphiboles between 0.2 and 0.425 mm were enriched by magnetic and gravimetric means. Sustained hand-picking of the separate led to a visual purity of >95%. These amphibole samples were irradiated at the McMasters reactor (Hamilton, Ontario, Canada). Ar isotope analyses were performed on a MAP™ 215-50B rare gas mass spectrometre (at the University of Bern). All isotopes were measured on the Faraday collector. Data listed in Table 5.3 were corrected for mass spectrometre background (0.06 fL for mass 36, 0.01 fL for mass 37 and 0.1 fL for mass 39) and discrimination (0.13%/amu favouring heavy masses, determined by measurements of a small pipette open to laboratory air). Furnace blanks always had atmospheric composition and ranged from 0.6 pL at 1000°C to 1 pL at 1500°C; they contained no detectable ^{37}Ar at any temperature. Additional information (e.g. radiogenic ^{40}Ar ($^{40}Ar^*$) concentrations, Cl/Ca and $^{40}Ar^*/^{40}Ar_{tot}$ ratios, etc.) can be easily derived from the data set in Table 5.3. The interference factors produced by neutron irradiation in the reactor were $(^{39}Ar/^{37}Ar)_{Ca}$=0.00067, $(^{38}Ar/^{37}Ar)_{Ca}$=0.00023, $(^{36}Ar/^{37}Ar)_{Ca}$=0.000255, $(^{40}Ar/^{39}Ar)_{K}$=0.011 and $(^{38}Ar/^{39}Ar)_{K}$=0.0118. Errors in Table 5.3 are in-run statistics only and purposefully do not take into account uncertainties of the J gradient, monitor age and decay constants.

			concentrations					atomic ratios									
nr.	weight [mg]	# of grains	U [ppm]	Pb rad. [ppm]	Pb non-rad. [pg]	Th/U (a)	$^{206}Pb/^{204}Pb$ (b)	$^{206}Pb/^{238}U$ (c,d)	error ±2σ [%]	$^{207}Pb/^{235}U$ (c)	error ±2σ [%]	$^{207}Pb/^{206}Pb$ (c,d)	error ±2σ [%]	age (c,d) $^{206}Pb/^{238}U$	age (c,d) $^{207}Pb/^{235}U$	age (c,d) $^{207}Pb/^{206}U$	error corr.
Phargam granite, **01B04**, Karakoram, 72°16'30"E/36°05'07"N																	
1	0.0030	2	757	14.03	0.6	0.84	3878	0.01625	0.35	0.10794	0.45	0.04818	0.25	103.91	104.08	107.96	0.88
2	0.0100	3	719	15.48	1.0	0.16	9934	0.02080	0.35	0.15576	0.39	0.05430	0.16	132.73	146.98	383.54	0.91
3	0.0042	1	55	1.01	1.6	0.94	164	0.01621	0.60	0.10681	4.13	0.04780	3.98	103.64	103.04	89.18	0.32
4	0.0065	2	629	66.91	0.8	0.13	35518	0.10333	0.34	1.34375	0.39	0.09432	0.11	633.9	864.8	1514.5	0.96
5	0.0038	3	442	14.04	0.4	0.22	10649	0.02995	0.65	0.23247	0.66	0.05629	0.48	190.20	212.20	463.90	0.73
6	0.0031	1	587	11.99	1.0	1.23	3072	0.01620	0.63	0.10838	0.86	0.04854	0.65	103.56	104.48	125.50	0.66
meta-dioritic amphibolite, **01A62**, Karakoram, 71°55'48"/35°44'08"N																	
7	0.0010	2	161	2.83	0.9	0.58	928	0.01646	0.48	0.10963	1.13	0.04830	1.02	105.25	105.63	114.05	0.43
8	0.0050	2	809	13.99	1.1	0.50	3788	0.01648	1.05	0.11066	1.16	0.04869	1.04	105.38	106.57	133.16	0.56
9*	0.0042	3	636	11.33	1.7	0.64	1687	0.01644	0.39	0.10965	0.54	0.04836	0.38	105.14	105.64	117.07	0.71
quartz diorite, **sh2500**, Suture, 71°57'25"E/35°43'01"N																	
10	0.0044	2	274	5.32	2.0	0.86	652	0.01677	0.72	0.11263	1.28	0.04879	1.10	107.04	108.37	137.58	0.51
11	0.0020	3	174	3.45	0.9	1.33	439	0.01677	0.78	0.11000	2.30	0.04757	2.12	107.21	105.96	78.04	0.39
12	0.0082	3	287	5.51	1.7	0.87	1497	0.01669	0.45	0.11113	0.70	0.04830	0.55	106.68	107.00	114.10	0.62
granitic dyke, **01A50b,** Suture, 71°54'49"E/35°40'13"N																	
13	0.0073	2	449	9.09	9.5	1.09	384	0.01674	0.36	0.11129	1.04	0.04823	0.95	107.00	107.14	110.35	0.41
14	0.0040	3	375	7.48	3.3	1.01	506	0.01678	0.37	0.11160	1.03	0.04823	0.95	107.29	107.45	110.48	0.39
15	0.0009	4	492	10.01	1.0	1.11	4796	0.01672	0.40	0.11130	0.49	0.04828	0.27	106.89	107.16	113.15	0.83
16	0.0113	3	491	10.47	1.7	1.34	3465	0.01671	0.44	0.11080	0.47	0.04809	0.25	106.83	106.69	103.74	0.85
17	0.0030	2	490	10.05	3.4	1.14	481	0.01673	0.40	0.11119	1.09	0.04820	0.98	107.00	107.10	108.90	0.44
basaltic sill, **20.1**, Suture, 72°01'20"E/35°46'22"N																	
18*	0.0032	1	119	1.96	0.3	0.13	1158	0.01673	0.80	0.11718	1.41	0.05078	1.27	107.00	112.50	230.99	0.45
19*	0.0020	2	196	3.87	1.4	0.93	466	0.01672	0.63	0.11260	1.42	0.04883	1.30	106.92	108.34	108.34	0.40
20*	0.0082	5	801	15.29	0.9	0.85	2945	0.01664	0.46	0.11108	0.54	0.04840	0.39	106.40	106.95	118.99	0.71

Table 5.1. *U and Pb isotopic results of zircons. Ages are given in Ma.*

			concentrations					atomic ratios									
nr.	weight [mg]	# of grains	U [ppm]	Pb rad. [ppm]	Pb non-rad. [pg]	Th/U (a)	$^{206}Pb/^{204}Pb$ (b)	$^{206}Pb/^{238}U$ (c,d)	error ±2σ [%]	$^{207}Pb/^{235}U$ (c)	error ±2σ [%]	$^{207}Pb/^{206}Pb$ (c,d)	error ±2σ [%]	age (c,d) $^{206}Pb/^{238}U$	age (c,d) $^{207}Pb/^{235}U$	age (c,d) $^{207}Pb/^{206}U$	error corr.
Mirkhani diorite, **01B25**, Kohistan, 71°44'06"E/35°27'54"N																	
21	0.0017	1	384	7.43	1.1	0.77	699	0.01750	0.78	0.11596	1.64	0.04807	1.43	111.82	111.40	102.52	0.49
22	0.0019	2	135	2.54	0.5	0.59	574	0.01743	2.31	0.11772	6.32	0.04899	6.03	111.39	113.01	147.28	0.31
23	0.0036	3	162	3.10	0.4	0.64	1669	0.01755	0.87	0.11803	1.39	0.04877	1.30	112.17	113.28	136.73	0.41
24	0.0012	3	291	5.48	3.1	0.64	143	0.01740	0.52	0.10954	3.51	0.04566	3.38	111.20	105.54	103.74	0.41
25	0.0026	2	338	6.19	4.0	0.52	258	0.01734	1.81	0.11679	2.32	0.04885	2.24	110.82	112.16	140.62	0.43
meta-gabbro, **01B24**, Kohistan, 71°46'01"E/35°24'25"N																	
26	0.0652	3	512	3.41	2.7	0.24	5356	0.00688	0.34	0.04454	0.41	0.04697	0.17	44.18	44.24	47.28	0.91
27	0.0398	4	430	2.94	1.5	0.24	5227	0.00706	0.42	0.04581	0.45	0.04706	0.26	45.36	45.48	52.03	0.82
28	0.0166	5	251	1.97	0.6	0.35	3538	0.00778	0.61	0.05065	0.67	0.04736	0.59	49.80	50.17	67.64	0.58
29	0.0170	3	640	4.56	0.7	0.31	7042	0.00714	0.34	0.04657	0.40	0.04727	0.21	45.89	46.21	62.88	0.85
granitic dyke, **01B22**, Kohistan, 71°47'29"E/35°29'09"N																	
30	0.0382	3	936	7.46	2.3	0.52	7331	0.00750	0.35	0.04893	0.40	0.04734	0.15	48.15	48.50	66.25	0.93
31	0.0202	5	196	5.65	0.5	0.06	14751	0.03024	0.34	0.23850	0.38	0.05721	0.13	192.00	217.2	499.7	0.94
32	0.0153	4	626	19.42	1.8	0.31	10398	0.03121	0.35	0.22110	0.39	0.05138	0.14	198.10	202.8	257.8	0.93
33	0.0120	3	414	7.79	0.6	0.11	9770	0.01962	0.35	0.13715	0.40	0.05071	0.16	125.20	130.5	227.4	0.92
34	0.0150	3	372	10.04	1.5	0.36	6251	0.02265	0.33	0.18757	0.40	0.05127	0.16	168.80	174.6	253.1	0.92
35	0.0063	4	621	15.70	0.6	0.13	10835	0.02570	0.47	0.19021	0.48	0.05537	0.30	163.61	176.8	357.2	0.80
36	0.0139	4	1094	10.76	0.7	0.15	13478	0.00940	0.61	0.06490	0.60	0.05007	0.37	60.32	63.9	198.2	0.81
37	0.0062	2	557	4.48	0.3	0.23	4994	0.00774	0.59	0.05123	0.59	0.04802	0.49	49.69	50.7	99.6	0.66

Table 5.1*ff. U and Pb isotopic results of zircons. Ages are given in Ma.*

			concentrations					atomic ratios									
nr.	weight [mg]	# of grains	U [ppm]	Pb rad. [ppm]	Pb non-rad. [pg]	Th/U (a)	$^{206}Pb/^{204}Pb$ (b)	$^{206}Pb/^{238}U$ (c,d)	error ±2σ [%]	$^{207}Pb/^{235}U$ (c)	error ±2σ [%]	$^{207}Pb/^{206}Pb$ (c,d)	error ±2σ [%]	age (c,d) $^{206}Pb/^{238}U$	age (c,d) $^{207}Pb/^{235}U$	age (c,d) $^{207}Pb/^{206}U$	error corr.
granitic dyke, **01A07**, Kohistan, 71°47'51"E/35°28'31"N																	
38	0.0059	2	339	2.32	1.9	0.36	423	0.00600	1.09	0.03944	2.72	0.04477	2.59	38.55	39.28	83.99	0.32
39	0.0056	2	689	4.66	0.5	0.58	3025	0.00623	0.81	0.04048	0.71	0.04716	0.61	40.01	40.30	57.21	0.69
40	0.0034	3	369	2.49	1.0	1.89	515	0.00603	0.67	0.03847	2.11	0.04628	2.00	38.74	38.33	12.40	0.32
41	0.0030	3	737	5.03	0.7	0.39	1198	0.00607	1.13	0.03969	1.52	0.04747	1.42	38.98	39.53	72.70	0.46
42	0.0053	4	591	4.72	0.9	0.22	1776	0.00763	0.66	0.05075	0.79	0.04825	0.74	49.00	50.27	111.34	0.49

(a) calculated on the basis of radiogenic $^{208}Pb/^{206}Pb$ ratios, assuming concordance.
(b) corrected for fractionation and spike.
(c) corrected for fractionation, spike, blank and common lead.
(d) corrected for initial Th disequilibrium, using an estimated Th/U ratio of 4 for the melt.
(*) zircons were not abraded.

Table 5.1fff. *U and Pb isotopic results of zircons. Ages are given in Ma.*

nr.	$^{176}Hf/^{177}Hf$ meas. (a)	±2σ [%] (b)	$^{176}Hf/^{177}Hf$ normal. (c)	$^{176}Hf/^{177}Hf$ (T) (d)	εHf (T)
Phargam granite, **01B04**, Karakoram					
1	N.D.	N.D.	N.D.	N.D.	
2	0.282814	7	0.282803	0.282790	4.1
3	0.282671	30	0.282655	0.282645	-1.8
4	0.282241	5	0.282225	0.282163	-4.8
5	0.282775	9	0.282759	0.282741	3.9
6	0.282854	9	0.282838	0.282828	4.7
meta-dioritic amphibolite, **01A62**, Karakoram					
7	0.282824	23	0.282808	0.282798	3.7
8	0.282740	10	0.282768	0.282758	2.3
9	0.282771	11	0.282799	0.282789	3.4
quartz diorite, **sh2500**, Suture					
10	0.282918	6	0.282946	0.282935	8.6
11	0.282861	24	0.282889	0.282878	6.6
12	0.282921	4	0.282949	0.282939	8.7
granitic dyke, **01A50b,** Suture					
13	0.283017	8	0.283011	0.283001	10.9
14	0.282937	9	0.282931	0.282921	8.1
15	0.282930	14	0.282919	0.282909	7.6
16	0.282963	10	0.282952	0.282942	8.8
17	N.D.	N.D.	N.D.	N.D.	
basaltic sill, **20.1**, Suture					
18	N.D.	N.D.	N.D.	N.D.	
19	0.282976	12	0.283004	0.282993	10.6
20	0.282951	11	0.282979	0.282969	9.8

(a) measured $^{176}Hf/^{177}Hf$.
(b) numbers refers to the last digits.
(c) corrected for fractionation, normalised to JMC standard 0.282160.
(d) as (c) and age corrected with $^{176}Lu/^{177}Hf$=0.005.

nr.	$^{176}Hf/^{177}Hf$ meas. (a)	±2σ [%] (b)	$^{176}Hf/^{177}Hf$ normal. (c)	$^{176}Hf/^{177}Hf$ (T) (d)	εHf (T)
Mirkhani diorite, **01B25**, Kohistan					
21	0.283085	7	0.283113	0.283102	14.6
22	0.283072	10	0.283100	0.283089	14.2
23	N.D.	N.D.	N.D.	N.D.	
24	0.283058	14	0.283086	0.283075	13.7
25	N.D.	N.D.	N.D.	N.D.	
meta-gabbro, **01B24**, Kohistan					
26	0.283082	3	0.283076	0.283072	11.8
27	0.283093	2	0.283087	0.283083	12.2
28	0.283087	4	0.283076	0.283071	11.9
29	0.283052	4	0.283041	0.283037	10.6
granitic dyke, **01B22**, Kohistan					
30	0.282589	3	0.282583	0.282578	-5.6
31	0.282520	5	0.282514	0.282495	-4.7
32	0.282635	3	0.282629	0.282610	-0.5
33	0.282772	5	0.282761	0.282749	2.5
34	0.282721	6	0.282710	0.282694	1.7
35	0.282558	5	0.282586	0.282570	-2.8
36	N.D.	N.D.	N.D.	N.D.	
37	0.282666	5	0.282694	0.282690	-1.6
granitic dyke, **01A07**, Kohistan					
38	0.282968	7	0.283062	0.283059	11.2
39	0.282950	11	0.283044	0.283040	10.5
40	0.282953	13	0.282981	0.282977	8.3
41	0.282967	10	0.282995	0.282991	8.8
42	0.282877	5	0.282905	0.282900	5.8

***Table 5.2**. Hafnium isotopic results of the dated zircons. Sample numbers correspond to the numbers in Table 5.1.*

Step	T (°C)	$^{40}Ar_{tot}$	^{39}Ar	^{38}Ar	^{37}Ar	^{36}Ar	Age ± 1σ
20.1 (22.2 mg; J = 3.65*10^{-3}; Ar* = 1905; $K_2$0 = 0.56; CaO = 7.4; Cl = 87)							
1	652	37.15 ± 0.01	0.367 ± 0.016	0.087 ± 0.014	1.26 ± 0.06	0.146 ± 0.011	0.0 ± 62
2	856	172.55 ± 0.00	2.834 ± 0.015	0.481 ± 0.021	5.31 ± 0.06	0.441 ± 0.008	96.5 ± 5.4
3	901	36.12 ± 0.15	0.731 ± 0.012	0.041 ± 0.018	2.32 ± 0.06	0.088 ± 0.015	89.8 ± 38
4	942	38.41 ± 0.04	0.662 ± 0.024	0.109 ± 0.022	4.53 ± 0.17	0.112 ± 0.009	54.8 ± 26
5	982	48.22 ± 0.06	1.017 ± 0.009	0.163 ± 0.020	8.00 ± 0.10	0.091 ± 0.007	136.8 ± 13
6	1001	87.98 ± 0.02	3.289 ± 0.018	0.414 ± 0.014	19.84 ± 0.13	0.125 ± 0.013	102.5 ± 7.1
7	1021	137.43 ± 0.14	6.085 ± 0.021	0.858 ± 0.011	37.40 ± 0.18	0.109 ± 0.013	113.7 ± 3.7
8	1040	81.23 ± 0.01	3.295 ± 0.014	0.436 ± 0.010	20.11 ± 0.11	0.055 ± 0.009	128.7 ± 4.7
9	1057	104.98 ± 0.10	4.547 ± 0.013	0.488 ± 0.020	27.51 ± 0.12	0.171 ± 0.009	80.4 ± 3.7
10	1077	404.05 ± 0.03	21.362 ± 0.026	2.407 ± 0.016	124.78 ± 0.36	0.170 ± 0.011	109.1 ± 0.8
11	1095	779.27 ± 0.18	42.593 ± 0.040	4.874 ± 0.018	252.99 ± 0.72	0.318 ± 0.012	106.2 ± 0.4
12	1125	132.06 ± 0.00	5.921 ± 0.015	0.749 ± 0.018	35.27 ± 0.14	0.139 ± 0.011	101.7 ± 3.4
13	1160	68.81 ± 0.04	2.658 ± 0.019	0.286 ± 0.014	15.34 ± 0.13	0.075 ± 0.014	115.1 ± 9.1
14	1490	460.86 ± 0.08	22.249 ± 0.027	2.806 ± 0.014	135.28 ± 0.40	0.276 ± 0.011	112.2 ± 0.8
01B16 (30.0 mg; J = 0.805*10^{-3}; Ar* = 787; $K_2$0 = 1.69; CaO =18.6; Cl = 383); 71°52'43"E/35°38'24"N							
1	649	30.814 ± 0.002	0.080 ± 0.001	0.012 ± 0.001	0.135 ± 0.004	0.075 ± 0.001	151.7 ± 4.4
2	890	98.728 ± 0.005	0.351 ± 0.001	0.057 ± 0.001	1.525 ± 0.006	0.146 ± 0.001	217.7 ± 1.2
3	930	39.827 ± 0.004	0.170 ± 0.001	0.028 ± 0.001	1.560 ± 0.011	0.032 ± 0.001	246.0 ± 2.5
4	970	52.294 ± 0.003	0.400 ± 0.001	0.079 ± 0.001	2.186 ± 0.008	0.024 ± 0.001	158.8 ± 0.7
5	988	88.635 ± 0.013	0.835 ± 0.001	0.157 ± 0.001	3.924 ± 0.012	0.022 ± 0.001	138.9 ± 0.4
6	1005	90.851 ± 0.024	0.913 ± 0.001	0.168 ± 0.001	4.229 ± 0.012	0.021 ± 0.001	131.2 ± 0.4
7	1025	88.582 ± 0.010	0.925 ± 0.001	0.160 ± 0.001	4.221 ± 0.014	0.018 ± 0.001	127.6 ± 0.5
8	1045	90.116 ± 0.013	0.959 ± 0.001	0.156 ± 0.001	4.341 ± 0.013	0.018 ± 0.001	125.2 ± 0.5
9	1068	70.295 ± 0.015	0.751 ± 0.001	0.116 ± 0.001	3.432 ± 0.010	0.017 ± 0.001	123.5 ± 0.5
10	1107	61.509 ± 0.010	0.613 ± 0.002	0.104 ± 0.001	3.007 ± 0.012	0.011 ± 0.001	134.2 ± 0.5
11	1158	78.290 ± 0.005	0.745 ± 0.001	0.136 ± 0.001	3.689 ± 0.012	0.018 ± 0.001	138.1 ± 0.4
12	1208	18.544 ± 0.000	0.168 ± 0.001	0.027 ± 0.001	0.833 ± 0.006	0.002 ± 0.001	150.4 ± 2.6
13	1441	107.241 ± 0.013	1.005 ± 0.001	0.178 ± 0.001	4.983 ± 0.015	0.031 ± 0.001	138.1 ± 0.4

***Table 5.3**. Ar-Ar stepwise heating results.All Ar concentrations are in picolitres per gram (pl/g). Errors are 1 sigma. Ar* denotes total ^{40}Ar minus atmospheric ^{40}Ar; the integrated K_2O and CaO values are given in wt%; Cl is given in ppm. These values are calculated from the total ^{39}Ar, ^{38}Ar and ^{37}Ar, the production ratios and the irradiation time. Ages are given in Ma.*

Step	T (°C)	$^{40}Ar_{tot}$	^{39}Ar	^{38}Ar	^{37}Ar	^{36}Ar	Age ± 1σ
01B24 (48.3 mg; J = 0.805*10^{-3}; Ar* = 2089; $K_2$0 = 1.23; CaO = 17.5; Cl = 618)							
1	645	53.919 ± 0.042	0.229 ± 0.007	0.023 ± 0.008	1.17 ± 0.05	0.111 ± 0.007	129.9 ± 12
2	908	84.312 ± 0.011	0.799 ± 0.008	0.192 ± 0.004	5.02 ± 0.06	0.112 ± 0.005	91.4 ± 2.8
3	969	170.201 ± 0.018	3.099 ± 0.011	1.109 ± 0.008	20.43 ± 0.10	0.133 ± 0.006	61.0 ± 0.8
4	990	324.508 ± 0.063	7.516 ± 0.010	2.734 ± 0.010	47.65 ± 0.15	0.130 ± 0.007	55.0 ± 0.3
5	997	163.088 ± 0.038	4.125 ± 0.010	1.450 ± 0.008	24.92 ± 0.09	0.052 ± 0.007	51.8 ± 0.6
6	1002	72.460 ± 0.003	1.789 ± 0.005	0.633 ± 0.005	10.47 ± 0.05	0.046 ± 0.006	47.6 ± 1.4
7	1013	42.202 ± 0.007	0.961 ± 0.007	0.311 ± 0.009	5.49 ± 0.05	0.036 ± 0.007	47.7 ± 2.8
8	1023	30.882 ± 0.001	0.604 ± 0.009	0.178 ± 0.005	3.55 ± 0.06	0.049 ± 0.007	39.5 ± 4.6
9	1032	30.267 ± 0.015	0.521 ± 0.007	0.178 ± 0.010	3.54 ± 0.05	0.025 ± 0.007	63.6 ± 5.7
10	1045	49.272 ± 0.019	0.991 ± 0.006	0.343 ± 0.005	6.42 ± 0.05	0.005 ± 0.007	69.1 ± 2.1
11	1075	154.391 ± 0.098	3.786 ± 0.010	1.371 ± 0.006	23.99 ± 0.10	0.080 ± 0.006	50.0 ± 0.6
12	1105	222.864 ± 0.056	5.487 ± 0.009	1.994 ± 0.009	34.98 ± 0.12	0.088 ± 0.006	51.9 ± 0.4
13	1159	376.300 ± 0.147	9.774 ± 0.012	3.568 ± 0.012	60.22 ± 0.18	0.106 ± 0.006	51.1 ± 0.2
14	1208	288.42 ± 0.070	7.620 ± 0.011	2.732 ± 0.010	46.83 ± 0.16	0.089 ± 0.006	49.8 ± 0.3
15	1316	263.37 ± 0.000	6.971 ± 0.013	2.440 ± 0.007	42.23 ± 0.14	0.104 ± 0.006	48.4 ± 0.3
16	1435	131.60 ± 0.002	3.276 ± 0.012	1.140 ± 0.008	20.05 ± 0.10	0.081 ± 0.006	47.7 ± 0.8

Table 5.3*ff. Ar-Ar stepwise heating results.All Ar concentrations are in picolitres per gram (pl/g). Errors are 1 sigma. Ar* denotes total ^{40}Ar minus atmospheric ^{40}Ar; the integrated K_2O and CaO values are given in wt%; Cl is given in ppm. These values are calculated from the total ^{39}Ar, ^{38}Ar and ^{37}Ar, the production ratios and the irradiation time. Ages are given in Ma.*

Chapter 6: Discussion and conclusions

The Karakoram-Kohistan Suture Zone comprises gabbros, diorites, andesitic lavas, turbidites, meta-ultramafites and Karakoram and Kohistan-derived volcano-sediments bounded and imbricated by sinistral and reverse faults dipping steeply northwest.

The southern Karakoram cover is represented by low-grade meta-pelites, meta-volcanoclastites and meta-carbonates of Paleozoic to mid-Cretaceous age. The Karakoram was the active margin of Eurasia from at least the Late Jurassic (145-150 Ma Hushe gneiss, Parrish in Searle 1991) to the mid-Cretaceous (e.g. 100-106 Ma Hunza Plutonic Unit, Fraser *et al*. 2001, Sergeev *et al*. 2001).

Deformation fabrics, preserved some kilometres north of the Karakoram-Kohistan Suture in the southern Karakoram, are older than 104 Ma. They may be attributed to Andean-type deformation during subduction at the Karakoram active margin. 105 to 107 Ma diorites intruded the southernmost Karakoram and the suture zone. Their deformation fabric is attributed to collision between the Karakoram and the Kohistan magmatic arcs. In the southernmost Karakoram, strain increases southeastwards, towards the suture. Sinistral transpression produced a strong suture-parallel foliation plane with predominantly subhorizontal stretching lineations and variably plunging fold axes in and adjacent to the suture zone. This implies a ‘suture-related’ deformation overprinting older fabrics.

Despite a strong imbrication in the suture zone, coherent lithologies do not show much duplication or inversion of the original polarity and thus have likely preserved some original paleogeographic distribution (Fig. 6.1). The lithologies represent the remnants of the marine basin trapped within the suture. Shallow water limestones, derived from both the Karakoram and Kohistan sides, are of Cretaceous age. *Calcareous turbidites* are also evidence for that marine basin, but their affiliation (Karakoram or Kohistan) could not be definitely deduced. Serpentinites, talcschists and ophicarbonates, poor in Ca-Al phases, are derived from a harzburgitic mantle. An intrusive, undeformed 107 Ma basaltic sill and a ca. 130 Ma quartz monzodiorite give a minimum age for deformation and serpentinisation of the meta-harzburgites. Thus, the meta-harzburgites were exposed near or at the sea floor of the southern Karakoram margin after serpentinisation and before the end of subduction-related magmatism in Albian times. They may be derived from the mantle exhumed along south-dipping low-angle detachment faults during rifting at the passive North-Gondwana margin (comparable to the Galicia margin, e.g. Boillot *et al.* 1987).

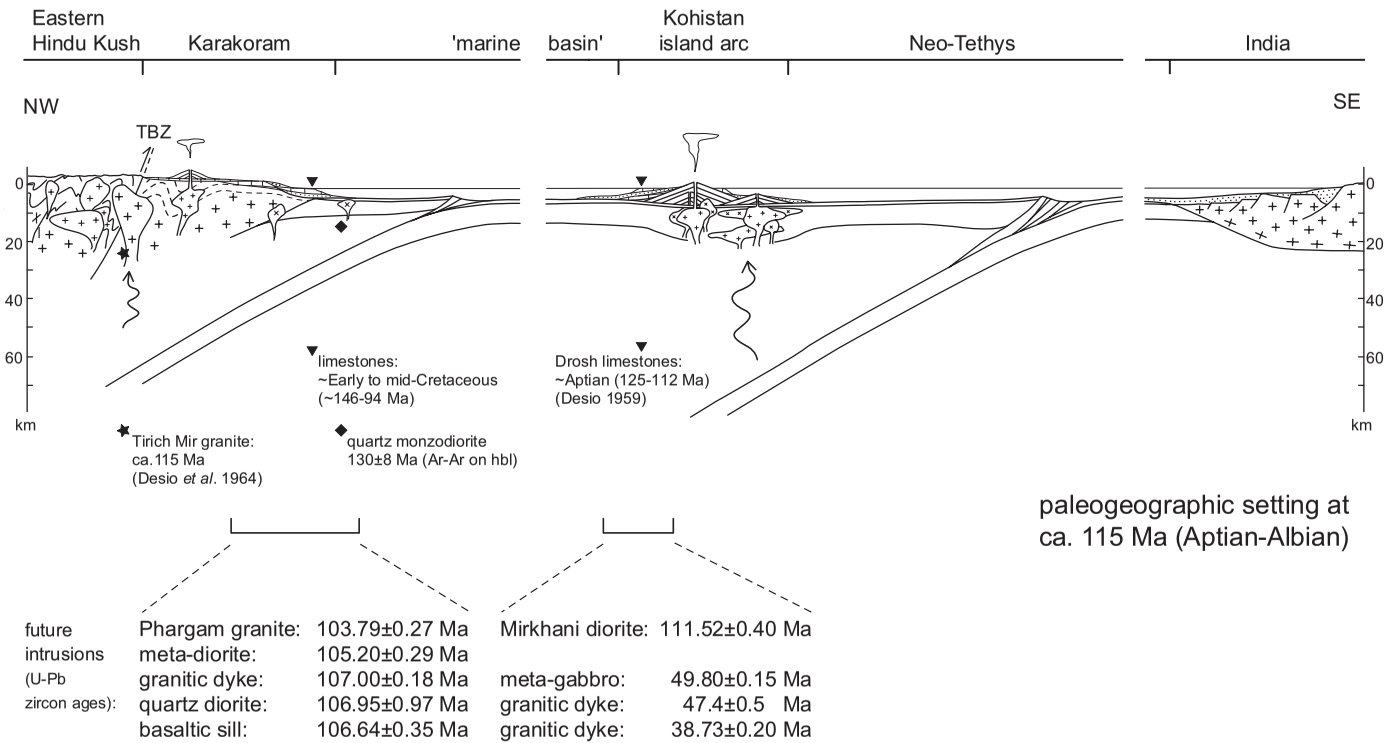

***Fig. 6.1**. Paleogeographic setting at about 115 Ma. The stratigraphic and radiometric ages are discussed in the chapters 2,3 and 5. TBZ: Tirich Boundary Zone.*

The lack of a complete ophiolitic sequence (association of peridotites, ultrabasic cumulates, gabbros, sheeted dykes and MORB-type pillow basalts) is consistent with a subcontinental mantle as protolith of the meta-harzburgites. The scarcity of undisputed exotic blocks and the absence of high-pressure rocks (such as blueschists) indicates that the major part of the marine basin between the Kohistan island arc and the Karakoram margin, as well as its possible accretionary prism units, has disappeared along the KKSZ during subduction of Neo-Tethys oceanic lithosphere and the subsequent accretion of the Kohistan island arc.

The Kohistan was an active island arc from its formation in the (Late?) Jurassic until accretion to the Asian margin in the mid-Cretaceous. The north-Kohistan lithologies are represented by basaltic to andesitic island arc volcanites, interlayered shallow marine Aptian limestones, alluvial fan or delta red clastites and a 112 Ma diorite.

Barremian-Albian Karakoram and Kohistan intrusions imply that there were two contemporaneous, north-dipping subductions in the Neo-Tethys, producing two magmatic, calc-alkaline arcs (Karakoram and Kohistan), a situation comparable to the present double-subduction producing the Izu-Bonin-Mariana Arc and the Luzon-Taiwan-Ryukyu Arc in the Philippine Sea. Distinct hafnium isotopes illustrate the different types of melt origins in these two arcs. A significant crustal component, caused by assimilation of continental crust, is documented in the Karakoram in accordance with its continental margin setting. The coeval mid-Cretaceous Kohistan intrusions show significantly different, MORB-type mantle sources constraining the intra-oceanic subduction setting of the island arc.

The two foliated intrusions dated at 50 (*meta-gabbro*) and 47 Ma (*granitic dyke*), indicate that ‘suture-related’ deformation continued until the Eocene. The 39 Ma undeformed *granitic dyke*, crosscutting the *meta-gabbros*, marks the minimum age of that deformation. The foliation and the subhorizontal stretching lineation in folded greenschist and amphibolite facies Kohistan units are parallel to those of the suture and Karakoram units and thus consistent with persisting sinistral transpression. However, it is unclear whether the deformation of the *meta-gabbro* unit is related to its magmatic emplacement or whether it is associated with a later, metamorphic event. The 44 Ma rim of the sampled *meta-gabbro* zircons may indicate such a post-crystallisation event.

To summarise, three phases of deformation along the Karakoram-Kohistan Suture have been recognised (Fig. 6.2):

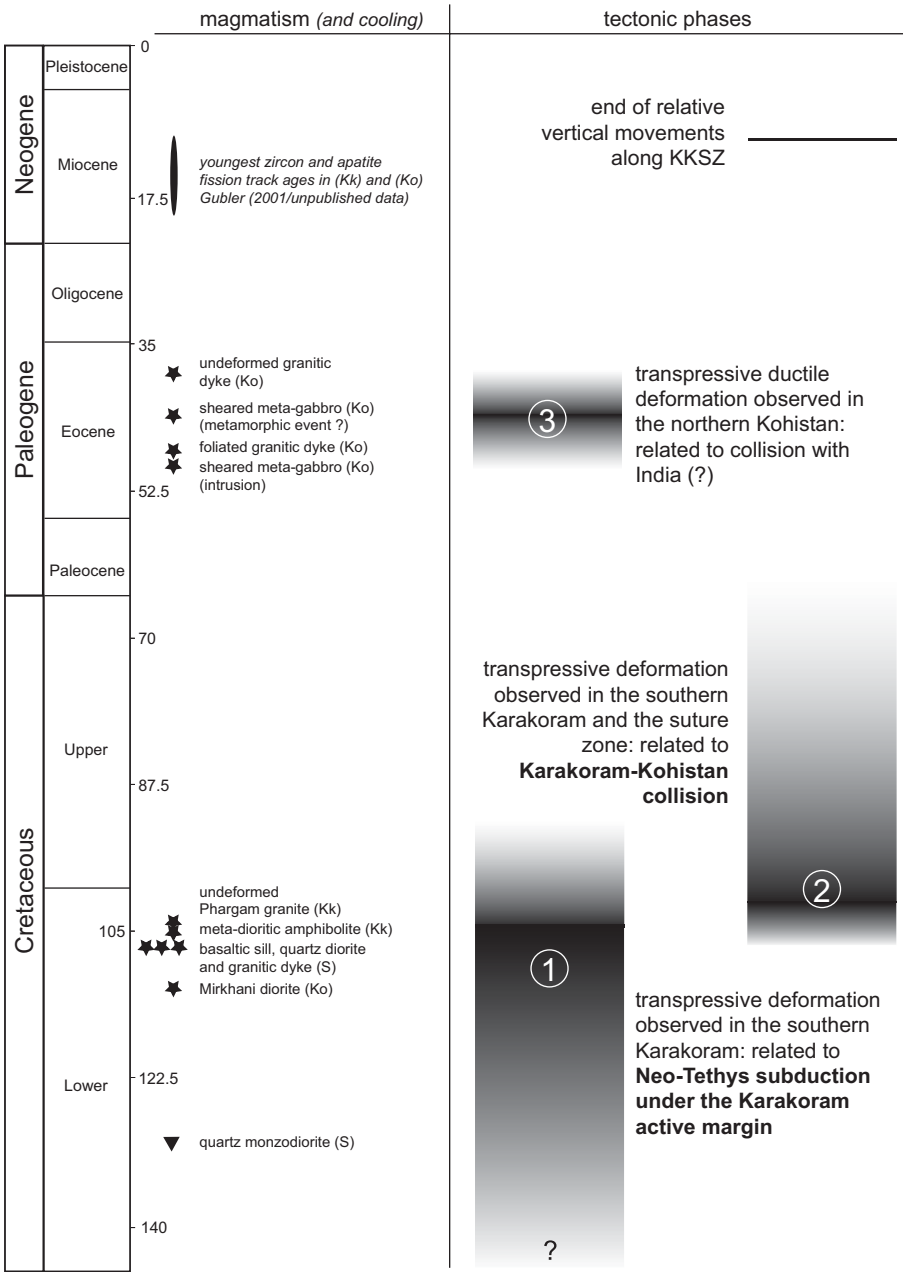

***Fig. 6.2**. Deformation phases (1,2 and 3: circled labels) along the KKSZ deduced from related magmatic phases. Stars mark the U-Pb zircon intrusion ages and the triangle the Ar-Ar age obtained in this study and described in chapters 3 and 5. Kk: Karakoram, S: Suture, Ko: Kohistan.*

(1) the oldest phase, documented in the southern Karakoram meta-sediments, is attributed to subduction-related magmatism between ca. 130 and 100 Ma. (2) a subsequent, sinistral transpression after 105 Ma is related to the Karakoram-Kohistan collision. The end of calc-alkaline, subduction-related magmatism in the southern Karakoram margin around 100 Ma (ages summarised in Table 2.1 on p.14) may indicate the onset of Karakoram-Kohistan collision with the closure of the Karakoram-Kohistan Suture probably in the early Late Cretaceous (ca. 100 to 90 Ma). (3) magmatism between 50 and 39 Ma and associated sinistral transpression in northern Kohistan suggests ongoing suture-related, ductile deformation until Eocene times.
Brittle faulting along the KKSZ reveals a brittle, sinistral transpression with a NW-SE to E-W oriented compression direction. The timing of brittle faulting is difficult to constrain, but zircon and apatite fission track ages indicate that vertical relative movements across the KKSZ ended by the early-mid Miocene. However, the principal stress axes of the majority of the calculated paleostress tensors fit the regional, present-day stress field that is reflected in the seismicity, and thus it may not be ruled out that the paleostress tensors represent 'sub-actual' brittle faulting.

The timing of the KKSZ closure, however, cannot be precisely constrained from the presented data. It must be younger than 105 Ma and maybe was finished before the mid-Late Cretaceous extension in the southern Karakoram and the intrusion of the Chilas complex that is related to the Kohistan arc splitting (discussed in chapter 2).
Nevertheless, it could be shown that the formation of the KKSZ is not a single event but involves several phases of deformation. Collision with, and underthrusting of India under the Eurasian margin (Kohistan, Karakoram etc.) may have played an important role in Eocene magmatism and deformation along the KKSZ. Ultra-high pressure metamorphism in the Indian slab is documented from coesite-bearing, 44.2±0.4 to 46.8±0.9 Ma zircon rims in Permian zircons from gneisses exhumed south of the Indus suture at (Spencer and Gebauer 1996, Kaneko *et al.* 2003). One can speculate that the emplacement of the Kohistan *meta-gabbro* at 50 Ma and the growth of metamorphic zircon rims at 44 Ma are related to the underthrusting of India.

Remaining open questions and suggestions for possible further work
The field work performed within the scope of this thesis is regarded as pioneering work. There are still open, major questions concerning the kinematic history of the KKSZ:
(1) the timing of the Karakoram-Kohistan collision and the closure of the KKSZ remains imprecise, between 105 and about 85 Ma.
(2) the width of the oceanic basin, separating the Kohistan island arc from the Karakoram margin before collision, remains unclear.

(3) the tectonic setting of Eocene magmatism and associated contemporaneous or subsequent ductile deformation, adjacent to the KKSZ in northern Kohistan requires more documentation to be understood.

Further, detailed work is needed for which some suggestions are listed below:
(1) microstructural analyses to determine tectonic transport directions along faults and shear zones.
(2) metamorphic petrography to precisely map gradients or jumps of the metamorphic facies across the suture or single faults.
(3) a detailed study of the Kohistan meta-gabbro unit, including the ultramafic enclaves and cross-cutting granitic dykes (pressure-temperature conditions, more geochronology, geochemistry and structural analyses on the ductile (magmatic or metamorphic?) deformation fabric) to constrain the tectonic setting during emplacement and exhumation.
(4) major element analyses on spinel in the serpentinites and talcschists within the suture to constrain their subcontinental, harzburgitic character.
(5) a stable isotope study on the calcite of ophicarbonates to certify their oceanic origin.
(6) sediment petrography (heavy minerals) of the Purit red sandstones to constrain their sedimentary facies, source region and timing of deposition (before or after the closure of the Karakoram-Kohistan Suture?).

Appendix A: Preliminary results from whole rock geochemistry

1. Introduction

Thirty-four samples from the KKSZ were selected for X-ray fluorescence (XRF) major and trace element, and Inductively Coupled Plasma-Mass Spectrometry (ICP-MS) trace element determination. The sampling localities are shown in Fig. B.1 and listed in Table B.1. Whole rock powders were made from all the 10 dated intrusions, two additional intrusions (01A29 from the Karakoram, and 01A77 from the Kohistan) and 22, mainly greenschist facies volcanites. The data are presented in basic major elements plots and spidergrams to illustrate the geochemical composition and variations between rocks of the three different tectonic units (Karakoram, Suture, Kohistan) and between different rock types of the same units.

2. Analytical methods

Rock samples of 0.4-1 kg were cut into representative pieces without lithological heterogeneity and crushed to sub-centimetre chips. For each sample, an aliquot of approximately 200 to 500 g was ground to powder in a tungsten carbide ring mill at ETH Zürich. Major and trace elements (Nb, Zr, Y, Sr, U, Rb, Th, Pb, Ga, Zn, Cu, Ni, Co, Cr, V, Ce, Nd, Ba, La, S, Sc, As) were measured by XRF at the Université de Genève and Lausanne on a Philips PW1400. The trace elements Rb, Sr, Zr, Y, Nb, Cs, Ba, Tm, Ta, Pb, Th and U, and rare earth elements were analysed at the Institut des Sciences de la Terre, de l'Environnement et de l'Espace de Montpellier (ISTEEM) on a Fisons (VG-Elemental) PQ2 + Turbo (PlasmaQuad II+) instrument following the procedure published by Ionov *et al.* (1992) and Godard *et al.* (2000).
In cases for which both methods were used to measure trace elements, ICP-MS data where kept and listed in Table B.2. In the case of Zr, the XRF data were kept because of zircon dissolution problems during sample preparation for ICP-MS, so that Zr may be underestimated in acidic and metamorphic rocks (J.-L. Bodinier, pers. comm.).

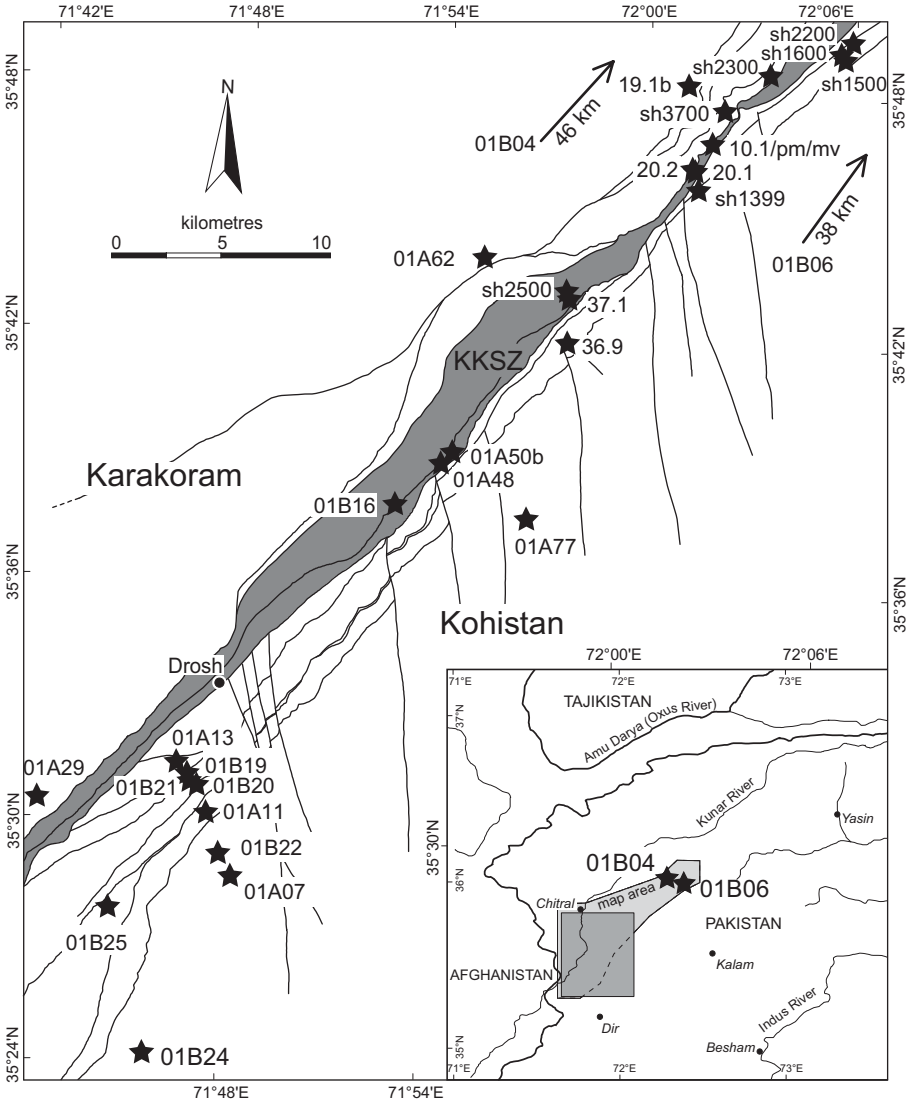

Fig. B.1. *Location of samples (numbered stars) analysed and listed in Table B.1, in a structural sketch map of the Karakoram-Kohistan Suture Zone (KKSZ, shaded) in the Drosh area. Inset: map area (light grey) and outline of this figure (darker grey box).*

		sample	rock type	GPS coordinates	lithology	XRF major + trace e.	ICP-MS trace elements	dating method
volcanites	Karakoram	14.7	dacite	72°02'04"E/35°47'29"N	Kk-VC	x	x	
		19.1b	greenstone	72°01'06"E/35°48'29"N	Kk-GD	x	x	
		20.2	dacite	72°01'19"E/35°46'24"N	Kk-VC	x	x	
		sh2300	basalt	72°04'56"E/35°50'03"N	Kk-VC	x	x	
		sh3700	basalt	72°02'03"E/35°47'23"N	Kk-VC	x	x	
	Suture	37.1	greenstone	71°57'25"E/35°43'03"N	Kk-VC	x	x	
		01A48	basalt	71°53'41"E/35°38'55"N	S-T	x	x	
		10.1	basalt	72°01'53"E/35°46'58"N	S-ST	x	x	
		10.1pm	basalt	72°01'53"E/35°46'58"N	S-ST	x	x	
		10.1mv	basalt	72°01'53"E/35°46'58"N	S-ST	x	x	
	Kohistan	01A02	basalt	71°44'23"E/35°30'06"N	Ko-DV	x	x	
		01B06	basalt	72°23'20"E/36°03'19"N	Ko-DV	x	x	
		01B19	andesite	71°45'45"E/35°31'25"N	Ko-DV	x	x	
		01B20	andesite	71°45'48"E/35°31'23"N	Ko-DV	x	x	
		01B21	basalt	71°45'50"E/35°31'18"N	Ko-DV	x	x	
		01A13	andesite	71°46'33"E/35°31'32"N	Ko-DV	x	x	
		36.9	greenstone	71°51'27"E/35°42'20"N	Ko-GGM	x	x	
		01A11	amphibolite	71°47'25"E/35°29'30"N	Ko-GBa	x	x	
		sh1399	greenstone	72°01'43"E/35°45'50"N	Ko-GBa	x	x	
		sh1500	amphibolite	72°05'37"E/35°49'11"N	Ko-GBa	x	x	
		sh1600	greenschist	72°05'25"E/35°49'30"N	Ko-GBa	x	x	
		sh2200	amphibolite	72°05'51"E/35°49'40"N	Ko-GBa	x	x	
plutonites	Karak.	01B04	granite	72°16'30"E/36°05'07"N	Kk-G	x	x	U-Pb
		01A62	amphibolite	71°55'48"E/35°44'08"N	KK-GD	x		U-Pb
		01A29	diorite	71°40'13"E/35°30'47"N	Kk-M	x	x	
	Suture	sh2500	diorite	71°57'25"E/35°43'01"N	S-GD	x		U-Pb
		01A50b	granitic dyke	71°54'49"E/35°40'13"N	S-GD	x	x	U-Pb
		20.1	basaltic sill	72°01'20"E/35°46'22"N	S-mD	x	x	U-Pb/Ar-Ar
		01B16	gabbro	71°52'43"E/35°38'24"N	S-GD	x	x	Ar-Ar
	Kohistan	01B25	diorite	71°44'06"E/35°27'54"N	Ko-MD	x	x	U-Pb
		01B24	gabbro	71°46'01"E/35°24'25"N	Ko-Ga	x	x	U-Pb/Ar-Ar
		01B22	granitic dyke	71°47'29"E/35°29'09"N	Ko-Dy	x	x	U-Pb
		01A07	granitic dyke	71°47'51"E/35°28'31"N	Ko-Dy	x		U-Pb
		01A77	granitic dyke	71°56'12"E/35°37'16"N	Ko-Dy	x	x	

Table B.1. *List of analysed volcanic and plutonic samples. The lithology abbreviations are like in chapter 3 and on the map (enclosed). KK: Karakoram, S: suture, Ko: Kohistan. VC: volcanoclastic and calcareous sequences, Kk-GD: sheared gabbros and diorites, T: calcareous turbidites, ST: serpentinites and talcschists, DV: Drosh volcanites, GBa: Gawuch meta-basalts, G: granites, M: Gambir monzonite, S-GD, gabbros and diorites, mD: mafic dykes, MD: Mirkhani diorite, Ko-GBa, meta-gabbros and -diorites, Dy: granitic dykes.*

3. Results

Results of the major and trace element data are compiled in Table B.2.

3.1 Major elements

The intrusions range from 46.4 to 72.0 wt% SiO_2 (Table B.2) covering a large range from basic to acid rocks. The calculated CIPW norm nomenclature (calculated with 'IGNEOUS' by T. Dunn, 1997, University of New Brunswick) of the intrusions are olivine-gabbro for sample 01B24, monzogabbro for sample 20.1, quartz monzodiorite for samples 01B16 and sh2500, monzodiorite for samples 01A29 and 01A62, granodiorite for samples 01B25, 01B22, 01B04 and 01B77 and granite for samples 01A07 and 01A50b. Two groups can be distinguished when plotted in a total alkalis versus silica (TAS) diagram (Fig. B.2): (1) a gabbro-diorite and (2) a granite group.

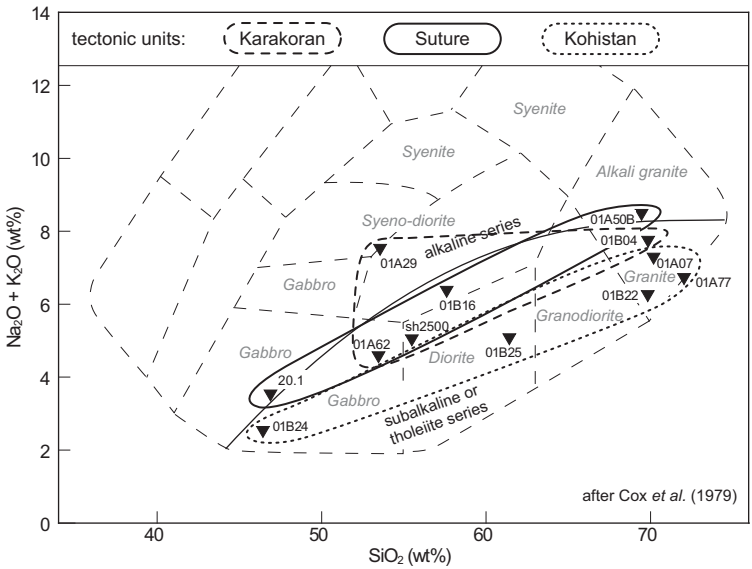

***Fig. B.2**. Chemical classification (total alkalis versus silica - TAS) diagram for plutonites after Cox et al. (1979) and Wilson (1989). The curved solid line subdivides the alkaline (above) from the subalkaline (tholeiitic) rocks (below). The majority of the intrusions plot into the subalkaline field. Note the trend of the Kohistan samples (light grey field) lying below the suture and Karakoram SiO_2-total alkali trend (darker grey fields).*

Samples 01B24 and 20.1 show the least 'evolved' character of group 1 with less than 47% wt SiO_2. The other group 1 samples (01A29, 01A62, sh2500, 01B16 and 01B25) have higher SiO_2 contents between 53 and 62 wt%. Group

2 granites are significantly more fractionated having SiO_2 contents of 69 to 72 wt%. The nomenclature for these rocks used in chapter 3 and on the map (enclosed) is a combination of thin section petrography, the CIPW norm calculation and the TAS diagram. Considering the samples in terms of tectonic setting, the Kohistan plutonic rocks define a SiO_2-total alkalis trend with lower total alkali contents than the Karakoram and suture plutons (Fig. B.2). The Karakoram and suture samples show similar total alkali and SiO_2 compositions.

Volcanites are illustrated using the TAS plot by Le Maitre *et al.* (1989, Fig. B.3). The Karakoram volcanites show a bimodal distribution. There is a 'low-silica' group with SiO_2 contents between 47 and 50 wt%, and a 'high-silica' group with SiO_2 contents between 65 and 77 wt%. Disregarding the 'high-silica' Karakoram samples, the plot shows a distribution similar to the plutonites in Fig. B.2. The Kohistan volcanites are all subalkaline and have lower total alkali contents than the suture and the 'low-silica' Karakoram volcanites.

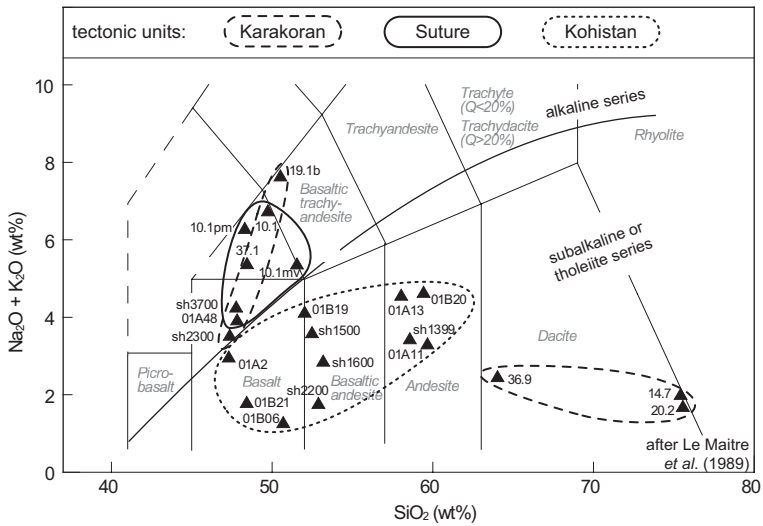

***Fig. B.3**. Chemical classification (total alkalis versus silica - TAS) diagram for volcanites after Le Maitre et al. (1989) and Wilson (1989). The curved solid line subdivides the alkaline (above) from the subalkaline (tholeiitic) rocks (below). Note the lower total alkali content of the Kohistan volcanites compared to the suture and 'low-silica' Karakoram volcanites.*

The field of the 'low-silica' Karakoram volcanites overlaps the suture volcanites field. This suggests that the two similar groups of volcanites may be derived from a similar or same magmatic source and thus erupted in the same area, i.e. the Karakoram active margin.

The suture volcanites all plot in the calc-alkaline field of the AFM diagram (Fig. B.4), whereas the Kohistan and Karakoram volcanites have generally higher FeO_{total} contents and plot on the calc-alkaline-tholeiitic differentiation trend line. The plutonic rocks plot all in the calc-alkaline field except the tholeiitic Kohistan *meta-gabbro*. The diagram further separates the significantly more differentiated, calc-alkaline 'group 2 granites' from the other, less differentiated samples.

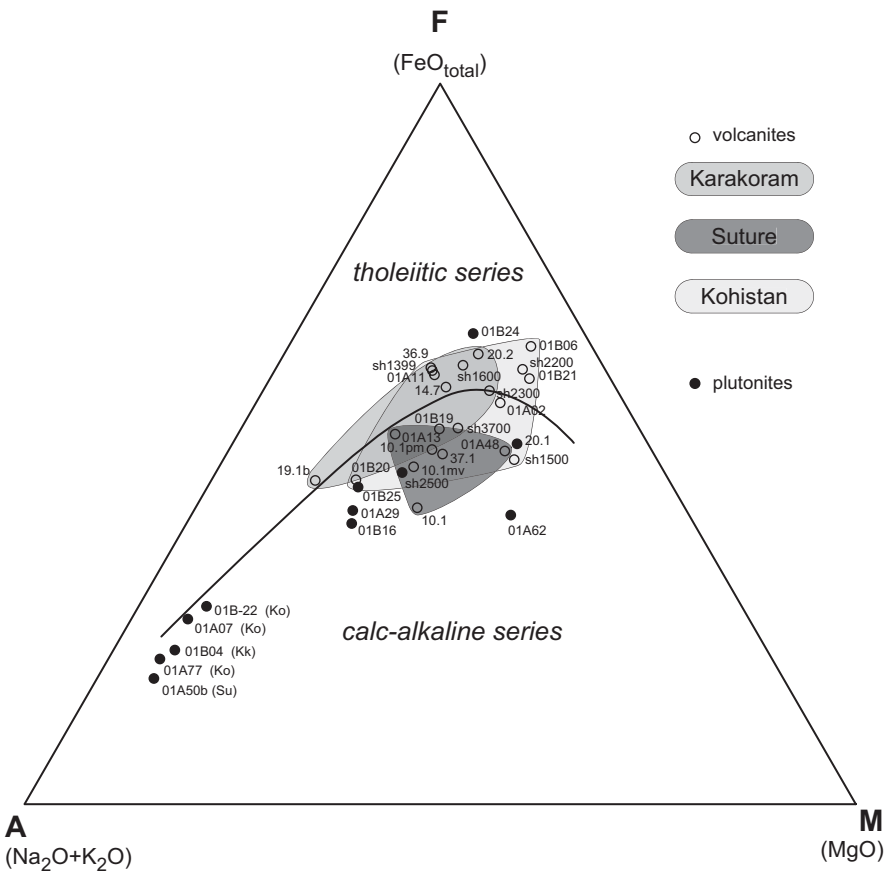

Fig. B.4*. AFM diagram with boundary (heavy line, after Kuno 1968) between the calc-alkaline field and the tholeiitic field. The intrusions (filled circles) plot all in the calc-alkaline field, except the tholeiitic Kohistan meta-gabbro (01B24). The 'group 2 granites' (01A50b, 01A77, 01B04, 01A07 and 01B22) represent the most differentiated calc-alkaline rocks. The volcanites (open circles in shaded fields) show less differentiation than the plutonites. The suture volcanites plot in the calc-alkaline field, whereas some of the Karakoram and suture volcanites plot in the tholeiitic field.*

tectonic unit	Karakoram					Suture				
sample nr.	14.7	19.1-b	20.2	sh2300	sh3700	37.1	01A-48	10.1	10.1pm	10.1mv
major elements [wt%]										
SiO_2	75.41	50.55	75.54	47.42	47.77	48.51	47.83	49.73	48.46	51.53
TiO_2	0.85	1.05	0.40	2.18	1.31	3.03	1.89	1.15	1.19	0.98
Al_2O_3	9.93	19.22	9.15	14.06	16.91	16.90	13.36	17.35	17.99	16.71
Fe_2O_3	5.54	8.05	7.53	13.04	10.08	11.85	10.99	8.54	9.90	8.25
MnO	0.18	0.18	0.31	0.18	0.17	0.17	0.18	0.11	0.20	0.17
MgO	2.11	2.26	2.87	6.25	5.04	6.39	7.52	5.57	4.94	4.25
CaO	2.65	8.26	0.86	10.32	10.09	3.78	10.11	4.85	8.93	7.25
Na_2O	1.00	1.77	0.66	3.36	2.23	3.05	3.67	6.00	3.54	3.05
K_2O	0.96	5.84	1.05	0.14	2.00	3.14	0.24	0.69	1.81	2.30
P_2O_5	0.07	0.67	0.11	0.19	0.27	0.75	0.15	0.27	0.24	0.23
Cr_2O_3	0.07	0.01	0.01	0.04	0.01	0.03	0.04	0.02	0.01	0.01
NiO	0.02	0.00	0.02	0.01	0.00	0.02	0.02	0.01	0.00	0.00
LOI	1.54	1.79	1.97	2.74	3.69	1.71	3.82	5.52	2.43	4.65
Total	100.32	99.64	100.48	99.93	99.58	99.33	99.83	99.82	99.65	99.38
trace elements [ppm]										
V*	87	149	126	370	301	238	370	220	239	193
Cr*	235	32	34	291	57	194	320	156	44	42
Co*	25	18	42	47	32	32	44	35	31	27
Ni*	111	13	132	95	27	119	110	56	29	30
Cu*	52	40	110	114	81	39	39	38	33	187
Zn*	73	90	90	105	87	147	78	71	113	94
Ga*	13	23	12	20	18	19	17	18	20	19
Y	17.99	29.11	19.24	29.53	23.48	34.03	24.24	16.77	21.32	21.66
Zr*	126	284	80	135	121	231	115	108	110	120
Th	9.51	18.27	6.96	1.07	4.28	4.48	0.89	3.46	3.05	4.63
U	1.419	3.858	1.065	0.313	1.000	0.889	0.225	0.839	1.227	0.977
Cs	3.16	1.77	2.20	0.13	5.85	4.50	0.23	0.44	0.52	1.27
Ba	185.34	785.02	160.48	19.22	196.54	314.08	81.13	124.74	317.01	317.59
Rb	61.73	188.55	38.21	1.03	98.53	102.11	3.38	18.29	52.48	76.98
Sr	121.41	716.78	67.71	410.26	554.66	91.89	197.69	228.06	579.98	480.97
Nb	13.14	22.00	7.23	10.27	9.99	50.34	7.96	9.19	8.69	10.94
Ta	0.978	1.237	0.523	0.660	0.632	2.929	0.529	0.570	0.560	0.666
Pb	30.24	31.01	8.76	1.09	4.58	12.56	1.02	2.51	4.92	5.78
S*	<3	<3	<3	<3	912	10	<3	<3	42	370
Sc*	14	8	14	41	23	29	46	41	20	18
As*	10	6	20	5	3	5	3	3	3	4
rare earth elements [ppm]										
La	35.63	64.69	21.67	9.44	24.49	24.66	7.55	22.31	19.90	25.54
Ce	78.54	130.79	36.09	25.43	52.83	67.32	20.35	45.86	43.46	51.75
Pr	8.59	13.84	5.25	3.50	6.27	8.75	2.94	5.36	5.11	5.75
Nd	33.02	52.31	20.36	17.48	26.14	37.63	14.61	22.08	21.93	23.36
Sm	5.59	8.47	3.63	4.62	5.14	7.66	3.95	4.39	4.52	4.50
Eu	1.13	2.00	0.69	1.68	1.62	2.29	1.48	1.56	1.48	1.44
Gd	4.19	7.08	3.46	5.68	5.13	7.86	4.80	4.15	4.70	4.43
Tb	0.559	0.978	0.534	0.919	0.744	1.146	0.768	0.594	0.673	0.664
Dy	3.44	5.75	3.54	6.15	4.74	7.02	5.00	3.49	4.28	4.09
Ho	0.660	1.087	0.727	1.183	0.897	1.334	0.975	0.634	0.848	0.826
Er	1.83	2.98	2.11	3.14	2.43	3.45	2.56	1.62	2.23	2.23
Tm	0.271	0.421	0.321	0.415	0.338	0.475	0.346	0.210	0.312	0.321
Yb	1.69	2.71	2.08	2.61	2.16	2.86	2.11	1.25	1.94	1.98
Lu	0.249	0.419	0.345	0.348	0.340	0.432	0.311	0.170	0.282	0.318

***Table B.2**. XRF and ICP-MS results. Stars mark trace elements that were measured by XRF.*

tect. unit	Kohistan									
sample nr.	01A-2	01B-6	01B-19	01B-20	01B-21	01A-13	36.9	01A-11	sh1399	sh1500
major elements [wt%]										
SiO_2	47.30	50.71	52.04	59.44	48.43	58.05	64.00	59.67	58.60	52.45
TiO_2	1.56	0.93	1.32	0.77	1.41	0.95	0.51	0.66	0.62	0.45
Al_2O_3	16.22	15.05	16.74	14.79	15.90	17.18	14.83	16.32	15.97	15.52
Fe_2O_3	10.81	10.54	8.91	5.50	10.78	7.90	7.03	9.34	9.85	10.04
MnO	0.25	0.18	0.17	0.15	0.19	0.17	0.17	0.16	0.19	0.17
MgO	5.65	4.81	4.04	2.12	5.64	2.98	2.22	3.09	3.20	7.30
CaO	10.08	10.03	5.58	5.25	9.58	5.33	6.15	7.20	7.86	9.19
Na_2O	2.83	1.15	2.95	1.95	1.42	3.21	1.39	2.97	3.09	2.69
K_2O	0.09	0.09	1.14	2.66	0.35	1.32	1.06	0.31	0.32	0.86
P_2O_5	0.22	0.10	0.19	0.15	0.15	0.21	0.18	0.10	0.09	0.06
Cr_2O_3	0.02	0.01	0.01	0.01	0.02	0.01	0.01	0.01	0.01	0.04
NiO	0.01	0.00	0.00	0.00	0.00	0.00	0.00	0.00	0.00	0.01
LOI	4.59	5.46	6.12	6.09	5.38	2.61	2.53	0.53	0.47	0.77
Total	99.62	99.07	99.22	98.87	99.25	99.93	100.07	100.37	100.28	99.55
trace elements [ppm]										
V*	331	346	295	130	352	161	113	233	272	283
Cr*	148	68	37	68	120	56	41	53	50	268
Co*	44	40	33	16	39	22	19	23	27	34
Ni*	60	17	13	7	29	14	5	8	10	55
Cu*	70	145	119	22	47	44	41	114	88	99
Zn*	95	84	96	78	98	100	88	84	92	73
Ga*	18	16	19	17	17	19	13	15	14	14
Y	20.87	18.71	20.03	21.59	24.21	22.28	20.75	19.43	17.09	10.58
Zr*	121	58	129	247	101	172	53	57	41	29
Th	1.71	0.71	1.95	5.97	2.67	6.12	1.04	0.54	0.64	0.27
U	0.489	0.201	0.569	1.202	0.737	1.633	0.369	0.126	0.173	0.112
Cs	0.27	1.06	8.54	19.56	2.93	5.20	0.62	0.16	0.08	0.53
Ba	54.91	44.13	262.09	425.59	159.99	483.32	150.87	34.33	51.36	79.07
Rb	1.31	1.80	32.30	94.30	8.74	47.34	19.64	4.81	2.57	17.38
Sr	628.40	95.33	311.90	227.98	339.00	524.52	482.19	104.79	384.95	168.40
Nb	9.94	1.44	9.76	3.72	9.76	18.77	1.64	1.13	1.09	0.44
Ta	0.539	0.077	0.521	0.159	0.546	1.231	0.085	0.064	0.067	0.024
Pb	8.57	2.52	3.24	40.14	9.91	16.09	5.07	2.52	3.14	1.30
S*	19	78	<3	<3	<3	<3	<3	<3	<3	9
Sc*	38	48	29	13	39	17	19	33	35	50
As*	16	<3	6	19	15	14	4	5	<3	5
rare earth elements [ppm]										
La	13.36	4.45	12.34	20.66	11.12	23.54	6.65	3.90	3.46	1.96
Ce	30.54	10.38	27.72	44.68	26.23	50.98	15.76	9.75	8.00	4.80
Pr	4.01	1.50	3.60	5.27	3.29	5.66	2.17	1.44	1.30	0.74
Nd	18.55	7.70	16.11	20.96	14.40	22.78	10.67	7.38	6.25	3.90
Sm	4.16	2.16	3.82	4.37	3.54	4.48	2.76	2.10	1.90	1.18
Eu	1.39	0.69	1.27	1.08	1.13	1.29	0.90	0.77	0.64	0.44
Gd	4.13	2.66	3.75	3.98	3.77	4.55	3.30	2.71	2.51	1.47
Tb	0.681	0.493	0.629	0.659	0.678	0.685	0.535	0.481	0.420	0.272
Dy	3.99	3.23	3.74	3.96	4.36	4.34	3.67	3.35	3.14	1.79
Ho	0.841	0.741	0.802	0.841	1.000	0.873	0.786	0.753	0.662	0.423
Er	2.25	2.14	2.26	2.36	2.93	2.35	2.29	2.15	1.92	1.23
Tm	0.321	0.324	0.321	0.331	0.423	0.344	0.330	0.324	0.281	0.191
Yb	1.93	2.05	2.07	2.10	2.86	2.21	2.21	2.20	1.88	1.20
Lu	0.296	0.355	0.331	0.317	0.448	0.345	0.326	0.353	0.289	0.206

***Table B.2ff**. XRF and ICP-MS results. Stars mark trace elements that were measured by XRF.*

tect. unit	Kohistan		Karakoram			Suture			
sample nr.	sh1600	sh2200	01B04	01A62	01A29	sh2500	01A50b	20.1	01B16
major elements [wt%]									
SiO_2	53.17	52.87	69.85	53.45	53.55	55.50	69.46	46.96	57.60
TiO_2	0.68	0.59	0.44	1.06	1.54	0.77	0.30	1.59	0.50
Al_2O_3	14.96	17.74	15.14	14.48	17.74	18.49	15.10	16.07	16.88
Fe_2O_3	10.80	10.02	2.32	8.75	7.62	7.25	1.97	11.11	6.05
MnO	0.28	0.16	0.05	0.17	0.14	0.15	0.03	0.19	0.09
MgO	4.00	4.88	0.80	8.39	3.52	3.52	0.73	7.70	3.07
CaO	6.81	10.31	1.85	7.54	5.62	7.67	2.43	9.09	6.30
Na_2O	2.62	1.38	4.11	3.26	4.97	3.51	2.71	2.51	4.79
K_2O	0.20	0.35	3.60	1.36	2.52	1.51	5.74	1.03	1.55
P_2O_5	0.08	0.07	0.13	0.22	0.64	0.22	0.06	0.24	0.25
Cr_2O_3	0.01	0.02	0.01	0.05	0.01	0.01	0.02	0.02	0.02
NiO	0.00	0.00	0.00	0.02	0.00	0.00	0.00	0.01	0.00
LOI	5.47	0.62	0.91	1.25	0.83	1.08	1.20	3.62	1.52
Total	99.07	98.99	99.21	100.00	98.69	99.68	99.74	100.14	98.61
trace elements [ppm]									
V*	288	341	32	229	125	147	44	280	145
Cr*	36	129	105	343	81	95	126	146	158
Co*	35	32	6	33	23	23	6	42	17
Ni*	12	14	6	106	18	16	6	73	25
Cu*	125	1003	11	59	25	20	8	41	71
Zn*	102	74	47	75	64	72	20	89	42
Ga*	15	17	17	15	20	18	14	17	17
Y	13.55	11.23	7.78	27*	26.26	19*	10.88	19.91	14.91
Zr*	35	29	137	90	273	105	128	83	90
Th	0.33	0.19	13.98	<2*	14.05	4*	11.87	2.61	5.42
U	0.108	0.073	1.857	<2*	2.567	<2*	2.205	0.471	1.274
Cs	0.14	0.15	1.33		4.32		0.63	0.70	0.17
Ba	35.02	22.33	693.67	395*	358.00	382*	853.40	138.66	1440.86
Rb	3.55	4.33	91.39	44*	66.50	60*	117.68	36.61	21.59
Sr	145.12	53.30	353.77	670*	673.14	537*	282.50	535.14	589.48
Nb	0.56	0.60	15.63	9*	54.22	9*	8.17	7.21	6.44
Ta	0.029	0.025	1.004		2.660		0.643	0.428	0.402
Pb	1.76	1.40	18.46	16*	6.00	12*	6.86	2.51	4.06
S*	<3	481	<3	21	188	29	<3	6	4613
Sc*	43	42	4	38	14	16	4	42	19
As*	4	5	4	4	6	5	4	4	6
rare earth elements [ppm]									
La	2.34	1.70	35.40	14*	57.06	23*	21.32	15.58	19.08
Ce	6.11	4.44	66.45	43*	96.41	33*	32.10	34.71	32.88
Pr	0.94	0.72	6.52		9.51		2.95	4.32	3.50
Nd	5.08	4.01	21.46	19*	33.46	18*	9.70	19.02	13.16
Sm	1.58	1.24	3.15		5.74		1.65	4.17	2.56
Eu	0.61	0.50	0.73		1.67		0.44	1.42	0.80
Gd	2.01	1.58	2.06		4.93		1.52	4.36	2.47
Tb	0.368	0.289	0.291		0.801		0.245	0.649	0.397
Dy	2.41	1.93	1.49		4.62		1.54	4.11	2.34
Ho	0.555	0.449	0.302		0.982		0.347	0.773	0.523
Er	1.64	1.32	0.83		2.67		1.07	2.01	1.51
Tm	0.249	0.203	0.118		0.378		0.172	0.268	0.231
Yb	1.57	1.29	0.74		2.42		1.18	1.70	1.53
Lu	0.254	0.221	0.115		0.357		0.175	0.249	0.232

***Table B.2fff**. XRF and ICP-MS results. Stars mark trace elements that were measured by XRF.*

tect. unit	Kohistan				
sample nr.	01B25	01B24	01B22	01A07	01A77
major elements [wt%]					
SiO_2	61.41	46.43	69.83	70.22	72.04
TiO_2	0.45	1.10	0.38	0.33	0.25
Al_2O_3	16.33	20.99	14.88	15.59	14.40
Fe_2O_3	5.89	12.18	2.67	2.76	1.83
MnO	0.11	0.16	0.04	0.05	0.04
MgO	2.39	3.87	0.77	0.76	0.55
CaO	5.53	11.69	2.92	2.58	2.26
Na_2O	2.94	2.11	3.24	3.41	3.64
K_2O	2.10	0.39	2.98	3.84	3.06
P_2O_5	0.15	0.09	0.12	0.13	0.08
Cr_2O_3	0.01	0.01	0.01	0.03	0.02
NiO	0.00	0.00	0.00	0.00	0.00
LOI	1.93	0.44	0.39	0.26	0.38
Total	99.24	99.45	98.22	99.96	98.55
trace elements [ppm]					
V*	127	418	38	40	24
Cr*	87	54	77	169	104
Co*	16	33	5	4	5
Ni*	6	5	3	7	4
Cu*	66	119	24	10	6
Zn*	38	77	52	51	35
Ga*	14	20	16	17	15
Y	12.98	10.15	3.54	7*	11.21
Zr*	86	30	212	139	140
Th	8.71	1.43	10.58	8*	12.23
U	1.531	0.284	0.183	<2*	2.261
Cs	1.36	0.25	0.55		0.64
Ba	604.72	56.25	1066.56	1035*	852.00
Rb	43.75	4.99	65.79	103*	120.19
Sr	414.79	392.75	396.16	652*	306.83
Nb	3.86	2.18	6.48	10*	8.32
Ta	0.213	0.131	0.153		0.649
Pb	2.97	3.37	13.52	24*	6.98
S*	<3	644	9	<3	<3
Sc*	17	31	4	5	6
As*	8	4	5	4	3
rare earth elements [ppm]					
La	19.40	4.92	42.59	28*	21.19
Ce	38.41	11.51	76.09	54*	31.89
Pr	4.32	1.54	7.18		2.91
Nd	16.87	6.95	23.09	26*	9.77
Sm	3.20	1.76	2.94		1.64
Eu	0.92	0.68	0.77		0.45
Gd	2.57	1.77	1.70		1.53
Tb	0.393	0.305	0.201		0.249
Dy	2.28	1.89	0.85		1.55
Ho	0.493	0.418	0.148		0.357
Er	1.44	1.18	0.33		1.10
Tm	0.213	0.163	0.038		0.173
Yb	1.45	1.09	0.20		1.22
Lu	0.233	0.173	0.028		0.191

***Table B.2ffff**. XRF and ICP-MS results. Stars mark trace elements that were measured by XRF.*

3.2 Trace elements

3.2.1 Karakoram samples

The MORB-normalised REE patterns of the Karakoram samples are shown in Fig. B.5. It shows a similar pattern with a significant positive Pb peak and negative Nb and Ta anomaly for all the volcanites, except for sample sh2300. This sample is depleted in the low field strength, large ion lithophile elements (LILE) Cs, Rb, Ba, Th, U and represents a more primitive (NMORB-type) volcanite than the others (Fig. B.5a). The plutonites show a trace element distribution similar to the volcanites, but they are less depleted in Nb-Ta relative to their neighbouring elements.

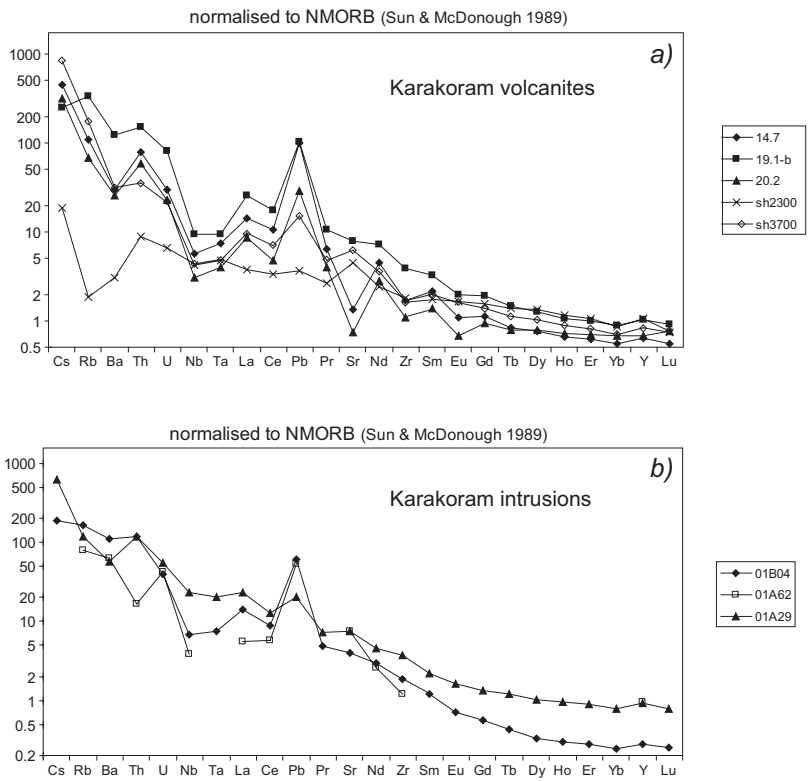

***Fig. B.5**. MORB-normalised trace element composition of the Karakoram (**a**) volcanites and (**b**) plutonites.*

On Fig. B.6, chondrite-normalised REEs of the Karakoram volcanites are plotted together with Karakoram intrusions. The light rare earth elements

(LREE, La to Nd) are enriched relative to the heavy rare earth elements (HREE, Tb to Lu), whereas the sample sh2300 shows a smaller difference between LREE and HREE than the others. The REE patterns of the three intrusions do not differ from volcanites, except sample 01B04, that is slightly depleted in HREE.

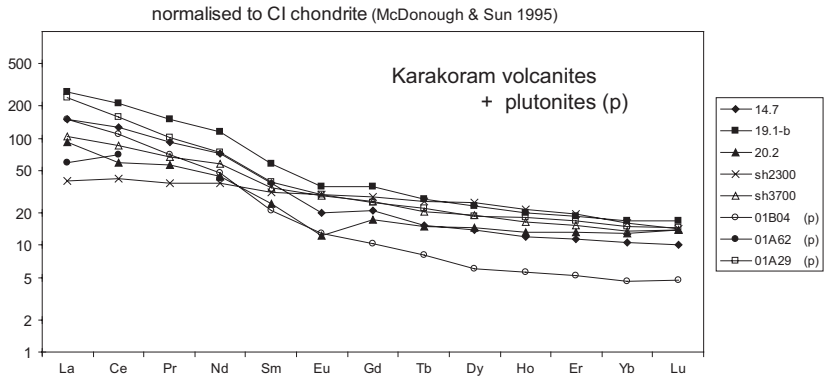

***Fig. B.6**. Chondrite-normalised rare earth element composition of Karakoram volcanites and plutonites (labelled with 'p').*

3.2.2 Suture samples

The MORB-normalised suture volcanites and plutonites show trace element patterns very similar to the Karakoram samples (Fig. B.7). Nb and Ta are less depleted than the Karakoram volcanites, or even slightly enriched relative to Th-U and LREE (sample 10.1_su). The suture plutonites show only small differences relative to the Karakoram plutonites, such as slightly enriched Cs, Nb, Ta and La (Fig. B.7b).

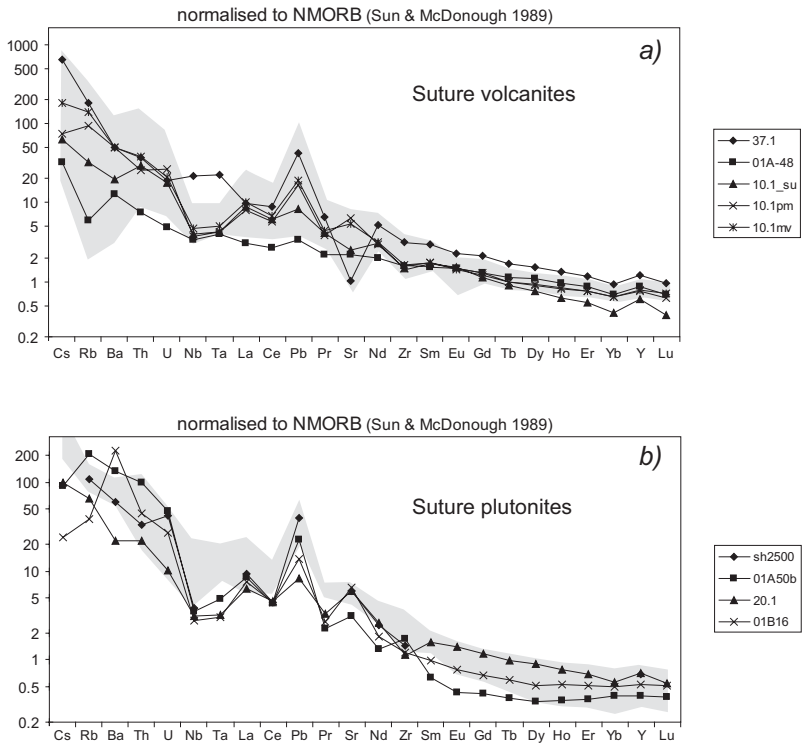

***Fig. B.7**. MORB-normalised trace element composition of the (**a**) suture volcanites and (**b**) plutonites. The shaded areas indicate the range of the Karakoram samples from Fig. B.5.*

There are no major difference between the chondrite-normalised REEs of the suture and Karakoram samples (Fig. B.8). But, the two suture plutonites 01A50b and 01B16 have less enriched LREE (La to Eu) patterns than the other samples.

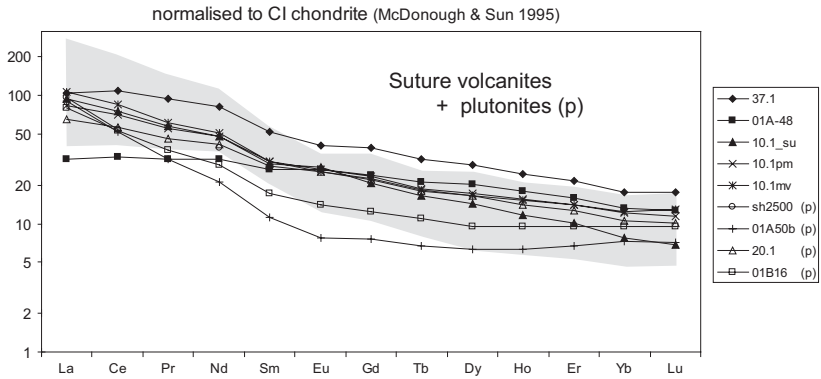

Fig. B.8. *Chondrite-normalised rare earth element composition of suture volcanites and plutonites (labelled with 'p'). The shaded area indicates the range of the Karakoram samples from Fig. B.6*

3.2.3 Kohistan samples

The MORB-normalised REEs of the Kohistan volcanites generally show a trend similar to the Karakoram and suture samples (Fig. B.9a). About half of the samples are more depleted, in particular in Nb, Ta, La and Ce, than the others.

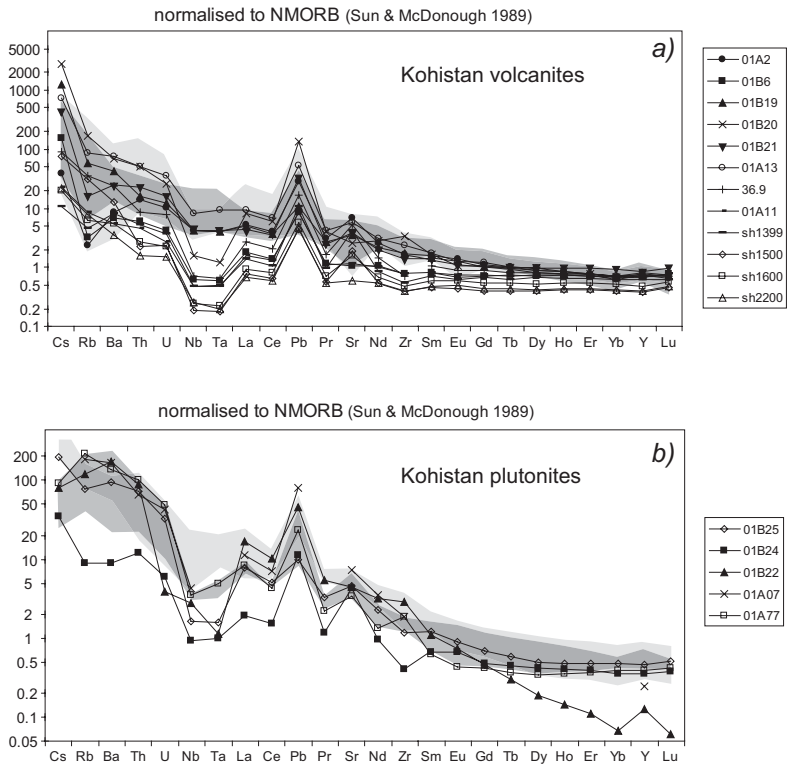

Fig. B.9. *MORB-normalised trace element composition of the (**a**) Kohistan volcanites and (**b**) plutonites. The shaded areas indicate the range of the Karakoram (light grey) and suture (dark grey) samples from Figs. B.5 and B.7.*

The MORB-normalised REE patterns of the Kohistan intrusions largely overlap with the suture intrusions field (Fig. B.9b). The tholeiitic *meta-gabbro* (01B24) however, is significantly more depleted in almost all trace elements. The *granitic dyke* (01B22) shows anomalously, increasingly depleted HREE compared to all the other samples.

The Kohistan volcanites on the chondrite-normalised REE spidergram are generally more depleted than the Karakoram and suture zone samples (Fig. B.10a). The two Kohistan volcanite units, the Drosh volcanites (samples 01A2 to 01A13) and the Gawuch greenschists and Gawuch meta-basalts (samples

36.9 to sh2200) can be distinguished: The Drosh volcanites have REE patterns similar to those of the suture volcanites, whereas the Gawuch meta-volcanites are depleted in LREE and show significantly flatter patterns than those of the Drosh volcanites.

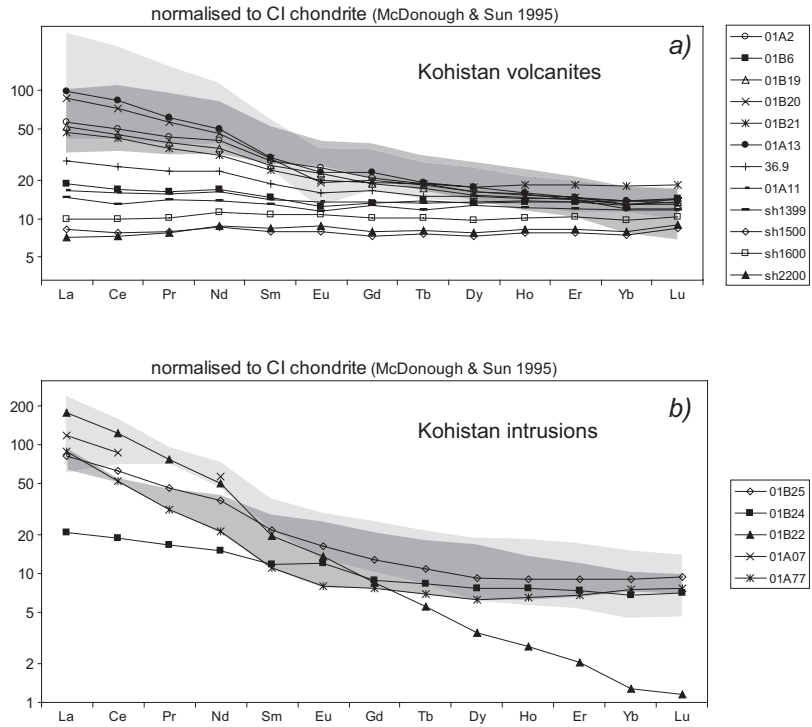

***Fig. B.10**. Chondrite-normalised rare earth element composition of Kohistan volcanites (**a**) and intrusions (**b**). The shaded areas indicate the range of the Karakoram (light grey) and suture (dark grey) samples from Figs. B.6 and B.8.*

The REE pattern of the Kohistan intrusions overlaps with those of the Karakoram and suture samples, except for samples 01B24 and 01B22. The tholeiitic *meta-gabbro* (01B24) has depleted LREE (La to Nd), the *granitic dyke* (01B22) increasingly depleted HREE (Tb to Lu).

3.3 Conclusions

Major element results (total alkalis and SiO_2) allowed to distinguish the alkaline Karakoram and suture volcanites (disregarding the 3 'high-silica' Karakoram samples) from the subalkaline Kohistan volcanites. Similarly, the Karakoram and suture plutonic rocks show distinctly, higher total alkalis-SiO_2 trends than the Kohistan plutonites. Thus, the calc-alkaline suture samples show a strong Karakoram affinity and are interpreted to represent a similar (or same?), subduction-related magmatism at the active Karakoram margin.
Trace element compositions confirm the above statement. They show similar compositions of Karakoram and suture samples that partly overlap with, and partly are more enriched than the Kohistan samples.

Appendix B: Stratigraphic age table

Era	Period	Epoch	Stage Age	Age [Ma]
Cenozoic	Neogene	Holocene		0.01
		Pleistocene	Upper	0.12
			Middle	0.78
			Lower	1.81
		Pliocene	Gelasian	2.59
			Piacenzian	3.60
			Zanclean	5.33
		Miocene	Messinian	7.25
			Tortonian	11.61
			Serravallian	13.65
			Langhian	15.97
			Burdigalian	20.43
			Aquitanian	23.03
	Paleogene	Oligocene	Chattian	28.4
			Rupelian	33.9
		Eocene	Priabonian	37.2
			Bartonian	40.4
			Lutetian	48.6
			Ypresian	55.8
		Paleocene	Thanetian	58.7
			Selandian	61.7
			Danian	65.5
Mesozoic	Cretaceous	Upper	Maastrichtian	70.6
			Campanian	83.5
			Santonian	85.8
			Coniacian	89.3
			Turonian	93.5
			Cenomanian	99.6
		Lower	Albian	112.0
			Aptian	125.0
			Barremian	130.0
			Hauterivian	136.4
			Valanginian	140.2
			Berriasian	145.5

Era	Period	Epoch		Stage Age	Age [Ma]
Mesozoic	Jurassic	Upper		Tithonian	145.5
				Kimmeridgian	150.8
				Oxfordian	155.0
		Middle		Callovian	161.2
				Bathonian	164.7
				Bajocian	167.7
				Aalenian	171.6
		Lower		Toarcian	175.6
				Pliensbachian	183.0
				Sinemurian	189.6
				Hettangian	196.5
	Triassic	Upper		Rhaetian	199.6
				Norian	203.6
				Carnian	216.5
		Middle		Ladinian	228.0
				Anisian	237.0
		Lower		Olenekian	245.0
				Induan	249.7
Paleozoic	Permian	Lopingian		Changhsingian	251.0
				Wuchiapingian	253.8
		Guadalupian		Capitanian	260.4
				Wordian	265.8
				Roadian	268.0
		Cisuralian		Kungurian	270.6
				Artinskian	275.6
				Sakmarian	284.4
				Asselian	294.6
	Carboniferous	Penn-sylvanian	Upper	Gzhelian	299.0
				Kasimovian	303.9
			Middle	Moscovian	306.5
			Lower	Bashkirian	311.7
		Missis-sippian	Upper	Serpukhovian	318.1
			Middle	Visean	326.4
			Lower	Tournaisian	345.3
					359.2

Stratigraphic age table: Carboniferous to Neogene (Data from International Commission on Stratigraphy 2003).

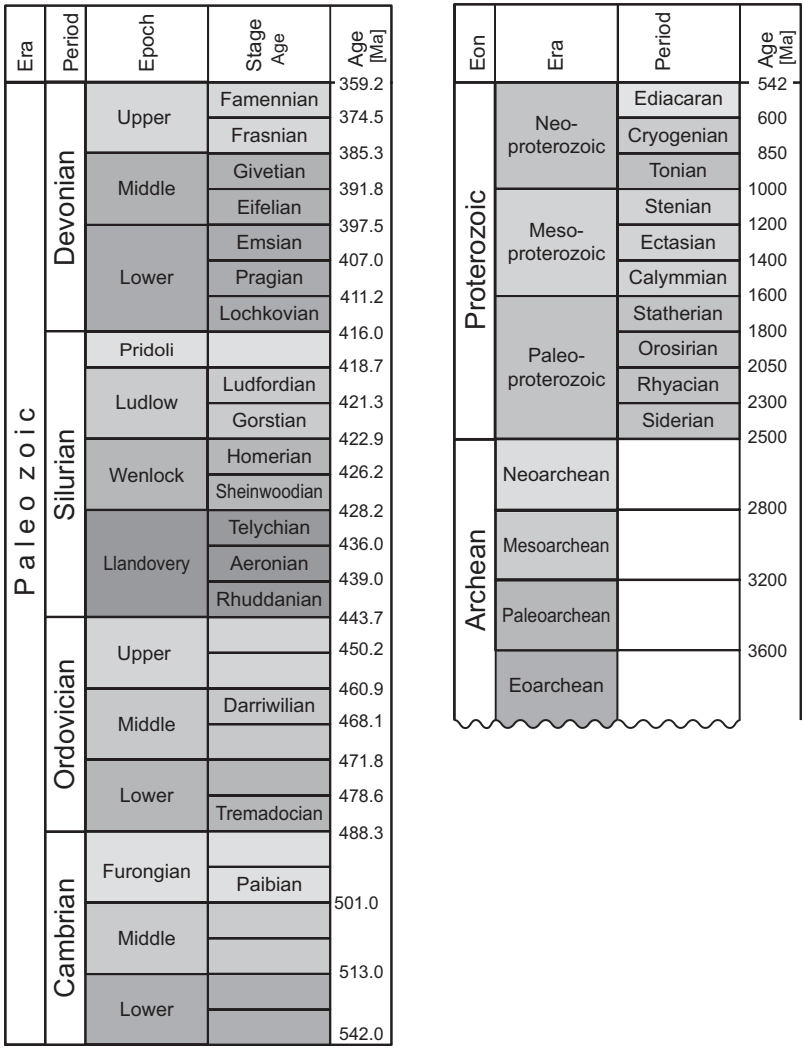

Stratigraphic age table: Precambrian to Devonian (Data from International Commission on Stratigraphy 2003).

References

Albarede, F., Simonetti, A., Vervoort, J.D., Blichert-Toft, J. and Abouchami, W., 1998, A Hf-Nd isotopic correlation in ferromanganese nodules: *Geophysical Research Letters*, v. 25, p. 3895-3898.

Anczkiewicz, R. and Vance, D., 2000, Isotopic constraints on the evolution of metamorphic conditions in the Jijal-Patan Complex and Kamila Belt of the Kohistan Arc, Pakistan Himalaya, *in* Khan, M.A., Treloar, P.J., Searle, M.P. and Jan, M.Q., eds., *Tectonics of the Nanga Parbat syntaxis and the western Himalaya*: *Geological Society Special Publications*, Geological Society of London, v. 170, p. 321-331.

Anczkiewicz, R., Oberli, F., Burg, J.P., Villa, I.M., Gunther, D. and Meier, M., 2001, Timing of normal faulting along the Indus Suture in Pakistan Himalaya and a case of major Pa-231/U-235 initial disequilibrium in zircon: *Earth and Planetary Science Letters*, v. 191, p. 101-114.

Anderson, E.M., 1905, The dynamics of faulting: *Transactions of the Edinburgh Geological Society*, v. 8, p. 837-402.

Arbaret, L., Burg, J.P., Zeilinger, G., Chaudhry, N., Hussain, S., Dawood, H., Khan, M.A., Treloar, P.J., Searle, M.P. and Jan, M.Q., 2000, Pre-collisional anastomosing shear zones in the Kohistan Arc, NW Pakistan, *in* Khan, M.A., Treloar, P.J., Searle, M.P. and Jan, M.Q., eds., *Tectonics of the Nanga Parbat syntaxis and the western Himalaya*: *Geological Society Special Publications*, Geological Society of London, v. 170, p. 295-311.

Argand, E., 1924, La tectonique de l'Asie: *Comptes-rendus du 13eme congrès géologique international*, Liège, p. 171-372.

Armijo, R., Carey, E. and Cisternas, A., 1982, The inverse problem in micro-tectonics and the separation of tectonic phases: *Tectonophysics*, v. 82, p. 145-160.

Bard, J.P., 1983, Metamorphism of an Obducted Island-Arc - Example of the Kohistan Sequence (Pakistan) in the Himalayan Collided Range: *Earth and Planetary Science Letters*, v. 65, p. 133-144.

Bard, J.P., Maluski, H., Matte, P. and Proust, F., 1980, The Kohistan sequence; crust and mantle of an obducted island arc, *in* Tahirkheli, R.A.K., Jan, M.Q. and Majid, M., eds., Proceedings of the International Committee on Geodynamics Group 6 meeting, Special Issue, *Geological Bulletin of the University of Peshawar*, v. 13, p. 87-94.

Beck, R.A., Burbank, D.W., Sercombe, W.J., Riley, G.W., Barndt, J.K., Berry, J.R., Afzal, J., Khan, A.M., Jurgen, H., Metje, J., Cheema, A., Shafique, N.A., Lawrence, R.D. and Khan, M.A., 1995, Stratigraphic

Evidence for an Early Collision between Northwest India and Asia: *Nature*, v. 373, p. 55-58.

Bernoulli, D. and Weissert, H., 1985, Sedimentary Fabrics in Alpine Ophicalcites, South Pennine Arosa Zone, Switzerland: *Geology*, v. 13, p. 755-758.

Blichert-Toft, J. and Albarède, F., 1997, The Lu-Hf isotope geochemistry of chondrites and the evolution of the mantle-crust system: *Earth and Planetary Science Letters*, v. 148, p. 243-258.

Blichert-Toft, J., Chauvel, C. and Albarède, F., 1997, Separation of Hf and Lu for high-precision isotope analysis of rock samples by magnetic sector multiple collector ICP-MS: *Contributions to Mineralogy and Petrology*, v. 127, p. 248-260.

Boillot, G., Recq, M., Winterer, E.L., Meyer, A.W., Applegate, J., Baltuck, M., Bergen, J.A., Comas, M.C., Davies, T.A., Dunham, K., Evans, C.A., Girardeau, J., Goldberg, G., Haggerty, J., Jansa, L.F., Johnson, J.A., Kasahara, J., Loreau, J.P., Lunasierra, E., Moullade, M., Ogg, J., Sarti, M., Thurow, J. and Williamson, M., 1987, Tectonic Denudation of the Upper Mantle Along Passive Margins - a Model Based on Drilling Results (Odp Leg-103, Western Galicia Margin, Spain): *Tectonophysics*, v. 132, p. 335-342.

Boulin, J., 1981, Afghanistan structure, Greater India concept and eastern Tethys evolution: *Tectonophysics*, v. 72, p. 261-287.

—, 1988, Hercynian and Eocimmerian Events in Afghanistan and Adjoining Regions: *Tectonophysics*, v. 148, p. 253-278.

Brookfield, M.E. and Reynolds, P.H., 1981, Late Cretaceous Emplacement of the Indus Suture Zone Ophiolitic Melanges and an Eocene-Oligocene Magmatic Arc on the Northern Edge of the Indian Plate: *Earth and Planetary Science Letters*, v. 55, p. 157-162.

Buchroithner, M.F., 1980, Outline of the Geology of the Afghan Pamirs: Tectonophysics, v. 62, p. 13-35.

Buchroithner, M.F. and Gamerith, H., 1978, Geological map of Pamir-e-Wakhan, 1:250,000, *in* De Granchy, R.S. and Kostka, R., eds., *Grosser Pamir: Oesterreichisches Forschungsunternehmen 1975 in den Wakhan-Pamir/Afghanistan*: *Graz, Akademische Druck- und Verlagsanstalt*.

Buchroithner, M.F. and Gamerith, H., 1986, On the geology of the Tirich Mir area, central Hindu Kush (Pakistan), *Jahrbuch der Geologischen Bundesanstalt, Geologische Bundesanstalt,* Vienna, Austria, v. 128, p. 367-381.

Buchroithner, M.F. and Zimmer, K., 1998, Geological Map of Chitral (Hindu Kush, North Pakistan), 1:100,000, *Institute for Cartography*, Dresden University of Technology.

Burg, J.P., Bodinier, J.L., Chaudhry, S., Hussain, S. and Dawood, H., 1998, Infra-arc mantle-crust transition and intra-arc mantle diapirs in the

Kohistan Complex (Pakistani Himalaya): petro-structural evidence: *Terra Nova*, v. 10, p. 74-80.

Burg, J.P., Célérier, B., Chaudhry, N., Ghazanfar, M., Gnehm, F. and Schnellmann, M., 2004, Fault analysis and paleostress evolution in large strain regions: methological and geological discussion of the southeastern Himalayan fold-and-thrust belt in Pakistan: *Journal of Asian Earth Sciences* (in press, corrected proof).

Célérier, B., 1995, Tectonic regime and slip orientation of reactivated faults: *Geophysical Journal International*, v. 121, p. 143-161.

Célérier, B., 1999, FSA: Fault Slip Analysis software: http://www.isteem.univ-montp2.fr/PERSO/celerier/software/fsa18.html.

Chandra, U., 1978, Seismicity, earthquake mechanisms and tectonics along the Himalayan Mountain range and vicinity: *Physics of the Earth and Planetary Interiors*, v. 16, p. 109-131.

Chauvel, C. and Blichert-Toft, J., 2001, A hafnium isotope and trace element perspective on melting of the depleted mantle: *Earth and Planetary Science Letters*, v. 190, p. 137-151.

Clift, P.D., Hannigan, R., Blusztajn, J. and Draut, A.E., 2002, Geochemical evolution of the Dras-Kohistan Arc during collision with Eurasia: Evidence from the Ladakh Himalaya, India: *The Island Arc*, v. 11, p. 255-273.

Coward, M.P., Windley, B.F., Broughton, R.D., Luff, I.W., Petterson, M.G., Pudsey, C.J., Rex Dave, C., Khan, M.A. and Ries Alison, C., 1986, Collision tectonics in the NW Himalayas, *in* Coward, M.P. and Ries-Alison, C., eds., *Collision tectonics*, *Geological Society Special Publications*, Geological Society of London, v. 19, p. 203-219.

Cox, K.G., Bell, J.D. and Pankhurst, R.J., 1979, *The interpretation of igneous rocks*: London, Allen and Unwin, 450 p.

Crawford, M.B. and Searle, M.P., 1992, Field Relationships and Geochemistry of Pre-Collisional (India-Asia) Granitoid Magmatism in the Central Karakoram, Northern Pakistan: *Tectonophysics*, v. 206, p. 171-192.

Danishwar, S., Stern, R.J. and Khan, M.A., 2001, Field relations and structural constraints for the Teru volcanic formation, northern Kohistan Terrane, Pakistani Himalayas: *Journal of Asian Earth Sciences*, v. 19, p. 683-695.

Debon, F., 1995, Incipient India-Eurasia Collision and Plutonism - the Lower Cenozoic Batura Granites (Hunza Karakoram, North Pakistan): *Journal of the Geological Society*, v. 152, p. 785-795.

Debon, F. and Khan, N.A., 1996, Alkaline orogenic plutonism in the Karakorum batholith: The Upper Cretaceous Koz Sar complex (Karambar valley, N Pakistan): *Geodinamica Acta*, v. 9, p. 145-160.

Debon, F., Le Fort, P., Dautel, D., Sonet, J. and Zimmermann, J.L., 1987a, Granites of western Karakorum and northern Kohistan (Pakistan); a

composite mid-Cretaceous to upper Cenozoic magmatism: *Lithos*, v. 20, p. 19-40.

Debon, F., Afzali, H., Lefort, P. and Sonet, J., 1987b, Major Intrusive Stages in Afghanistan - Typology, Age and Geodynamic Setting: *Geologische Rundschau*, v. 76, p. 245-264.

Dercourt, J., Ricou, L.E. and Vrielynck, B.E., 1993, Atlas Tethys, *Paleoenvironmental Maps*: Gautier-Villars, Paris.

Desio, A., 1959, Cretaceous beds between Karakorum and Hindu Kush ranges (central Asia): *Rivista Italiana di Paleontologia e Stratigrafia*, v. 65, p. 221-229.

—, 1963, Review of the geologic 'formations' of the western Karakorum (central Asia): *Rivista Italiana di Paleontologia e Stratigrafia*, v. 69, p. 475-501.

—, 1966, The Devonian sequence in Mastuj valley (Chitral, north West Pakistan): Rivista Italiana di Paleontologia e Stratigrafia, v. 72, p. 293-320

Desio, A. and Martina, E., 1972, Geology of the Upper Hunza Valley, Karakorum, West Pakistan: *Bollettino della Societa Geologica Italiana*, v. 91, p. 283-314.

Desio, A., Tongiorgi, E. and Ferrara, G., 1964, On the geological age of some granites of the Karakorum, Hindu Kush and Badakhshan (Central Asia): *Proceedings of the 22nd International Geological Congress*, Dehli, p. 479-496.

Desio, A., Premoli, S.I. and Rossi, R.C., 1977, On the Cretaceous outcrop in the Chumarkhan and Laspur valleys, Gilgit-Chitral, NW Pakistan: *Rivista Italiana di Paleontologia e Stratigrafia*, v. 83, p. 561-574.

DiPietro, J.A. and Isachsen, C.E., 2001, U-Pb zircon age from the Indian Plate in Northwest Pakistan and their significance to Himalayan and pre-Himalayan geologic history: *Tectonics*, v. 20, p. 510-525.

Dronov, V.I., Gazdzicki, A. and Melnikova, G.K., 1982, Die triassischen Riffe im suedoestlichen Pamir: *Facies*, v. 6, p. 107-128.

Ekström, G., Dziewonski, A.M., Maternovskaya, N.N. and Nettles, M., 2003, Global seismicity of 2001; centroid-moment tensor solutions for 961 earthquakes: *Physics of the Earth and Planetary Interiors*, v. 136, p. 165-185.

Erlank, A.J., Smith, H.S., Marchant, J.W., Cardoso, M.P. and Ahrens, L.H., 1978, Section 72-Hafnium, in Wedepohl, K.H., ed., *Handbook of Geochemistry*: Berlin-Heidelberg, Springer.

Etchecopar, A., Vasseur, G. and Daignieres, M., 1981, An inverse problem in microtectonics for the determination of stress tensors from fault striation analysis: *Journal of Structural Geology*, v. 3, p. 51-65.

Fermor, L.L., 1922, General report for the year 1921: *Records of the Geological Survey of India*, v. 54.

Fraser, J.E., Searle, M.P., Parrish, R.R. and Noble, S.R., 2001, Chronology of deformation, metamorphism and magmatism in the southern Karakoram Mountains: *Geological Society of America Bulletin*, v. 113, p. 1443-1455.

Fröhlich, C. and Giardini, D., 1992, Triangle diagrams; ternary graphs to display similarity and diversity of earthquake focal mechanisms: *Physics of the Earth and Planetary Interiors*, v. 75, p. 193-198.

Gaetani, M., 1997, The Karakorum Block in Central Asia, from Ordovician to Cretaceous: *Sedimentary Geology*, v. 109, p. 339-359.

Gaetani, M. and Leven, E., 1993, Permian stratigraphy and fusulinids from Rosh Gol (Chitral, E Hindu Kush): *Rivista Italiana di Paleontologia e Stratigrafia*, v. 99, p. 307-326.

Gaetani, M., Garzanti, E., Jadoul, F., Nicora, A., Tintori, A., Pasini, M. and Khan, K.S.A., 1990, The North Karakorum side of the Central Asia geopuzzle: *Geological Society of America Bulletin*, v. 102, p. 54-62.

Gaetani, M., Jadoul, F., Erba, E., Garzanti, E., Treloar, P.J. and Searle, M.P., 1993, Jurassic and Cretaceous orogenic events in the North Karakoram; age constraints from sedimentary rocks, *in* Treloar, P.J. and Searle, M.P., eds., *Himalayan tectonics*, *Geological Society Special Publications*, Geological Society of London, v. 74, p. 39-52.

Gaetani, M., LeFort, P., Tanoli, S., Angiolini, L., Nicora, A., Sciunnach, D. and Khan, A., 1996, Reconnaissance geology in upper Chitral, Baroghil and Karambar districts (northern Karakorum, Pakistan): *Geologische Rundschau*, v. 85, p. 683-704.

Gaetani, M., Zanchi, A., Angiolini, L., Olivini, G., Sciunnach, D., Brunton, H., Nicora, A. and Mawson, R., 2004, The Carboniferous of the Western Karakoram (Pakistan): *Journal of Asian Earth Sciences*, v. 23, p. 275-305.

Gansser, A., 1964, *The Geology of the Himalayas*: *Interscience*, 289 p.

George, M.T., Harris, N.B.W., Butler, R.W.H., Treloar, P.J. and Searle, M.P., 1993, The tectonic implications of contrasting granite magmatism between the Kohistan island arc and the Nanga Parbat-Haramosh Massif, Pakistan Himalaya, *in* Treloar, P.J. and Searle, M.P., eds., *Himalayan tectonics*, *Geological Society Special Publications*, Geological Society of London, v. 74, p. 173-191.

Godard, M., Jousselin, D. and Bodinier, J.L., 2000, Relationships between geochemistry and structure beneath a palaeo-spreading centre: a study of the mantle section in the Oman ophiolite: *Earth and Planetary Science Letters*, v. 180, p. 133-148.

Godfrey, L.V., Lee, D.C., Sangrey, W.F., Halliday, A.N., Salters, V.J.M., Hein, J.R. and White, W.M., 1997, The Hf isotopic composition of ferro-manganese nodules and crusts and hydrothermal manganese deposits: Implications for seawater Hf: *Earth and Planetary Science Letters*, v. 151, p. 91-105.

Golonka, J., Ross, M.I., Scotese, C.R., Embry, A.F., Beauchamp, B. and Glass, D.J., 1994, Phanerozoic paleogeographic and paleoclimatic modeling maps, Pangea; global environments and resources, *Canadian Society of Petroleum Geologists*, v. 17.

Gubler, V., 2001, Fission track analysis in North Pakistan, Diploma thesis, ETH Zürich, unpublished, 85 p.

Guillot, S., Garzanti, E., Baratoux, D., Marquer, D., Maheo, G. and de Sigoyer, J., 2003, Reconstructing the total shortening history of the NW Himalaya: *Geochemistry Geophysics Geosystems*, v. 4, no. 7, 1064.

Hanson, C.R., 1989, The northern suture in the Shigar Valley, Baltistan, northern Pakistan, *in* Malinconico, L.L.J. and Lillie, R.J., eds., *Tectonics of the western Himalayas*, *Geological Society of America*, *Special Paper*, v. 232, p. 203-215.

Hayden, H.H., 1915, Notes on the Geology of Chitral, Gilgit and the Pamir: *Records of the Geological Survey of India*, v. 45, p. 271-335.

Hildebrand, P.R., Noble, S.R., Searle, M.P. and Parrish, R.R., 1998, Tectonic significance of 24 Ma crustal melting in the eastern Hindu Kush, Pakistan: *Geology*, v. 26, p. 871-874.

Hildebrand, P.R., P., S.M., Shakirullah and van Heijst, H.J., 2000, Geological evolution of the Hindu Kush, NW Frontier Pakistan; active margin to continent-continent collision zone, *in* Khan, M.A., Treloar, P.J., Searle, M.P. and Jan, M.Q., eds., *Tectonics of the Nanga Parbat syntaxis and the western Himalaya*: *Geological Society Special Publications*, Geological Society of London, v. 170, p. 277-293.

Hildebrand, P.R., Noble, S.R., Searle, M.P., Waters, D.J. and Parrish, R.R., 2001, Old origin for an active mountain range: Geology and geochronology of the eastern Hindu Kush, Pakistan: *Geological Society of America Bulletin*, v. 113, p. 625-639.

Honegger, K., Dietrich, V., Frank, W., Gansser, A., Thoni, M. and Trommsdorff, V., 1982, Magmatism and Metamorphism in the Ladakh Himalayas (the Indus-Tsangpo Suture Zone): *Earth and Planetary Science Letters*, v. 60, p. 253-292.

International Commission on Stratigraphy, 2003, International Stratigraphic Chart: www.eas.purdue.edu/chronos/Divisons_GeolTimeUSGS.pdf.

Ivanac, J.F., Traves, D.M. and King, D., 1956, The geology of the north-west portion of the Gilgit agency: *Records of the Geological Survey of Pakistan*, v. 8, p. 3-29.

Jaeger, J.J., Courtillot, V. and Tapponnier, P., 1989, Paleontological View of the Ages of the Deccan Traps, the Cretaceous Tertiary Boundary and the India-Asia Collision: *Geology*, v. 17, p. 316-319.

Jagoutz, O., Launeau, P. and Burg, J.P., 2001, The NW-Himalaya (Pakistan-Afghanistan) seen from Space: *Journal of Asian Earth Sciences,*

Special Abstracts Issue: 16th Himalaya-Karakorum-Tibet Workshop, Austria, 2001, v. 19.

Jan, M.Q., 1988, Geochemistry of Amphibolites from the Southern Part of the Kohistan Arc, N-Pakistan: *Mineralogical Magazine*, v. 52, p. 147-159.

Jan, M.Q. and Howie, R.A., 1981, The Mineralogy and Geochemistry of the Metamorphosed Basic and Ultrabasic Rocks of the Jijal Complex, Kohistan, NW Pakistan: *Journal of Petrology*, v. 22, p. 85-126.

Jan, M.Q. and Mian, I., 1971, Preliminary geology and petrography of Swat Kohistan: *Geological Bulletin of the University of Peshawar*, v. 6, p. 1-32.

Jan, M.Q. and Tahirkheli, R.A.K., 1979, Petrography of the amphibolites of Swat and Kohistan, In: *Geology of Kohistan, Karakoram Himalaya, northern Pakistan: Geological Bulletin of the University of Peshawar*, v. 11, p. 51-64.

Kakar, S.K., Mian, S.B. and Khan, J., 1971, The geology of Jandul valley, western Dir: *Geological Bulletin of the University of Peshawar*, v. 6, p. 54-73.

Kaneko, Y., Katayama, I., Yamamoto, H., Misawa, K., Ishikawa, M., Rehman, H.U., Kausar, A.B. and Shiraishi, K., 2003, Timing of Himalayan ultrahigh-pressure metamorphism: sinking rate and subduction angle of the Indian continental crust beneath Asia: *Journal of Metamorphic Geology*, v. 21, p. 589-599.

Kapp, P., Murphy, M.A., Yin, A., Harrison, T.M., Ding, L. and Guo, J.H., 2003, Mesozoic and Cenozoic tectonic evolution of the Shiquanhe area of western Tibet: *Tectonics*, v. 22(4), 1029.

Kazmi, A.H. and Jan, M.Q., 1997, *Geology and tectonics of Pakistan*, Graphic Publishers. Nazimabad, Pakistan, 554 p.

Khan, J., 1979, Geology of the Baraul Valley, Dir: *Geological Bulletin of the University of Peshawar*, v. 11, p. 153-162.

Khan, M.A., Jan, M.Q., F., W.B., Tarney, J., F., T.M., Malinconico L. L., J. and J., L.R., 1989, The Chilas mafic-ultramafic igneous complex; the root of the Kohistan island arc in the Himalaya of northern Pakistan, *in* Malinconico, L.-L. and Lillie, R.-J., eds., *Tectonics of the western Himalayas*, *Geological Society of America, Special Paper*, v. 232, p. 75-94.

Khan, M.A., Jan, M.Q., Weaver, B.L., Treloar, P.J. and Searle, M.P., 1993, Evolution of the lower arc crust in Kohistan, N. Pakistan; temporal arc magmatism through early, mature and intra-arc rift stages, *in* Treloar, P.J. and Searle, M.P., eds., *Himalayan tectonics, Geological Society Special Publications*, Geological Society of London, v. 74, p. 123-138.

Khan, S.D., Stern, R.J., Manton, M.I., Copeland, P., Kimura, J.I. and Khan, M.A., 2004, Age, geochemical and Sr-Nd-Pb isotopic constraints for mantle source characteristics and petrogenesis of Teru volcanics,

Northern Kohistan terrane, Pakistan: *Tectonophysics*, v. 393, p. 263-280.

Khan, T., Khan, M.A., Jan, M.Q. and Latif, M., 1995, Geology of a part of the Kohistan Terrane between Gilgit and Chilas, North Pakistan; regional tectonic implications: *First Nepal geological congress*, v. 12, p. 9.

Kretz, R., 1983, Symbols for Rock-Forming Minerals: *American Mineralogist*, v. 68, p. 277-279.

Krogh, T.E., 1973, Low-Contamination Method for Hydrothermal Decomposition of Zircon and Extraction of U and Pb for Isotopic Age Determinations: *Geochimica Et Cosmochimica Acta*, v. 37, p. 485-494.

-, 1982a, Improved Accuracy of U-Pb Zircon Dating by Selection of More Concordant Fractions Using a High-Gradient Magnetic Separation Technique: *Geochimica Et Cosmochimica Acta*, v. 46, p. 631-635.

-, 1982b, Improved Accuracy of U-Pb Zircon Ages by the Creation of More Concordant Systems Using an Air Abrasion Technique: *Geochimica Et Cosmochimica Acta*, v. 46, p. 637-649.

Kuno, H., 1968, Differentiation of basalt magmas, in Hess, H.H. and Poldervaart, A., eds., *Basalts: The Poldervaart treatise on rocks of basaltic composition*: New York and London, Interscience Publishers. v. 2, p. 623-688.

Lacassin, R., Valli, F., Arnaud, N., Leloup, P.H., Paquette, J.L., Haibing, L., Tapponnier, P., Chevalier, M.L., Guillot, S., Maheo, G. and Xu, Z.Q., 2004, Large-scale geometry, offset and kinematic evolution of the Karakorum fault, Tibet: *Earth and Planetary Science Letters*, v. 219, p. 255-269.

Lawrence, R.D., Hasan Khan, S., Nakata, T., Buckman, R.C. and Hancock, P.L., 1992, Chaman Fault, Pakistan-Afghanistan, Major active faults of the world; *results of IGCP Project 206*.

Le Fort, P., 1994, Discovery of crystalline basement and Early Ordovician marine transgression in the Karakorum mountain range; Pakistan: *Geology*, v. 22, p. 941-944.

Le Fort, P., Michard, A., Sonet, J. and Zimmermann, J.L., 1983, Petrography, geochemistry and geochronology of some samples from the Karakoram Axial Batholith, Pakistan, in Shams, F.A., ed., *Granites of Himalayas, Karakoram and Hindu Kush*: Lahore, University of Lahore, p. 277-387.

Le Maitre, R.W., Bateman, P., Dudek, A., Keller, J., Lameyre Le Bas, M.J., Sabine, P.A., Schmid, R., Soresen, H., Streckeisen, A., Woolley, A.R. and Zanettin, B., 1989, *A Classification of Igneous Rocks and Glossary of Terms*: Oxford, Blackwell, 252 p.

Ludwig, K.R., 2001, Isoplot/Ex: *Berkeley Geochronology Center, v. Special Publication*.

Matsushita, S. and Huzita, K., 1965, Geology of the Karakoram and Hindu Kush. *Results of the Kyoto University Scientific Expedition to the Karakoram and Hindu Kush*. Kyoto, Japan: Kyoto University Press, 160 p.

Mcdonough, W.F. and Sun, S.S., 1995, The Composition of the Earth: *Chemical Geology*, v. 120, p. 223-253.

Miller, D.J., Loucks, R.R. and Ashraf, M., 1991, Platinum-Group Element Mineralization in the Jijal Layered Ultramafic-Mafic Complex, Pakistani Himalayas: *Economic Geology and the Bulletin of the Society of Economic Geologists*, v. 86, p. 1093-1102.

Molnar, P. and Tapponnier, P., 1975, Cenozoic Tectonics of Asia - Effects of a Continental Collision: *Science*, v. 189, p. 419-426.

Mostrioukov, A.O. and Petrov, V.A., 1994, Catalogue of Focal Mechanisms of Earthquakes 1964-1994: *Materials of the World Data Center B*, *Moscow*, p. 87.

NEIC, 2004, http://neic.usgs.gov/neis/epic/epic.html.

Nowell, G.M., Kempton, P.D., Noble, S.R., Fitton, J.G., Saunders, A.D., Mahoney, J.J. and Taylor, R.N., 1998, High precision Hf isotope measurements of MORB and OIB by thermal ionisation mass spectrometry; insights into the depleted mantle: *Chemical Geology*, v. 149, p. 211-233.

O'Brien, P.J., Zotov, N., Law, R., Khan, M.A. and Jan, M.Q., 2001, Coesite in Himalayan eclogite and implications for models of India-Asia collision: *Geology*, v. 29, p. 435-438.

Parrish, R.R. and Tirrul, R., 1989, U-Pb age of the Baltoro Granite, Northwest Himalaya and implications for monazite U-Pb systematics: *Geology*, v. 17, p. 1076-1079.

Pascoe, E.H., 1923, General report for the year 1922: *Records of the Geological Survey of India*, v. 55.

—, 1924, General report for the year 1923: *Records of the Geological Survey of India*, v. 56.

Patchett, P.J. and Tatsumoto, M., 1980, Hafnium isotope variations in oceanic basalts: *Geophysical Research Letters*, v. 7, p. 1077-1080.

Pearce, J.A., Kempton, P.D., Nowell, G.M. and Noble, S.R., 1999, Hf-Nd element and isotope perspective on the nature and provenance of mantle and subduction components in Western Pacific arc-basin systems: *Journal of Petrology*, v. 40, p. 1579-1611.

Pearce, J.A. and Peate, D.W., 1995, Tectonic Implications of the Composition of Volcanic Arc Magmas: *Annual Review of Earth and Planetary Sciences*, v. 23, p. 251-285.

Pegler, G. and Das, S., 1998, An enhanced image of the Pamir Hindu Kush seismic zone from relocated earthquake hypocentres: *Geophysical Journal International*, v. 134, p. 573-595.

Peltzer, G. and Tapponnier, P.I., 1988, Formation and evolution of strike-slip faults, rifts and basins during the India-Asia collision; an experimental approach: *Journal of Geophysical Research*, v. 93, p. 15085-15117.

Petterson, M.G. and Treloar, P.J., 2004, Volcanostratigraphy of arc volcanic sequences in the Kohistan arc, North Pakistan: volcanism within island arc, back-arc-basin, and intra-continental tectonic settings: *Journal of Volcanology and Geothermal Research*, v. 130, p. 147-178.

Petterson, M.G. and Windley, B.F., 1985, Rb-Sr dating of the Kohistan arc-batholith in the Trans-Himalaya of North Pakistan, and tectonic implications: *Earth and Planetary Science Letters*, v. 74, p. 45-57.

—, 1986, Petrological and geochemical evolution of the Kohistan arc-batholith, Gilgit, N. Pakistan: *Geological Bulletin of the University of Peshawar*, v. 19, p. 121-149.

Petterson, M.G., Windley, B.F., and Luff, I.W., 1991, The Chalt Volcanics, Kohistan, N Pakistan; high-Mg tholeiitic and low-Mg calc-alkaline volcanism in a Cretaceous island arc; *Geology and geodynamic evolution of the Himalayan collision zone*; Part 1, in Sharma, K. K., ed.: *Physics and Chemistry of the Earth*: Oxford-New York-Toronto, v. 17, p. 19-30.

Philip, H. 1987, Plio-Quaternary evolution of the stress field in Mediterranean zones of subduction and collision: Annales Geophysicae, Series B: *Terrestrial and Planetary Physics*, v. 5, p. 301-319.

Pudsey, C.J., 1986, The Northern Suture, Pakistan; margin of a Cretaceous island arc: *Geological Magazine*, v. 123, p. 405-423.

Pudsey, C.J., Coward, M.P., Luff, I.W., Shackleton, R.M., Windley, B.F., and Jan, M.Q., 1985, Collision zone between the Kohistan Arc and the Asian Plate in NW Pakistan: *Transactions of the Royal Society of Edinburgh: Earth Sciences*, v. 76, p. 463-479.

Pudsey, C.J., Schroeder, R., Skelton, P.W., and Gupta, V.J., 1985b, Cretaceous (Aptian/Albian) age for island-arc volcanics, Kohistan, N. Pakistan, *in* Gupta, V.J., ed., *Geology of Western Himalayas (Contributions to Himalayan Geology)*, *Hindustan Publishing Corporation*. Delhi, India. v. 3, p. 150-168.

Ramsay, J.G. and Huber, M.I., 1987, *The techniques of modern Structural Geology, Volume 2: Folds and Fractures*: London, Academic Press, 392 p.

Ricou, L.E., 1994, Tethys Reconstructed - Plates, Continental Fragments and Their Boundaries since 260-Ma from Central-America to South-Eastern Asia: *Geodinamica Acta*, v. 7, p. 169-218.

Robertson, A.H.F., Collins, A.S., Wang, C., Wilson, C.J.L., and Searle, M.P., 2002, Shyok suture zone, N Pakistan; late Mesozoic-Tertiary evolution of a critical suture separating the oceanic Ladakh Arc from the Asian continental margin: *Journal of Asian Earth Sciences (15th*

international Himalaya-Karakoram-Tibet workshop), v. 20, p. 309-351.

Robinson, J., Beck, R., Gnos, E., and Vincent, R.K., 2000, New structural and stratigraphic insights for northwestern Pakistan from field and Landsat Thematic Mapper data: *Geological Society of America Bulletin*, v. 112, p. 364-374.

Roecker, S.W., 1982, Velocity Structure of the Pamir-Hindu-Kush Region - Possible Evidence of Subducted Crust: *Journal of Geophysical Research*, v. 87, p. 945-959.

Rolland, Y., Pecher, A., and Picard, C., 2000, Middle Cretaceous back-arc formation and arc evolution along the Asian margin; the Shyok suture zone in northern Ladakh (NW Himalaya): *Tectonophysics*, v. 325, p. 145-173.

Rolland, Y., Maheo, G., Guillot, S., and Pecher, A., 2001, Tectono-metamorphic evolution of the Karakorum Metamorphic complex (Dassu-Askole area, NE Pakistan): exhumation of mid-crustal HT-MP gneisses in a convergent context: *Journal of Metamorphic Geology*, v. 19, p. 717-737.

Rolland, Y., Picard, C., Pecher, A., Carrio, E., Sheppard, S.M.F., Oddone, M., and Villa, I.M., 2002, Presence and geodynamic significance of Cambro-Ordovician series of SE Karakoram (N Pakistan): *Geodinamica Acta*, v. 15, p. 1-21.

Rossi, C., and Farioli, A., 1977, Rudists and nerineids of north-west Pakistan Cretaceous: *Revista Italiana di Paleontologia e Stratigrafia*, v. 65, p. 91-96.

Schärer, U., Copeland, P., Harrison, T.M., and Searle, M.P., 1990, Age, cooling history, and origin of post-collisional leucogranites in the Karakoram Batholith; a multi-system isotope study: *Journal of Geology*, v. 98, p. 233-251.

Schaltegger, U., G. Zeilinger, Frank, M., and Burg, J.P., 2002, Multiple mantle sources during island arc magmatism: U-Pb and Hf isotopic evidence from the Kohistan arc complex, Pakistan: *Terra Nova*, v. 14, p. 461-468.

Schaltegger, U., Frank, M., and Burg, J.P., 2003, A 120 million years record of magmatism and crustal melting in the Kohistan Batholith: *Geophysical Research Abstracts*; *EGS-AGU-EUG Joint Assembly*, Nice, France, v. 5.

Schreiber, A., Wittekindt, H.P., Wolfart, R., and Weippert, D., 1972, Geology and Petroleum Potentials of Central and South Afghanistan: *American Association of Petroleum Geologists Bulletin*, v. 56, p. 1494-1519.

Searle, M.P., 1991, *Geology and tectonics of the Karakoram Mountains*, Chichester, UK. J. Wiley and Sons. 358 p.

Searle, M.P., and Tirrul, R., 1991, Structural and thermal evolution of the Karakoram crust: J*ournal of the Geological Society of London*, v. 148, p. 65-82.

Searle, M.P., Rex, A.J., Tirrul, R., Rex, D.C., Barnicoat, A.C. and Windley, B.F., 1989, Metamorphic, magmatic, and tectonic evolution of the central Karakoram in the Biafo-Baltoro-Hushe regions of northern Pakistan, *in* Malinconico, L.-L. and Lillie, R.-J., eds., *Tectonics of the western Himalayas, Geological Society of America, Special Paper*, v. 232, p. 47-74.

Searle, M.P., Parrish, R.R., Tirrul, R., and Rex, D.C., 1990, Age of Crystallization and Cooling of the K2 Gneiss in the Baltoro Karakoram: *Journal of the Geological Society*, v. 147, p. 603-606.

Searle, M.P., Crawford, M.B., and Rex, A.J., 1992, Field Relations, Geochemistry, Origin and Emplacement of the Baltoro Granite, Central Karakoram: *Transactions of the Royal Society of Edinburgh-Earth Sciences*, v. 83, p. 519-538.

Searle, M.P., Khan, M.A., Fraser, J.E., Gough, S.J., and Jan, M.Q., 1999, The tectonic evolution of the Kohistan-Karakoram collision belt along the Karakoram Highway transect, North Pakistan: *Tectonics*, v. 18, p. 929-949.

Sengör, A.M.C., 1984, The Cimmeride orogenic system and the tectonics of Eurasia, *Geological Society of America, Special paper*, v. 195, 85 p.

Sergeev, S., Burg, J.P., and Chaudhry, N., 2001, Albian magmatism in the Karakorum Arc (Hunza Valley, Pakistan): New bracketing Ages for the Karakorum-Kohistan Accretion: *Journal of conference abstracts, EUG 11*, Strasbourg, v. 6(1), p. 597.

Smith, H.A., 1993, Characterization and timing of metamorphism within the Indo-Asian suture-zone, Himalayas, northern Pakistan. Ph.D. thesis: Hannover, New Hampshire, Dartmouth College, 196 p.

Spencer, D.A., and Gebauer, D., 1996, SHRIMP evidence for a Permian age and 44 Ma metamorphic age for the Himalayan eclogites (Upper Kaghan, Pakistan): Implications for the subduction of Tethys and the subdivision terminology of the NW Himalaya, in Marcfarlane, A.M., Sorkhabi, R.B., and Quade, J., eds., *Himalaya-Karakoram-Tibet Workshop 11th*, Flagstaff, Arizona, USA, *Abstracts*, p. 147-150.

Stacey, J.S. and Kramers, J.D., 1975, Approximation of terrestrial lead isotope evolution by a two-stage model.: *Earth and Planetary Science Letters*, v. 26, p. 207-221.

Sun, S.S. and McDonough, W.F., 1989, Chemical and isotopic systematics of oceanic basalts: implications for mantle composition and processes, *in* Saunders, A.D. and Norry, M.J., eds., *Magmatism in oceanic basins*, Geological Society of London, Special Publication, v. 42, p. 313-345.

Tahirkheli, M., Tahir Shah, M. and Khan, M.A., 1997, Mineralogical, isotopic and fluid inclusion studies of copper mineralisation in Drosh-Shishi area, Chitral, Northern Pakistan, *in* Hussain, S.S. and Dawood, H., eds., *Economic Geology of Pakistan*. Islamabad, *Pakistan Museum of Natural History, Pakistan Science Foundation*, Ministry of Science and Technology, Islamabad, p. 59-71.

Tahirkheli, R.A.K., Mattauer, M., Proust, F., Tapponnier, P., Abul, F. and DeJong, K.A., 1979, The India-Eurasia suture zone in northern Pakistan; synthesis and interpretation of recent data at plate scale, Geodynamics of Pakistan, *Geological Survey of Pakistan*. Quetta Pakistan.

Talent, J.A., Conaghan, P.J., Mawson, R., Molloy, P.D. and Pickett, J.W., 1982, Intricacy of tectonics in Chitral (Hindu Kush); faunal evidence and some regional implications, Himalayan geology, Volume 41: Calcutta India, *Geological Survey of India - Miscellaneous Publications*, p. 77-101.

Tapponnier, P., Mattauer, M., Proust, F., and Cassaigneau, C., 1981, Mesozoic Ophiolites, Sutures, and Large-Scale Tectonic Movements in Afghanistan: *Earth and Planetary Science Letters*, v. 52, p. 355-371.

Tapponnier, P., Peltzer, G., and Armijo, R., 1986, On the mechanics of the collision between India and Asia, *in* Coward, M.P. and Ries-Alison, C., eds., *Collision tectonics, Geological Society Special Publications*, Geological Society of London, v. 19, p. 115-157.

Tatsumi, Y., Hamilton, D.L., and Nesbitt, R.W., 1986, Chemical Characteristics of Fluid Phase Released from a Subducted Lithosphere and Origin of Arc Magmas - Evidence from High-Pressure Experiments and Natural Rocks: *Journal of Volcanology and Geothermal Research*, v. 29, p. 293-309.

Thakur, V.C., Virdi, N.S., Rai, H., and Gupta, K.R., 1981, A Note on the Geology of Nubra-Shyok Area of Ladakh, Kashmir, Himalaya: *Journal of the Geological Society of India*, v. 22, p. 46-50.

Tonarini, S., Villa, I.M., Oberli, F., Meier, M., Spencer, D.A., Pognante, U., and Ramsay, J.G., 1993, Eocene Age of Eclogite Metamorphism in Pakistan Himalaya - Implications for India Eurasia Collision: *Terra Nova*, v. 5, p. 13-20.

Treloar, P.J., Rex, D.C., Guise, P.G., Coward, M.P., Searle Michael, P., Windley, B.F., Petterson, M.G., Jan, M.Q., and Luff, I.W., 1989, K-Ar and Ar-Ar geochronology of the Himalayan collision in NW Pakistan; constraints on the timing of suturing, deformation, metamorphism and uplift: *Tectonics*, v. 8, p. 881-909.

Treloar, P.J., Brodie, K.H., Coward, M.P., Jan, M.Q., Khan, M.A., Knipe, R.J., Rex, D.C., Williams, M.P., Salisbury, M.H., and Fountain, D.M., 1990, The evolution of the Kamila shear zone, Kohistan, Pakistan, *in*

Fountain, D. M. and Salisbury, M. H., eds., *Exposed cross-sections of the continental crust*, Volume Series C: *Mathematical and Physical Sciences*. 317, D. Reidel Publishing Company. Dordrecht-Boston International, p. 175-214.

Treloar, P.J., Petterson, M.G., Jan, M.Q., and Sullivan, M.A., 1996, A re-evaluation of the stratigraphy and evolution of the Kohistan Arc sequence, Pakistan Himalaya; implications for magmatic and tectonic arc-building processes: *Journal of the Geological Society of London*, v. 153, p. 681-693.

Vervoort, J.D., Patchett, P.J., Gehrels, G.E., and Nutman, A.P., 1996, Constraints on early Earth differentiation from hafnium and neodymium isotopes: *Nature*, v. 379, p. 624-627.

Vervoort, J.D., Patchett, P.J., Blichert-Toft, J., and Albarede, F., 1999, Relationships between Lu-Hf and Sm-Nd isotopic systems in the global sedimentary system: *Earth and Planetary Science Letters*, v. 168, p. 79-99.

Weinberg, R.F., and Dunlap, W.J., 2001, Comment on 'Middle Cretaceous back-arc formation and arc evolution along the Asia margin: the Shyok Suture Zone in northern Ladakh (NW Himalaya)' by Rolland and Pecher: *Tectonophysics*, v. 340, p. 265-268.

Weinberg, R.F., Dunlap, W.J., and Whitehouse, M., 2000, New field, structural and geochronological data from the Shyok and Nubra valleys, northern Ladakh: linking Kohistan to Tibet, *in* Khan, M.A., Treloar, P.J., Searle, M.P. and Jan, M.Q., eds., *Tectonics of the Nanga Parbat syntaxis and the western Himalaya: Geological Society Special Publications*, Geological Society of London, v. 170, p. 253-275.

White, W.M., and Patchett, J., 1984, Hf-Nd-Sr Isotopes and Incompatible Element Abundances in Island Arcs - Implications for Magma Origins and Crust-Mantle Evolution: *Earth and Planetary Science Letters*, v. 67, p. 167-185.

Wilson, M., 1989, *Igneous Petrogenesis*: London, Unwin Hyman.

Woodhead, J.D., Hergt, J.M., Davidson, J.P., and Eggins, S.M., 2001, Hafnium isotope evidence for 'conservative' element mobility during subduction zone processes: *Earth and Planetary Science Letters*, v. 192, p. 331-346.

World Stress Map, Release, 2004, http://www-wsm.physik.uni-karlsruhe.de.

Yamamoto, H., 1993, Contrasting Metamorphic P-T-Time Paths of the Kohistan Granulites and Tectonics of the Western Himalayas: *Journal of the Geological Society*, v. 150, p. 843-856.

Yamamoto, H., and Nakamura, E., 1996, Sm-Nd dating of garnet granulites from the Kohistan complex, northern Pakistan: *Journal of the Geological Society*, v. 153, p. 965-969.

Yamamoto, H., Nakamura, E., Khan, M.A., Treloar, P.J., Searle, M.P., and Jan, M.Q., 2000, Timing of magmatic and metamorphic events in the

Jijal Complex of the Kohistan Arc deduced from Sm-Nd dating of mafic granulites, *in* Khan, M.A., Treloar, P.J., Searle, M.P. and Jan, M.Q., eds., *Tectonics of the Nanga Parbat syntaxis and the western Himalaya: Geological Society Special Publications*, Geological Society of London, v. 170, p. 313-319.

Zanchi, A., 1993, Structural evolution of the North Karakoram cover, North Pakistan, *in* Treloar, P.J., and Searle, M.P., eds., *Himalayan tectonics, Geological Society Special Publications*, Geological Society of London. v. 74, p. 21-38.

Zanchi, A., and Gaetani, M., 1994, Introduction to the geological map of the North Karakorum terrain from the Chapursan Valley to the Shimshal Pass 1:150,000 scale: *Rivista Italiana di Paleontologia e Stratigrafia*, v. 100, p. 125-136.

Zanchi, A., and Gritti, D., 1996, Multistage structural evolution of Northern Karakorum (Hunza region, Pakistan): *Tectonophysics*, v. 260, p. 145-165.

Zanchi, A., Gaetani, M., and Poli, S., 1997, The Rich Gol metamorphic complex; evidence of separation between Hindu Kush and Karakorum (Pakistan): *Compte Rendus de l'Académie des Sciences, Series IIA - Earth and Planetary Science*, v. 325, p. 877-882.

Zanchi, A., Poli, S., Fumagalli, P., and Gaetani, M., 2000, Mantle exhumation along the Tirich Mir fault zone, NW Pakistan; pre-mid-Cretaceous accretion of the Karakoram terrane to the Asian margin, *in* Khan, M.A., Treloar, P.J., Searle, M.P. and Jan, M.Q., eds., *Tectonics of the Nanga Parbat syntaxis and the western Himalaya: Geological Society Special Publications*, Geological Society of London, v. 170, p. 237-252.

Zeilinger, G., 2002, Structural and geochronological study of the lowest Kohistan complex, Indus region in Pakistan, NW Himalaya, Ph.D. thesis, ETH Zürich, 243 p.

Zeilinger, G., Burg, J.P., Chaudhry, N., Dawood, H., and Hussain, S., 2000, Fault systems and Paleo-stress tensors in the Indus Suture Zone (NW Pakistan): *Journal of Asian Earth Sciences*, v. 18, p. 547-559.

Zeitler, P.K., 1985, Cooling History of the Nw Himalaya, Pakistan: *Tectonics*, v. 4, p. 127-151.

Zeitler, P., Tahirkheli, R.A.K., Naeser, C., Johnson, N., and Lyons, J., 1981, Preliminary fission track ages from the Swat valley, Northern Pakistan: *Geological Bulletin of the University of Peshawar*, v. 13, p. 63-65.

Curriculum Vitae

Stefan Heuberger, born on August 6, 1976 in St.Gallen, Switzerland
citizen of Sirnach (TG), Rickenbach (TG) and Wilen (TG), Switzerland

Education

2004 - present	Post graduate course “Räumliche Informationssysteme”, ETH Zürich.
2001 - 2004	Ph.D. at the Geological Institute, Departement of Earth Sciences, ETH Zürich. Ph.D. thesis: “Kinematics of the Karakoram-Kohistan Suture Zone, Chitral, NW Pakistan”. Supervisors: Prof. Dr. J.-P. Burg and Prof. Dr. U. Schaltegger
1999 - 2001	Diploma thesis at the Geological Institute, Departement of Earth Sciences, ETH Zürich. Title: “Mapping and structural analysis on the North-Kohistan Suture (Upper Shishi Valley, Chitral, NW Pakistan). Supervisor: Prof. Dr. J.-P. Burg.
1996 - 2001	Study and Diploma (M.Sc.) in Earth Sciences, Departement of Earth Sciences, ETH Zürich.
1991 - 1996	Grammar school, type C (mathematical and natural sciences), Kantonsschule am Burggraben, St.Gallen.
1989 - 1991	Secondary school, Katholische Kantonssekundarschule, St.Gallen.
1983 - 1989	Primary school, Boppartshof, St.Gallen.

International conferences and workshops

International Geological Congress (IGC 32), Firenze (I), 2004;
EGS-AGU-EUG Joint Assembly, Nice (F), 2003;
Himalaya-Karakoram-Tibet Workshop (HKTW 18), Monte Verità (CH), 2003;
Symposium Tektonik-Strukturgeologie-Kristallingeologie (TSK 9), Erlangen (D), 2002;
Structure and Tectonics of Convergent Plate Margins, Summer School/ Workshop, Zahradky Castle (CZ), 2002;
Geological Interpretation of Airborne Geophysical Data Sets, LMTG Toulouse (F), 2002;
Himalaya-Karakoram-Tibet Workshop (HKTW 16), Graz (A), 2001.